Delft University of Technology

Towards a Stall Model for the Fokker 100

A foundation for research regarding the influence of a swept wing configuration on aerodynamic stall

Peter C. Luteijn BSc

June 30th, 2020

TUDelft

THIS PAGE IS INTENTIONALLY LEFT BLANK

Towards A Stall Model For The Fokker 100

A foundation for research regarding the influence of a swept wing configuration on aerodynamic stall

by

Peter C. Luteijn BSc

to obtain the degree of Master of Science
at the Delft University of Technology,
to be defended publicly
on Thursday June 30th, 2022 at 2:00 PM.

Student number	:	9534256	
Project duration	:	June 1, 2018 – June 30, 2022	
Thesis committee	:	Dr. ir. C. C. de Visser,	TU Delft, chairman, supervisor
		Dr. ir. D. M. Pool,	TU Delft
		Dr. ir. W. van der Wal,	TU Delft, external

TU Delft

"To my mother who isn't with me anymore."

"To my father who cannot think anymore."

"Thank you for all you have given me,

and all that I could have asked for …"

Preface

This thesis can be considered a technical extensive archaeological research project, a pioneering endeavor in salvaging a Dutch historical legacy. And should therefor not be taken lightly, because the efforts invested, and resources needed to reach this foundation for future research, wasn't as apparent as one might think. It forced the course of this thesis to solely focus on the data preparation phase on the road to aerodynamic stall model identification.

Straight from the start it wasn't clear if the Fokker supplied historical documentation, and datasets were sufficient for proper stall model research. Although having been able to decipher the Fokker/NLR compressed measurement's database at Fokker Services BV (Hoofddorp), actually knowing if the obtained stall flight-tests are useful, is a whole different game. Some quick preliminary study into the available data showed gaps, corruptions, and discontinuities, where some crucial parameters (Fokker terminology for a data measurement sets) were completely missing. Luckily this did not impair most raw data measurements, and leaves this research with more than enough usable datasets in the end.

After having managed to achieve a decent grip on the available data, the second obstacle showed his face. In order to accurately determine the aerodynamic forces and moments acting on the aircraft, a mass model must be available. At first, it was presumed that the inertial data was present in the Fokker archive files, or at least obtainable through the "Standard Calculations" documentation supplied by Fokker. This was not the case, and lead to the decision requesting more information form Fokker, where they gave us loading documentation and prototype inertial data. Both aiding in the creation of a highly accurate mass model, capable of simulating fuel and water ballast tank loading.

A third hurdle was also quickly identified as missing and/or incomplete Fokker calculated engine thrust values. Where stall model identification is concerned, thrust-output is always considered to be part of the equation and thus cannot be ignored. Most thrust calculations where available during the actual stall, but never covered a complete recording. All required measurement datasets were available, but the calculation methods were severely lacking in completeness. It was therefore decided to create an engine model based OLS techniques, which resulted in fairly accurate results for the left-engine. Yet the right-engine wasn't overly exited during testing, and as is discussed did not achieve the same fidelity.

Having obtained a highly accurate mass- and a reasonably working engine model, things moved into an area where everything could be managed better. After having spent a large amount of time on the mass- and engine model, flight path reconstruction still had to be performed. Where one can imagine, that trying to filter data that is not your own, might be tampered with, and yield broken filters. As such was the case, which lead to heavily simplifying the kinematic model to a six state aerodynamic model, leading to an acceptable converging filter performance.

All this was mostly done by February 2020, but still needed a large amount of work in the writing department. And as faith has it, the Covid crisis started while I was in the midst of a severe family dispute, with a very sick parent on top of this. I will not go into any details, but these activities took most of my physical and mental resources, leading to a heavily delayed graduation. During this time my supervisor dr.ir. Coen de Visser has been an abundant resource of positivity and motivation, I am happy that he stuck with me, and helped me to bring this thesis to an end. It is very much appreciated, while I am still sad that I wasn't able to obtain my research goal due to the nature of this pioneering thesis work. I believe this body of work will aid future research willing to use historical commercial flight-testing data, while at the same time preserving a Dutch national aviation legacy.

As to an equally important note, this thesis would not have been possible if it weren't for the continuous assistance from Dirk van Os (Chief Engineer, Fokker Services BV). Dirk's encyclopedia-like knowledge regarding the Fokker aircraft has been of immeasurable benefit to this thesis, and to other projects that have sparked of the TU Delft / Fokker partnership. Furthermore, I would like to express my gratitude to dr.ir. Daan Pool, who has always been fiercely critical/helpful and an abundant source of new ideas. While off coarse not forgetting the complete academic staff at the department of Control & Operations who have always provided aid and assistance with anything that came my way, especially Harold Thung who helped with setting up the Fokker SQL database.

Finally leaving with a small note about the people I have studied with, specially the members of the (late-) Upperhouse student-room on the third floor in the main building. It has been a privilege getting to know you all, and meeting everyone for beers on Wednesdays and Fridays. Simon, Sven, Mark, Imrul, Jerry, Michiel, Jesse E., Jesse H., Joeri, Bas, Stephan, it has been an amazing time, I will miss getting coffees with that horrible panda-bear!

Peter C. Luteijn BSc
Delft, June 2022

THIS PAGE IS INTENTIONALLY LEFT BLANK

Contents

THIS PAGE IS INTENTIONALLY LEFT BLANK

List of Figures

List of Tables

Nomenclature

General Acronyms

ASMI	Aerodynamic Stall Model Identification
CG	Center of gravity
EKF	Extended Kalman Filter
FAA	Federal Aviation Administration
GE	General Aviation
ICAO	International Civil Aviation Organization
IEEE	Institute of Electrical and Electronics Engineers
IEKF	Iterated Extended Kalman Filter
IQR	Inter-quartile range
JAR21	Joined Aviation Requirements 21
LOC	Loss of Control
LQE	Linear Quadratic Estimation
NDA	Non Disclosure Agreement
NLR	Nationaal Lucht- en Ruimtevaartlaboratorium
NRC-IAR	National Research Council - Institute for Aeronautical Research
NTSB	National Transportation Safety Board
SI	International System of Units
SRS	Simona Research Simulator
TCDS	Type Certificate Data Sheets

Fokker Acronyms - Aircraft

ENG	Engines
F100	F28 ~ MK-0100
F130	F28 ~ MK-0130
F27	Fokker Friendship (prop, straight-wing)
F28	Fokker Fellowship (jet, swept-wing)
F50	F27 ~ MK-0050
F60	F27 ~ MK-0604
F70	F28 ~ MK-0070
FUS	Fuselage
HSB	Horizontal stabilizer
MUC	Main undercarriage
NUC	Nose undercarriage
OEW	Operating empty weight
OI	Operator items
PROTO	Prototype designation
SERIE	Serie designation
SI	Standard items
VSB	Vertical stabilizer
WNG	Main wing

Fokker Acronyms - MRVS

ABBR	Parameter abbreviation
ACID	Aircraft serial number
ACMK	Aircraft mark
ACTP	Aircraft type
AFT	Rear section of the aircraft
ATAC	Air Transport Association - Chapter
ATAS	Air Transport Association - Section
CAT	Flight-test category
CDT	Cumulative time (decimal-vector)
CDV	Cumulative parameter value (decimal-vector)
COMP	Compression used
DATE	Flight date
DESCR	Parameter description
DMOD	Delta-Modulation
DRON	Data reduction order number
DRSN	Data reduction station name
DT	Incremental time (decimal-vector)
DV	Incremental parameter (decimal-vector)
DW	ASCII character measurement string
EQD	Equidistant delta-modulation
FFA	Frequency vectors
FLID	Flight number
FOR	Front section of the aircraft
FTC	Flight test card
IEEE-754	IEEE Standard for Floating-Point Arithmetic
MK	Aircraft mark identifier
MPID	Measurement part identity
MPNB	Measurement part number
MRVS	Measurement and Registration Processing System
NaN	Blunder value (Not a Number)
NEQD	Non-Equidistant delta-modulation
PARL	Parameter-list identification
PFTA	Performance Flight-Test Analysis
PM	Time shifting (decimal-vector)
PRID	Item (project-identification)
PROFAN	Performance Flight Analysis
PSC	Parameter status code
PSRD	Process selection retrieval date
PSRT	Process selection retrieval time
R	Parameter resolution
RCID	Recording number
REF	Reference time
RFT	Request for test number
RT0	Start time recording
RTU	Recording time unit
RUN	Run number
SEQ	Sequence number
sFTP	Secure file transfer protocol
STA	Station
STB	Standard calculations
SWVN	Software version number
T	Time resolution
T0	Time first sample
TE	Time last sample

TH49	Technicalreference manual 49	
TM	Parameter time (float-vector)	
TRAS	Character delimited export of raw flight-test data	
TRC	Type representation code	
TTSD	Type time series data	
UNIT	Parameter unit	
UPRS	Parameter presentation unit	
USER	MRVS user code	
UT	Unit of parameter time	
VAL	Parameter value (float-vector)	
VLEN	Vector length	
VPB	Flight-Test Management System	
W0	First sample value	
WE	Last sample value	

Fokker STB Variables

A_{ref}	Nozzle area	[m^2]
CGA	Centre of gravity actual	[-]
CGR	Centre of gravity ramp	[-]
D_{phiea}	Altitude correction	[-]
D_{phiel}	Thrust rev. correction	[-]
D_{phies}	Freestream correction	[-]
EPR	Engine pressure ratio	[-]
$FQCC$	Internal STB result	[kg]
$FQCWTA$	FQC center tank actual	[kg]
$FQCWTR$	FQM center tank	[kg]
FQC	Centre tank (DFGS)	[kg]
$FQMTR1$	FQM main tank (left)	[kg]
$FQMTR2$	FQM main tank (right)	[kg]
FQM	Fuel quantity - ramp mass	
$GRWGD$	Gross weight corrected	[kg]
$GRWGMG1$	Gross weight (FMS1GD)	[kg]
$GRWGMG2$	Gross weight (FMS2GD)	[kg]
$IPREC$	Intake recovery pressure	[-]
$MACC$	Corrected mach-number	[-]
MAC	Mean aerodynamic chord	[mm]
MR	Ramp mass	[kg]
MT	Actual Mass	[kg]
$N1$	Rot.shaft speed (low pressure)	[-]
$N2$	Rot.shaft speed (high pressure)	[-]
$PHIE$	Thrust param.	[-]
PHI	Corrected thrust param.	[-]
$PRFTAS$	Engine ram ratio	[-]
$PSCC$	Corrected static pressure	[N/m^2]
$THGNC$	Gross nozzle thrust	[N]
$WBBBKA$	Bag ballast AFT (begin)	[kg]
$WBBBKF$	Bag ballast FOR (begin)	[kg]
$WBBKA$	Bag ballast AFT	[kg]
$WBBKF$	Bag ballast FOR	[kg]

Greek Symbols

α	Angle of attack	[deg]
ϵ	Error variable, or	[-]
	Angle	[deg]
Γ	Discretized noise input matrix, or	
	Wing dihedral	[deg]
γ	Flightpath angle	[deg]
Φ	Discretized system transition matrix	
ϕ	Roll angle	[deg]
ψ	Yaw angle	[deg]
ρ	Density	[kg/m^3]
θ	Pitch angle	[deg]

Math Symbols

$\mathbb{I}$	Inertial tensor	[kg/m^2]

Diacritics

−	Vector	
∧	Estimate	

Roman Symbols

$\bar{c}$	Chord	[mm]
$\bar{u}$	Input vector	
$\bar{x}$	State vector	
$\bar{y}$	Output vector	
$\bar{z}$	Measurement vector	
$\hat{\bar{x}}$	State estimate vector	
$\hat{\bar{y}}$	Output estimate vector	
$\hat{\bar{z}}$	Measurement estimate vector	
A	State matrix	
B	Input matrix	
b	Wing span	[mm]
C	Coefficient, or	[-]
	Output matrix	
F	Force, or	[N]
	Reference frame	
G	Origin of frame F_b, i.e. CG	
I	Mass moment of inertia	[kg/m^2]
i	Incidence angle	[deg]
J	Mass product of inertia, or	[kg/m^2]
	Optimization function	
K	Gain, or	[-]
	Kalman gain matrix	[-]
M	Mach number, or	[-]
	Moment	[kg/m]
m	Mass	[kg]
N	Total number of elements	[-]
O	Observability matrix, or Frame origin	
P	State covariance matrix	
p	Roll rate, or	[rad/s]
	Presure (static)	[Pa]
Q	Input noise covariance matrix	
q	Pitch rate, or	[rad/s]
	Dynamic pressure	[Pa]
R	Measurement noise covariance matrix	
r	Yaw rate, or	[rad/s]
	Position (vector)	[mm]
Re	Reynolds number	[-]
u, v, w	Velocity in the axis system	[mm]
V	Velocity	[m/s]
X, Y, Z	Axis system	
x, y, z	Position in the axis system	[mm]

Superscripts

See subscripts for ref.frame annotations.

Subscripts

0	Initial condition, or Threshold
∞	Freestream
af	Airfoil
le	Streamwise distance from airfoil leading edge
w, wl, wr	Water tank, left, right
w	Wing
x, y, z	Along the {x,y,z}-axis
xx, yy, zz	Relative to the {x,y,z}-axis
xy, xz, yz	Relative to the {xy,xz,yz}-plane
i, j, k, n, m	Index symbols
$k+1$	One-step ahead
$k+1, k$	Predicted estimate
$k+1, k+1$	Optimal estimate
p	Pressure
t	Wing twist

Subscripts - Reference frames

a	Aerodynamic (air-path) reference frame
b	Body-Fixed reference frame
C	Earth-Centered, Earth-Fixed reference frame
k	Kinematic (flight-path) reference frame
O	Vehicle Carried Normal Earth reference frame
r	Vehicle reference frame
$r, 40$	Vehicle reference frame at 40% MAC
W	Vehicle-nose reference frame

1 Introduction

As of 2019 the Federal Aviation Administration (FAA) requires that all simulator-based pilot training is mandated to include stall recovery scenarios. Hence, the reason for having accurate stall modeling capable of handling high angles of attack. This project revolves around the ongoing research conducted at the Control & Simulation division at the department of Control & Operations, where recently a partnership has been set up between Fokker Services B.V. and Delft University of Technology.

At the end of November 2017, Henri Werij dean of the Faculty Aerospace Engineering, signed a non-disclosure agreement (NDA) with Fokker Services B.V. under guidance of Wim Huson (Aviation Consultant at Use2Aces) and Dirk van Os (Chief Engineer at Fokker Services) to set up this relationship with the TU Delft to protect and save a legacy in Dutch aviation history for future aspiring engineers. Where the goal of this partnership is to allow for an exchange of information, where Fokker selectively opens its doors to willing participating researchers of the TU Delft to aid them in their studies by giving access to decades of engineering expertise. Through this opportunity a first step is made with a focus on aerodynamic stall, by investigating historical flight-test recordings contained in Fokker's DEC Alpha mainframe at Fokker Services B.V., Hoofddorp.

Between '80 and '95, the Fokker company conducted numerous flight-tests using the Fokker 100 prototype aircraft in regard to stall characteristics. Notably, this is a swept wing aircraft configuration with two jet-engine's mounted on the rear fuselage, and being the first of its kind being subjected to rigorous testing at the Fokker flight-test facilities. This provides a unique research opportunity, specially when considering that actual flight-test data is very expensive, and often not obtained without any risk. Let alone the fact that most aircraft manufacturers consider flight-test data to be trade secrets, and possible uses are not without legal ramifications if not handled properly.

The necessity for aerodynamic stall research is apparent considering the FAA requirements, specially when understanding the fact that aerodynamic stall is a highly dynamic, non-stationary condition that can lead to very dangerous upset conditions if not corrected in time. According to the National Transportation Safety Board (NTSB) accidents attributed to "loss of control in-flight" (LOC) account for the primary cause of fatal accidents in general aviation (GE)[5, 6, 33, 44]. And of further interest NTSB reports on pilot error being primary cause of LOC due to irrecoverable upset conditions regarding aerodynamic stall [41, 42, 43, 45].

To meet FAA requirements, aerodynamic stall has been an ongoing research topic at the Control & Simulation division and has started a "Stall task Force" research group back in 2015 by creating a stall model capable of simulating these dangerous upset conditions in a safe environment at the Simona Research Simulator (SRS) facility at the faculty of Aerospace Engineering, Delft University of Technology. Current research has resulted in the development of a partial flight envelope model capable simulating the stall dynamics of the faculty's research aircraft (Cessna Citation II 550), which includes an implementation of Kirchhoff's flow separation model together with a simple stall buffet model [65, 67].

Which subsequently leads to this thesis main goal for research, the current stall model is undergoing continuous development, and with the Fokker partnership opens up a doorway to compare and test the current stall model in regard to different aircraft. Because the aircraft configuration regarding the Cessna Citation II (CII) and the Fokker 100 (F100) are quite similar, i.e. both engines mounted on the rear fuselage, and wing on the bottom part of the fuselage. Only difference in regard to configuration can be contributed to size, tail section (CII is conventional and F100 has a T-Tail) and main wing sweep angle. This provides the research-group with an unique opportunity, leading to a research-topic into investigating the effects of wing sweep angles on the aerodynamic stall model. Which is by definition the largest difference, not forgetting that the main wing has a primary relationship with aerodynamic stall. Hence, the sweep angle is forth assumed to be an important and a worthy research topic, specially considering its novelty within modeling aerodynamic stall. By adapting the most recent methods developed by the Stall Task Force group to identify the most important key aerodynamic stall parameters, an attempted will be made to yield new insights regarding sweep angle versus modeling aerodynamic stall [68].

1.1. Research objective

Research into Aerodynamic Stall Model Identification (ASMI) is an ongoing endeavor to create a model that achieves the highest fidelity, that aids in upset recovery training of pilots in Flight Simulator Training Devices (FSTD). Because aircraft's come in various shapes and sizes it can be stated that one aircraft stall model does not sufficiently provide full understanding of what occurs during a stall in regard differences in configuration. On top of that, obtaining proper flight-test data is a time-consuming, and a very expensive exercise, specially when large commercial aircraft are concerned. The partnership with Fokker allows for a highly appreciated, and novel step in stall model identification, which has lead to the following research objective.

"The research objective is to obtain a better understanding regarding the influence of a swept-wing aircraft configuration towards aerodynamic stall model identification by augmenting a multivariate orthogonally selected stall model structure based on Kirchhoff's theory for flow separation."

In order to attain the research objective the following questions will be answered.

MAIN Towards determining the influence of a swept-wing aircraft configuration on the aerodynamic stall model using the historic Fokker 100 flight-test data on archive, what is needed to achieve this?

- SUB_1 In preparation, can the historic flight-test data be properly formatted for research into aerodynamic stall model identification? Where parallel to the available data, do methods exist that properly define; a mass- & engine-model, aiding in executing a reconstruction of the flight path?
- SUB_2 Can the current aerodynamic stall model be properly applied to identify, verify, and validate (including both longitudinal and lateral-directional dynamics), changes in control surface effectiveness, and dynamic effects by current stall identification methods, in regard to recent research done using Cessna Citation II as a test-bed?
- SUB_3 What new model structure can be proposed through means of augmenting the current stall model allowing for swept-wing analysis, and optimization in model quality?

This research is limited to purely investigate the influence of a swept-wing configuration on the current aerodynamic stall model. Because flight testing has already been conducted in the early 90's, where quasi-steady aerodynamic stall maneuvers where performed. No extra flight-testing is needed to facilitate this research with mandatory training/validation data. And regarding the relationship Fokker-TUD, flight-test data is readily available, allowing for a feasible attempt to perform research into the newly acquired Fokker data-sources.

1.2. Organization

The organization of this thesis depends on the steps required to create a model that can be used in a simulation. As is presented in Figure 1.1, a road map is given from data acquisition to simulation, and ultimately leading to a test-bed for human-in-loop experiments and pilot training. The various fields residing in the road map all have their own unique methods and techniques, and are briefly explained.

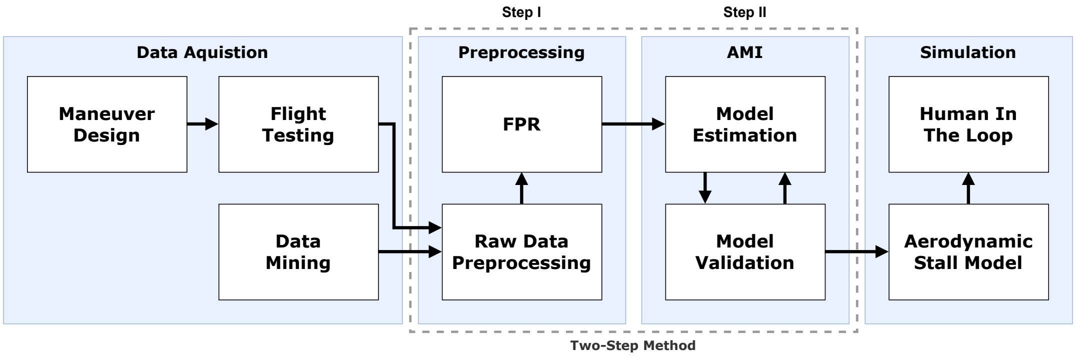

Figure 1.1: Road map to aerodynamic stall model identification, from data acquisition to simulation.

Data acquisition This part contains the processes concerned with maneuver design, actual flight-testing, and data mining. Before a model can be created, training and validation data need to be obtained. Design of a specific maneuver is crucial to model identification, in order to catch all facets concerned during the flight-testing phase an aircraft needs to be properly excited during a recording. If not executed well enough, certain aerodynamic model parameters might not be observed, negatively influencing the general model.

The Faculty of Aerospace Engineering partially owns a research laboratory aircraft (i.e a Cessna Citation II 550, briefly discussed in Chapter 2) together with the Netherlands Aerospace Centre (NLR), making it possible to design maneuvers, and actually record these during flight-testing. On the other hand, as to data mining, extensions to the aircraft fleet (i.e. Fokker F70/100 swept-wing, and F50/60 straight-wing aircraft, briefly discussed in Chapter 5) are now as previously stated made available through an SQL database (Appendix H). Hence, the partnership between Fokker and the TU Delft allows for making use of historical flight-test data. Regarding this thesis focus is on the Fokker F100, it does completely limit the control on how flight-testing is performed, i.e. no maneuver design is possible.

Preprocessing Data preprocessing (Step 1) is a vital step on the road to model identification and simulation. As is explained in literature, this is the first step part of the Mulder et al. Two-Step Method [37]. Here the raw data needs to be properly formatted and/or up-sampled, before the aircraft's state can be properly estimated regarding the reconstruction of flight path (as is discussed in Chapter 4).

Aerodynamic model identification (AMI) To identify the relevant parameters part of an arbitrary aerodynamic model, input from the preceeding Step 1 is required. Because the focus in this thesis is on creating a stall model, the new acronym "Aerodynamic Stall Model Identification (ASMI)" is henceforth used (as is discussed in Chapter 3).

This second step in the Mulder et al. Two-Step Method focuses on using recent techniques proposed by Van Ingen regarding model parameter selection [37, 67]. And is followed by the aerodynamic model parameter estimation process by making use of training flight-test data. Proposed methods are validated by comparing the estimated parameters with the validation flight-test data.

Simulation Once a model has been found to be sufficient for accurately modeling a ”stall” maneuver, it can be implemented for simulation purposes in FSTD’s. This can be both part of validating the model even further by running human-in-the-loop experiments, e.g. testing human perception regarding parameter influence to improve model fidelity. This with the intent to ultimately function as a training opportunity for pilots.

1.3. Road to towards a Fokker stall model

This thesis is a first attempt at setting up an aerodynamic stall model for the Fokker F100, which is based on know-how and research literature mainly published by the Stall Task-Force at Delft University of Technology, and a few other external published resources. Aircraft flight-tests, reports, and personal contact (Dirk van Os) predominantly define the success of this thesis, and future research. Therefore, a satisfactory outcome relies on valuable information given by, and interaction with Fokker Services (Hoofddorp).

As can be seen in Figure 1.1, data acquisition is the first part that is needed on the road to a Fokker stall model. As the university does not have the capability to perform new specifically designed flight-tests, the only thing left is to use historic flight-test recordings obtained from the archive at Fokker Services. With the advent of the Fokker-TUDelft partnership, these records have become available and are now accessible through a C&S department based SQL database (Apendix H).

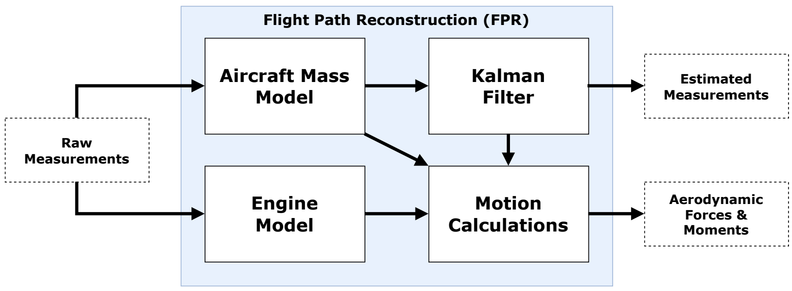

Figure 1.2: Parts needed to reconstruct of the aircraft’s flight path during step 1, i.e data preprocessing.

The second part in the road map is the first step of the Mulder et al. Two-Step Method [37]. This a newly to be researched part on the road towards a Fokker aerodynamic stall model. Methods regarding the preprocessing of raw Fokker data do not exist, and need to be formatted in a way state estimation processes can be applied, after which the flight path can be reconstructed (Chapter 8). This last process (FPR) in the second part of the road map posses a problem, and in Figure 1.2 details its inner workings.

In sequential order, an aircraft mass model (Chapter 6) needs to be defined that is capable providing details regarding the center of gravity (CG), and the corresponding moment of inertia tensor ($\mathbf{I}_{CG}$). A Kalman filter is to be applied for finding true/optimal measurements (Chapter 8), this is where the aircraft’s state is estimated to reconstruct the flight path. Nb. the center of gravity (CG) is needed to correct these raw measurements in regard to the location of onboard sensors, e.g. the inertial measurement unit (IMU) is located in the cabin, aligned with the wing root trailing edge, starboard side (green box, Appendix E.1). Thus, in the presence of filtered measurements, and aircraft inertia, the aerodynamic forces and moments can be calculated in addition of the acting modeled engine forces (Chapter 7).

As the process in Figure 1.2 shows, two important aircraft models need to be researched, i.e. a mass- and engine model. At the same time, the raw Fokker recordings need to be Kalman filtered in order to progress towards the Mulder et al. second step. Be aware, that very little is known at this point, and it is expected that this might be more trouble than initially thought.

In advent step (I) of Mulder et al. Two-Step Method being successful, an estimation of the aerodynamic stall model parameters can be permitted in step (II), i.e. the third part on the road map. This specific part revolves around techniques created by Van Horssen et al. and Van Ingen, where aerodynamic parameters are estimated using ordinary least square estimations (OLS) in conjunction with a model structure selection routine, based on multivariate orthogonal function modeling research done by Morelli et al. [36, 37, 66, 67]. The reader is reminded that this part by itself can lead to several other topics for research purposes, and it is pointed out that an ongoing interaction exists between methods/definitions of model estimation and validation. Nonetheless, all findings regarding the thesis outcome are presented at the end of this report (Chapter 9).

The ”ideal” finish line on the road towards identification of a Fokker stall model is represented by high fidelity simulation of actual aerodynamic stall for uses in human-in-the-loop experiments, and/or research regarding methods used in pilot training. What needs to be researched most importantly is the possibility an actual high fidelity Fokker stall model can exist, which can be used to test various hypotheses regarding the influence of aircraft configuration. Here, wing-sweep effects on the aerodynamic stall model are regarded as a top research goal. Yet getting to this point requires a solid foundation that needs to be put in place warranting this future research, which is inevitably the objective of this thesis.

I

Literature review and methodology

2

Research vehicle - Citation II 550

Without addressing the new research flight-test data made available by Fokker Services BV, i.e. regarding the Fokker 100/70 prototype aircraft. All the current research flight-test data has, and still is, predominantly obtained by performing specific maneuvers (and in this case stall) using the jointly owned Cessna Citation by the Aerospace Engineering faculty witch is part of Delft University of technology, and the Royal Netherlands Aerospace Center (NLR). Hence, it should therefor be of no surprise to the reader that the NLR research aircraft, on which the current stall model is based, is the primary focus of the preliminary part of this thesis. And all Fokker aircraft related topics are discussed in the main part of this thesis.

The Cessna Citation II (550) aircraft with call-sign PH-LAB, is equiped with an advanced flight test instrumentations system (FTIS), capable of recording all sensor outputs in to a flight-log. These sensor locations are informatively presented in Figure 2.1a, and accompanied by a definition for the body reference frame in Figure 2.1b. Notice the presence of the air-data boom, critical for stall model research.

Aircraft dimensions and inertial values for dry mass are given in Table 2.2, and function as an illustration to highlight the Citation's general properties.

Table 2.1 presents the sensor specifications, detailing the corresponding sample frequency (f_s), variance in signal noise (σ^2), signal unit, and sensor bus location. Note that air-data boom specifications are contained in this table, as normal vane measurements are recorded similarly. Angle-of-sideslip is only measured by making use of the air-data boom, and allows for accurate directional airflow measurements [32].

Table 2.1: Cessna Citation II 550, sensor specifications. Adapted from Van Ingen.

Signal	f_s [Hz]	σ^2 (var)	Unit	Sensor
x	1.0	1.1·10−2	m	GPS
y	1.0	1.1·10−0	m	GPS
h	1.0	2.2·10−2	m	GPS
$\dot{x}$	1.0	2.3·10−5	m/s	GPS
$\dot{y}$	1.0	2.4·10−5	m/s	GPS
$\dot{h}$	1.0	1.0·10−4	m/s	GPS
ϕ	52.1	1.6·10−4	rad	TARSYN
θ	52.1	2.6·10−5	rad	TARSYN
ψ	52.1	1.1·10−4	rad	GYROSYN
V_{TAS}	16.7	4.8·10−2	m/s	DADC
α_v	100.0	2.5·10−2	rad	SYNCHRO
β_v	100.0	1.2·10−2	rad	SYNCHRO
A_x	52.1	3.9·10−5	m/s^2	IMU
A_y	52.1	3.8·10−4	m/s^2	IMU
A_z	52.1	2.7·10−3	m/s^2	IMU
p	52.1	5.2·10−2	rad/s	IMU
q	52.1	8.5·10−3	rad/s	IMU
r	52.1	3.1·10−3	rad/s	IMU
δ_e	100.0	8.1·10−4	rad	SYNCHRO
δ_a	100.0	8.2·10−3	rad	SYNCHRO
δ_r	100.0	2.3·10−3	rad	SYNCHRO

Table 2.2: Cessna Citation II 550, PH-LAB dimensions & dry mass. Adapted from Van Ingen.

(a) Dimensions.

Symbol	Value	Unit	Name
b	15.9	m	Wing span
$\bar{c}$	2.09	m	Wing chord
S	30.0	m^2	Wing area

(b) Mass & inertia.

Symbol	Value	Unit	Name
m_{dry}	4,157	kg	Mass
$I_{xx,dry}$	12,392	kg-m^2	Inertia along x-axis
$I_{yy,dry}$	31,501	kg-m^2	Inertia along y-axis
$I_{zz,dry}$	2,252.2	kg-m^2	Inertia along z-axis

PH-LAB Stall maneuvers Flight-testing done with the PH-LAB (plus air-data boom) mainly occurred at altitudes of 5500 meters, where two stall maneuvers were performed. Notably a *wings-level symmetric* and *accelerated right-hand turn* stall maneuver, where an attempt was made to better identify aerodynamic model parameters by distinguishing angle-of-attack rate ($\dot{\alpha}$) from pitch rate (q) effects. On top of that special piloting techniques were implemented as proposed by Morelli et al., composed out of two components. First part focuses on keeping the aircraft as close as possible to the flight condition, and the second part attempts to excite the aircraft with (semi-)random disturbances. These specialized maneuvers have never been part of the Fokker testing regime, and are therefore omitted from research.

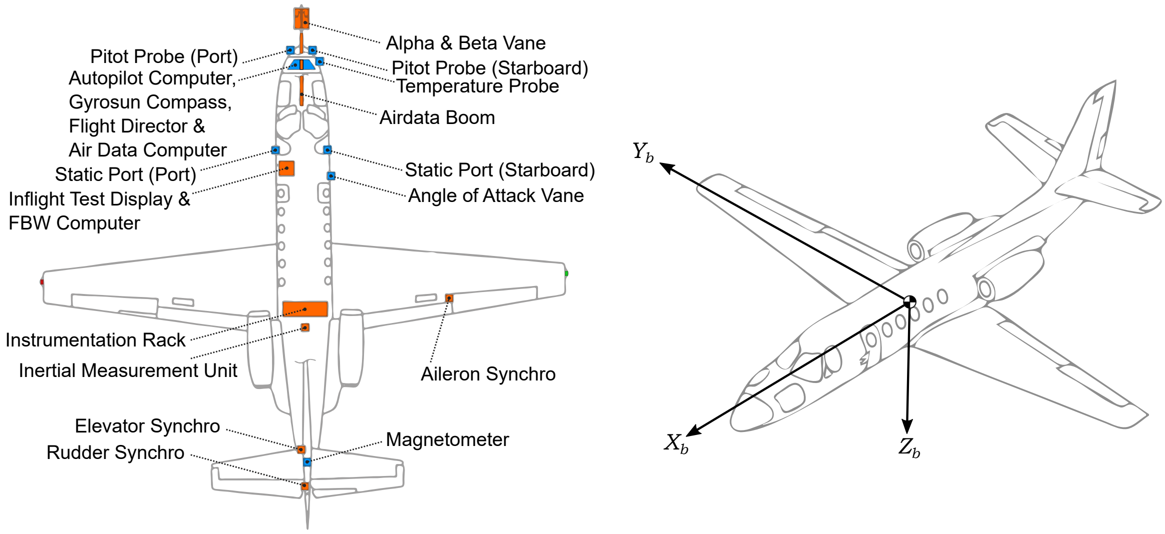

(a) Sensor setup. (b) Body axis reference frame ($\mathbb{F}_b$)

Figure 2.1: Cessna Citation II (550) sensor setup and body axis reference frame. Adapted from Van Horssen.

3

State of the art

This section discusses the theoretical content and methodology used in identifying a aerodynamic stall model. First part is making an educated selection of which flight-test data is relevant for research. When this is done the flight path needs to be reconstructed to yield terms that are not found through normal measurement. Having obtained all the relevant model terms, the process of identifying the stall model can be initiated by defining the model candidate terms needed to identify the dynamic stall model structure after which the aerodynamic parameters are computed using an ordinary least squares estimation process.

3.1. Definition of stall

At its core stall is considered to be a highly dynamic, non-stationary condition that allows for an uncontrolled (partial) separation of airflow from an aircraft's wing. If left uncorrected, dangerous upset effects are inevitable with often fatal consequences for the occupants. In all cases, stall depends highly on the angle-of-attack (α) and the free stream Mach number (M_∞), but still can be categorized into four parts, i.e. aerodynamic (most common), dynamic (occurs in helicopter blades, acrobatics), deep (wing turbulence influences elevator and rudder control), and Mach (separation due to high speed) stall.

3.1.1. Aerodynamic

Visual progression of aerodynamic stall and its effect on lift is best explained by Van Ingen, and is repeated here in Figure 3.1a by a C_L-α curve, and in Figure 3.1b by a side view representation of the flow separation from the wing per point within the C_L-α curve.

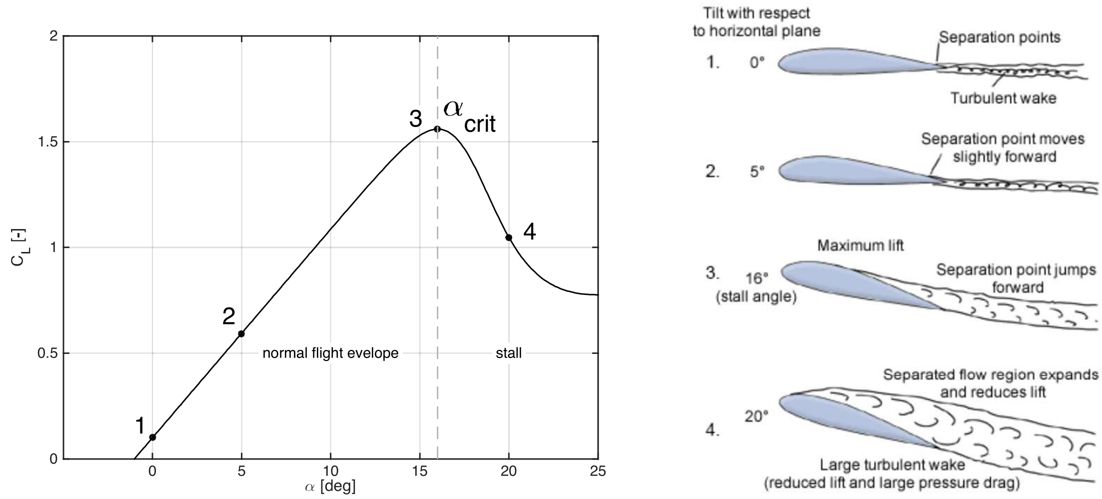

(a) Typical C_L-α curve.

(b) Flow separation.

Figure 3.1: Aerodynamic stall example. Adapted from Van Ingen [67].

Points 1 ($\alpha \approx 0^{\circ}$) to 4 ($\alpha > \alpha_{crit}$), where the last point exists in the stall regime, beyond the point (3) of maximum lift (aka α_{crit}). And as can be seen in Figure 3.1b, the wing airfoil is commonly thick and rough, where separation occurs from trailing to leading edge during normal flight, and regular angle-of-attack rates [17, 67].

3.1.2. Dynamic

Although dynamic stall effect are ”some-what” outside the scope of this thesis, it is briefly touched. As the name suggest, ”dynamic” emphasizes the notion of rapid change, and is found to occur most in ”flapping” helicopter wings, or anything else that flaps under the effect of gusting airflows. A flapping oscillation of a wing occurs most in the realm of the insects (or TU Delft DelFly), which almost entirely depends on dynamic stall to create lift [3, 34].

Note that this type of stall, which is also a non-linear unsteady aerodynamic effect, occurs when airfoils rapidly change the angle-of-attack. Because of this rapid change, a strong vortex can be formed and shed from the leading edge of the airfoil which travels backwards over the wing. This vortex contains high-velocity airflow’s, and momentarily increases the wings lift. But as soon as it has past the trailing edge, lift dramatically is reduced and puts the wing in a normal ”aerodynamic” stall [2, 34].

Furthermore, in the vicinity of high angles-of-attack and three-dimensional flow, a stall delay can occur. Rapid changes in angles-of-attack will allow the airflow to be substantially be more attached to the airfoil, leading to even higher achievable angles-of-attack. This allows for a momentarily delayed stall with a significantly higher lift coefficient than the steady-state maximum [4].

3.1.3. Deep

Deep (or super) stall is the most dangerous type of stall that can occur, and heavily depends on aircraft configuration, i.e. tail type, and engine location. E.g. the Fokker 100/70 is one of these aircraft’s, where a deep stall can lead to a seriously dangerous situation, as it is fitted with a T-Tail and two rear fuselage mounted engines. As can be seen in Figure 3.2, aerodynamic stall has already occurred, the wake that is being generated by the wing’s separation of airflow plus engine nacelles, and is blown along the velocity vector (V) into the aircraft’s stabilizer and rudder. This critically influences pitch and rudder control effectiveness, and to a certain degree even engine performance. In flight-testing it is common practice to come prepared with an emergency stall-recovery system, like vertically mounted rockets in the rear-tail (Fokker 70/100 testing), and/or a parachute system to literally pull the aircraft out of the deep stall [52].

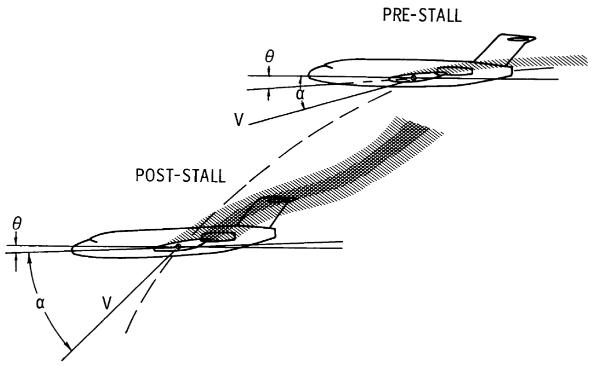

Figure 3.2: Deep stall wake flow pattern. Adapted from NASA Technical Memorandum [52].

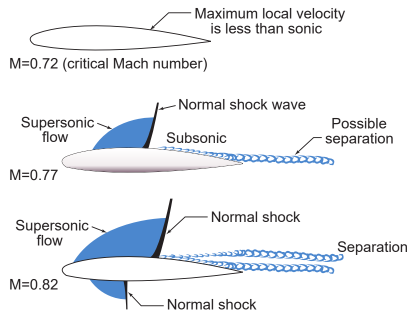

Figure 3.3: Mach tuck effect. Adapted from Aerodynamics for Naval Aviators [23].

Formally, deep stall penetrates the angles-of-attack (α) where pitch control effectiveness is reduced by the main wing, and engine nacelle wakes. It is a locked-in condition where recovery is impossible, and can be represented by a single value for α, given a particular aircraft configuration, where there is no pitching moment (trim point) [58].

3.1.4. Wing tip

Wing configuration is equally important, where sweep and taper are applied to the wing's airfoil making it differ from root to tip. This yields a varying aerodynamic lift characteristic in regard to a typical straight wing. Without twisting the wing along the chord, stall generally occurs at the tip first. This causes an imbalance in lift, because a swept-wing is commonly constructed such that the lift at wing root is forward of CG, and tip is well aft of the CG. This means that if the tip stalls first, an added nose-up moment is created, dangerously upsetting the balance [20].

3.1.5. Mach tuck

The mach tuck effect is a type of high-speed stall as can be seen in Figure 3.3, which occurs when the shock wave above the wing moves towards aft as aircraft speed increases with regard to Mach number. This is caused predominantly by two conditions, an aft moving center of pressure, and a decrease in wing down-wash velocity at the trailing edge, leading to a nose-down pitching moment. Per example, Obert states that the Fokker 28 can not have such handling characteristics (needs positive longitudinal stability) in high altitude, high speed conditions [47].

3.2. Aerodynamic Stall model identification

Aerodynamic stall model identification (ASMI) is build up using two sub-models, i.e. two models that separate from each other are capable of simulating the stall buffet, and aerodynamic stall. Here the stall buffet model is high frequency in nature, and attempts to recreate the heavy shaking of the aircraft's wing under the influence of an ever-increasing turbulence caused by the separation of flow due to an increasing angle-of-attack. Because continued research has been split up into a buffet, and an aerodynamic stall part, the buffet model is outside the scope of this thesis, and is thus not discussed.

The aerodynamic stall model is hence low-frequency in nature, as it attempts to fit a non-linear curve based on Kirchhoff's theory for flow separation [10], to a measured set of flight-test data. Here, aerodynamic forces and moments acting on the aircraft are calculated through state estimation techniques to reconstruct the aircraft's flight path (Chapter 4), and these are used to "guess" the aerodynamic stall model parameters (i.e. training the model).

3.2.1. Kirchhoff's theory for flow separation

Kirchhoff's theory for flow separation is considered to be the beating heart of the ASMI research efforts, where it is specifically restricted to perform longitudinal lift calculations. Where modeling of Kirchoff's theory is concerned, the focus is put on having an X-variable as a function of time, depending on the angle of attack (α) and the rate $\dot{\alpha}$, as presented in Equation 3.1 defining the stall dynamics with static tuning-parameters a_1, α^*, τ_1 and τ_2 [8, 10, 65].

$$\tau_1 \frac{dX}{dt} + X = \frac{1}{2}\left[1 - \tanh\{a_1\left(\alpha - \tau_2\dot{\alpha} - \alpha^*\right)\}\right] \tag{3.1}$$

Furthermore, Van Horssen points out in Equation 3.1 that the pair a_1 and α^* influences the steady conditions ($\dot{\alpha} \approx 0$) of the stall model, vane does not move much. But more importantly, explains this indicates that both τ_1 and τ_2 can only be estimated during stall ($\dot{\alpha} \neq 0$) due to the stall event exciting the system.

$$C_L = C_{L_\alpha}\left(\frac{1+\sqrt{X}}{2}\right)^2 \alpha \tag{3.2}$$

To be clear, the X-variable describes the location as a fraction of the point where flow separation occurs on the wing (see figure 3.4). And according to equation 3.2, can be used to either calculate a lift coefficient (C_L) depending on the lift-coefficient derivative (C_{L_α}) with respect to the changing angle-of-attack (α) in three-dimensional flow. Or to be used in estimation of the X-variable in the presence of obtained aerodynamic force and moments, i.e. needed for the ASMI process.

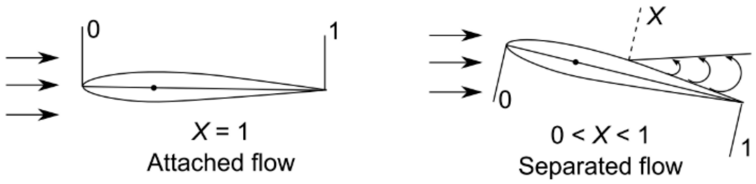

Figure 3.4: Definition of X-variable. Adapted from Dias [8].

The influence of these tuning-parameters is defined as follows; the abruptness of stall (a_1), where high values of a_1 indicate very abrupt stall behavior as seen in Figure 3.5. Half chord angle of attack (α^*), i.e. the location on the wing where the angle-of-attack is measured to be half-way ($X = 0.5$), an higher α^* leads to a higher critical angle-of-attack (α_{crit}), as seen in Figure 3.6. Transient effects (τ_1), influence the separation point rate of change (dX/dt) which can speed up or delay stalling (high τ_1 equals a large delay), as seen in Figure 3.7. And lastly hysteresis effects (τ_2), as can be seen in Figure 3.8 flow separation occurs later with a positive angle-of-attack rate ($\dot{\alpha}$) at higher values of τ_2 [8, 11, 65].

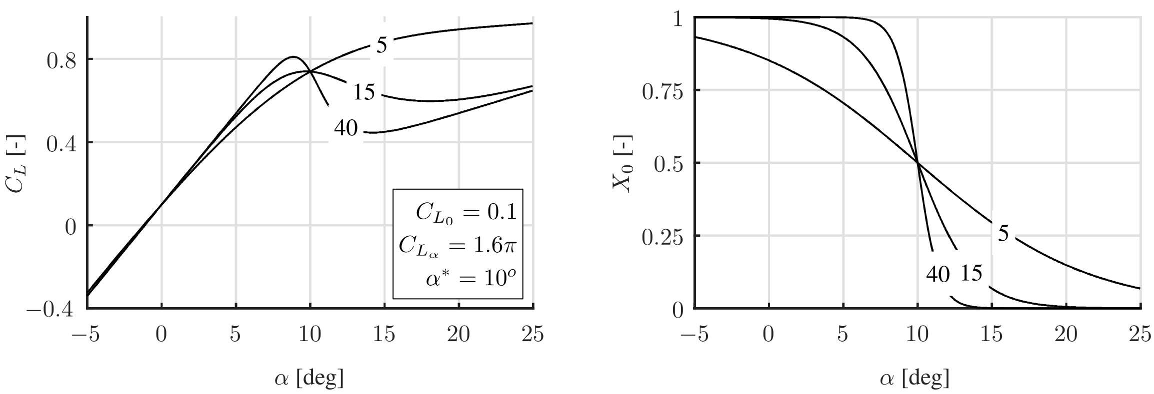

(a) Lift coefficient (C_L) vs angle-of-attack (α).

(b) Flow separation point (X_0) vs angle-of-attack (α).

Figure 3.5: Effect of abruptness of stall ($a_1 = \{5, 15, 40\}$) on Kirchhoff's flow separation differential equation. Adapted from Fischenberg and Dias [8, 11].

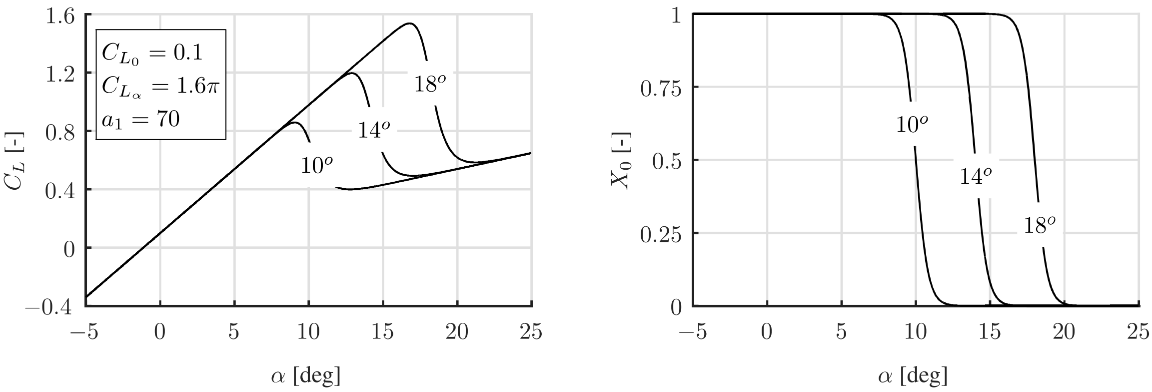

(a) Lift coefficient (C_L) vs angle-of-attack (α).

(b) Flow separation point (X_0) vs angle-of-attack (α).

Figure 3.6: Effect of the half chord angle-of-attack ($a^* = \{10°, 14°, 18°\}$) on Kirchhoff's flow separation differential equation. Adapted from Fischenberg and Dias [8, 11].

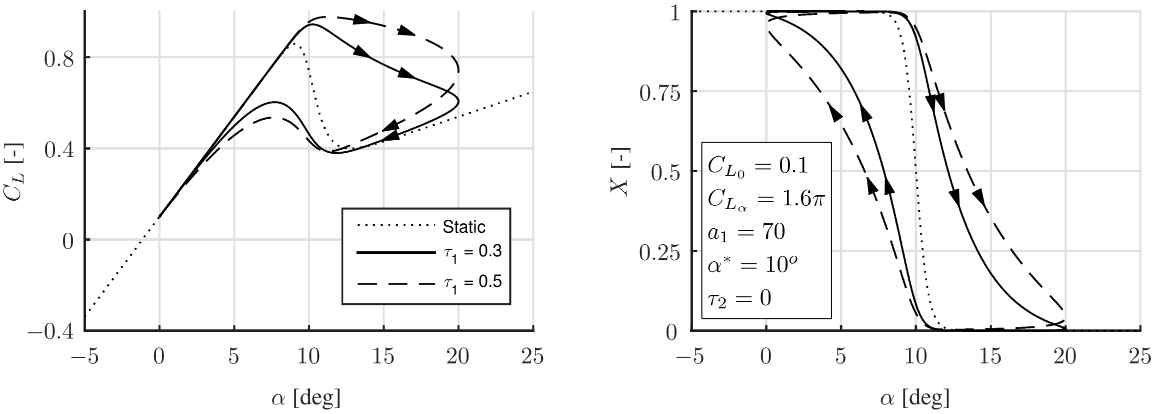

(a) Lift coefficient (C_L) vs angle-of-attack (α).

(b) Flow separation point (X_0) vs angle-of-attack (α).

Figure 3.7: Effect of transient response (τ_1) on Kirchhoff's flow separation differential equation. Adapted from Fischenberg and Dias [8, 11].

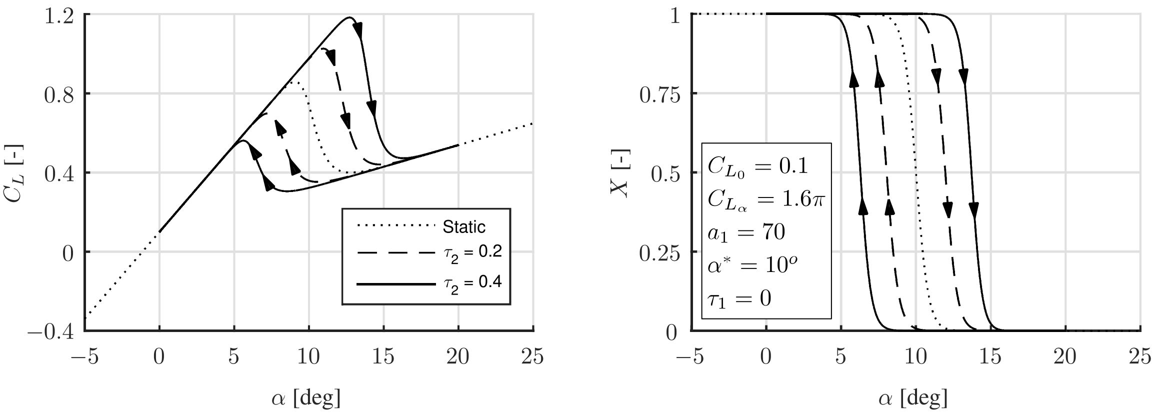

(a) Lift coefficient (C_L) vs angle-of-attack (α).

(b) Flow separation point (X_0) vs angle-of-attack (α).

Figure 3.8: Effect of hysteresis (τ_2) on Kirchhoff's flow separation differential equation. Adapted from Fischenberg and Dias [8, 11].

3.2.2. Current advancements in stall modeling

Regarding ASMI, an initial attempt was made by Van Horssen et al. in the academic paper "Aerodynamic Stall Modeling for the Cessna Citation II based on FLight Test Data" [66], where angle-of-attack measurements were originally recorded using the Citation's fuselage mounted angele-of-attack (α) vanes in the absence of being able to measure the angle-of-sideslip (β). This research was followed up by Van Ingen in his unpublished academic paper/thesis "Stall Model Identification of a Cassna Citation II from Flight Test Data Using Orthogonal Model Structure Selection" [67], where for the first time a nose mounted boom was used to measure the free stream angle-of-attack (α), and more importantly the angle-of-sideslip (β).

Initial stall research

The aerodynamic model was first constructed by Van Horssen et al., where the pitch rate terms (C_{L_q}, C_{D_q}, C_{m_q}) were omitted from the longitudinal model (Equations 3.3, 3.4, 3.5), although C_{L_1} was identifiable. Note that the stall model has an additional term $(1-X)$ to compensate for stall effect parameters (C_{D_X}, C_{m_X}) in decreasing drag force and pitch moment equations [8].

$$\hat{C}_L = C_{L_0} + C_{L_\alpha}\left\{\frac{1+\sqrt{X}}{2}\right\}^2\alpha \tag{3.3}$$

$$\hat{C}_D = C_{D_0} + C_{D_\alpha}\alpha + C_{D_X}(1-X) \tag{3.4}$$

$$\hat{C}_m = C_{m_0} + C_{m_\alpha}\alpha + C_{m_{\delta_e}}\delta_e + C_{m_X}(1-X) \tag{3.5}$$

Regarding the lateral model, no angle-of-sideslip measurements were available in the absence of an air-data boom. A work-around was created by Van Horssen et al. by calculating the difference in lift/-drag for both wings separately, where its difference allows for the calculation of a rolling (C_l) and yawing (C_n) moment [66]. This lateral part is not further addressed, because the air-data boom has become available for future research, and therefore no further research is warranted.

Aerodynamic parameters are thus estimated through solving an optimization problem non-linearly, using a trust-region-reflective algorithm [35]. Here two techniques are used to ensure finding a global optimum, and not a local one, i.e. parameters were constrained ($\{C_{D_0}, C_{L_\alpha}\} > 0$) and multiple sets (500) of initial conditions were ran.

A method was found to estimate the transient effect parameter (τ_1) from the stall buffet. This was made possible by first estimating all other parameters with the hysteresis effect included τ_2 using a nonlinear least squares approach [1], while keeping transient effect parameter (τ_1) fixed and using the cost function given in Equation 3.6. After the first estimation step, a second step is preformed to determine transient effect parameter (τ_1). It was found that there was a delay in recorded versus modeled stall buffet, a routine was created to obtain this parameter from this specific difference.

$$J = \left\{\hat{C}_L(\theta,x) - C_L\right\}^2 + \left\{\hat{C}_D(\theta,x) - C_D\right\}^2 + \left\{\hat{C}_m(\theta,x) - C_m\right\}^2 \tag{3.6}$$

Model comparison applied to the validation dataset, showed that the identified aerodynamic parameters for lift force (C_L) showed the best results, followed by drag force (C_D). Parameters regarding the pitching moment (C_m) were difficult to estimate using the quasi-steady stall maneuvers. And regarding the longitudinal model, it is stated that quasi-steady stall maneuvers are sufficient in proper identification of degradation of pitch response, change in pitch stability, hysteresis effects, and stall buffet behavior. Lateral stability effects were problematic, degradation of roll- and yaw response could not be identified, where only an uncommanded roll response could be modeled.

Continued stall research

Continued research was done by Van Ingen optimizing the stall model which yielded agreeing results with new flight-test data, which now contained an air-data boom making angles-of-sideslip measurements possible. New stall model parameters were introduced through a process called Orthogonal Model Structure Selection (which is explained in Section 3.2.3), where a multivariate orthogonal function modeling algorithm, which was originally first described through research done by Morelli et al., and was used in identifying and selecting the most effective aerodynamic stall model parameters [36]. Here the resulting new stall model is presented for the longitudinal ($\hat{C}_L$, $\hat{C}_D$, $\hat{C}_m$) / lateral ($\hat{C}_Y$, $\hat{C}_l$, $\hat{C}_n$) forces and moments in Equations 3.7-3.12.

$$\hat{C}_L = C_{L_0} + C_{L_\alpha}\left\{\frac{1+\sqrt{X}}{2}\right\}^2 \alpha + C_{L_{\alpha^2}}(\alpha - 6^\circ) \tag{3.7}$$

$$\hat{C}_D = C_{D_0} + C_{D_\alpha}\alpha + C_{D_{\delta_e}}\delta_e + C_{D_X}(1-X) + C_{D_{C_T}}C_T \tag{3.8}$$

$$\hat{C}_Y = C_{Y_0} + C_{Y_\beta}\beta + C_{Y_p}\frac{pb}{2V} + C_{Y_r}\frac{rb}{2V} + C_{Y_{\delta_a}}\delta_a \tag{3.9}$$

$$\hat{C}_l = C_{l_0} + C_{l_\beta}\beta + C_{l_p}\frac{pb}{2V} + C_{l_r}\frac{rb}{2V} + C_{l_{\delta_a}}\delta_a \tag{3.10}$$

$$\hat{C}_m = C_{m_0} + C_{m_\alpha}\alpha + C_{m_{X_{\delta_e}}}\max\left(\frac{1}{2},X\right)\delta_e + C_{m_{C_T}}C_T \tag{3.11}$$

$$\hat{C}_n = C_{n_0} + C_{n_\beta}\beta + C_{n_r}\frac{rb}{2V} + C_{n_{\delta_r}} \tag{3.12}$$

In relation to the initial proposed stall model by Van Horssen et al., some significant additional terms were added to the model equations. Except for the pitch rate (q) which is similar to the initial stall model, no related terms are found to have any influence on the Citations stall dynamics. Note that the pitch rate related terms are commonly included in the standard Citations dynamic model [62], it is assumed by Van Ingen that the contribution of q on the lift-, and drag forces, or pitch moment is small. And he suspects that the absence of pitch rate is due to poorly excited measurement, where performing a 3211-input on the elevator straight before the stall might yield better measurement data to identify the pitch rate related terms. Furthermore, no significant changes in control effectiveness were observed regarding the aileron and rudder. And according to Van Ingen might also be subjected to 3211-inputs before stall to identify even more possible missing related terms.

As can be seen in the model equations (3.8 & 3.11) for drag force ($\hat{C}_D$) and pitching moment ($\hat{C}_m$), the thrust coefficient (C_T) is selected as a new regressor. Important here is to understand that this term is added to handle errors generated by the Citation's engine model.

Use of Kirchhoff's X-variable was already deemed beneficial in previous research done [8, 66], but it's influence on the elevator control (δ_e) effectiveness regarding the model for pitching moment ($\hat{C}_m$) in Equation 3.11 is something that very new. As can be seen, even special mathematical operations are possible, e.g. static pitch stability (C_{m_α}) is expected to change during stall. Hence, the additional term $\max\left(\frac{1}{2},X\right)$.

Van Ingen concludes that the Kirchhoff X-variable is just a single variable attempting to describe a whole set of possible dynamics occurring a stall maneuver, and a great simplification of reality. And points out that possible other methods might exist to improve the general stall model. In regard to the initial model by Van Horssen et al., using model structure selection significantly improved model accuracy expressed in percentage difference in mean-squared-error (MSE), ranging from +543% up to +2313%. This is a big improvement of the new stall model, where $\hat{C}_L$ (2313%), $\hat{C}_D$ (2050%), and $\hat{C}_n$ (1864%) performing the best.

3.2.3. Orthogonal model structure selection

The current process of identifying a stall model based on flight-test data is given in the block diagram in Figure 3.9, depicting a three step sub-process in the ”second” step of the two-step system identification[37].

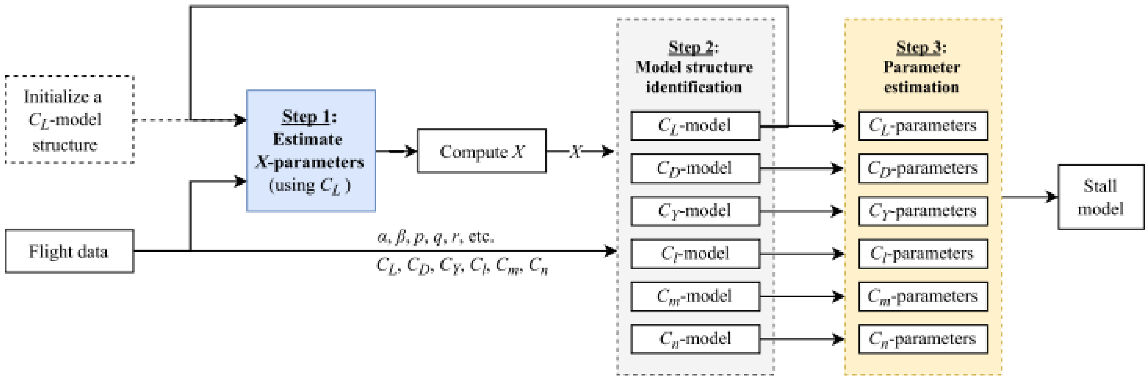

Figure 3.9: Block diagram of steps and flow in the system identification approach. Adapted from Van Ingen[67].

Step 1 - Estimate X-parameter This step yields a new base regressor X as a function of time, computed using the estimated Kirchoff tuning-parameters, which is used in the next step. Note that, these parameters are estimated using a non-linear optimization approach, where previous research done by Van Ingen favored a gradient based method (i.e. interior point, active set, sequential quadratic programming, trust region reflective & Levenberg-Marquardt) [67]. No direct measurement of X exists, these tuning-parameters are therefor fixed, and the X-variable is computed using the simplified longitudinal force dynamics function C_L in Equation 3.2.

Step 2 - Model structure selection The second step attempts to find a model structure that ”builds-up” the dynamic equations from scratch (see block diagram in Figure 3.10), and only selecting the candidate model terms (Equation 3.13) that contribute the most.

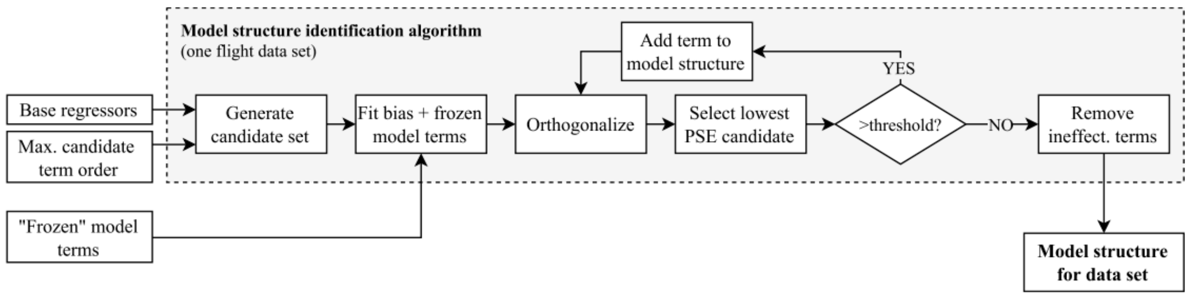

Figure 3.10: Block diagram of model structure identification algorithm. Adapted from Van Ingen[67].

This process is called Multivariate Orthogonal Function modeling (MOF), and starts by orthogonalization of the candidate terms and iteratively compare their independent contributions through computing the lowest change in predicted squared error (PSE) until a sufficient amount of matching terms are found. This is done for all dynamic model equations[36, 67].

$$\bar{1}, \alpha, \dot{\alpha}, \beta, \dot{\beta}, p, q, r, \delta_a, \delta_e, \delta_r, C_T, M, X, (1-X), \left(\frac{1+\sqrt{X}}{2}\right)^2, \max\left(\frac{1}{2}, X\right) \tag{3.13}$$

As on can see the four interesting effects are added to the model candidate terms as presented in Equation 3.13. Where the X is an effect that reduces/disappears during stall, $(1-X)$ is the opposite of

X and only takes effect during flow separation, $\left(\frac{1+\sqrt{X}}{2}\right)^2$ Kirchoff's term, and $\max\left(\frac{1}{2}, X\right)$ is an effect that changes during stall.

This shows the utility a MOF approach has to selecting the model terms, i.e. the influence of Kirchoff's X-variable as a function of time can now be tested on the measured aircraft forces/moments, thus statistically and mathematically building a specific dynamic stall model.

The MOF process is ended by outputting the matrix of selected regression variables A, i.e. the model structure to be handed over to the step 3 parameter estimation process[67].

Step 3 - Parameter estimation Ordinary least squares estimation (OLS), Equation 3.14, is used to compute the aerodynamic parameters contained in the previously defined model structure.

$$\hat{y} = A\Theta \tag{3.14}$$

Through minimizing the error, $\eta = \bar{y} - \hat{y}$, a closed form solution can be found as follows (equation 3.15).

$$\hat{\Theta} = \left(A^T A\right)^{-1} A^T \bar{y} \tag{3.15}$$

4 State estimation

The state estimation is a particular field of study that concerns itself with estimation the true state $\bar{x}$ of a known dynamic system of which the (aero)dynamic parameters $\bar{\theta}$ are unknown. The goal of this chapter is to present the reader with the current "state of the art" techniques developed and used by the faculty's Control & Simulation (C&S) department. Furthermore, advances obtained with respect to the state estimation during flight conditions where aerodynamic stall occurs using the faculty's research aircraft the Cessna Citation 550.

Definition of State Estimation

Obtaining the best estimate of the state $\bar{x}$ while parameter $\bar{\theta}$ is unknown[1].

In regard to this thesis, the focus is mainly on the reconstruction of a specific flight path (see Chapter 8). Various techniques are possible, but the primary method of solving these kinds of estimation problems is Kalman filtering, which is also known as Linear Quadratic Estimation (LQE), and is uniquely capable in finding these true state estimates using all available sensory measurements, i.e. " ... finding the best estimate or prediction of a signal which is buried in the random noise"[50]. Nb sensor measurement signals are often distorted by noise which adds to uncertainty, where some understanding of the system's dynamics and the measured inputs/outputs an estimate can be obtained that has the capacity to highly accurately describes what the current true state can be.

Notably, Kalman filtering has numerous applications in technology, where it has a common application in guidance, navigation, and control of vehicles, particularly aircraft and spacecraft. Furthermore, it is a widely applied tool in time series analysis, and is used in fields such as signal processing and econometrics. Also, these types of filters are one of the main topics in the field of robotic motion planning and control, included in trajectory optimization, and have a wide application in the field of modeling a central nervous system's control of movement. Due to the time delay between issuing motor commands and receiving sensory feedback. Subsequently, the usage of Kalman filters supports the realistic model for making estimates of the current state of a muscular motor system, and issuing updated commands.

Various flavors of Kalman filters exists, historical results, findings, and their application within the C&S division are briefly discussed in Section 4.1, but most importantly the primary filters used in this thesis are the Iterated Extended Kalman Filter (IEKF), see Section 4.4, and the Unscented Kalman Filter (UKF), see Section 4.5, which will be discussed later on.

[1] Mentioned by dr.ir. D.M. Pool during his lecture on state estimation part of the System Identification of Aerospace Vehicles course at the Faculty of Aerospace Engineering, Delft University of Technology.

4.1. Current techniques and advances

At it's core, state estimation is well known in the field of general systems theory, being part of the realm concerned with observer models, as can be seen in Figure 4.1.

This system-observer model assumes that the state matrix A and input matrix B are known. i.e. the observer has a information about the dynamics of the system and understands how the output matrix C handles the output (or measurements). Here, the state $\bar{x}$ can be approximated through finding an estimate $\hat{\bar{x}}$, this is achieved through comparing the system output $\bar{z}$ with the observer output $\hat{\bar{z}}$ by means of a cost function and multiplying it with a gain K, which is in turn fed back to the observer system.

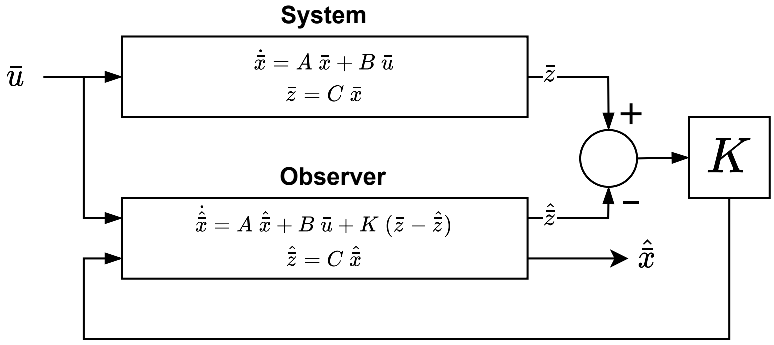

Figure 4.1: Simple system-observer model.

A first order differential equation is derived from the system and observer equations, regarding the size of the error ϵ that occurs when estimating the state $\bar{x}$, where in this particular example $\epsilon = \bar{x} - \hat{\bar{x}}$. As is presented in Equation 4.1, the way this error behaves is determined by the time invariant state A and output B matrices and the gain K matrix. Given the $pair(A, C)$ is detectable (even observable), a stable system (i.e. converging to the smallest error possible) can be designed where the K matrix values are bounded by the eigenvalues of $(A - KC)$ which must exist in the left half of the phase plane in order for the filter to properly converge[48].

$$\dot{\epsilon} = (A - KC)\,\epsilon \tag{4.1}$$

4.1.1. Kalman filtering

In principle, Kalman filtering (which carries its inventors name Rudolf Eugene Kalman[29]) operates similar but per measurement step updates another version of gain K matrix shown in Figure 4.1, with regard to the changing cost function, i.e. this makes the gain matrix varying per update, and minimizes the error between system and observer substantially. The algorithm loops through a set of steps, where the filter produces predictions of the current state variables based on a model of the system dynamics. Estimates are corrected using a per-step-varying weighted average, based on uncertainties within sensor measurements and bias, with more weight being given to correcting states with an higher uncertainty yielding a presumed optimal ”truthful” estimate.

A high level overview of this process is presented in Figure 4.2, which has been adapted upon from Van den Hoek's thesis [62]. Here can be seen an input vector $\bar{u}$, and noise input vector $\bar{w}$ influencing the unknown system dynamics at the current step k within the dataset. An important concept is the understanding of system dynamics versus model, because the model is used to guess the ”unkown” behavior of these dynamics. Forth, the same dynamics are observed and predicted $\bar{z}(k+1)$ one-step-ahead (i.e. $k+1$), and an output noise vector $\bar{v}(k+1)$ is added, where for all intends and purposes it is only added when unscented Kalman filtering (UKF) is concerned (see Section 4.5).

Likewise, as was presented in the simple system-observer model in Figure 4.1, an one-step-ahead prediction $\hat{\bar{z}}(k+1, k)$ is produced by the model, and is compared to the predicted observation $\bar{z}(k+1)$, this is called the filter innovation. And is afterwards used to compute the optimal state estimate $\hat{\bar{x}}(k+1,k+1)$, which is done in combination with the Kalman gain matrix K that ensures filter convergence.

Note that, the error between observation and estimation needs to converge to zero, as is explained on a simpler level as is pointed at in equation 4.39, of course the procedure is more elaborate within the Kalman filter.

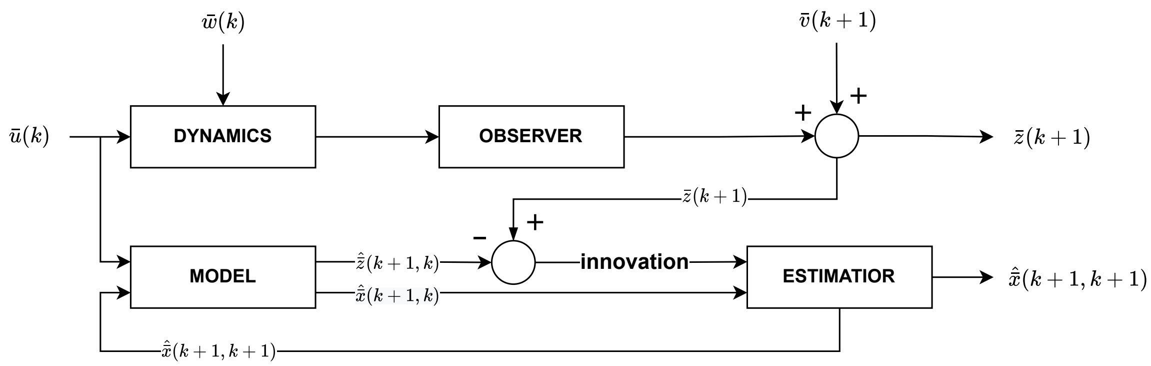

Figure 4.2: High level overview of the general Kalman filtering sequence. Adapted from Van den Hoek [62].

N.B. Figure 4.2 represents the basic linear Kalman filter, and is based on a set of linear stochastic differential equations (SDE's). These sets of equation's have the following form, as is discussed in Kalman's original 1960's paper [29, 65].

$$\begin{aligned} \dot{\bar{x}}(t) &= \boldsymbol{A}\bar{x}(t) \ + \ \boldsymbol{B}\bar{u}(t) \ + \ \boldsymbol{G}\bar{w}(t) \\ \bar{y}_n(t) &= \boldsymbol{C}\bar{x}(t) \ + \ \boldsymbol{D}\bar{u}(t) \ + \ \quad \bar{v}(t) \end{aligned} \tag{4.2}$$

$$\bar{z}(t_k) = \bar{y}_n(t_k) + \bar{v}(t_k) \quad , \quad k = 1, 2, \ldots \tag{4.3}$$

As a final note, measurement errors are Gaussian in nature, thus the filter uses an exact conditional probability estimate and assumes a zero mean probability distribution. This information is mostly obtained a posteriori, or from the sensor instrument manufacturer[29].

4.1.2. Filter types and general application

Several types of Kalman filters and smoothers have extensively been studied in previous work done by Van den Hoek (2016) and Van Horssen (2016). Van Ingen (2017) continues their work in his thesis on dynamic stall modeling of the Cassna Citation [62, 65, 67]

Filters and smoothers

Work done by Van Horssen[65] compares the results obtained between Kalman filters and smoothers using the faculties search aircraft (Cessna Citation 550). Specifically, Van Horssen compares an Iterated Extended Kalman (IEKF) filter based on the work done by Mulder et al. with an Unscented Kalman Filter (UKF) based on the combined work done by Julier, Wan and van der Merwe, and Teixeira et al. [28, 37, 56, 72]. Subsequently Van Horssen also investigated the use of Kalman smoothers, he states the offline nature of flight path reconstruction warrants its use. Two smoothers are compared by him namingly the Haykin's Euler discretization approximation [19], and a Rauch-Tung-Striebel smoother [51]. Of which the later is implemented by Van Horssen in the previously mentioned IEKF and UKF filters, based on research done by Hartikainen et al. for the IEKF, and Särkkä for the UKF [18, 54].

Performance

In his conclusion Van Horssen states that the performance is not significantly different, notes that the IEKF runs about eight time faster than the UKF, while on the other hand the UKF is less dependent on the choice of the initial condition and the covariance matrix. Moreover, the specific choice of process and measurement noise covariance matrices does not need to be very precise with regards to the UKF filtering. The use of smoothers is discuraged by Van Horssen, according to his findings performance was worse in terms of the verctical variables, think of body normal velocity w and angle of attack α, due to errors in IMU measurements and an upwash phenomena acting on the angle of attack vane, and therefore only considers IEKF and UKF Kalman filters[65].

Sensor location and fudge factoring
Furthermore, Van Horssen points out that the location and corrections made with respect to the center of gravity is of importance, and found to greatly improve the results[65]. Doing so requires rotational acceleration variables, obtained through differentiation of the pre-filtered (low-pass) angular velocity variables. Vertical wind component W_{zE} could not be estimated, Mulder introduces a fudge factor in the order of magnitude that ranges within 0.1 to 0.2 m/s[37], it is assumed errors are relatively small.

Data pre-processing
Recordings are processed offline, this decreases the need for a Multi-Rate Kalman Filter (MRKF). Note that, all flight-test recording data used in the C&S research was interpolated to both account for disjoint recording times, and the varying sample rates recorded by the aircraft's onboard sensors. This was specifically tested by Van den Hoek, where he compared a spline interpolation approach with a multi-rate IEKF. Yielding lower RSME results using the spline interpolation[62].

Furthermore, Van Ingen pre-filtered the recording data with a low-pass filter at differing cut-off frequencies (see Table 4.1) [62, 65, 67]. This supposedly was added to remove high frequency vibrations (i.e. stall buffet), related to the air-data boom. No reasoning to why different cut-off frequencies were used, and why a low-pass filter had been applied, was given. In theory, a Kalman filter should be able to handle this, without pre-filtering and possibly losing information regarding the system's dynamics.

Table 4.1: Low-pass cut-off frequencies (f_c) of the pre-filtered measurement data. Adapted from Van Ingen.

f_c [Hz]	Signal Source
1.5	A_x, A_y, A_z, p, q, r
4.0	$\alpha, \beta, \dot{\beta}, \dot{\alpha}, \delta_a, \delta_e, \delta_r, \dot{p}, \dot{q}, \dot{r}$

4.1.3. Additional up- and sidewash air-data boom filtering

The main body of work done regarding the handling of up- and sidewash filtering of the air-data boom air-data coming from a boom mounted on the aircraft's nose, was first discussed in De Visser's PhD thesis work. Handling is specifically based on measurement techniques proposed by Laban (1994) [7, 32]. Further research regarding this type of airdata measurement was subsequently found in following thesis work done by Van Horssen, and later Van Ingen.

Importantly, Van Ingen revealed inconsistencies regarding the system state observability, due to badly converging up- (C_{α_0},$C_{\alpha_{up}}$) and sidewash (C_{β_0},$C_{\beta_{si}}$) parameters that were used in the preceding research [67]. Hence, the next to be discussed navigation system equations (Section 4.2) experienced some major changes because of this.

Therefore, a prelude (or recap if preferred) is given regarding the air-data boom equation needed to define the newly used navigation system equations. According to Laban, and mentioned by Van Ingen, the use of vanes connected to a boom create two types of errors within the α-β airdata measurement, i.e. *i)* aircraft fuselage induced flow effects, and *ii)* flow velocity components induced by the aircraft's body rotation. As is illustrated for the first error type in Figure 4.3, both types are specifically related to the fact that local airflow velocity (u_v, v_v, w_v) at the vanes is not equal to the flow velocity (u, v, w) around the aircraft's center of gravity [32, 67].

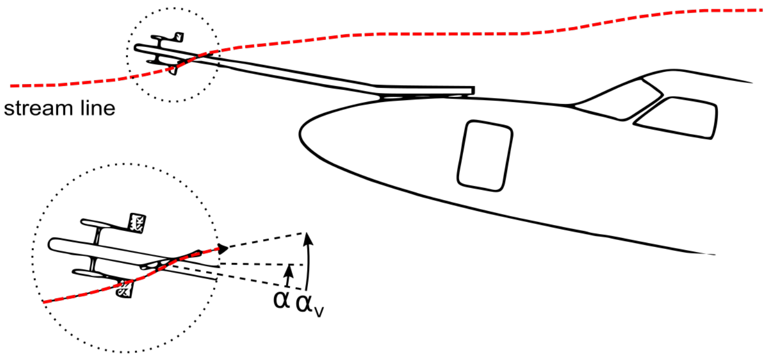

Figure 4.3: Fuselage induced (α_v) versus geometric (α) angle of attack. Adapted from Laban (1994).

As is presented in equations 4.4 and 4.5, Laban proposes an calculated approximation of the induced fuselage measurements (α_v, β_v) as a function of the true geometric (α, β) angles of attack , and side slip. Note that these equation are the raw equations found by Laban, extended by De Visser in his PhD research on model identification, illustrating the addition of 3 "quasi" static location variables (x_{v_α}, x_{v_β}, z_{v_β}), and 4 extra variables ($C_{\alpha_{up}}$, $C_{\beta_{si}}$, C_{α_0}, C_{β_0}) to the state vector. The quasi static location variables change incrementally with respect to the aircraft's center of gravity, this is dependent on the mass distribution of the aircraft and can change every flight. The extra state variables are defined as the fuselage upwash coefficient ($C_{\alpha_{up}}$) with an unknown wind component (C_{α_0}), and the fuselage sidewash coefficient ($C_{\beta_{si}}$) with an equally unknown wind component (C_{β_0}).

$$\alpha_v = \arctan\left(\frac{w_v}{u_v}\right) \approx \left(1 + C_{\alpha_{up}}\right)\alpha - \frac{x_{v_\alpha}\left(q - \lambda_q\right)}{u} + C_{\alpha_0} \tag{4.4}$$

$$\beta_v = \arctan\left(\frac{v_v}{u_v}\right) \approx \left(1 + C_{\beta_{si}}\right)\beta + \frac{x_{v_\beta}\left(r - \lambda_r\right)}{u} - \frac{z_{v_\beta}\left(p - \lambda_p\right)}{u} + C_{\beta_0} \tag{4.5}$$

, where $\alpha = \arctan(w/u)$, and $\beta = \arctan(v/u)$.

Kinematic relations w.r.t. the addition of the 4 new state variables are presented in the following equations. Up- and sidewash state variables in 4.6 and 4.7.

$$\{\dot{C}_{\alpha_{up}}, \dot{C}_{\beta_{si}}\} = 0.01 w_N \frac{\pi}{180} \tag{4.6}$$

$$\{\dot{C}_{\alpha_0}, \dot{C}_{\beta_0}\} = 0 \tag{4.7}$$

Van Ingen removed three ($C_{\alpha_0}, C_{\beta_0}, C_{\beta_{si}}$) of these state variables in order to get some proper conversion, reasoning was rooted in complications resulting from improper state convergence on the real flight test datasets. By only making use of upwash state variable $C_{\alpha_{up}}$ (see equations 4.35 & 4.36), Van Ingen was able to show that the resulting system offered good and reliable convergence behavior.

4.2. Navigation equations

For Kalman filtering to work the system needs to be defined, this section presents the equations that aid in this definition based on the Cessna Citation II system dynamics obtained from the work done by Van Horssen / Van den Hoek, and continued by Van Ingen. This first part is rooted in setting up the navigation system equations that describe the aircraft's position, velocity, and attitude under the influence of accelerations/angular rates and biases influencing the system, as is algebraically presented by equation 4.8. In Appendix C.1 the full navigation system dynamics is presented, where in this section the following equations that span this system are separately discussed[67].

$$\dot{\bar{x}} = f(\bar{x}(t), \bar{u}(t), \bar{w}(t)) \tag{4.8}$$

, where $\bar{x}(t)$ is the state vector (equation 4.9), $\bar{u}(t)$ is the input vector (equation 4.10), and $\bar{w}(t)$ is the process noise vector (UKF only, equation 4.11).

$$\bar{x} = \left[\begin{array}{cccccccccccccccccccc} x_E & y_E & z_E & u & v & w & \phi & \theta & \psi & \lambda_x & \lambda_y & \lambda_z & \lambda_p & \lambda_q & \lambda_r & W_{xE} & W_{yE} & W_{zE} & C_{\alpha_{up}} & C_{\beta_{si}} & C_{\alpha_0} & C_{\beta_0} \end{array}\right]^T \tag{4.9}$$

$$\bar{u} = \left[\begin{array}{cccccc} A_x & A_y & A_z & p & q & r \end{array}\right]^T \tag{4.10}$$

$$\bar{w} = \left[\begin{array}{cccccc} w_x & w_y & w_z & w_p & w_q & w_r \end{array}\right]^T \tag{4.11}$$

4.2.1. Position

First part of the navigation system equations is the position of the aircraft relative to the Earth-Centerd Earth-Fixed (ECEF) frame ($O_E X_E Y_E Z_E$) of reference.

$$\dot{x}_E = [\, u\cos\theta + (v\sin\phi + w\cos\phi)\sin\theta \,]\cos\psi - (v\cos\phi - w\sin\phi)\sin\psi + W_{xE} \tag{4.12}$$

$$\dot{y}_E = [\, u\cos\theta + (v\sin\phi + w\cos\phi)\sin\theta \,]\sin\psi + (v\cos\phi - w\sin\phi)\cos\psi + W_{yE} \tag{4.13}$$

$$\dot{z}_E = -\,u\sin\theta + (v\sin\phi + w\cos\phi)\cos\theta + W_{zE} \tag{4.14}$$

Wind velocities (W_{xE}, W_{yE}, W_{zE}) are added to function as a bias variable, this occurs through corrections the Kalman filter automatically makes when comparing true airspeed with ground speed.

4.2.2. Velocity

Change in body velocities ($\dot{u}, \dot{v}, \dot{w}$) are expressed as function of accelerations (A_x, A_y, A_z) and angular rates (p, q, r) acting within the aircraft's body frame ($GX_bY_bZ_b$) of reference, w.r.t . standard gravity (g_0) and velocity (u, v, w). Sensor measurements are imperfect, therefor bias states (λ_x, λ_y, λ_z, λ_p, λ_q, λ_r) are added to account for errors in measurement. When using UKF filtering, extra states ($w_x, w_y, w_z, w_p, w_q, w_r$) need to be added to help with estimating process noise in sensor.

$$\dot{u} = (A_x - \lambda_x - w_x) - g_0\sin\theta - \left(q - \lambda_q - w_q\right)w + (r - \lambda_r - w_r)\,v \tag{4.15}$$

$$\dot{v} = \left(A_y - \lambda_y - w_y\right) - g_0\cos\theta\sin\phi - (r - \lambda_r - w_r)\,u + (r - \lambda_r - w_r)\,w \tag{4.16}$$

$$\dot{w} = \left(A_y - \lambda_z - w_z\right) - g_0\cos\theta\cos\phi - \left(p - \lambda_p - w_p\right)v + \left(q - \lambda_q - w_q\right)u \tag{4.17}$$

4.2.3. Attitude

Change in attitude ($\dot{\phi}, \dot{\theta}, \dot{\psi}$) is defined by the Euler angles (ϕ, θ, ψ) and angular rates (p, q, r) relative to the body frame ($GX_bY_bZ_b$) of reference. Here sensor bias and process noise for UKF filtering is added.

$$\dot{\phi} = \left(p - \lambda_p - w_p\right) + \left(q - \lambda_q - w_q\right)\sin\phi\tan\theta + (r - \lambda_r - w_r)\cos\phi\tan\theta \tag{4.18}$$

$$\dot{\theta} = \left(q - \lambda_q - w_q\right)\cos\phi - (r - \lambda_r - w_r)\sin\phi \tag{4.19}$$

$$\dot{\psi} = \left(q - \lambda_q - w_q\right)\frac{\sin\phi}{\cos\theta} + (r - \lambda_r - w_r)\frac{\cos\phi}{\cos\theta} \tag{4.20}$$

4.2.4. Sensor bias, wind and boom

It is assumed that sensor bias is constant, i.e. does not vary with time or any other environmental variable. As given in equation 4.21, changes in these variables are set to zero.

$$\{ \dot{\lambda}_x , \dot{\lambda}_y , \dot{\lambda}_z , \dot{\lambda}_p , \dot{\lambda}_q , \dot{\lambda}_r \} = 0 \tag{4.21}$$

Likewise, an assumption is made about the changes in wind velocity. According to research done by Van Horssen (2016), wind acts like a standard normally distributed random variable w_N, where the constant 0.01 seems to yield good results[65].

$$\{ \dot{W}_{xE} , \dot{W}_{yE} , \dot{W}_{zE} \} = 0.01 w_N \tag{4.22}$$

And as previously explained in section 4.1.3, regarding the air-data boom, only one state variable is considered, i.e. $C_{\alpha_{up}}$.

$$\dot{C}_{\alpha_{up}} = 0 \tag{4.23}$$

4.3. Observation equations

Prediction and correction are two important steps of the Kalman filtering process, i.e measurements are needed for correcting. Not all the needed measurements are directly available, for instance the angle of attack and sideslip angle which are a vital part within stall model identification! On the other hand some measurements can be directly be read off the sensor, i.e. aircraft attitude and position.

4.3.1. Position

Position in the Citation 550 is also directly read from the GPS system, and measured w.r.t. to the ECEF reference frame.

$$x_{GPS} = x + v_{x_{GPS}} \tag{4.24}$$
$$y_{GPS} = y + v_{y_{GPS}} \tag{4.25}$$
$$z_{GPS} = -z + v_{z_{GPS}} \tag{4.26}$$

4.3.2. Velocity

Velocity in the Citation 550 is also directly read from the GPS system, and measured w.r.t. to the ECEF reference frame.

$$\dot{x}_{GPS} = [\, u\cos\theta + (v\sin\phi + w\cos\phi)\sin\theta \,]\cos\psi - (v\cos\phi - w\sin\phi)\sin\psi + W_{xE} + v_{\dot{x}_{GPS}} \tag{4.27}$$
$$\dot{y}_{GPS} = [\, u\cos\theta + (v\sin\phi + w\cos\phi)\sin\theta \,]\sin\psi + (v\cos\phi - w\sin\phi)\cos\psi + W_{yE} + v_{\dot{y}_{GPS}} \tag{4.28}$$
$$\dot{z}_{GPS} = u\sin\theta - (v\sin\phi + w\cos\phi)\cos\theta + W_{zE} + v_{\dot{z}_{GPS}} \tag{4.29}$$

4.3.3. Attitude

Aircraft attitude is defined using the Euler angles, i.e pitch angle phi, roll angle $theta$ and yaw angle psi. Which are directly measured from the AHRS system.

$$\phi_{AHRS} = \phi + v_{\phi_{AHRS}} \tag{4.30}$$
$$\theta_{AHRS} = \theta + v_{\theta_{AHRS}} \tag{4.31}$$
$$\psi_{AHRS} = \psi + v_{\psi_{AHRS}} \tag{4.32}$$

(4.33)

4.3.4. Airdata

True airspeed measurement is obtained from the DADC, and is used for the body velocity (u, v, w) corrections.

$$V_{TAS} = \sqrt{u^2 + v^2 + w^2} + v_{TAS_{DADC}} \tag{4.34}$$

Boom vane angle of attack α_v and sideslip β_v measurements.

$$\alpha_v \approx \left(1 + C_{\alpha_{up}}\right)\alpha - \frac{x_{v_\alpha}\left(q - \lambda_q\right)}{u} + v_{\alpha_{boom}} \tag{4.35}$$

$$\beta_v \approx \beta + \frac{x_{v_\beta}\left(r - \lambda_r\right)}{u} - \frac{z_{v_\beta}\left(p - \lambda_p\right)}{u} + v_{\beta_{boom}} \tag{4.36}$$

, where $\alpha = \arctan(w/u)$, and $\beta = \arctan(v/u)$.

4.4. Iterated Extended Kalman Filtering

As was discussed in previous section 4.1.2, only the IEKF and UKF are considered applicable for estimating states where non-linear behavior is concerned. But first the Iterative Extended Kalman Filter (IEKF) is discussed, which is capable of optimizing the extended Kalman Filter (EKF) routine that linearizes the state and observation, and is followed by a first order approximation (Jacobian) leaving some residual uncertainty in the optimal solution.

This residual uncertainty can be a problem in getting the filter to properly converge, thus a repeating sequence of steps (iterations) are added to the EKF. These iterations are used to minimize the fractional error between predicted one-step-ahead state estimates, with the recalculated predicted observation measurements leading to a change of the Kalman gain matrix.

This process thus recursively recalculates the optimal state within a single measurement step, until the error between the initial optimal state, and the newly calculated optimal state drops below an acceptable level, thus canceling the iteration process. Upon reaching this threshold, the process which is now conveniently called the Iterated Extended Kalman Filter (IEKF), continues the state estimation for the next step in the set of measurements. The IEKF is therefore an iterative semi-optimal extension of the EKF.

A MATLAB function can be called to specifically handle the Kalman filtering routine, and runs the Kalman routine as a function of the initially guessed state $\underline{x}_0$ with some initial prediction error covariance matrix P_0, the set of current output measurements $\underline{z}_{k,k}$, the set of current input measurements $\underline{u}_{k,k}$, system input noise covariance matrix Q, system output noise covariance matrix R, and a specific time-step dt.

4.4.1. Noise covariance

Preceding the execution of the IEKF function some preliminary actions are required, i.e the system input system noise covariance matrix Q (equation 4.37) and the output sensor noise covariance matrix R (equation 4.38) is set according to aircraft sensor specifications.

$$Q = diag\begin{bmatrix} \sigma^2_{w_x} & \sigma^2_{w_y} & \sigma^2_{w_z} & \sigma^2_{w_p} & \sigma^2_{w_q} & \sigma^2_{w_r} \end{bmatrix} \tag{4.37}$$

$$R = diag\begin{bmatrix} \sigma^2_{v_x} & \sigma^2_{v_y} & \sigma^2_{v_z} & \sigma^2_{v_{\dot{x}}} & \sigma^2_{v_{\dot{y}}} & \sigma^2_{v_{\dot{z}}} & \sigma^2_{v_\phi} & \sigma^2_{v_\theta} & \sigma^2_{v_\psi} & \sigma^2_{v_{V_{TAS}}} & \sigma^2_{v_\alpha} & \sigma^2_{v_\beta} \end{bmatrix} \tag{4.38}$$

, where special attention has to be paid to the varying standard deviations of the Airdata System per requirement of investigation.

4.4.2. Initiation procedure

The initial optimal state estimate $\hat{\hat{x}}_0$ has to be guessed, and can influence the filter performance greatly. Often a random value, close in the neighborhood of the true state is used. Meaning, that for this Kalman process it has been chosen to be within an reasonable range, and at the same time respecting every unique state value range. This initial value is chosen in such a way that it is far enough to be an incorrect measurement, but still has a reasonable value that one might expect to be measured.

Equally, the corresponding initial covariance optimal error estimate P_0 has to be chosen. This is done by taking the variance of the initial state, and the true state, and solely paying respect to the diagonal values. By multiplying this initial covariance estimate with some large value should make it a ”little bit” more difficult for the filter to correct this initial error, i.e. first few steps during filter initiation.

On a final note, filter initiation is known to be a bit of a black-art (not exact), as in there are many roads that lead to a solution, and none are seemingly either better or worse at first glance. In most cases creating something that ”works” is often enough, but slight unsuspecting differences can break the process, and one needs to be weary about this!

4.4.3. Filter process

The filter process runs through all measurement datasets, where each step’s sub-process is briefly explained. NB. the IEKF is in essence an eight-step filter process, that repeats on every measurement step with a specific dataset. This IEKF process contains an optimization routine that attempts to minimize residual error before continuing to the finalizing step.

Iterative process
The nominal states are updated using the current measurement, and re-linearizing the system using the improved nominal states [7, 37]. Thus, the generalized process-flow of the iterative process as given in figure 4.4, is spanned by three repeating steps.

Preceding the iterations, an iterator η_1 is defined, i.e. the perturbed nominal state. This iterator equals the previously predicted one-step-ahead state in step one. Subsequently, the fifth step is concerned with recalculating the Jacobian of the measurement transition, sixth step recalculated the Kalman gain matrix K and the seventh step updates the measurement/predicted state and calculates the error with the previously defined iterator. This process is repeated recursively upon having the error between iterators drop below a given threshold ε_0. When this happens, the optimal estimated state is found, and passed on to step eight.

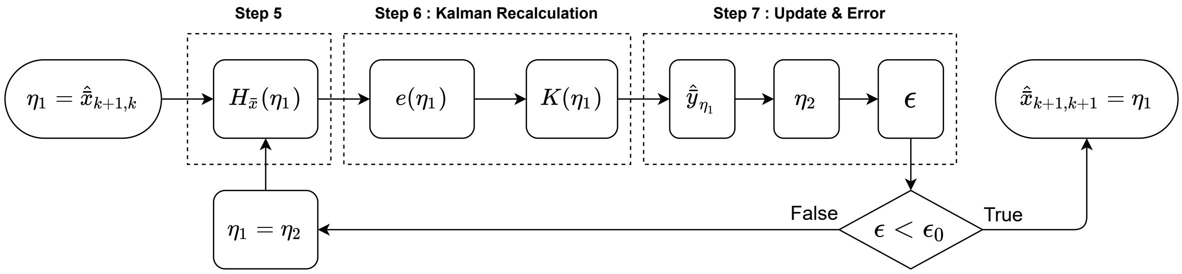

Figure 4.4: Iterative process added to the Extended Kalman Filter (EKF) concerning the optimal state estimation, accounting for uncertainties within the first order approximations of every measurement step.

The routine will break its iterative process if a specified number of iterations is reached, or drops below a given level of significance ε.

$$\varepsilon = \frac{||\eta_2 - \eta_1||}{||\eta_1||} \tag{4.39}$$

Step 1: One-Step-Ahead Prediction
The one-step-ahead state, i.e. the predicted state $\hat{\underline{x}}_{k+1,k}$, is computed using a 4th order Runge-Kutta integration.

$$\hat{\underline{x}}_{k+1,k} = \hat{\underline{x}}_{k,k} + \int_{t_k}^{t_{k+1}} \underline{f}\left(\hat{\underline{x}}_{k,k}, \hat{\underline{u}}^*_{k,k}, t\right) dt \quad , \quad \hat{\underline{u}}^*_{k,k} = \hat{\underline{u}}_{k,k} \tag{4.40}$$

Step 2 : Calculate Jacobian of the state transition
The Jacobian state transition is calculated by taking the derivative of the system matrix f for every state variable (Equation C.6). Next to the Jacobian, the system input noise matrix G is computed every time, which is needed for the discretization process in the next step.

$$F_{\underline{x}}(\bullet) = \frac{\partial}{\partial \underline{x}} f\left(\hat{\underline{x}}_{k+1,k}, \hat{\underline{u}}^*_{k,k}\right) \quad , \quad \hat{G} = G\left[\hat{\underline{x}}_{k+1,k}\right] \tag{4.41}$$

Step 3 : Discretization of the state transition and input matrix
The linear difference equation (equation 4.42) is obtained by discretization of the time varying state-space model, computing its predicted discretized version using equation 4.41.

$$\delta \underline{x}_{k+1,k} = \Phi_{k+1,k}(\bullet) \cdot \delta \underline{x}_{k+1,k} + \Gamma_{k+1,k}(\bullet) \cdot \delta \underline{w}_{d,k} \tag{4.42}$$

Step 4 : Covariance of state prediction error
The covariance matrix of the state prediction error $P_{k+1,k}$ is computed according to equation 4.43

$$P_{k+1,k} = \Phi_{k+1,k}(\bullet) \cdot P_{k,k} \cdot \Phi^T_{k+1,k}(\bullet) + \Gamma_{k+1,k}(\bullet) \cdot Q_{d,k} \cdot \Gamma_{k+1,k}(\bullet)^T \tag{4.43}$$

Step 5 : Measurement equation Jacobian recalculation
The Jacobian of the measurement transition (equation 4.44) is computed for the predicted state, it takes the derivative of all elements within the observation matrix (Appendix C.7) for all state variables.

$$H_{\underline{x}}[\eta_1] = \frac{\partial}{\partial \underline{x}} h[\eta_1] \tag{4.44}$$

Local observability analysis
By simple means the local nonlinear observability can be proven by making use of Lie derivatives. Allowing for a construction of the O matrix to be build that can be compared to the analysis done for linear systems [24, 71]. This way the state observability is analyzed at this point in the process, i.e. when state is not observable the Kalman filter will not converge. When running the filter a warning is given if this is the case. If the rank of O is equal to the number of states n, then the system is observable and the Kalman filter will converge.

$$O = \begin{bmatrix} \partial_{\underline{x}} h \\ \partial_{\underline{x}}\left(L_f h\right) \\ \vdots \\ \partial_{\underline{x}}\left(L_f^{(n-1)} h\right) \end{bmatrix} \quad , \quad \begin{matrix} L_f h = \partial_{\underline{x}} h \cdot f \\ L_f L_f h = \partial_{\underline{x}}\left(L_f h\right) \cdot f \\ L_f L_f L_f h = \partial_{\underline{x}}\left(L_f L_f h\right) \cdot f \\ \vdots \end{matrix} \tag{4.45}$$

Step 6 : Kalman gain calculation
The Kalman gain matrix K is obtained by first computing the matrix of innovation e and subsequently computing the gain itself as follows.

$$e[\eta_1] = H_{\underline{x}}[\eta_1] \cdot P_{k+1,k} \cdot H_{\underline{x}}[\eta_1]^T + R \tag{4.46}$$

$$K[\eta_1] = \frac{P_{k+1,k} \cdot H_{\underline{x}}[\eta_1]^T}{e[\eta_1]} \tag{4.47}$$

Step 7 : Measurement and state estimate update
The final step within the iterative process updates the measurement prediction $\underline{\hat{z}}_{\eta_1}$.

$$\underline{\hat{z}}_{\eta_1} = h[\eta_1] \tag{4.48}$$

Followed by the predicted state iterator η_2, i.e. iterative version of the measurement update.

$$\eta_2 = \hat{x}_{k+1,k} + K[\eta_1] \cdot \left(\underline{z}_{k,k} - \underline{\hat{z}}_{\eta_1} - H_{\underline{x}}[\eta_1] \cdot (\underline{\hat{x}}_{k+1,k} - \eta_1)\right) \tag{4.49}$$

Step 8 : Covariance matrix of state estimation error
Upon reaching the required precision in error during the iterative process, the predicted state η_1 is set equal to the optimal estimated state $\underline{\hat{x}}_{k+1,k+1}$.

$$\underline{\hat{x}}_{k+1,k+1} = \eta_1 \tag{4.50}$$

The optimal estimated error covariance matrix $P_{k+1,k+1}$, as being the final part needed in the IEKF process, is obtained as follows.

$$P_{k+1,k+1}[\eta_1] = \left(I - K[\eta_1] \cdot H_{\underline{x}}[\eta_1]\right) \cdot P_{k+1,k} \cdot \left(I - K[\eta_1] \cdot H_{\underline{x}}[\eta_1]\right)^T + K[\eta_1] \cdot R \cdot K[\eta_1]^T \tag{4.51}$$

This final step ends the IEKF process for one measurement, the newly found optimal estimate is stored in a data structure. The process continues as long as measurements are provided.

4.5. Unscented Kalman Filtering

A brief description is given regarding the Unscented Kalman Filtering (UKF), as it is mainly used in recent research done by Van Ingen and Van den Hoek in regard to stall model identification [62, 67]. For the reconstruction of the state no linearization is needed, and is an adaptation on the scaled unscented transformation by Julier [28]. The UKF process which will be described next, is a result of this adaptation and was created through the work of Wan and van der Merwe, and Teixeira et al. [56, 72].

4.5.1. General information

The UKF is a popular type of filter found in many applications regarding the state reconstruction of the flight path of an aircraft. And finds it's strengths in being robust to problems that might occur upon filter initiation, where the choice of initial state and covariance matrix might cause the filter to diverge. On the other hand, the filter process is more tedious, and can heavily influence the computer processing time depending on the number variables contained within state, process- and observation noise vectors. This is a slowing factor, compared to the IEKF.

4.5.2. Process

The process is started by first grouping of the sigma points (X) in a matrix of $2L+1$ sigma vectors, with L being the state vector. These points are used by propagation through the system dynamics equations.

$$\mathrm{X}_0 = \bar{x} \qquad , \tag{4.52}$$

$$\mathrm{X}_i = \bar{x} + \sqrt{(L+\lambda)P_x} \quad , \quad i = 1, \dots, L \tag{4.53}$$

$$\mathrm{X}_i = \bar{x} - \sqrt{(L+\lambda)P_x} \quad , \quad i = L+1, \dots, 2L \tag{4.54}$$

Equations 4.52, 4.53 & 4.54 contain the expected value ($\bar{x} = E[x]$), the covariance matrix P_x of x, where $P_x = E\left[(x-\bar{x})(x-\bar{x})^T\right]$. And Equation 4.55 presents the λ parameter as is defined as follows, where α and κ are used as scaling parameters.

$$\lambda = \alpha^2 (L+\kappa) - L \tag{4.55}$$

With regards to the sigma vectors, in Equations 4.56, 4.57 & 4.58 the weights are defined as follows.

$$W_0^m = \lambda/(L+\lambda) \tag{4.56}$$

$$W_0^c \ = \lambda/(L+\lambda) + (1-\alpha^2+\beta) \tag{4.57}$$

$$W_i^m = W_i^c = 1/\{2(L+\lambda)\}, \quad i = 1, \dots, 2L \tag{4.58}$$

In the research done by Julier on these UKF weights, a β scaling parameter is added, where this value should be non-negative, and have a value of 2 for optimal effect regarding Gaussian distributions [28].

This leads to the availability of three tuning parameters of the UKF process, where the values of α and β are used to set the distribution size of the sigma points around the mean, presented in Figures 4.5 and 4.5 by Van Horssen.

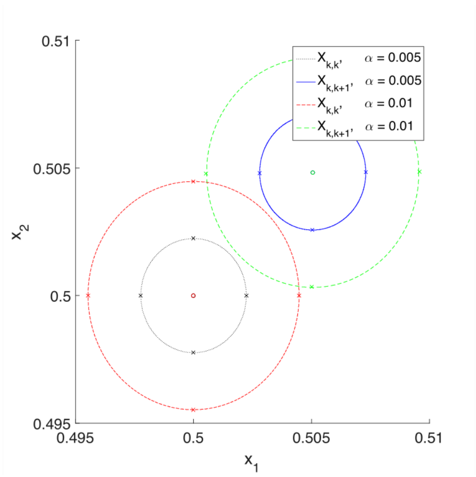

Figure 4.5: Effect of the α tunning parameter on the UKF process. Adapted from Van Horssen [65].

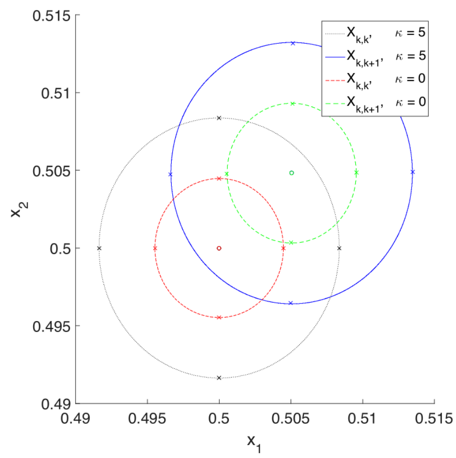

Figure 4.6: Effect of the κ tunning parameter on the UKF proccess. Adapted from Van Horssen [65].

Work done by Wan and van der Merwe defined the parameter value for α to best be in orders -3 of magnitude, within a range between 0 and 1 [72]. Regarding the κ parameter value, as long as $\lambda \neq 0$, can be both negative and positive. With according to Julier, making the calculation of a non-positive, semi-definite covariance matrix $P_{k,k+1}$ a possibility in the event λ has a negative value. Non-positive semi-definite covariance matrices will break the UKF process, and can be avoided by calculating around $X_{0|k,k+1}$ as Equation 4.64 shows [28].

As is mentioned by Van Ingen, the previous Citation flight-test data is filtered using an UKF that makes use of the in Table 4.2 presented parameters with their chosen filter values [67].

Table 4.2: UKF Parameters used in previous research, obtained from Van Ingen [67].

Parameter	Allowable Range	Chosen Value
α	$[0,1]$	0.3
κ	$\neq \left(\frac{1}{a^2}-1\right)L$	0
β	$[0,\inf)$	2

4.5.3. Implementation

The UKF processes is implemented first by appending the state vector $\bar{x}_{k,k}$ onto process noise variables $\bar{v}_{k,k}$, and observation noise variables $\bar{w}_{k,k}$. This then becomes the augmented state vector $\bar{x}^a_{k,k} = \left[\bar{x}^T\,\bar{v}^T\,\bar{w}^T\right]$, where Equation 4.59 presents the augmented **estimated** state vector with length L.

$$\hat{\bar{x}}^a_{k,k} = E\{\bar{x}^a_{k,k}\} = \{\hat{\bar{x}}\,\bar{0}\,\bar{0}\} \tag{4.59}$$

And in Equation 4.60 the corresponding augmented covariance matrix is given, note that it is assumed that the noise zero-mean Gaussian distributed, thus the expected value for the noise vectors is therefore zero.

$$P^a_{k,k} = E\left\{\bar{x}^a_{k,k} - \hat{\bar{x}}^a_{k,k}\right\} = \begin{bmatrix} P_{k,k} & 0 & 0 \\ 0 & Q & 0 \\ 0 & 0 & R \end{bmatrix} \tag{4.60}$$

Combining the grouped sigma points (Eqs. 4.52, 4.53 & 4.54), with their weights (Eqs. 4.56, 4.57 & 4.58), the augmented sigma points $X^a_{k,k}$, as given in Equation 4.61, can be constructed. Where the dimension of L is spanned by the state space, input - and process noise.

$$X^a_{k,k} = \hat{\bar{x}}^a_{k,k}\left[1 \quad 1+\sqrt{(L+\lambda)P^a_{k,k}} \quad 1-\sqrt{(L+\lambda)P^a_{k,k}}\right] = \left[(X^x)^T \quad (X^v)^T \quad (X^w)^T\right] \tag{4.61}$$

State prediction
With the obtained augmented sigma points from Equation 4.61, the prediction step (Equation 4.62) is in sight where the points belonging to the state are transformed throught the system navigation equation f. After this, the predicted state estimate (Equation 4.63), and covariance matrix (Equation 4.64) are calculated by making use of the sigma weights.

$$X^x_{k+1,k} = X^x_{k,k} + \int_{t_k}^{t_{k+1}} f\left(X^x_{k,k}, \bar{u}_k, X^v_{k,k}\right) dt \tag{4.62}$$

$$\hat{\bar{x}}_{k+1,k} = \sum_{i=0}^{2L} W_i^m X^x_{i|k+1,k} \tag{4.63}$$

$$P_{k+1,k} = \sum_{i=0}^{2L} W_i^c \left[X^x_{i|k+1,k} - \hat{\bar{x}}_{k+1,k}\right]\left[X^x_{i|k+1,k} - \hat{\bar{x}}_{k+1,k}\right]^T \tag{4.64}$$

Here it should be noted that Van Ingen added the $\bar{u}_k$ variable to Equation 4.62, i.e. input at time k.

Measurement prediction
The predicted augmented sigma points $\mathrm{X}^{x}_{k+1,k}$ are transformed again through the measurement prediction step (Equation 4.65) using the observation equation h, this yields the measurement prediction $\hat{\bar{y}}_{k+1,k}$ (Equation 4.66).

$$\Upsilon_{k+1,k} = h\left(\mathrm{X}^{x}_{k+1,k}, \mathrm{X}^{w}_{k,k}\right) \tag{4.65}$$

$$\hat{\bar{y}}_{k+1,k} = \sum_{i=0}^{2L} W_i^m \Upsilon_{k+1,k} \tag{4.66}$$

Covariance prediction
With both the state $\mathrm{X}^{x}_{k+1,k}$ and measurement $\Upsilon^{x}_{k+1,k}$ predicted sigma points obtained, innovation $P_{\hat{y}_k,\hat{y}_k}$ (Equation 4.67) and cross $P_{\hat{y}_k,\hat{y}_k}$ covariance (Equation 4.68) matrices can be calculated.

$$P_{\hat{y}_k,\hat{y}_k} = \sum_{i=0}^{2L} W_i^c \left[\Upsilon_{k+1,k} - \hat{\bar{y}}_{k+1,k}\right]\left[\Upsilon_{k+1,k} - \hat{\bar{y}}_{k+1,k}\right]^T \tag{4.67}$$

$$P_{\hat{y}_k,\hat{y}_k} = \sum_{i=0}^{2L} W_i^c \left[\mathrm{X}_{i|k+1,k} - \hat{\bar{x}}_{k+1,k}\right]\left[\Upsilon_{k+1,k} - \hat{\bar{y}}_{k+1,k}\right]^T \tag{4.68}$$

State update
Through a simple matrix operation using the covariance prediction (Equation 4.69) the Kalman gain can be obtained.

$$K_{k+1} = P_{\hat{x}_k,\hat{y}_k} P^{-1}_{\hat{x}_k,\hat{y}_k} \tag{4.69}$$

After which the state (Equation 4.70) and covariance (Equation 4.71) is updated to the corrected "optimal" estimate.

$$\hat{\bar{x}}_{k+1,k+1} = \hat{\bar{x}}_{k+1,k} + K_{k+1}\left(\bar{y}_{k+1} - \hat{\bar{y}}_{k+1,k}\right) \tag{4.70}$$

$$P_{k+1,k+1} = P_{k+1,k} - K_{k+1} P_{\hat{y},\hat{y}} K^T_{k+1} \tag{4.71}$$

II

Thesis research

5

Research vehicle - Fokker 100 (MK-0100)

The Fokker 100 (see Figure 5.1) is a medium-sized, twin-turbofan jet airliner from Fokker Services B.V. (TCDS), the largest such aircraft built by the company before its bankruptcy in 1996. The type possessed low operational costs and initially had scant competition in the 100-seat short-range regional jet class, contributing to strong sales upon introduction in the late 1980s.

Figure 5.1: Fokker 100 (F28-MK-0100) with aircraft registration code PH-OFN standing on the tarmac. Source Andreas Fietz, Planespotters. Fair-use.

Table 5.1: Fokker 100 - Specs.

Wing span	b	28.08	m
Wing area	S	93.50	m^2
Aspect ratio	A	8.43	-
Root chord	c_{root}	5.60	m
Tip chord	c_{tip}	1.26	m
Taper ratio	λ_w	0.24	-
Fuselage diameter	D_f	3.30	m
1/4 chord sweep angle	$\Lambda_{\frac{1}{4}}$	17.45	deg

However, an increasing number of similar airliners were brought to market by competitors during the 1990s, leading to a substantial decline in both sales and long-term prospects for the F100. Fokker also encountered financial difficulties and was bought up by Deutsche Aerospace AG, which in turn had financial troubles of its own, restricting its ability to support multiple regional airliner programs. Accordingly, in 1997, production of the Fokker 100 was terminated after 283 air-frames had been delivered.

By July 2017, a total of 113 Fokker 100 aircraft remained in airline service with 25 airlines around the world. Although airlines are currently retiring the aircraft, there are still large numbers in operation in both Australia and Iran [25].

5.1. Specifications

The F28 Mark 0100 “Fokker 100” is based on the Fokker F28 Mark 4000 re-engineed with two Rolls-Royce RB.183 Tay high by-pass ratio turbofans and a fuselage stretched by 18.83 ft (5.74 m), where in Figure 5.2 an impression is presented regarding aircraft dimensions.

Its wing is wider by 9.8 ft (3.0 m), has new flaps and larger ailerons, and extended leading and trailing edges improve aerodynamics and increase the wing chord. The landing gear is strengthened and has new wheels and brakes, and the horizontal stabilizer is widened by 4.6 ft (1.4 m).

Maximum weights are increased while fuel capacity, max speed and ceiling remain the same, passenger capacity went from 85 to 109. The flight deck went digital with a flight management system, an autopilot/flight director including CAT III autoland, thrust management system, electronic flight instrument displays and full ARINC avionics.

The new wing was claimed to be 30% more efficient in cruise, while retaining the simplicity of a fixed leading edge. The cockpit was updated with a Rockwell Collins DU-1000 EFIS. Like the Fokker Fellowship, the Fokker 100 retained the twin rear fuselage-mounted engines and T-tail configuration, like the Douglas DC-9 family. It lacks the F28 eyebrow windows above the cockpit [25, 26].

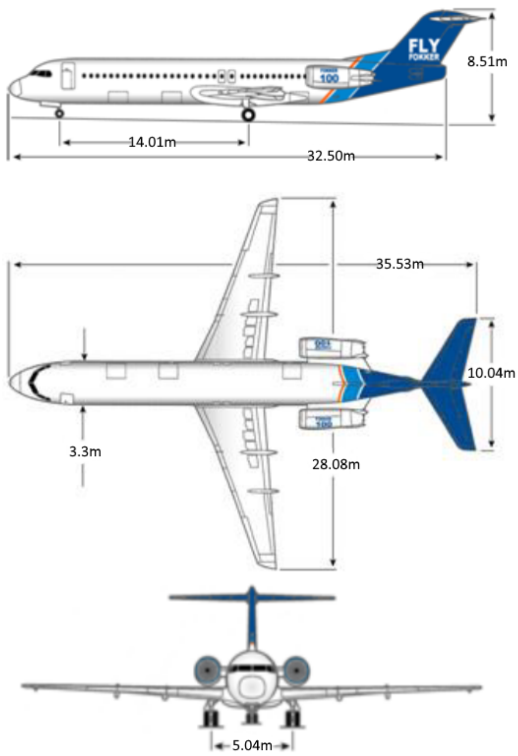

Figure 5.2: Fokker 100 - Schematic overview.

5.2. Airfoil

From literature, it is found that the F100 airfoil is twisted to guard against stall occurring first at the wing tip. In the event of such a stall, this counters an unwanted noise-up moment [64]. As can be seen in Figure 5.3, a side view of the airfoils is presented. Here clearly the airfoil twist is shown, based on F100 Aerodynamic data obtained from the thesis research done by Van Eijndhoven, supervised by Obert [46, 64]. From this research important information was obtained as to foil characteristic dimensions, location, and angles of twist. A compact overview of these values are given in Table 5.2, where b_w is the span-wise fractional location, ϵ_t is the angle of twist , $i_{w,n}$ is the incidence angle, and the coordinates are defined as x_{le}, y_{le}, z_{le} on the axis fixed at the leading edge of the wing root and wing-chord c.

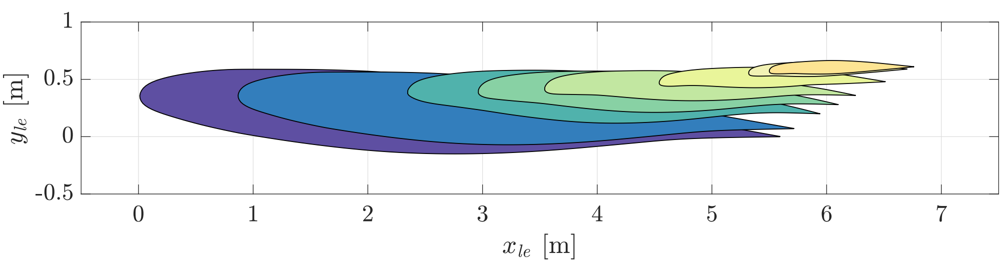

Figure 5.3: Fokker 100 - Side view of wing airfoils, obtained through F100 Aerodynamic Data [46].

Equation 5.1 is used to calculate the angle of twist between two airfoils, this was used in Table 5.2 to highlight relative twist (and create the side view figure).

$$\epsilon_{t,n_w} = i_{w,n_w+1} - i_{w,n_w} \tag{5.1}$$

Table 5.2: Fokker 100 - Airfoil alignment data w.r.t the wing-root's leading edge. Adapted from F100 Aerodynamic Data [46].

n_w	airfoil, n_{af}	b_w [-]	ϵ_t [deg]	$i_{w,n_{af}}$ [deg]	x_{le} [m]	y_{le} [m]	z_{le} [m]	c [m]
1	1 - root	0.00	0.00	3.66	0.00	0.00	0.00	5.60
2	1	0.12	-0.24	3.42	0.86	1.70	0.07	4.86
3	2 - kink	0.33	-0.65	3.01	2.34	4.60	0.20	3.60
4	3	0.46	-1.58	2.08	2.96	6.44	0.28	3.14
5	4	0.59	-2.45	1.21	3.54	8.18	0.36	2.71
6	5	0.79	-3.95	-0.29	4.54	11.16	0.48	1.97
7	6	0.96	-5.13	-1.47	5.32	13.52	0.59	1.38
8	6 - tip	1.00	-5.40	-1.74	5.50	14.04	0.61	1.26

6
Mass model

It is imperative to have a good mass model where corrections to measurements and/or estimations of the aerodynamic parameters are concerned. In other words, a more accurate mass model leads to a higher quality of parameter estimation, which is in essence a primary goal of this thesis. As primer, the end result of the determination of the Fokker 100 prototype mass model is presented in Figure 6.1, which provides a visual impression of the discretized mass distribution of the aircraft by plotting the weight normalized masses in three dimensions.

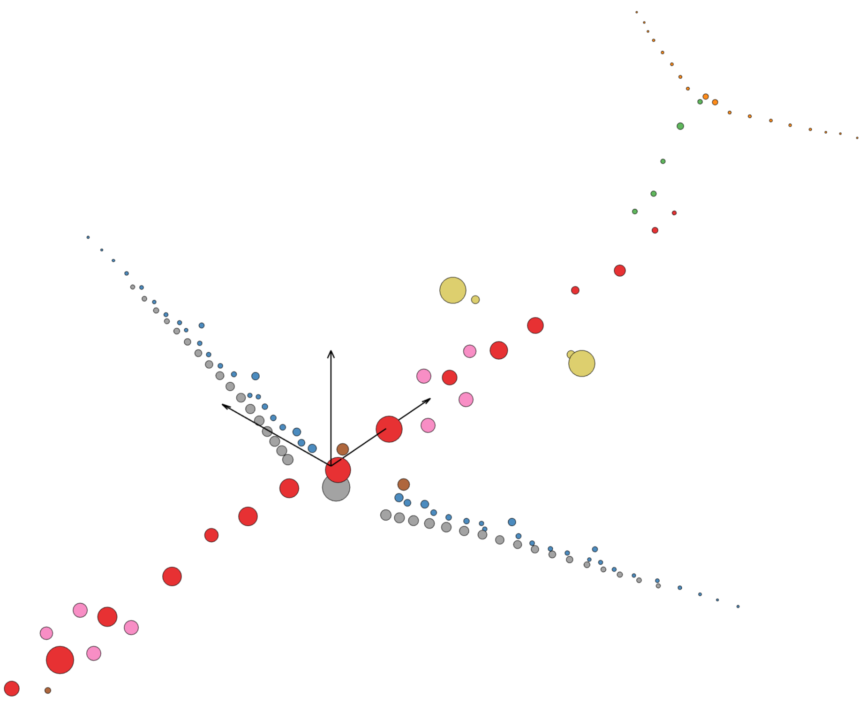

Figure 6.1: Schematic overview of the Fokker 100 mass model with total fuel loading (grey), full water ballast tanks (pink), fuselage sections (red), engines (yellow), main wing sections (blue), vertical (green) and horizontal (orange) stabilizer portraits a discretized weight normalized mass distribution.

Initially it was assumed that the weight and balance documentation[15] provided by Fokker and the information contained within the MRVS database would be enough to yield some valid figures for obtaining information about the aircraft's center of gravity and it's inertia w.r.t. this important location within the aircraft vehicle reference frame F_r (see Appendix B). This was not the case, where the database only provides lift force information, which is insufficient when constructing an aerodynamic model that requires knowledge regarding all forces and moments.

Furthermore, no working routines or off-the-shelf models capable of describing the aircraft's inertial products and moments per recorded flight-test could not be found at Fokker Services. It is assumed that there might exist such a model or functioning routine, but finding it would require multiple trips to Hoofddorp and more hours spend digging in out-dated Fokker Fortran code. Therefore more research was done by investigating Fokker provided standard calculation (STB) documentation for the Fokker 70/100[12, 13, 14].

After rigorous investigation of the STB methods used to determine the center of gravity, and something that could describe the aircraft's inertia in meaningful manor, only half-methods were encountered with lots of missing data and references to tables that were either lacking proper unit definitions or had no information in them at all. Although most parameters described in the STB are well documented, the weight and balance parameters should be avoided at all cost. N.b. presented STB methods are equally tedious and over-complicated.

At this point only two options remained, first one implied making an assumption about the aircraft's section masses, i.e. fuselage, wings, etc. All based on the available MRVS parameters contained in the database, such as the actual mass (MT, Appendix D.1), actual center of gravity (GCA, Appendix D.2), fuel and water ballast weights. Or using two inertial tensors found in simulator documentation. Where the first one would require numerous assumptions and the latter would be severely under defined. Both suggested options would inevitably raise questions about the estimated aerodynamic parameter validity, and thus leaves this thesis hanging without any prospect on providing an answer to the main research question.

Through luck and a lot of researching the STB's references, a link was found pointing to a report containing inertial data regarding the Fokker 100 prototype. After requesting the documents at Fokker Services, chief engineer Dirk van Os responded with the sought for technical document containing all the inertial data regarding the prototype[21]. In the wake of this discovery, another report was found by Van Os containing a large amount of load cases concerning the Fokker 100 production/series aircraft, this yielded vital information regarding fuel loading and payload stowing schemes[73]. As will be discussed in this chapter, the data contained in these documents lead to a properly defined mass model, where an excerpt of the most important weight and balance data can be found in Appendix E.

This chapter first discusses the theory used in defining the inertial tensor in Section 6.1, relevant aircraft sections definitions of mass in Section 6.2, influence of the water ballast tanks in Section 6.3, modeling of fuel loading and distribution in Section 6.4 and the validation of the aircraft's inertial model in Section 6.5.

6.1. Determination of the inertial tensor

Within a system of point masses the inertial tensor is determined through a simple process. As illustrated in process flow Figure 6.2, location and mass are a first priority, thus need to be defined properly in order to determine the center of gravity G. Having found its specific location, the inertial tensor can be found by determining all mass moments and products relative to the location of the center of gravity, i.e. the body-fixed reference system F_b origin.

A schematic description of the inertial axis system is given in Figure 6.3, where two frames of reference can be distinguished. The first frame of reference is the vehicle-nose reference frame F_W as defined by the coordinate system $(O_W X_W Y_W Z_W)$ w.r.t. to the aircraft's nose and fuselage center-line (see Appendix B), this is a right-handed axis system. The second one is the body-fixed reference frame F_b as defined by the coordinate system $(G X_b Y_b Z_b)$, the location of this frame is variable within the vehicle-nose reference frame and equally depicts a right-handed axis system[38].

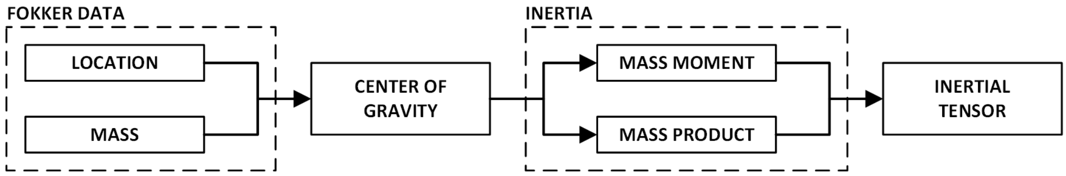

Figure 6.2: Simplified overview of the processes concerned with the determination of the inertial tensor.

It's important to properly convert the right-handed to the left-handed system to avoid miss placing vital mass elements of the aircraft (see Figure B.5 for left- versus right-handed axes systems). Note that, frames used by Fokker contradict the defined frames of reference used in literature, which for instance arbitrarily chooses its origin location of the vehicle F_r frame of reference using a left-handed axis system[38]. Yet Fokker uses right-handed frames that have been rotated 180 degrees about the center-line in the x-direction for all specified aircraft sections (see Appendix B), but claims they are left-handed which is not the case[21]. And for the vehicle F_r, vehicle-nose F_W and vehicle-40 $F_{r,40}$ frames of reference an upward pointing z-axis. Thus axis system as described in Figure 6.3 uses a right-handed, z-axis upward pointing frames of reference, i.e. the vehicle-nose F_W and body-fixed F_b frames of reference. All aircraft discretized mass elements are converted to F_W of which a list containing all the locations exists (see Appendix E), providing a means to derive useful information about the center of gravity and the acting moments/products around it.

Taking this knowledge in account and having all mass elements defined in one frame important data can be determined, like for instance the center of gravity within the right-handed vehicle-nose F_W frame of reference. Having information on the CG, relevant balancing details can be expressed in percentages of mean aerodynamic chord. The distance between O_r and G along the x-direction is defined as a fraction of the mean aerodynamic chord mac, and is the center of gravity actual (CGA) MRVS parameter output value as described in Appendix D.2, which is used to verify MRVS STB values with routines created for this thesis. On a special note, Fokker defines the origin O_r at station 15799 from O_W along the fuselage center-line in x-direction (see Appendix B).

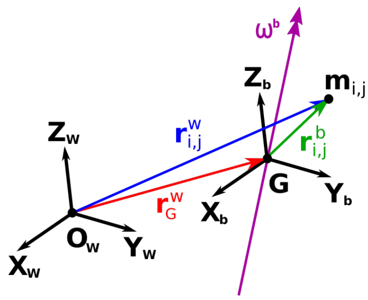

Figure 6.3: Schematic representation of the inertial axis system expressed in the nose vehicle reference frame F_W at its origin O_W w.r.t. the aircraft's center of gravity in G in the body-fixed reference frame F_b.

Thus, discretized aircraft masses are defined as the relevant groups or elements of point-masses m_i in the vehicle-nose frame F_W. With their locations defined by the vectors r_i^W in the vehicle-nose F_W and r_i^b in the body-fixed F_b reference frame, where i is an integer defining which mass element of the aircraft is selected. And the previously mentioned remaining vector r_G^W that defines the aircraft's center of gravity and at the same time defines the origin G of the body-fixed reference frame F_b.

Rotation vector $\boldsymbol{\omega}^b$ illustrates the notion that all rotations (and of coarse translations) occur w.r.t. the origin in G as it represents the aircraft's center of gravity in the body-fixed frame of reference.

6.1.1. Local mass element locations per aircraft section

Fokker supplied inertial data as can be found under the weight and balance information in Appendix E. By itself this data does not give the exact locations of every mass element in the aircraft, but it does supply all the moments and masses corresponding to each element with respect to a section's local origin 0_i^W, where i defines the section origin's index. As shown in equation 6.1, a simple computation procedure is capable of easily converting and obtaining all mass locations.

$$\mathrm{r}_{i,j}^W = 0_i^W + \frac{\mathrm{M}_{i,j}}{m_{i,j}} \quad \forall \quad i = 1,2,\ldots,N \quad , \quad j = 1,2,\ldots,k_i \quad , \quad k_i \in \mathbb{N} \tag{6.1}$$

Hence, the location of a mass element is found through dividing the local internal moment vector $\mathrm{M}_{i,j}$ by its local mass $m_{i,j}$, yielding to the local arm with respect to its local mass element. Note that the index j defines the mass index w.r.t. to a section defined by index i, where N defines the total number of sections in the aircraft and k_i defines the total number of section mass elements. Specifically every mass element belongs to a unique section of the aircraft, i.e. fuselage, wings, vertical-/horizontal stabilizers, engines, undercarriage, fuel loading and water ballast tank contents. Subsequently, the moment vector $\mathrm{M}_{i,j}$ is spanned by the three moments around all three axis in the local origin 0_i^W defined by the ith index, where the moment vector has the following form $\left[\, M_x^{(i,j)}, M_y^{(i,j)}, M_z^{(i,j)} \,\right]^T$. A correction is applied by adding it's local section origin 0_i^W, this puts the mass element in the vehicle-nose F_W frame of reference.

By obtaining all locations of the mass element centers of gravity, it is stated that these positions define the local principle axes, i.e. moments around these axes are considered to be zero (see Equation 6.2).

$$\sum M_x^{(i,j)} = \sum M_y^{(i,j)} = \sum M_z^{(i,j)} = 0 \tag{6.2}$$

6.1.2. Center of gravity location

Using equation 6.3, a set of all discretized mass elements in the vehicle-nose F_W frame of reference allows for computation of the variable center of gravity origin location G in F_W, which is defined by the vector r_G^W in the vehicle-nose F_W frame of reference[49].

$$\mathrm{r}_G^W = \frac{\sum_{i=1}^{N} \sum_{j=1}^{k_i} m_i \, \mathrm{r}_{i,j}^W}{\sum_{i=1}^{N} \sum_{j=1}^{k_i} m_{i,j}} \tag{6.3}$$

The previously defined mass element locations $\mathrm{r}_{i,j}^W$ with their corresponding masses $m_{i,j}$ form the global location of the aircraft's center of gravity. In essence all masses are multiplied by their locations and summed, subsequently divided by the total aircraft mass. This includes the operating empty weight (OEW), fuel loading and water tank ballast contents.

6.1.3. Mass moment- and product of inertia

After having obtained the aircraft's global center of gravity, the mass moment- and product of inertia can be computed w.r.t. to this variable point G. First all mass element locations need to be computed w.r.t. the global center of gravity, by use of Equation 6.4 the mass element location $\mathrm{r}_{i,j}^b$ in the body-fixed F_b frame of reference is obtained.

$$\mathrm{r}_{i,j}^b = \mathrm{r}_G^W - \mathrm{r}_{i,j}^W \tag{6.4}$$

The vector $\mathrm{r}_{i,j}^b$ is spanned by the body-fixed coordinate system, i.e. $\left[x_{i,j}, y_{i,j}, z_{i,j}\right]^T$, where the superscript b has purposely been left out allowing for space to denote quadratic operations regarding moment of inertia computations. These inertial moment computations are shown in Equations 6.5, 6.6 and 6.7, and thus define the all moments of inertia w.r.t. the origin G in the body-fixed F_b frame of reference[49].

$$I_{xx}^{b} = \sum_{i=1}^{N}\sum_{j=1}^{k_i} I_{xx}^{(i,j)} + \sum_{i=1}^{N}\sum_{j=1}^{k_i} m_{i,j}\left(y_{i,j}^{2} + z_{i,j}^{2}\right) \tag{6.5}$$

$$I_{yy}^{b} = \sum_{i=1}^{N}\sum_{j=1}^{k_i} I_{yy}^{(i,j)} + \sum_{i=1}^{N}\sum_{j=1}^{k_i} m_{i,j}\left(x_{i,j}^{2} + z_{i,j}^{2}\right) \tag{6.6}$$

$$I_{zz}^{b} = \sum_{i=1}^{N}\sum_{j=1}^{k_i} I_{zz}^{(i,j)} + \sum_{i=1}^{N}\sum_{j=1}^{k_i} m_{i,j}\left(x_{i,j}^{2} + y_{i,j}^{2}\right) \tag{6.7}$$

Again the indexes i and j define the mass element j w.r.t. the the aircraft section i, N defines the total number of aircraft sections and k_i defines the total number of mass elements contained in a unique i[th] section of the aircraft. All mass elements have predetermined mass moments of inertia as can be found in Appendix E, obtained through the Fokker 100 prototype mass, moments and moments of inertia technical data[21].

The three equations 6.8, 6.9 and 6.10 define the mass products of inertia (I_{xy}, I_{xz}, I_{yz}) for a given specific mass element j contained in a section of the aircraft's structure i, and w.r.t. a plane spanned by the coordinate system $(GX_bY_bZ_b)$ as defined for the body-fixed F_b frame of reference for which symmetry can be tested. Hence, the choice of the frame of reference is as vital for the mass products as it is for the mass moments of inertia, i.e. a measure of symmetry[49].

$$I_{xy}^{b} = I_{yx}^{b} = \sum_{i=1}^{N}\sum_{j=1}^{k_i} I_{xy}^{(i,j)} + \sum_{i=1}^{N}\sum_{j=1}^{k_i} m_{i,j}\, x_{i,j}\, y_{i,j} \tag{6.8}$$

$$I_{xz}^{b} = I_{zx}^{b} = \sum_{i=1}^{N}\sum_{j=1}^{k_i} I_{xz}^{(i,j)} + \sum_{i=1}^{N}\sum_{j=1}^{k_i} m_{i,j}\, x_{i,j}\, z_{i,j} \tag{6.9}$$

$$I_{yz}^{b} = I_{zy}^{b} = \sum_{i=1}^{N}\sum_{j=1}^{k_i} I_{yz}^{(i,j)} + \sum_{i=1}^{N}\sum_{j=1}^{k_i} m_{i,j}\, y_{i,j}\, z_{i,j} \tag{6.10}$$

Next to being a important part of analyzing the aircraft dynamics of translating and rotating bodies, the products of inertia also functions as a measure of symmetry. As the name suggests, a product is involved that multiplies any two combinations of out three coordinates of a mass element in three-dimensional space that share a common plane. The sum of a large series of these mass elements would in theory return a zero value if any number of two paired elements are aligned, equal in mass and relative distance with respect to a shared point of reference. Hence, the non-zero value is for that matter a magnitude of imbalance in the plane spanned by two coordinate axes. On another note, products define how rotating around an axis gives angular momentum relative to a different axis, thus angular momenta can be decoupled in the principle axis system of inertia.

Furthermore, all products will yield a zero value when a Cartesian coordinate system has all it's three axis aligned with the principle axis of inertia, i.e. the principle axis are defined by the directions of the eigenvectors [9]. Note that it is possible that a Cartesian coordinate system has one axes aligned with one principle axis, thus two axes have a zero valued product while the remaining axis does not necessarily has to be zero as well, e.g. alignment occurs along the x-axis thus $I_{xy} = I_{xz} = 0$ with $I_{yz} \in \mathbb{R}$[9].

6.1.4. Inertial tensor

On the diagonal the moment of inertia elements are found and off-diagonal the products. As is illustrated in Equation 6.11, the inertial tensor I_G^b values are relative to the center of gravity G in the body-fixed F_b frame of reference.

$$\mathrm{I}_G^b = \begin{bmatrix} I_{xx}^b & -I_{xy}^b & -I_{xz}^b \\ -I_{yx}^b & I_{yy}^b & -I_{yz}^b \\ -I_{zx}^b & -I_{zy}^b & I_{zz}^b \end{bmatrix} \tag{6.11}$$

Thus the inertial tensor I_G^b is a square (3x3), real and symmetric matrix, and is thus diagonalizable. Hence, let the tensor be represented by a matrix A, then it is orthogonally diagonalizable if there exists an orthogonal matrix P such that $P^{-1}AP$ is a diagonal matrix D. As Equation 6.12 suggests, matrix A must be symmetric in order for it to be orthogonally diagonalizable [9].

$$A^T = (PDP^T)^T = (DP^T)^T P^T = PD^T P^T = PDP^T = A \tag{6.12}$$

Obtaining the inertial tensor's eigenvectors subsequently yields the tensor's principle inertial axis, of which is known that the products of inertia are always to be equal to zero. The question arises whether the principle axis align with axis of the frame of reference at hand, as it is previously mentioned that this some times might not be the case[9, 49].

Given that for all local section elements in the aircraft the moments of inertia are known (see Appendix E.2), it is accepted that all elements exist in the same plane of reference and have not been rotated. With the explicit exception to the vertical stabilizer and the fuel tanks. Moments of inertia are always relative to the local section element's center of gravity, furthermore the sum of moments w.r.t the center of gravity is thus equal to zero for every local element. Because no more information is supplied by Fokker, it is assumed that mass symmetry exists in these points. Strengthened by the fact that all moments relative to the local axis equate to zero, it is assumed that for most local mass elements per section of the aircraft there exists no product of inertia, i.e. equal to zero and local axis are aligned with all the local inertial axes.

$$[\, I_{xy}^{(i,j)}\, ,\, I_{xz}^{(i,j)}\, ,\, I_{yz}^{(i,j)}\,] \;=\; 0 \quad \exists \quad i = 1,2,\ldots,N \quad j = 1,2,\ldots,k_i \quad k_i \in \mathbb{N} \tag{6.13}$$

This is expressed in Equation 6.13, the products of inertia are zero for most mass elements contained in their respective section of the aircraft, except for a few other cases to be discussed in the next chapter sections.

6.2. Section and mass definitions

The operating empty weight (OEW) is used to define the Fokker 100 prototype aircraft's static masses, i.e. one fuselage, two wing, one vertical stabilizer, two horizontal stabilizer wing, two engine and undercarriage sections (see Table 6.1). The water ballast tanks are mentioned as quasi static, although water tank masses in most recordings are assumed to be static, a few recording test-cards mention the fact that during the flight masses were pumped between tanks to change center of gravity and inertial characteristics (see Appendix F).

Table 6.1: Fokker 100 prototype maximum section masses, based on the Fokker prototype load case documentation[21].

Section	Mass [kg]
Fuselage	16954.8
Wings (2x)	4369.0
Vertical Stabilizer	506.5
Horizontal Stabilizer (2x)	630.8
Engines (2x)	5149.9
Nose Undercarriage	124.0
Main Undercarriage (2x)	955.6
Operating Empty Weight (OEW)	28690.5
Fuel Tanks (left, right & center)	10306.0
Water Ballast Tanks (8x)	5300.0
Total	44296.5

A more formal description (see Equation 6.14 and Table 6.1) of the OEW would be spanned by the airframe- and engine structure weight (i.e. all residual fuel, engine oil, water, etc.), the manufacturers empty weight (MEW). This includes fixed equipment like avionics, cabin fight-test setup, utilities to name a few, i.e. the standard items (SI), and of coarse the flight-/cabin crew, i.e. operator items (OI) [40].

$$\mathrm{OEW} = \mathrm{MEW} + \mathrm{SI} + \mathrm{OI} \tag{6.14}$$

Comparing the by Fokker supplied technical reports ”Fokker 100 Load Cases” for the production aircraft, created by former Fokker employee Zwarts[73], to the prototype load case as found in the Fokker documentation ”Water in ballast tanks, moments and moments of inertia of the prototypes F28 MK0100” created by former Fokker employee Th. Heinkens[21] (see Appendix E), lead to a basic formulation of the Fokker 100 prototype mass model. Where Zwarts uses a slightly different approach in defining the OEW for the production aircraft, and speaks of a basic minimum weight (BMW) at 21711.1 Kilogram. This is simply a derived form of the formal OEW and is obtained by subtracting the following weights, i.e. cabin attendants, seats, crew luggage, wardrobe, galleys, containers, stores, stowage units, cabin chairs, luggage bins, carpets, service equipment and toilets (chemicals included). Reason for this very low minimum was based on covering the critical loads which occur at minimum weights (i.e. local accelerations) for all customer production aircraft [73]. This limits the use of Zwarts's report for this thesis, because it does not take the prototype cabin configuration (see Appendix E.1) in account. Nb. as can be seen in Table 6.14, which is based on Heikens data for the prototype, the OEW is 28,690.5 kg and significantly differs from the BMW. A reasonable assumption would be that the unaccounted 6979.4 kg of mass is part of the test prototype test equipment (SI) and possibly the crew (OI) as well.

Because SI-/OI weights, locations are to a large extend unknown, it is assumed that these values are part of the fuselage data provided by Heinkens[73], although the flight-test cards do mention the crew numbers and their specific roles (this is usually a crew number between 3 and 7 with a mean of 3 people, see Appendix F). Furthermore, while researching prototype data, crew member weight records were not encountered. But on the other hand, cabin setup data was found (see Appendix E.1) and with some actual incomplete mass values. Cross-checking the cabin data yielded no basis for trusting the cabin setup, i.e. knowing where certain cabin mass elements had been placed says nothing about their individual, inertial and unknown characteristics (e.g two 500 kg computer rigs have different dynamics w.r.t. some empty seats)[69].

Another important contribution to the total aircraft mass is the fuel contained in the aircraft's left-, right and center wing tanks. It is essential to understand that the wing fuel loading is only discussed by Zwarts, while no fuel-loading is mentioned in Heinkens's report regarding the prototype load case. Where Heinkens created a very detailed document that accurately describes the prototype F100 aircraft, specifically detailing all section mass elements and their respective moments and moments of inertia (including the water ballasts tanks), it was created without any no fuel loading information. Only Zwarts discusses fuel loading in regard to the production (series) aircraft, the tank configuration is the same as is found in the very old F28 ”Fellowship” which predates the F100. Furthermore, Zwarts provides interesting information regarding the total fuel mass contained in the main wing tanks as a function of main wing fuel center of gravity along the X_W and Y_W axes in vehicle-nose F_W frame of reference, and for the Z_W axis the main wing fuel tank levels (see Appendix E.5). Subsequently, details are given about the separate wing tank locations in between rib-stations (Appendix E.4.1 and E.4.2). Thus, there are reasonable grounds for assuming that the prototype tank configuration is similar to the mentioned F28 ”Fellowship” and production aircraft’s fuel tanks.

Thus, the technical reports produced by Zwarts and Heinkens form the mass model basis for the Fokker 100 prototype. The model in its simplest form is broken up in three parts, i.e. the operating empty weight (OEW), fuel masses contained in three tanks and the eight water ballast tanks (see Figure 6.4). Adding all masses yields a total mass of 44296.5 kg, but when considering a maximum design ramp weight of 43320.0 kg a difference of 976.5 kg is found[73]. Non of the technical documents available discuss prototype design masses, therefore it is assumed that fuel ramp and water ballast tank masses were chosen such that the design weights were never violated (as the recording data suggests only a few tanks were used per flight (see Appendix F).

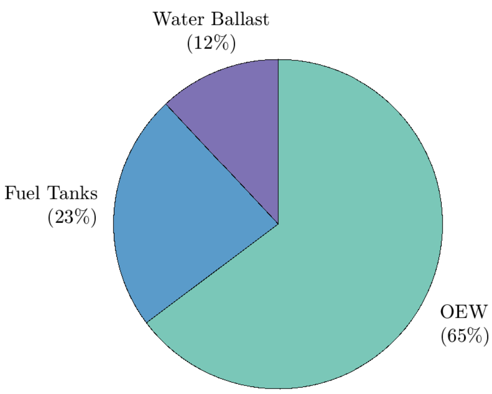

Figure 6.4: Main masses Pie chart which compares the maximum water ballast and fuel tank mass to the operating empty weight (OEW) for Fokker 100 prototype aircraft, based on Fokker 100 prototype/production loads cases [21, 73].

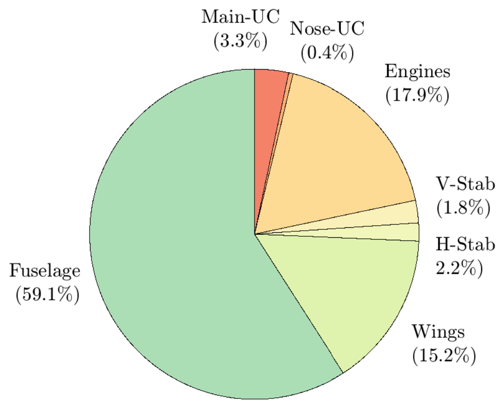

Figure 6.5: Section masses Pie chart of the operating empty weight (OEW) for the Fokker 100 prototype aircraft, based on Fokker 100 prototype the loads case [21].

The OEW section masses as given in Table 6.1 are visually presented in Pie chart Figure 6.5, and provide some insight in the mass ratio’s of the prototype aircraft’s operating empty weight. Note that this information based on Heikens’s document and takes in account double masses for specific aircraft sections, i.e. the total wing mass does not belong to one wing but to two (Appendix E.2.2). This is the same for the engines (Appendix E.2.4), horizontal stabilizer (Appendix E.2.3) and the main undercarriage (Appendix E.2.5). Special attention needs to be paid when computing center’s of gravity regarding the in section local mass elements, moment and moments of inertia, these need to be divided by two and corrected w.r.t. the proper coordinate system, i.e. the vehicle-nose F_W frame of reference.

Important assumptions | Section & mass definitions

Summarizing, some important assumptions have to be made about the Fokker 100 prototype sections and their corresponding discretized masses. In order to perform relevant analysis of the recorded flight-tests, the mass model obeys the following listed assumptions.

- Mass model is only valid for Fokker 100 prototype flight-test analysis.
- Fuselage masses as defined by Heinkens[21] include the SI/OI masses, i.e. the prototype flight-test equipment (SI) and flight crew (OI) with a combined mass of 6979.4 kilograms.
- All operating empty weight (OEW) masses, moments and moments of inertia are defined by Heinkens[21] as is provided in Appendix E.2.
- All locally defined mass elements per section and part of the OEW have their local axes aligned with the local principle inertial axes, i.e. the product of inertia are locally equal to zero.
- Fuel tank sections are similar to the production and old F28 'Fellowship' aircraft's as defined by Zwarts[21], provided in Appendices E.4 and E.5.
- Water ballast is defined by Heinkens [73].

6.3. Water ballast tanks

Influence and dynamics regarding the water ballast tanks has been provided in the Heinkens documentation, detailing the exact tank locations (see Appendix E.1) and there specific center of gravity as function of tank content mass[21]. Heinkens defines two types of water tanks, i.e. two small water tank with a maximum mass of 550 kg and six large tank of 700 kg of (liquid) water, with a total maximum mass of 5300 liters of water. Although the tank locations are known in the xy-plane, the tanks center of gravity on the z-axis and the corresponding moments of inertial are represented by specific datasets that contain a limited number of elements. By making use of theses available tank datasets, a simple least squares regression is performed in order to obtain the coefficient's of the corresponding, fitted polynomials capable of precisely interpolating tank properties as a function of kilograms water mass m_w contained in the tank.

Polynomial regression is used according to Equation 6.15 that allows for modeling the tank contents as a polynomial function. In this case Matlab's `polyfit` function is used, where n defines the polynomial's order and p_i defines the corresponding n$^{\text{th}}$ order coefficients for all $i = 1, \ldots, n+1$. By applying this curve-fitting method to the water tank center of gravity dataset along the Z_W axis, the coefficients of two polynomials are found that allows interpolation of the tank content values regarding the small-/large water tank (see Table E.12) [31, 59].

$$y_p(x) = p_0 + p_1 x_i + p_2 x_i + \cdots + p_n x_i^n + \epsilon_i \quad \forall \quad i = 1, 2, \ldots, m \tag{6.15}$$

The obtained polynomial's pZ_{ws}^W and pZ_{wl}^W are graphically represented in Figure 6.6, where the subscripts wl, ws define the left-/right water tank and superscript W defines the vehicle-nose F_W reference frame. Nb water ballast tank dataset point have been included for reference, and is strengthened by the coefficient of determination r-squared r^2 value. This tests goodness-of-fit for linear regression models, where the dataset difference with the polynomial is represented as a relationship/variance fraction, i.e. between 0 and 1 where 1 equals a perfect fit.

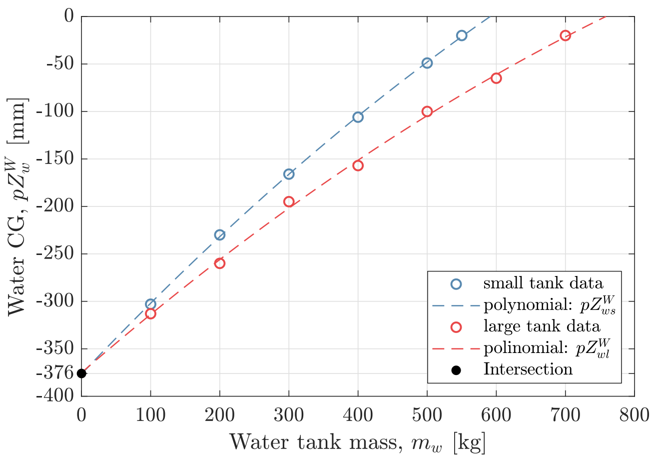

Figure 6.6: Water tank center of gravity in z-direction in F_W.

As determined by the R-squared values for both polynomials, the curves in Figure 6.6 form a reasonable model that is capable of delivering the water tank's center of gravity as function of its contents. Note that on the figures vertical axis a point is found where both curve intersect, this point represents the zero tank mass value and subsequently is the same for both tanks.

A similar approach is applied to the available small-/large water tank inertial datasets, provided by Heinkens [21]. Again the r-squared is computed to test the goodness-of-fit regarding the linear regression used to obtain the first-/second order polynomial that define the inertial model of a specified water tank. Of coarse the first order polynomial has a nice straight line, crossing all data points, and is thus equal to one.

The Figures 6.7a and 6.7b below present a graphical illustration of the obtained water tank inertial polynomials as a function of water tank mass m_w contents w.r.t. the small-/large tank sizes. Again the polynomial function are identified through their sub-/superscripts, where the subscript denotes the inertial axis and tank size, and the superscript denotes the frame of reference, i.e. $pI^W_{xx,ws/wl}$, $pI^W_{yy,ws/wl}$ and $pI^W_{zz,ws/wl}$. The third order polynomials all have high r^2 values, which indicates that all curves found through the linear regression have a satisfactory goodness-of-fit given the water tank inertial datasets. Similarly, the nth order polynomials regarding the water tank inertia are given in Table E.13.

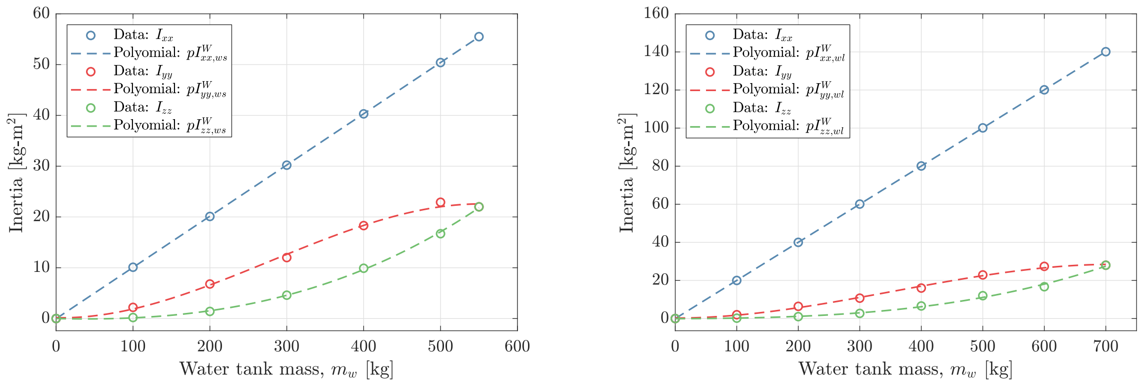

(a) Small water tank interia. (b) Large water tank interia.

Figure 6.7: Water ballast tank inertial polynomials as function of tank contents in kilograms (liquid) water mass, curves are fitted on the Fokker 100 prototype load case data[21].

With the in Section 6.1 discussed products of inertia in mind, it is noticed that no data regarding these products has been provided by Heinkens. It is therefor assummed that the water tank's local center of gravity axes system is always aligned with the principle inertial axes system, yielding zero valued products of inertia in all water ballast loading cases.

Important assumptions | Water ballast

By comparing the small- versus large water tank's inertia based on the information provided by Heinkens[21], similar inertial behavior is found around the y/z-axis for both tanks, yet the moments of inertia found around the x-axis yields a far larger difference. This is strange, because it is known that moments of inertia of cylindrical objects usually have two similar large values and one to be significantly smaller [49]. This contradicts Heinkens's values, and on top of that no sloshing seems to be considered. One can imagine a rotating liquid mass around the x-axis along the cylinder's length would pose little resistance to rotation. Because little is known regarding the methods used by Heinkens in determining the water tank moments of inertia, it's assumed they are correct, and are implemented as a part of the global mass model of the Fokker 100 prototype.
Nevertheless, it should not be overlooked that the provided values can contain errors. And on a final note, water tank mass moments of inertia w.r.t. the global mass model are always relative to the aircraft's center of gravity, thus due to tank location and the parallel axis theorem[49] it is assumed that the local water tank's inertia will have little influence on the overall model, and is thus unnoticeable.

- Water ballast tank levels are given in the flight-test cards and archive files part of the SQL database. Both have been "manually" added to the mass model routine, and should be checked if other flights are selected!
- Pumping of water mid-flight is known due to these changes are recorded at the respective recording numbers.

6.4. Fuel loading and distribution

Influence of the fuel loading on the aircraft's dynamics is significant and can not be neglected. Percentage-wise, where Figure 6.4 clearly shows that the maximum fuel contribution to the total aircraft mass w.r.t. maximum take-off weight (MTOW) conditions can start at 23%, and increase to 26.4% when no water ballast is used! The relevance of a proper fuel model is obvious, and needs to be researched.

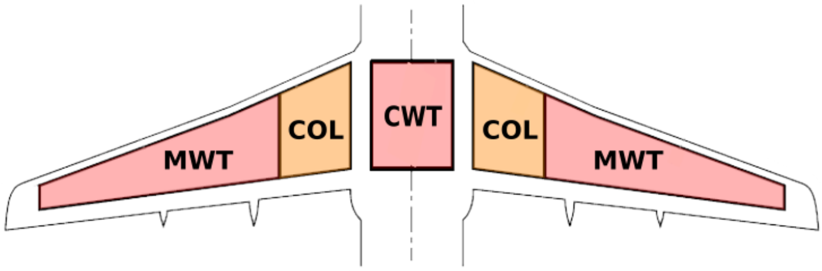

Figure 6.8: Fuel tank schematic of the Fokker 100 aircraft, detailing the locations of the collector sub-tanks (COL) part of the main wing sub-tanks (MWT) and center wing tank (CWT). Adapted from Fokker weight and balance manual[15].

The Fokker 100 prototype aircraft has three bottom-draining fuel tanks (see Figure 6.8), the left-/right main wing tanks (MWT) with 3855 kg of maximum fuel capacity and one center wing tank (CWT) with 2610 kg maximum fuel capacity, total maximum fuel capacity equates to 10320 kg. Note that the main wing tank consists of 17 sub-tanks, separated by the wings rib-stations, where the first two wing sub-tanks belong to the collector system (COL) with a maximum capacity of 750 kg, the other 15 sub-tank segments house a total of 3105 kg of fuel in single wing. The collector system is always filled, untill no fuel remains in the other main wing sub-tanks or center tank. Nb. the order of tank usage is center wing tank first, 15 sub-tanks in the main wing second and the collector system last, i.e. CWT $\rightarrowtail$ MWT $\rightarrowtail$ COL. Furthermore, fuel is pumped with the aircraft's balance in mind, thus at any point in time there exists an equal amount of fuel in the left-/right main wings unless mentioned otherwise[73].

Judging from figure 6.8, it can be stated that two locations for the fuel tank centers of gravity are needed, to be precise the main wing cg_{mwt} and center wing tank cg_{cwt} centers of gravity. Given the main wing tank, three spacial coordinates as function of fuel load are needed in F_W to, i.e. the coordinate along the centerline X^W_{mwt} & Z^W_{mwt}, and y-coordinate Y^W_{mwt} along the wing. Subsequently, the center wing co-ordinates are defined in a similar fashion, where only the X^W_{cwt} and Z^W_{cwt} are needed due to y-coordinate is assumed to be on the centerline (i.e. Y^W_{cwt} is zero).

Figure 6.9: Overview of fuel loading and distribution.

As is presented in the overview (see Figure 6.9), the determination of the mass products and moments of inertia are found through a series of steps, where the global fuel center of gravity is the second part in the process, and in more detail Figure 6.10. Here term global is used to point out the fact that the Fokker fuel loading graphs are used from the Zwart's report[73], it is assumed that these graphs are found empirically and provide a single point portraying the center of gravity for either the main or center wing tanks. These graphs are then curve fitted to provide a more accurate estimation to facilitate the cg estimation and it's further applications.

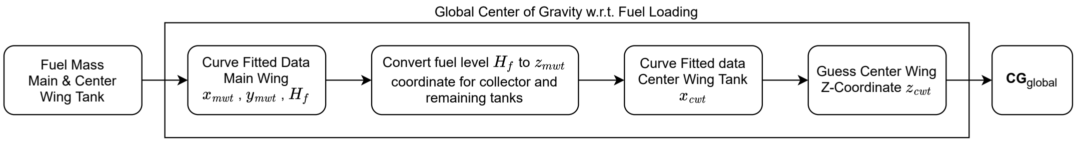

Figure 6.10: Process flow in the determination of the global fuel center of gravity of the main and center wing tanks.

The main wing global fuel cg x/y-coordinates are fairly easily found, but the z-coordinante is given as a fuel level, this particular problem is therefore handled separately in the following section. Furthermore, the center wing tank z-coordinate is guessed, this is done because the provided reports yielded no information regarding its exact location other then the tank is situated between the main wing roots bounded by the fuselage.

Subsequently a fuel mass distribution is found by modeling the filling of the tanks according to the Fokker fuel level schemes, while mass and location are now known the inertia of the fuel system is quickly computed. The next two subsections with explain how this process is applied to the both the main wing fuel tanks (Section 6.4.1) as the center wing fuel tank (Section 6.4.2).

6.4.1. Main wing fuel tank

A precise top/front schematic of the main wing fuel tank segments is provided by Zwarts (see Appendix E.4.1 & E.4.2), where Appendix E.4.3 depicts the manual estimation of the main wing fuel segment dimensions, needed for the sizing of the segments and finally the calculation of the added moment of inertia generated by the fuel loading. Note that figures E.9 & E.10 show the location of a point A, this defines the location of the empirically found center of gravity of the main wing fuel tank given by Zwarts's graph in figure E.13. To make a proper estimate of main wing fuel tanks moment of inertia, a combination is made between the empirical data supplied by Zwarts and the calculated wing tank dimensions, i.e. the moments of inertia regarding every wing tank segment w.r.t. the empirical location of the center of gravity.

Global center of gravity coordinates For this to work, the fuel loading curves provided by Zwarts (see Appendix E.5) are curved fitted to yield cg coordinate data as a function of fuel mass. Only the graphs themselves have been supplied, no usable data was found in the accompanied tables included by Zwarts in his report[73]. These fuel loading graphs house vital information concerning the aircraft's wing- and centerwing fuel mass as a function of a specified location of the center of gravity along a specific axis in the vehicle reference frame.

Therefore, a semi rough estimate is made by accurately guessing relevant data-points by hand, and fitting an arbitrary polynomial on the extracted data-points. Note that by "hand" actually means that this is achieved by making use of the graphic and plotting tools in Microsoft Excel. An arbitrary graph is overlapped with an excel chart-axis, and is scaled to fit the dimensions. Using MATLAB's `polyfit` function aids perfectly with fitting a curve to the data-points in the printed graphs (e.g. the wing dimensions have been located in the same manor). The resulting plots of the curve fitted data-points are presented for the total main wing tank x-coordinate in figure 6.11, center wing x-coordinate in figure 6.12, and main wing tank y-coordinate in figure 6.13. The specific curve polynomial coefficients with their respective R-squared values (all close to 1) are given in table E.17 of Appendix E.4.

As a side note, weight and balance tables regarding the main wing X^W_{mwt} and center wing X^W_{cwt} fuel tank x-coordinate were later found in tables E.19 & E.20 of the Aircraft Operation Manual[16], this verified the obtained data from the graphs, but more importantly supplied new data regarding the center wing tank presented in figure 6.12.

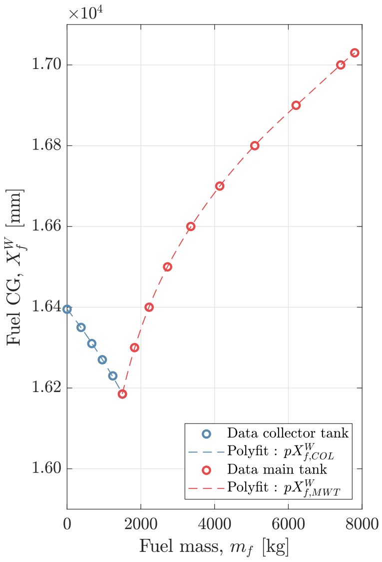

Figure 6.11: Curve fitted polynomial for main wing fuel center of gravity along the X_W axis versus the total wing fuel mass contained in both wings.

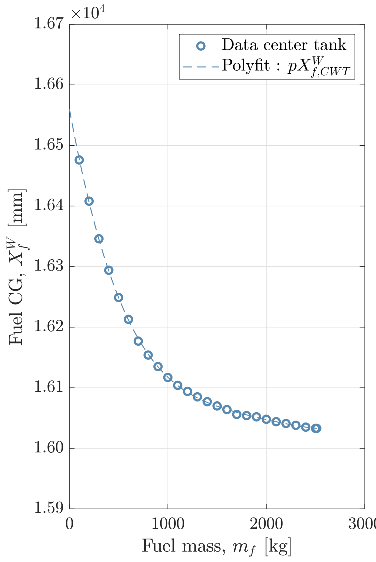

Figure 6.12: Curve fitted polynomial for center wing fuel center of gravity along the X_W axis versus the center wing fuel mass.

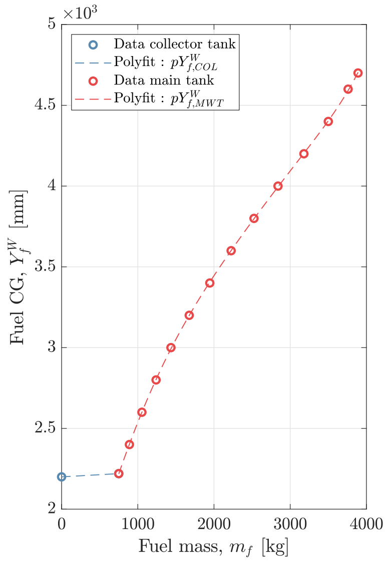

Figure 6.13: Curve fitted polynomial for main wing fuel center of gravity along the Y_W axis versus the total wing fuel mass contained in one wings.

Having now found X_{mwt}^W & Y_{mwt}^W using the polynomial curve fitting approach on Zwarts's graphs only one coordinate remains regarding the main wing tank, i.e. the z-coordinate Z_{mwt}^W defining the center of gravity associated with the fuel along z-axis in the F_W frame of reference. As can be seen in Appendix E.4.1 & E.4.2 there is only information available regarding the fuel level H_f inside the main wing fuel tank, this significantly complicates estimation of the z-coordinate! For now this is left to be dealt further down the road, and focus is placed on properly fitting a curve on the associated graph (see Figure E.13) depicting the fuel level H_f with respect to point A in the top/front wing fuel tank views.

As can be observed in figure E.13, the curve does not follow a simple polynomial. Because of this a different approach is used, i.e. fitting the fuel level H_f to a simple logit function as presented in equation 6.16. Reasoning for this approach has to do with the asymptotic behavior near the ends of the fuel level curves for main and collector wing fuel tank segments. N.b. fitting a polynomial simply did not work, and thus did not yield anything to compare with.

$$\hat{H}_f(\bar{\Theta}, m_f) = \Theta_0 + \Theta_2 \log\left(\frac{m_f - \Theta_3}{\Theta_4 - (m_f - \Theta_3)}\right) \tag{6.16}$$

, where $\hat{H}_f$ is the fitted fuel level in millimeters, m_f is the total main wing tank fuel mass in kilograms, and $\bar{\Theta}$ is the parameter vector.

Thus as presented in equation 6.17, the logit function as described in equation 6.16 is fitted by applying an optimization routine that minimizes the mean squared error (MSE) between the provided data points for the fuel level H_f and the estimated/fitted fuel level $\hat{H}_f$. Optimization is obtained through making use of MATLAB's `fmincon` function, that is capable of fitting any arbitrary constrained and parameterized non-linear function to a specific set of datapoints, by minimization the previously mentioned MSE.

$$\hat{\Theta} = argmin J(\bar{\Theta}, m_f) \quad \text{with} \quad J(\bar{\Theta}, m_f) = \frac{1}{N}\left(H_f - \hat{H}_f\right)^T \left(H_f - \hat{H}_f\right) \tag{6.17}$$

, where $\hat{\Theta}$ is the estimated parameter vector, and N is the number of points contained within the dataset.

Initial and upper/lower boundaries are presented for the collector wing tank segments in Table 6.2 and for the main wing tank segments in Table 6.3. No particular prefab design system was used in the determination of these initial parameter values and boundaries, other that going at it more or less by trail and error. One thing that can be mentioned is the effect of the upper/lower boundaries on the choice of initial parameter values, meaning that the initial parameter values are chosen first and the boundary values are adjust w.r.t. the initial parameter values. Finally all parameter values are mostly within an order of magnitude comparable to the values found on the x/y-axis of the graph.

Table 6.2: Initial parameter values and boundaries of the collector tank segments optimization process.

	Θ_1	Θ_2	Θ_3	Θ_4
$\bar{\Theta}_0$	350	120	1	800
$\bar{\Theta}_{upper}$	1000	300	500	1000
$\bar{\Theta}_{lower}$	0	50	-500	500

Table 6.3: Initial parameter values and boundaries of the remaining wing tank segments optimization process.

	Θ_1	Θ_2	Θ_3	Θ_4
$\bar{\Theta}_0$	1	100	1	8600
$\bar{\Theta}_{upper}$	1000	300	500	4000
$\bar{\Theta}_{lower}$	-1000	0	-500	3000

The result of this constrained minimization optimization process is presented in figure 6.14, where the collector (750kg) and main wing (3105kg) fuel levels are plotted as a function of their respective fuel mass capacities. Although it seems the plotted graphs exceed the maximum capacity, the function output is always limited to not go beyond any other values w.r.t. maximum capacity of the collector and main wing fuel tank. The estimated parameter values, or coefficients if you will, are presented in appendix Table E.18. The final resulting MSE are found to be around 2.4mm for the collector and 3.2mm main wing fuel levels, R-sqaured values are in both case nearly equal to 1.

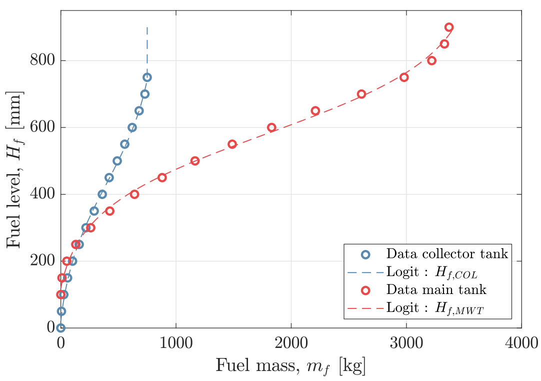

Figure 6.14: Curve fitted fuel level contained inside the collector- and main wing tank as a function of a single wing fuel mass.

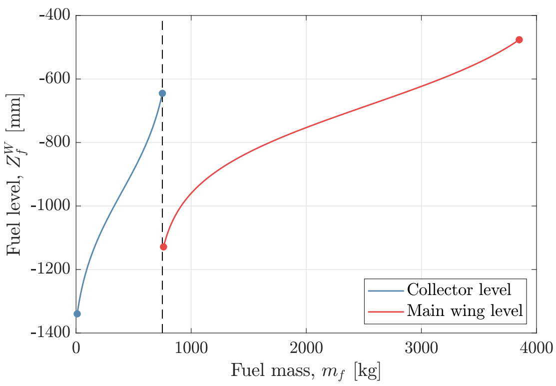

Figure 6.15: Mass optimized fuel level relative to the z-axis in F_W contained inside the collector- and main wing tank as a function of wing fuel mass.

The curves in Figure 6.15 show the fuel levels translated into z-coordinates in the F_W frame of reference, this is later on needed for the calculation of the fuel tank moments of inertia. Based on the wing dihedral of 2.5°, known origin of the origin of the wing with the fuselage, and the location of point A, the precise position of the fuel in the wing is expressed as fuel level coordinate Z_f^W in F_W.

Tank dimensions and sizing The wing fuel tank segments have been manually estimated as is explained in Appendix E.4.3, and subsequently the tank sizing in Appendix E.4.4. Tank sizing, or tuning, is done with the fuel density in mind, where according to Zwarts this density ρ_f is set at 798 kg/m^3. By changing the varying tank segments lengths along the body x-axis while keeping width/height constant, the total tank volume will correspond linearly to the sum of segmented fuel tank masses, i.e. equates to the total wing fuel load. This yields a reasonable assumption regarding the tank sizing.

The resulting "sized" tank locations within left wing top/front views have been plotted in figure 6.16 & 6.17 and function as measure of verification. note that the blue lines correspond with the "guesstimated" true tank locations obtained from the Zwarts report, the red boxes visualize the manually sized tank locations that when summed yield the total designed wing fuel mass.

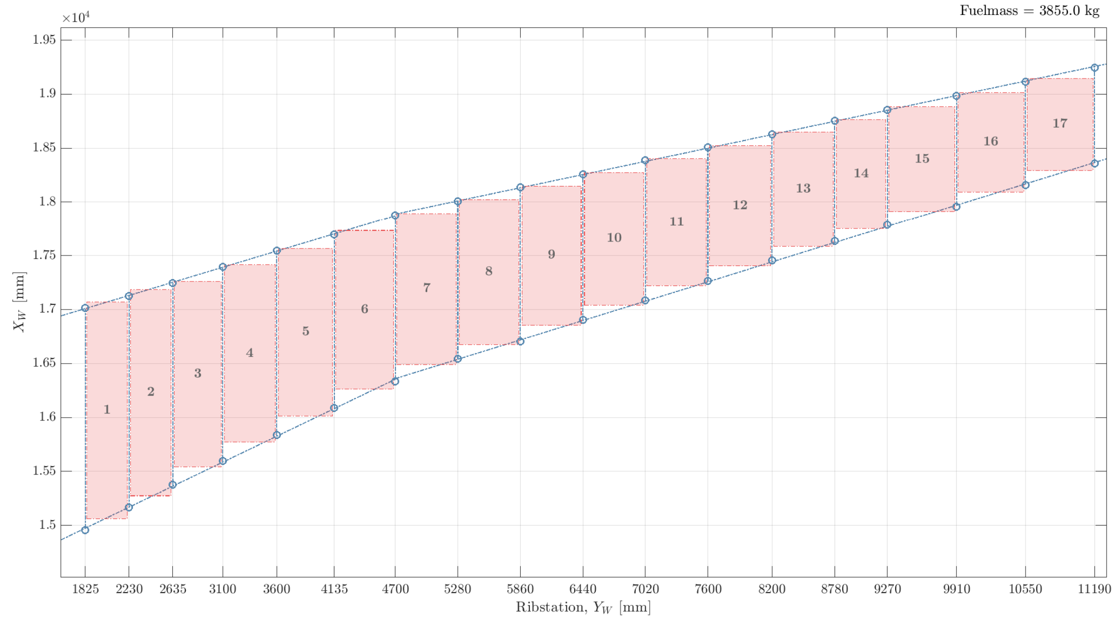

Figure 6.16: Top view of main left wing fuel tank segment locations.

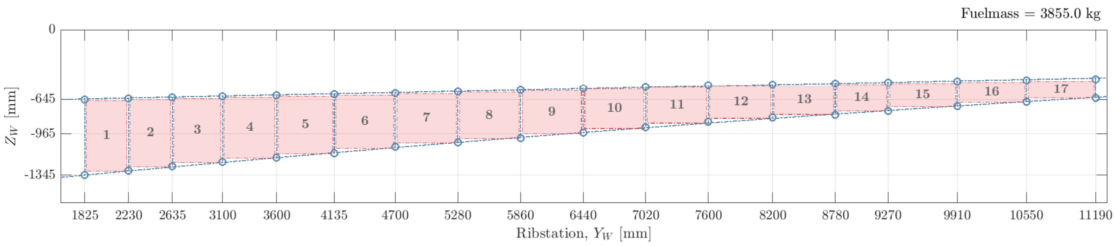

Figure 6.17: Front view of main left wing fuel tank segment locations.

Having a decent assumption regarding the known tank locations and sized tank dimensions, an optimization routine for filling up the tank is constructed (see Figure 6.18). Reasoning for such a method is the fact that empirical fuel level H_f does not produce the desired actual fuel load obtained through geometric computation of the assumed segmented tank locations and sizes. In other words, a given fuel mass yields a particular empirical fuel level H_f, but when applying this fuel level to the geometry of the assumed fuel system a different fuel loading mass is found when summing up all the segmented tank parts! This optimization routine is presented in Figure 6.18, and depicts a schematic block diagram of the optimization process that corrects the fuel mass error ϵ_f induced by the difference between fuel masses defined empirically m_f versus the geometrically calculated m_{H_f}.

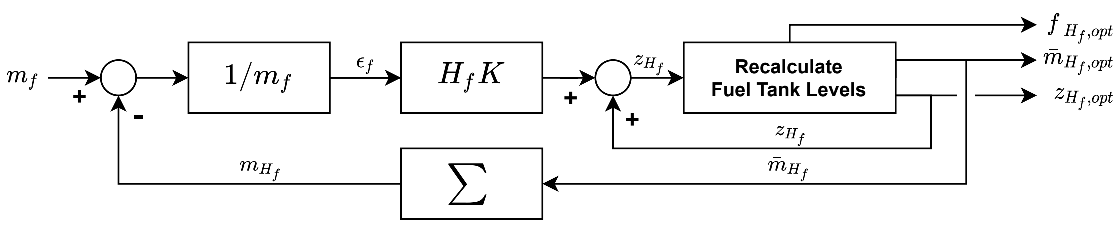

Figure 6.18: Optimization block diagram of main wing fuel loading by comparing empirical versus calculated fuel levels.

The result of this process is shown in figure 6.19, where the filling of the tanks is demonstrated. Note that collector tanks 1 & 2 are filled first, and afterwards the remaining 15 main wing tank segments are filled according to the fitted fuel level curves H_f.

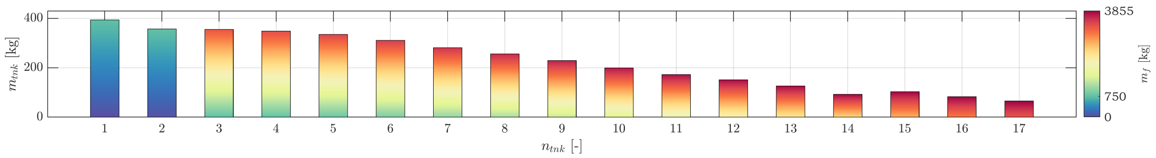

Figure 6.19: Sequential fuel mass distribution by filling up all tank segments from tanks segment 1 to 17, collector tanks segments 1/2 are filled first and drained last.

6.4.2. Center wing fuel tank

The center wing fuel tank is a simple rectangular box assumed to be situated between the left/right wing roots connecting to the fuselage, with a maximum capacity of 2610 kg[73]. The cg location along the x-axis in F_b due to fuel loading is presented in figure 6.12, where the fitted curve polynomial coefficients are used to estimate it's cg. Because the center wing tank is right in the middle of the aircraft, the y-coordinate Y_f^W is set to zero.

Tank dimensions are constraint by the aircraft's dimensions at the location of the wing root. Again not much is known about these dimensions other than a guessed tank depth of 700 mm (along Z^W) and width of 2720 mm (along Y^W), leaving an undetermined length value (along X^W). As with the fuel loading and distribution in the main wing the same fuel density is used, i.e. 798 kg/m^3[73]. Length is then calculated to have a value of 1718 mm.

Table 6.4: Center wing tank guessed location and dimensions.

	X^W mm	Y^W mm	Z^W mm
Location (origin)	16506	0	965
Dimension	1718	2720	700

Geometric location of the center wing tank is modeled as a point mass w.r.t. the location given in Table 6.4. Fuel loading is handled the same way as is done in the wing mounted tanks, i.e. fuel levels are relative to the CWT origin. Note that the cg_{cwt} moves as function of fuel loading along the x-axis X^W (see Figure 6.12), this is done to stay as close as possible to empirical data supplied by Zwarts[73].

6.4.3. Implementation of inertial values

The inertia of both the center and main wing tanks is calculated by using a very simple and well known theory from classic mechanics (see figure 6.20). Every tank is a box, and in every tank fuel resides, meaning that this fuel can be equally well be treated as a box. By making use of the equation 6.18 the moment of inertia can be easily computed for every tank segment.

$$I_{XX} = \frac{1}{12} m \left(b^2 + c^2\right) \quad , \quad I_{YY} = \frac{1}{12} m \left(a^2 + c^2\right) \quad , \quad I_{ZZ} = \frac{1}{12} m \left(a^2 + b^2\right) \tag{6.18}$$

It should be noted that by using this approach the fuel is considered to be a solid box, no shushing is assumed. Furthermore, it is understood that modeling a tank can be done to a great extend of precision, specially considering that fluctuations in fuel mass was measured during the recording of the flight test. Sadly this aspect is beyond the scope of this thesis, and therefore a greatly simplified system like this one is chosen.

The location of the fuel center of gravity cg_f, rectangular "solid" fuel dimensions and mass are calculated for every tank. Using these values with the methods for integration of inertial mass described in section 6.1, the fuel loading and distribution model is capable of providing an educated guess w.r.t. global inertial state of the aircraft as a function of fuel loading.

Important assumptions | Fuel loading and distribution

Although the fuel loading and distribution is modeled using empirical data obtained form the Zwart's report[73], it can not accurately represent an actual fuel loading scenario due to the absence of proper testing and data that can validate this. That being said it is the best data and model currently available, but caution is advised when using this model and it should only be used for educational purposes.

- Bottom draining fuel tanks, with drain order : CWT (2610kg) → MWT (2x3105kg) → COL (2x750kg).
- The global fuel loading model is a rough combination of empirical loading data and aircraft geometry.
- Empirical data is obtained from graphs found in the Zwarts report[73], and is curve fitted to obtain information regarding the center of gravity as a function of fuel mass.
- Tank dimensions are manually sized to fit the known fuel loads.
- Fuel levels in the main- and collector wing tanks are optimized to match the computed fuel tank mass with the corresponding empirical fuel levels.
- At all times the computed inertia due to fuel loading is relative to the empirically found center of gravity due to fuel loading.
- Fuel inertia inside the local tank segments is modeled as a solid, depicting a simple rectangular box. No sloshing is considered.

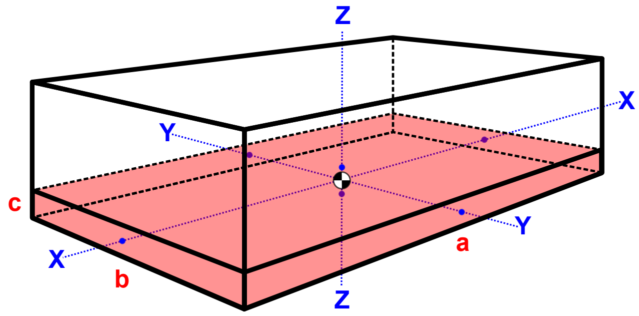

Figure 6.20: Simple rectangular tank-segment model, shaded red area is "solid" fuel.

6.5. Validation of mass model

By this point all nessecary components needed to build up the inertial tensor as previosuly discussed in section 6.1 are available. Every mass element in the static aircraft frame (i.e. fuselage, engines, etc.), water tanks, and fuel tanks is accounted for. N.b. every fuel configuration can be simulated, even the landing gears have been made ready.

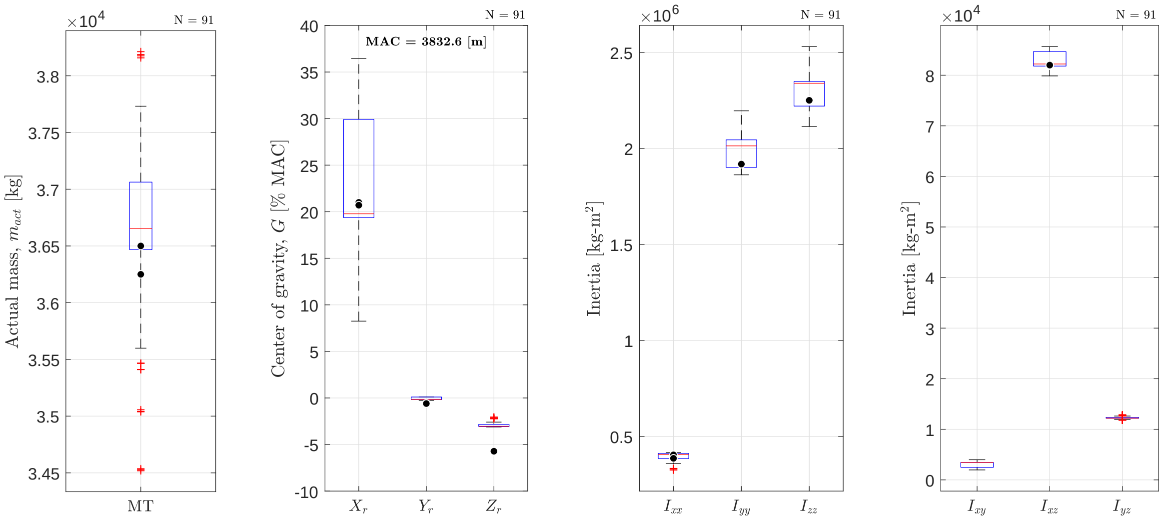

(a) Actual mass. (b) Center of gravity. (c) Inertial moments. (d) Inertial products.

Figure 6.21: Verification box plot's of measured in-flight actual masses, the center of gravity G locations in F_r and mass moments-/products of inertia relative to G in F_b based on 91 stall flight-test recordings conducted with the Fokker 100 prototype, where the black dot's function as points of reference of two load cases supplied by Fokker Services, Hoofddorp.

The massmodel is run by making use of 91 F100 Proto flight test recordings and their results have been plotted as a boxplots, this is then verified with two F100 simulator load cases providing information regarding the actual mass, center of gravity, and moments/products of inetria. The verification points are printed inside the boxplots as a black dot as can be seen in figure 10.18.

Although the amount of load cases provided by Fokker is not a lot to say the least, it does validate the massmodel to a certain extend. One can argue that all Fokker simulator load cases are close enough, i.e. within at least 50% of all 91 recordings. Also it must be mentioned that the provided load cases only cover one product of inertia (i.e. I_{xz}), the other two products have been neglected by Fokker. This is probably due to the assumption that these two products contribute little with respect to the total inertial system.

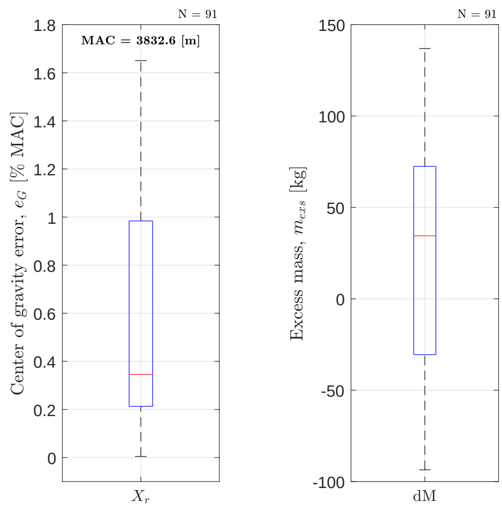

(a) Center of gravity. (b) Actual mass.

Figure 6.22: Verification box plot's of differences in documented centers of gravity and MRVS supplied actual mass versus the calculated values obtained using the created algorithms for the Fokker 100 prototype aircraft.

As an extra measure, rough cg values along the x-axis were found in the flight test cards and noted for validation. In boxplot figure 6.22a the relative error percentages between calculated and recorded are shown, and do not exceed in the most extreme cases error values larger than 1.6% MAC, where the median is situated around a relative error of 0.3% MAC. This check functions as measure of merit regarding the methods used in calculating the aircraft's actual mass and it's direct correlation to determining the cg.

A similar thing is done w.r.t. the actual mass. There are two ways in determining the actual mass, i.e.

the summed total number of all mass element that define the aircraft, and the mass supplied by the Fokkers MRVS division in the recordings. **Be warned**, initially comparing these two masses yielded very large differences in orders of 1500 to 6000 kilograms. At this point the calculated masses where compared to the limited amount of actual mass values in the recordings themselves, which later on were found to be incorrect. Upon further investigation a discrepancy was found when carefully comparing the flight test cards actual mass values with those from the recording, they differed considerably! Thus using the flight test card values yielded a result as presented in figure 6.22b where again a relative error is given in percentages, and clearly shows that the calculated mass balance is correct. Meaning that all masses are accounted for, making the mass model very reliable.

6.5.1. Influences due to loading

As an addition, the following graphs display the results of loading the aircraft in sequential order of relevant tanks, up to full weight and beyond MTOW for purpose of illustration. Note that in this scheme the fuel is loaded symmetrically with regard to both wings, afterwards the water ballast tanks simultaneously filled up to the maximum limit. Where the water ballast tanks are concerned various loading schemes are possible, but are disregarded because tank contents and changes have been rigorously recorded in the flight-test cards. Furthermore, performing a water ballast sensitivity analysis falls outside the immediate scope of this thesis.

Center of gravity

In Figures 6.23a-6.23c the moving center of gravity under loading is presented. For reference, loading-points have been added to these figures, where it immediately shows its large impact on the aircraft's cg. Due to simultaneous water ballast loading an AFT moving cg isn't highlighted, but the AFT water ballast tanks do make this possible. The same holds for the lateral moving cg due to water ballast loading.

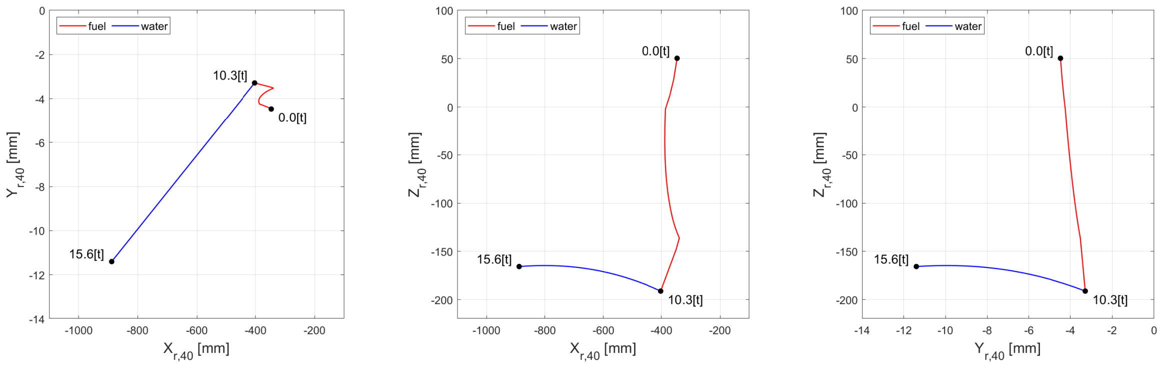

(a) xy-plane (b) xz-plane (c) yz-plane

Figure 6.23: Center of gravity due to full fuel/water loading in the vehicle reference frame at 40% MAC ($F_{r,40}$).

Moments and product of inertia
First, in Figures 6.24a and 6.24b, an overview is presented to point out the relative differences between moments and products of inertia.

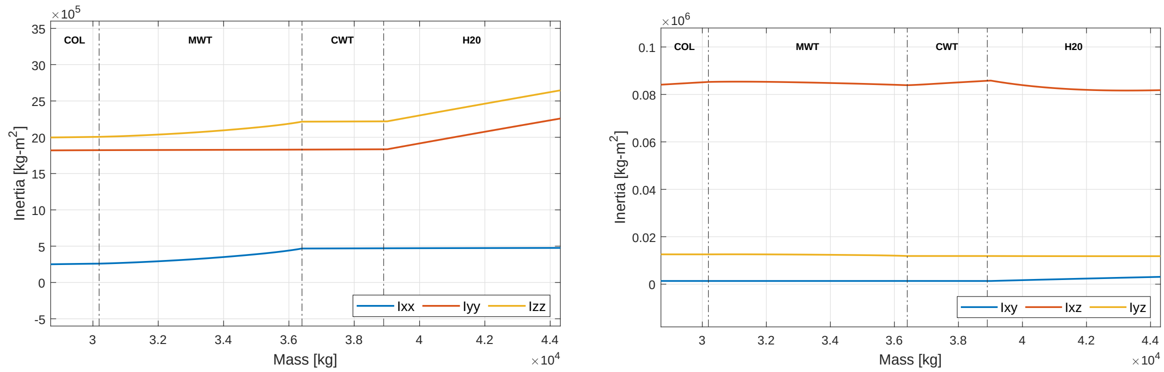

(a) Moments of inertia (I_{xx}, I_{yy}, I_{zz}).

(b) Products of inertia (I_{xy}, I_{xz}, I_{yz}).

Figure 6.24: Mass moments- and products of inertia overview regarding standard load cases of the Fokker 100 prototype aircraft, i.e. the total inertial influence of fuel loading and water tanks.

Figure 6.25 illustrates a more detailed view of the inertial behavior due to loading regarding the moments of inertia (I_{xx},I_{yy},I_{zz}). As expected, loading the wings with fuel adds a bit more than 2.1x10^5 kg-m^2 to the inertial rolling moment (I_{xx}), and is marginally influenced by the water tanks. Equally, inertial pitching/yawing moments (I_{yy},I_{zz}) show a clear increase due to filling of the water tanks, where yawing experiences an additional 2.1x10^5 kg-m^2 due to fuel loading.

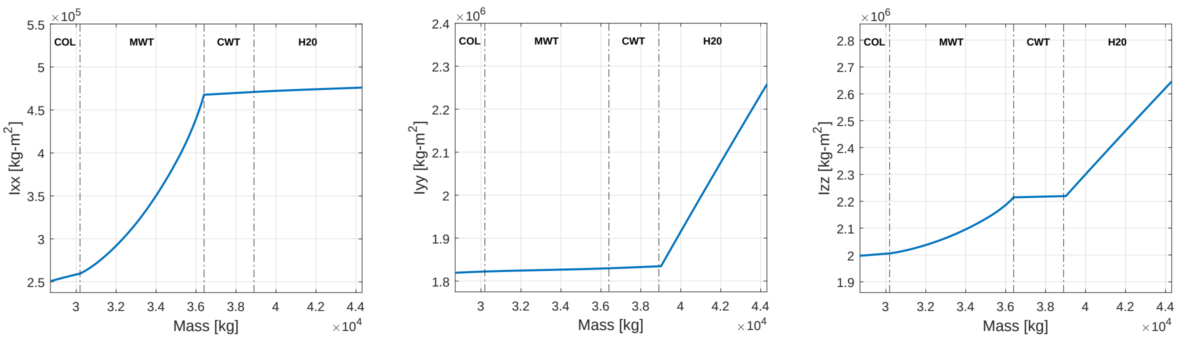

(a) Mass moment of inertia about the x-axis (I_{xx}).

(b) Mass moment of inertia about the y-axis (I_{yy}).

(c) Mass moment of inertia about the z-axis (I_{zz}).

Figure 6.25: Detailed mass moments of inertia in standard load cases of the Fokker 100 proto aircraft, i.e. the total inertial influence of fuel loading and water tanks.

Subsequently, the products of inertia (I_{xy},I_{xz},I_{yz}) are presented in Figure 6.26. Here it is important to understand that the product of inertia is a method of describing the aircraft's symmetry relative to body axes (F_b), i.e. with respect to a ***moving*** center of gravity (G) under the influence of fuel/water loading. When masses are symmetrically distributed in xy-, yz-, and zx-planes, products are zero.

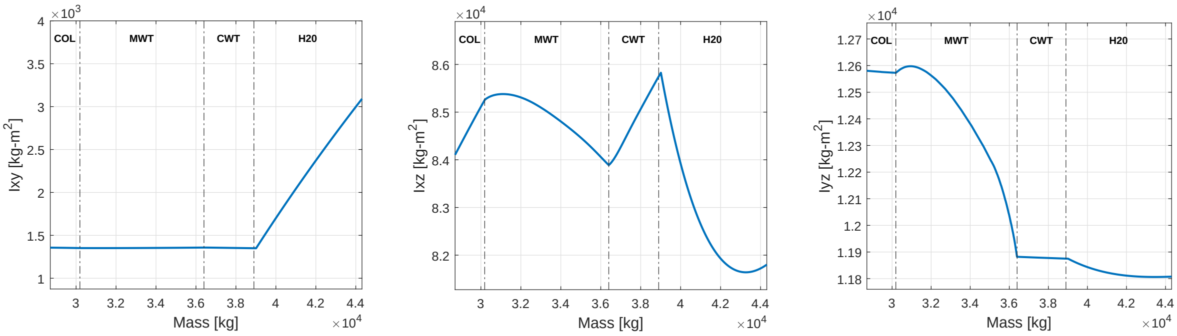

(a) Mass product of inertia in the xy-plane (I_{xy}).

(b) Mass product of inertia in the xz-plane (I_{xz}).

(c) Mass product of inertia in the yz-plane (I_{yz}).

Figure 6.26: Detailed mass products of inertia in standard load cases of the Fokker 100 proto aircraft, i.e. the total inertial influence of fuel loading and water tanks.

Figure 6.26a details the xy-plane, where initially due to even fuel loading the static sectional masses do not change asymmetry. This can be explained by symmetry in fuel-tank location where both wings look the same, i.e. cancel each other out in the xy-plane. But filling water-tanks does change this value significantly, by doubling in value. Note that *all* water-tanks are *evenly* filled, and no other filling scheme is explored. This does however show that water-tanks are very influential in regard to the xy-plane asymmetries.

Second in line is the xz-plane (Figure 6.26b), and details some interesting loading behavior. Here, due to cg shifting the inertial product increases and decreases, which is most dominantly represented by the water-tank filling. As can be seen in the cabin configuration (Figure E.1), front water tank group is placed further away from the CG than aft tanks. Filling contributes to evening out asymmetries, but because the aft tanks are filled at the same time, I_{xz} does not fully go to zero.

Finally, the yz-plane (Figure 6.26c) shows a minor change, and is related to the wing tank rising fuel levels. As this fuel level rises, the local fuel cg moves closer to body axes, leading to a drop in inertial mass product (I_{yz}) value. Note that the water tanks seem to perform counter intuitively in regard to the rising fuel level, this is caused by the amount of flight flight-test instrument gear. Their cumulative large mass is assumed to have a slightly higher local cg than the filled water tanks, adding a lower water cg slightly (100 kg-m^2) drops this inertial product.

7 Engine model

Speyside whiskey is a well-known single malt Scotch whiskey, distilled in Strathspey, the area around the Spey river in northeastern Scotland. Next to be being famous for producing the one of the finest whiskey's in the world, Scotland is also very much known for it's contributions to the aviation industry (Rolls Royce).

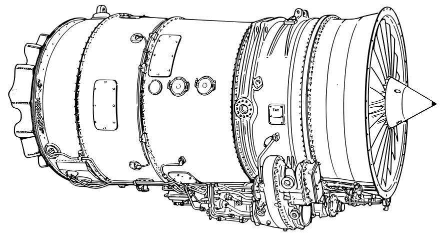

Figure 7.1: An arbitrary illustration of the Rolls-Royce Tay 620/650 jet-engine. Adapted from Jane's Information Group [25].

Table 7.1: Rolls-Royce F100 Proto (11242) Tay 620-15 Specifications [25].

Manufacturer	:	Rolls-Royce
Country	:	United Kingdom
Designation/name	:	Tay 620-15
Airflow	:	176 [kg/s]
Bypass ratio	:	3.2 [-]
Length	:	2405 [mm]
Diameter	:	1118 [mm]
Dry Weight	:	1422 [kg]
T-O Rating	:	61.6 [kN]
Engine serial (L)	:	16021
Engine serial (R)	:	16022

One of those contributions are the Rolls-Royce supplied Tay 620/650 engines (Table 7.1), which are installed on the Fokker 70/100 aircraft. This chapter discusses the modeling of this engine type/model, as it is well known that engine thrust is an important part of the aircraft dynamics and can not easily be neglected! Some minor research was done to determine the role the engine plays and to what extend it can be implemented. Therefore a first simple technical background is presented in Section 7.1, this to illustrate the engine characteristics, and it's integration within the various aircraft systems.

Regarding the initial research on the engine, the standard calculations documentation (STB) for the Fokker 70/100 provided a starting point, which yielded some interesting but mostly lacking and incomplete information on reconstructing engine thrust based on sensory data contained within the MRVS database, and marginally available pre-calculated thrust values. The latter is illustrated in Figure 7.2 and 7.3, here the time traces are illustrated showing the Engine Pressure Ratio (EPR) versus the STB calculated gross thrust along the engine's center line (THGNC) for both the left and right engines. As one can clearly see, the lack of information with regards to the EPR time-traces, which is arbitrarily chosen because all sensory data is of equal length seem to justify the necessity for a calculated thrust value as is discussed in Section 7.2.

Thus attempting to reconstruct the thrust calculation w.r.t the provided STB schemes yielded no usable routines capable of correctly calculating the thrust. Large gaps in missing table data halted this reconstruction, therefore something else had to be thought of to at least give some reasonable representation of the aircraft's engine thrust during the stall maneuver. Note that during stall the engines are running at an idle thrust setting, thus the amount of thrust can be considered negligible, i.e. thrust generally ranges in the neighborhood of 3.8kN (see 7.7). A choice was made to either go back to Fokker Services and try to do some heavy searching in the archive, or basically accept a small error in the thrust calculation, where doing extra work in going back to Hoofddorp is outside of the scope of this thesis. A simple OLS engine model was therefore constructed using the currently available information at hand, as is discussed in Section 7.3.

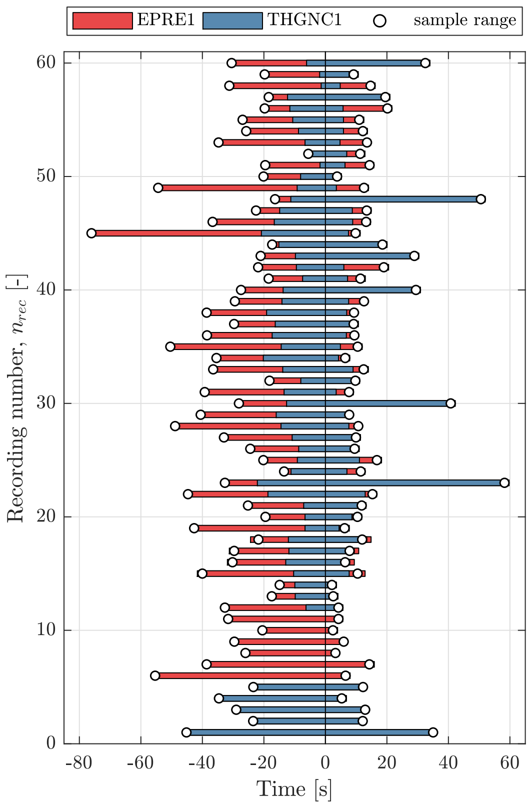

Figure 7.2: Available MRVS data: Left engine comparison EPRE1 vs THGNC1. Obtained from flight-test recordings, Appendix F.2.

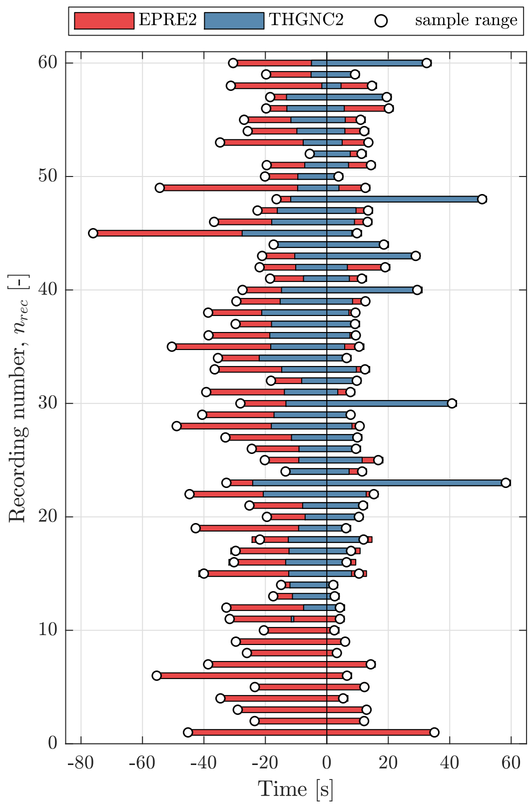

Figure 7.3: Available MRVS data: Right engine comparison EPRE2 vs THGNC2. Obtained from flight-test recordings, Appendix F.2.

7.1. Technical overview

Two fuel-efficient twin-spool, high bypass ratio, 61.6 kN turbofan engines power the Fokker 100, namely the Rolls-Royce Tay 620, or Tay 650. Note that low- pressure spool comprises a single-stage fan and a three-stage compressor driven by a three-stage turbine. In addition the aircraft's fuel burn is remarkably low due to efficiencies obtained in fuel-system and aerodynamic design. A reliable short field performance is obtained through a combination of low weight and good low speed capability. Turbofans are fitted with thrust reversers and pylon-mounted on sides of rear fuselage. The airstream through the fan bypass, and turbine exhaust are mixed before discharge through a nozzle which incorporates this two-door thrust reverser, and the engines are equipped with fire detection and extinguishing systems. Starting the engines is initiated by an air-starter-motor. [16, 25]

Electrics The integrated drive generator powers the aircraft's electrical systems by generating three-phase 115 V AC at 400 Hz, which is for a part passed through three Transformer Rectifiers Units (TRU) generating 28 V DC power, while emergency power is handled by two batteries.[16]

Hydraulics Through two independent systems, hydraulic power given through 4 engine-driven pumps, i.e. for the use of flight control surfaces, landing gear and steering, brakes, thrust reversers, and the speed brake.[16]

Pneumatics Air conditioning, cabin pressurization, engine starting and anti-icing, dependent on bleed-air which is tapped from the compressors of both engines. Note that hydraulic fluid and water tanks are also pressurized this way.[16]

7.2. STB Thrust calculation method

Although this method was disregarded, it still functions as a basis for understanding the thrust OLS model as is described later in Section 7.3. Reasons for disregarding the STB method sparked mostly from unavailable table data which is vital for the scheme to work. Furthermore the STB literature also pointed to the existence of thrust calculation software, both solutions required further investigation, and most definitely some research to be done at the Fokker facilities in Hoofddorp, The Netherlands.

Moving on, the STB thrust calculation for the Fokker 100 is obtained through an intricate scheme of characteristic values, computations and specific variables dependent on information contained within two stb-tables (see Figure 7.4). Here one can observe distinct color-coding, i.e. dark-green is the final output value of the gross thrust along the engine's center-line (THGNC), light-green/blue are the primary calculation processes needed for the value of of THGNC, purple are the secondary calculation processes, red defines table-look-ups, and white defines the dependent sensory inputs needed for the thrust calculation.

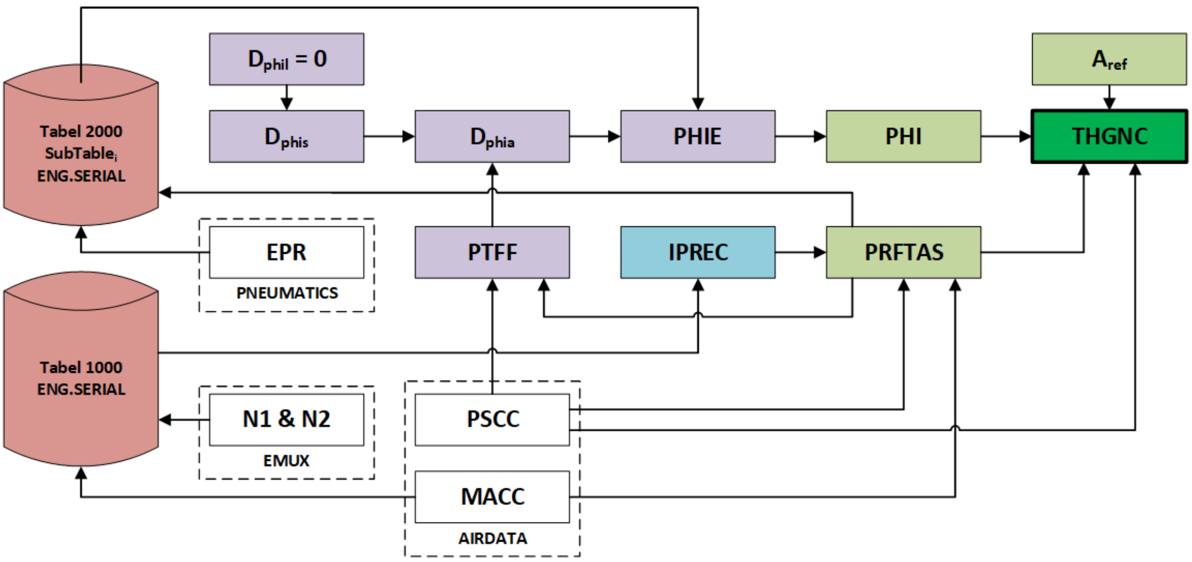

Figure 7.4: STB Thrust calculation scheme of THGNC thrust parameter for the Rolls-Royce Tay 620/650 engines [12, 13].

Gross thrust along the nozzle center-line (THGNC) is calculated using equation 7.1, using the unique engine nozzle surface (A_{ref}) in squared meters, the unit value calculations of corrected thrust parameter (PHI), and the unit value calculation of the engine ram ratio (PRFTAS). The resulting thrust value is in Newtons[12, 13].

$$THGNC = (PHI \cdot PRFTAS - 1) \cdot PSCC \cdot A_{ref} \tag{7.1}$$

, where PSCC is the measured corrected static pressure in Newtons per squared meter.

Corrected thrust parameter (PHI) is calculated using equation 7.2, where PHI is a unit value which is obtained through addition of the PHIE parameter (used for the calibration of the thrust parameter, i.e. "EPR method 1") with a multiple of environment parameters.

$$PHI = PHIE + D_{phies} + D_{phiea} + D_{phiel} \tag{7.2}$$

Here it should be noted that uncorrected thrust parameter (PHIE) in equation 7.2 is obtained from a table lookup operation, where the value of PHIE is related to the EPR measurement and the calculated engine ram ratio (FPRTAS). Furthermore the environmental parameters are spanned by the free stream suppression correction (D_{phies}), the altitude correction (D_{phiea}), and the nozzle leakage through thrust reverser correction (D_{phiel}). The latter is set to zero when no thrust reversing is active[12, 13, 30, 57, 61].

Engine ram ratio (PRFTAS) is calculated using equation 7.3, where one term clearly is defined as being related to isentropic flow, i.e. a pressure ratio as function of the free-stream Mach-number, multiplied by the inverse unit value of the intake recovery pressure (IPREC).

$$PRFTAS = (IPREC - 1) \cdot \left(1 + \frac{k-1}{2} MACC^2\right)^{\frac{k}{k-1}} \tag{7.3}$$

, where k is the heat capacity ratio, i.e. $k = cp/cv$.

In addition, IPREC is obtained through table lookup using the measured rotational speed of the low/high pressure turbine and compressor spool (N1&N2), and the corrected Mach number (MACC)[12, 13, 63, 70].

7.2.1. Disregarded STB method

As can be seen in the schematic overview of the STB calculations illustrated in Figure 7.4, the gross nozzle thrust (THGNC) is dependent on a lot of parameters all varying w.r.t. an unique engine serial number! To name a few, nozzle area (A_{ref}), correction parameters (D_{phies},D_{phiea},D_{phiel}), trim settings (F_{trim},W), specific ranges for PHIE & PHI parameters. NB in their own separate cases, most of these parameters use the corrected thrust parameters (PHI) and are dependent one coded ranges for specific EPR measurements, ram ratios (PRFTAS), and nozzle leakage parameters (NOZL). When taking in account the incomplete dependent tables 1000 & 2000, the reconstruction of this thrust calculation becomes impossible.

The only way this thrust reconstruction can properly be done is to go back to researching the old Fokker technical reports that hint on the availability of existing engine analysis software (Verbeek, 1986), and engine performance software (Van der Laan, 1987)[63, 70]. This will probably result in having to find more information, where the amount of work/time needed to set this up is expected to be beyond the scope of this thesis. The STB method is therefore disregarded, and demands a different approach. Nonetheless, the reader is left with some leads to technical reports to investigate the STB thrust calculation method further.

7.3. OLS Thrust model

Due to not having enough information available to reconstruct the STB thrust calculation method, as is described in Section 7.2, a different approach is needed. A simple ordinary least squares (OLS) model is created using the available data found in the MRVS database. NB, the STB calculation scheme (see Figure 7.4) already hinted at the "obvious" available dependent variables (regressors) needed to estimate the OLS model coefficients. Thus by using the available MRVS calculated gross nozzle thrust data-points as a response variable with regard to the available measurements should in theory yield something that could come close modeling the MRVS calculated thrust.

7.3.1. Dependent and response variables

As one can see within the STB scheme, the engine thrust is dependent on four measurements, i.e. the engine pressure ratio (EPR), corrected static pressure (PSCC), corrected Mach-number (MACC), and the low/high pass shaft speeds (N1&N2).

Because the corrected mach number (MACC) is missing from numerous recordings it is replaced with the measured mach number (MAPI), which is obtained through the impact/static pressure ratio measured by the pitot tube based on the STB calculation[13] for isentropic flow (equation 7.4).

$$MAPI = \sqrt{\frac{2}{k-1}\left[\left(1+\frac{PI}{PS}\right)^{\frac{k-1}{k}} - 1\right]} \tag{7.4}$$

, where k is the heat capacity ratio [-], i.e. $k = cp/cv$. PI is the impact pressure ($PI = PT - PS$) [N/m^2], PS is the static pressure [N/m^2], and PT is the total pressure [N/m^2].

For similar reasons the corrected static pressure (PSCC) is replaced with the pitot tube measured static pressure PS. Following, the dependent variables (sensor measurement) span matrix $\boldsymbol{X}$ in equation 7.5. And in addition to these five engine regressors, a single column populated with ones $\bar{X}_0$ is added for the zero β-coefficient (β_0) estimation.

$$\boldsymbol{X} = [\ \bar{X}_0\ , \ \bar{X}_{MAPI}\ , \ \bar{X}_{PS}\ , \ \bar{X}_{EPR}\ , \ \bar{X}_{N1}\ , \ \bar{X}_{N2}\ ] \tag{7.5}$$

$$\bar{y} = \bar{y}_{THGNC} \tag{7.6}$$

Subsequently in equation 7.7 the engine's coefficient vector $\hat{\beta}$ is obtained through algebraic operation, where $\bar{y}$ is populated with the MRVS calculated data-points nozzle thrust along the engine's center-line (THGNC).

$$\hat{\beta} = \left(\boldsymbol{X}^T\boldsymbol{X}\right)^{-1}\boldsymbol{X}^T\,\bar{y} \tag{7.7}$$

, where $\hat{\beta} = [\ \beta_0\ , \ \beta_{MAPI}\ , \ \beta_{PS}\ , \ \beta_{EPR}\ , \ \beta_{N1}\ , \ \beta_{N2}\ ]^T$.

7.3.2. Recording datasets

Selection of the training/validation datasets needed for estimation of the engine model's coefficients are presented in Appendix F.2, where specifically the clean configuration stall maneuvers have been selected. For the left engine 58 out of 87 recordings have MRVS calculated thrust data, and the right side has 59 out of 87 recordings. For an even distribution all recorded data is sorted w.r.t. mean altitude, and split on the basis of odd/even numbers where the training-set (Apendix F.2.1) uses the even numbers and odd for the validation-set (Appendix F.2.2). Again, it should be pointed out that the MRVS calculated thrust (THGNC) time-series itself is sparsely populated compared to the direct sensor measurement data (see Figures 7.2 and 7.3), where in most cases far more data-points and longer sample times are found.

With this in mind, and next to all the recordings that had no MRVS calculated thrust data contained within a specific flight-test, several more thrust recordings where removed by hand due to not having a complete measurement, i.e. dataset did not include the full stall manoeuvre (F100-TUD recordings 120L/R, 127L/R, 239L/R, 240L/R, 486L and 510L/R). In other words, all recordings were used regardless of sample length and distinct coverage, as long as the stall manoeuvre was contained within a clean aircraft configuration.

7.3.3. Bagplot presentation of bivariate data

A bagplot method is used to portrait the differences between the left/right engine recordings, this adds to the convex hull method used by De Visser (2011) through visually extending the amount of information contained in a single plot. Defining valid model ranges becomes more insightful, where more importantly the fence is actually found by using the convex hull method of all the bag plus loop data points (outliers excluded) thus not infringing on the plain convex hull plots[7].

More specifically, a bagplot (see example in Figure 7.5) is a bivariate generalization of two univariate boxplots which is proposed in a paper by Rousseeuw, Ruts & Tukey (1999). With regards to the normal convex hull method used by De Visser (2011), this type of plot provides more detail regarding the location (depth median), spread (size of the bag), correlation (orientation of the bag), skewness (bag shape and loop), and tails (points near the boundary of the loop and outliers) of the data. Bagplots presented here are created using the LIBRA[2] academic public license, i.e. a large library of MATLAB code maintained by the KU Leuven for Robust Analysis[1] and is available on Github[2] [7, 53].

As can be seen in Figure 7.5, a bagplot consists of a darker colored bag that contains 50% of the data ($N/2$ observations), a fence that separates inliers from outliers (usually not included, but shown as a red dotted line for illustration purposes), and the loop that acts as a shell around the bag constraint by the fence (i.e. an outer boundary that is the convex hull of the bag plus all non-outliers). Furthermore, some statistical characteristics can be considered through calculation and/or straight observation from the plot itself, where previously mentioned depth median is the point with the highest halfspace depth defined by the cross-hair, and the lighter colored loop acts as one would expect two whiskers in a normal boxplot to behave [53].

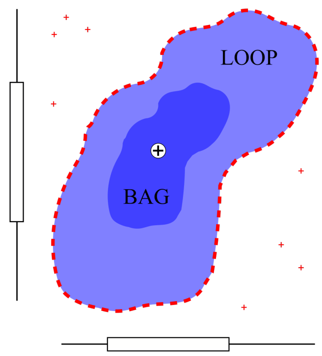

Figure 7.5: Bagplot example, where the bag is shaded dark, loop shaded light, cross-hair defines the depth median, and for purpose of illustration the normally not included red dotted line defines the fence.

Practical methods for detecting outliers, i.e. the red colored data points outside the fence (see Figure 7.5), are only valid for cases based on the assumption of elliptical symmetry of the underlying distribution. Note that the Rousseeuw, Ruts & Tukey (1999) paper does not properly account for any skewness in the supplied datasets. The LIBRA[2] software for bagplots is therefore equipped with routines that take skewness in account based on methods proposed in a paper by Hubert & Van der Veeken (2008), where generalization of the Stahel-Donoho outlyingness is used. To be clear, a measure of outlyingness is assigned to every observation by projecting pursuit techniques that are governed by univariate robust measures of location and scale. By using a robust measure of skewness, the measure of outlyingness can be adjusted to allow skewness in the data. Outliers in skewed data are thus found to be the observations that correspond to this adjusted value [22].

7.3.4. Flight-envelope analysis of the engine data

Henceforth, the flight-envelope regarding measurements that are concerned with the engine model will be presented using the Bagplot method. Thus from the given Bagplots in Figures 7.6a and 7.6c one can visualize the operational envelope to what extend the OLS engine model is bounded by the limited available thrust data, in relation to the in Figure 7.6b presented total available recording data.

[1]ROBUST@Leuven, `wis.kuleuven.be/statdatascience/robust`.
[2]LIBRA on Github, `github.com/mwgeurts/libra`.

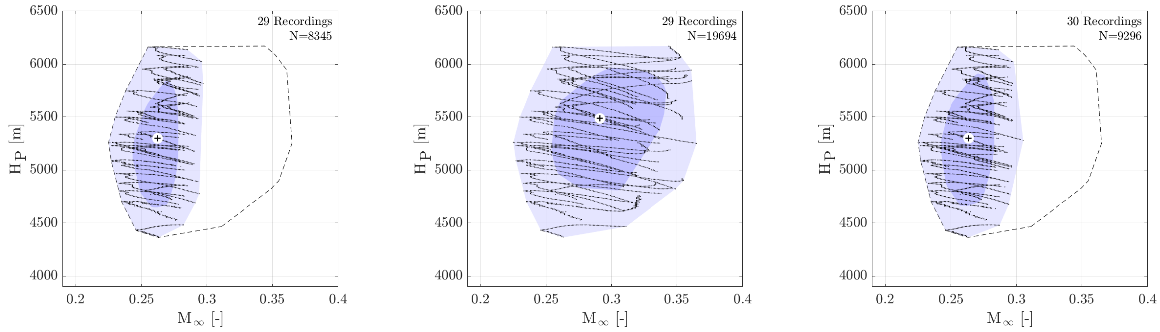

(a) Left engine trimmed. (b) All recorded data-points. (c) Right engine trimmed.

Figure 7.6: Training dataset for the OLS engine model flight-envelope. Bagplots of the free stream mach number M_∞ (MAPI) versus pressure height H_P (PA), where the black dotted line in the left/right engine plots corresponds with the fence of all recorded data-points.

Instantly the lacking MRVS available thrust data stands out in the presented training datasets, i.e. both left and right engines have less about half of the data points available in full range of the total recorded sensor measurements. Left/right engines both have a similar elliptical spread of the data points, i.e. within a Mach number of 0.23-0.30 and 4300-6100 meters altitude. Both bags are similar in size and orientation, thus correlated the same way w.r.t altitude versus Mach. No outliers are detected, i.e. data points outside the fence and judging from the size of the loop w.r.t. the bag the quality of the modeled behavior wil be best within this region.

The left sides of the loop (and fence) depict the lowest mach within the recording, i.e. the aircraft's moment of stalling. Right of the bag loop shows the higher Mach values within the available recordings that have been trimmed w.r.t. the MRVS calculated thrust. Anticipating the OLS thrust estimation plots, this observation can be visually verified using the MRVS calculated thrust plots in Figure 7.13. Not all data has been presented here, but it functions as an example to show the difference between all available data and the MRVS thust calculated. Most recording data is contained within the thrust idle glide phase (i.e. pre-stall), where the bag clearly shows this disposition, where stall recovery is quick and fast so less data is available.

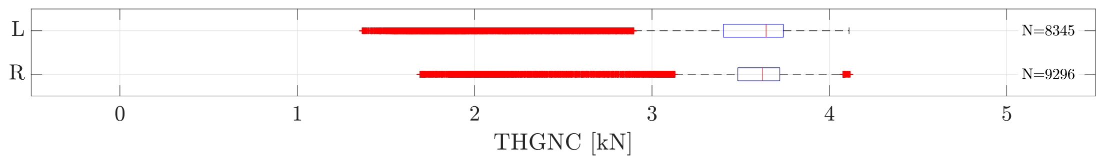

Figure 7.7: Training dataset thrust range boxplot.

In addition to the Bagplots, Figure 7.7 shows a boxplot of the available MRVS calculated thrust (THGNC), which shows the idle thrust setting to be more or less continuously set in the range of 3.6 kN. The drop in thrust is assumed to be a direct effect of the aircraft's stalling on the engine intake airflow. Figure 7.8 helps with this assumption, namely because the turbine gas temperature increases around the moment of stall (left engine, blue line, highlighted). According to Dirk van Os (Chief Enigineer at Fokker Services), this temperature increase results from a stagnation in the airflow allowing its temperature to increase, i.e. slows down and generating less thrust. This is an interesting measurement, and might be useful in helping to identify stalling conditions. Subsequently, the right engine (red line) shows a sudden decrease in temperature, which could be the result of the aircrafts attitude realtive to the wind and a rotating motion in a specific direction.

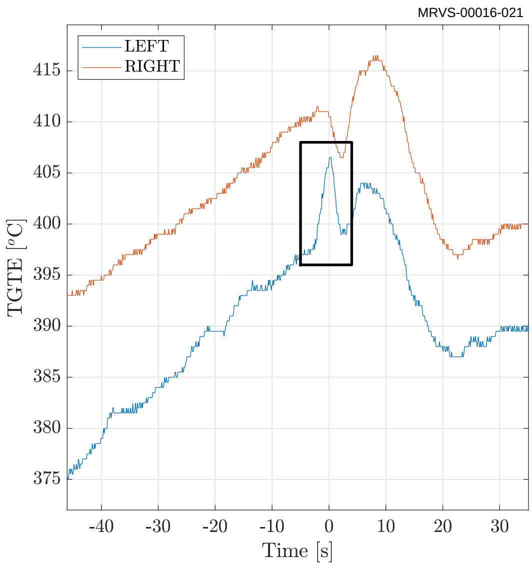

Figure 7.8: Pre-Stall increase of turbine gas temperature (TGTE) for the left engine due to air-flow stagnation, highlighted by the boxed in region.

7.3.5. Coefficient estimation

All corresponding coefficients are determined using the OLS scheme presented in section 7.3.1 and are shown in Figure 7.9. For the generalized β-coefficients, the mean is taken for every coefficient belonging to a specific recording dataset. These generalized β-coefficients are represented by the black dots and define the OLS engine model, one for every set of recordings per engine.

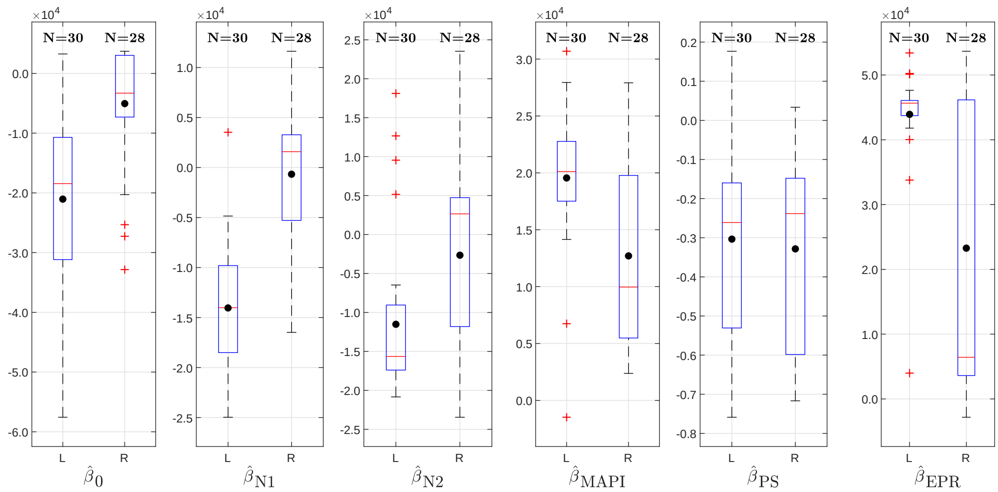

Figure 7.9: OLS engine model β-coefficients, black dots represent the mean 'generalized' values.

Table 7.2 presents the numeric mean β-coefficients, used by the engine model based on the training-set data.

Table 7.2: OLS engine model β-coefficients

Engines	β_0	β_{N1}	β_{N2}	β_{MAPI}	β_{PS}	β_{EPR}
Left	-2.105e+04	-1.404e+04	-1.152e+04	1.955e+04	-3.035e-01	4.392e+04
Right	-5.053e+03	-6.670e+02	-2.653e+03	1.270e+04	-3.285e-01	2.327e+04

7.3.6. Validation of OLS engine model

The engine model is validated using the validation-set (see Appendix F.2.2), these are the odd numbered recordings out of a sorted set w.r.t. average altitude (mean). Two statistical measurements are used to test the quality of the engine model, i.e. the Coefficients of Determination (R^2) and Root-Mean-Squared Error (RMSE). As an aid in understanding the inner workings of the engine model, Figure 7.13 is included. This figure shows a group of plots, where the left column coincides with the left engine, and vice versa. Plots are sorted w.r.t. RSME value ranging from lowest (top) to highest (bottom).

Coefficients of Determination

R-Squared (R^2) reveals how well a model is able to 'follow' the validation data (goodness of fit). This is achieved by obtaining the fractional relation between the squared sum of residuals (errors) and the total sum of squares relative the mean value, i.e. the smaller this number is the better the OLS model fits the actual validation data. Hence, deducting this value from 1 yields a measure by which models can be compared, i.e. the closer an R^2 value comes to 1, the better it fits.

Starting with the left engine in Figure 7.10a, shows a bagplot of the R^2 versus the average pressure height. Here 29 recordings are used to validate the OLS model and yields an interesting result, i.e. the best goodness of fit seems to build up at altitudes between 5000 to 5500 meters. Furthermore, going lower or higher in altitude seems to influence the value of R^2 negatively. Data is spread quite widely, where the bag a lot larger than the loop, the median data sits around 5500 meters with an R^2 a little less than 0.5.

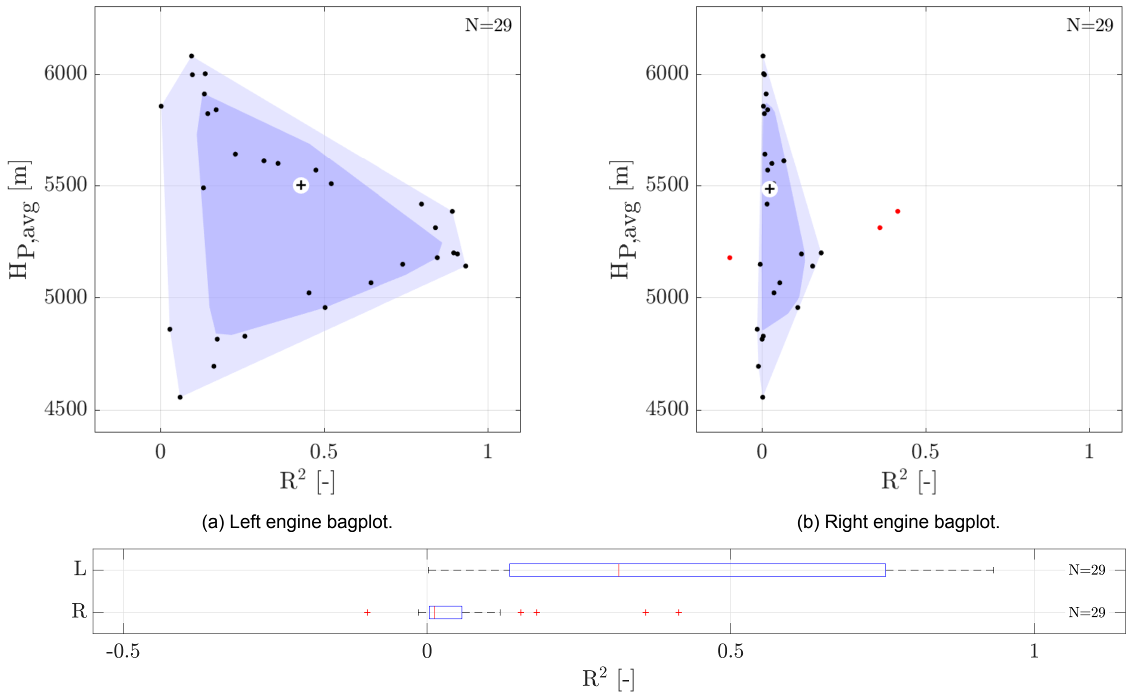

(a) Left engine bagplot.

(b) Right engine bagplot.

(c) Univariate boxplot.

Figure 7.10: Validation of engine OLS model: R^2 versus average pressure height ($H_{P,avg}$), w.r.t. MRVS thrust validation-set recordings.

Right engine shows more stressing results, the bulk of the R^2 values reside between values of 0 and 0.2, not to mention the three outliers of which one is negative. Negative R^2 values are possible, this usually occurs when the hyperplane exceeds modeled data allowing value outside the range 0 to 1. The difference between the left/right engine model is most likely due to the fact right side recordings sets are not excited to their limits, left engine has more going on. On top of this, the outliers on the fence's right-side show the best results (R^2 around 0.4) adds to this statement. Further analysis is required ...

Root-Mean-Squared Error

By use of a Root-Mean-Squared Error (RSME) a different type analysis is applied w.r.t. the R^2 method. RSME returns information about the absolute distance overall modeled data is spaced from the actual recorded data in a single figure of merit. This validation is done for both left/right engines (see Figures 7.11a and 7.11b). Straight off, a similar distribution is observed w.r.t. altitude, where the least amount of errors occur between the 5000 to 5500 meter in height. Thus most regressions come close to the depth median, and leads to the conclusion of two skewed datasets with a strong dependence to altitude. As can be seen in Figure 7.11c, a univariate boxplot is presented to illustrate the results in a 2D manor, here it shows that the largest number of regressions are below an RMSE of 1kN. This is a very small value, specially when one imagines the goal of this thesis which requires the engine setting to be at idle, and that the aircraft's 28.6 tons OEW (see Table 6.1) compared to 100 kg-force is a factor of 286 larger. The error is therefore assumed to be insignificantly small, and can be considered for research purposes within this specific flight-envelope.

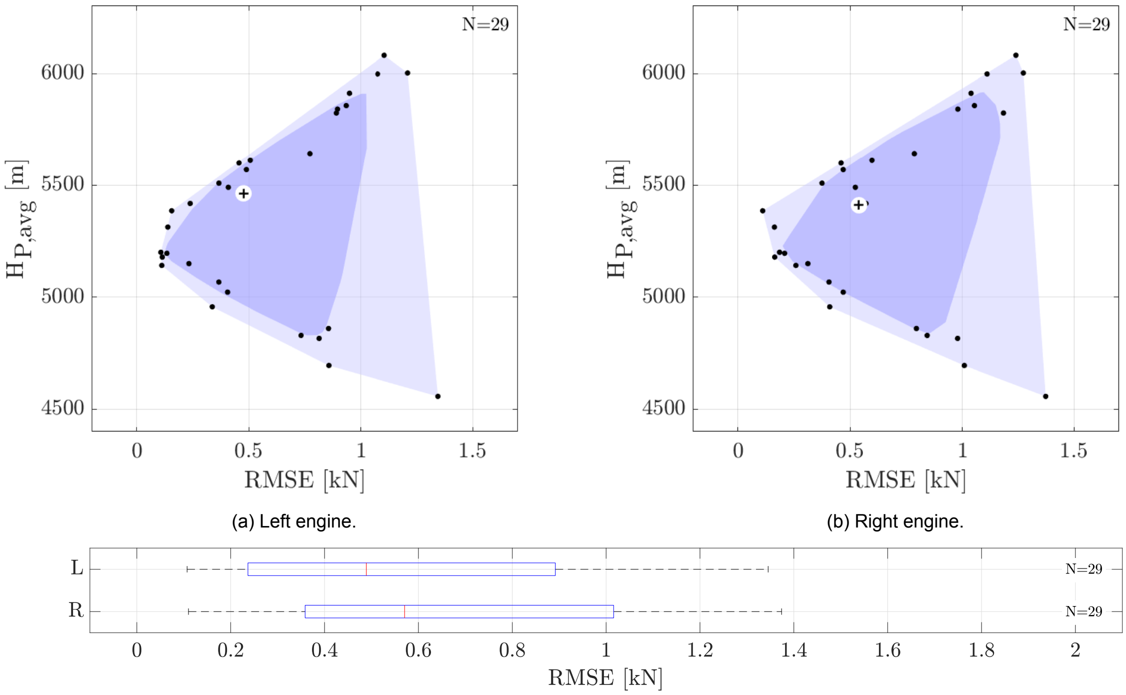

(a) Left engine.

(b) Right engine.

(c) Univariate boxplot.

Figure 7.11: Validation of engine OLS model: RMS-Error versus average pressure height ($H_{P,avg}$), w.r.t. MRVS thrust validation-set recordings.

Thus, it should be assumed, although the right engine shows very low RSME values, that the R^2 suggests some problems with this right engine model. Best would be to get the original software for computing the correct thrust, or do more tests. Sadly this would require a lot more research and flight testing, not to mention the altitude and configuration dependence! These requirements are therefore passed on as a recommendation for future academic work.

Sensitivity analysis
Model sensitivity is added to display the resulting reactions due changing the β-coefficients one-by-one, and w.r.t to an arbitrarily chosen coefficient range the variances accounted for (VAF) are tested. Note that, all coefficients are tested with regards to the case where the least amount of RSME was found per engine. Left engine model looks like it is performing at an optimal level, on the other hand (as expected) the right side does not.

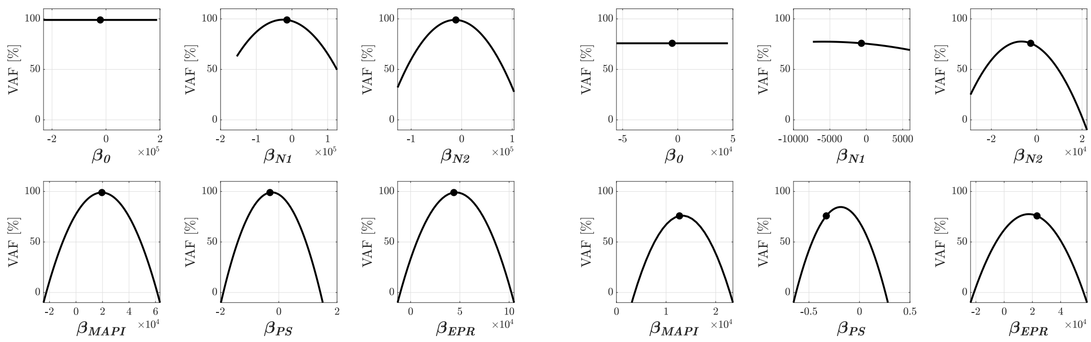

(a) Left engine. (b) Right engine.

Figure 7.12: Sensitivity analysis of the engine OLS model: Variances Accounted For (VAF).

Important assumptions | Engine OLS Model

It was not possible to recreate the calculation scheme found in the Fokker STB documentation, therefore an engine OLS model is created based on the calculation method proposed by the STB. Here 5 independent variables are used to estimate the engine model's β-coefficients, i.e. engine rmp's (N1&N2), engine pressure ratio's (EPR), the free stream mach-number (MAPI) and static pressure (PA).

- Regressors data is (unfiltered) raw.
- Fokker STB method is disregarded due to incompleteness of available data sources, where as workaround the OLS approach is considered.
- Due to the thrust (THGNC) response variable sparse availability, the model's validity regarding aircraft's velocity expressed in mach-numbers reside between values of 0.23 and 0.3.
- Model is most reliable between altitudes of 5000 to 5500 meters, and valid between 4500 to 6000 meters with acceptable errors.
- Right-side training data is poorly excited, which results in problems regarding the fitting of the engine OLS model to the validation data. This also accounts for the left-engine, yet here the model performs significantly better due to high R^2 results.
- Overall encountered absolute errors in the engine model (i.e. RMSE's) are insignificantly small in all cases using the validation datasets. The OLS engine is therefor assumed to be good enough for research that considers low speed flying with engines in an idle setting.

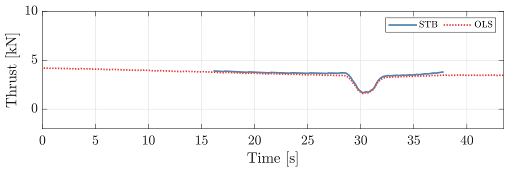

(a) MRVS-00050-123, Left engine, RMSE=0.107kN, R^2=0.896.

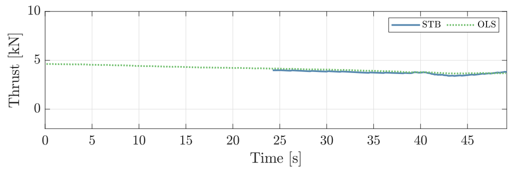

(b) MRVS-00048-017, Right engine, RMSE=0.110kN, R^2=0.414.

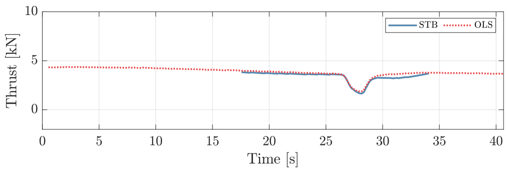

(c) MRVS-00052-093, Left engine, RMSE=0.138kN, R^2=0.841.

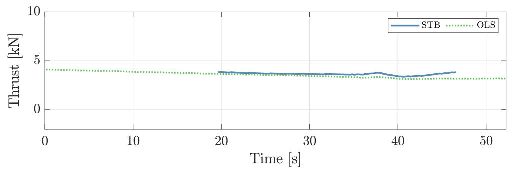

(d) MRVS-00051-019, Right engine, RMSE=0.208kN, R^2=0.120.

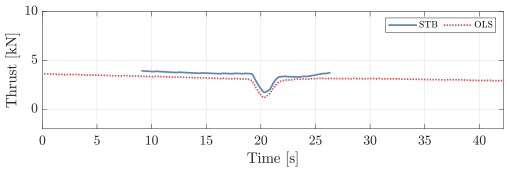

(e) MRVS-00052-095, Left engine, RMSE=0.337kN, R^2=0.503.

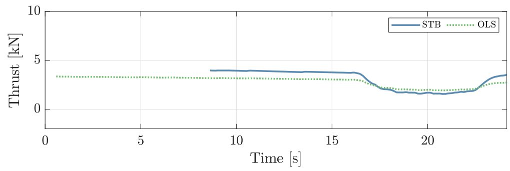

(f) MRVS-00021-029, Right engine, RMSE=0.405kN, R^2=0.054.

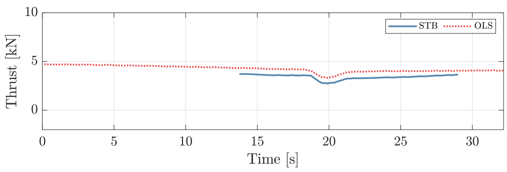

(g) MRVS-00040-025, Left engine, RMSE=0.408kN, R^2=0.131.

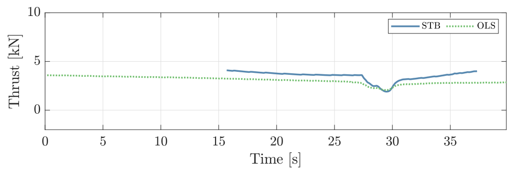

(h) MRVS-00048-019, Right engine, RMSE=0.469kN, R^2=0.037.

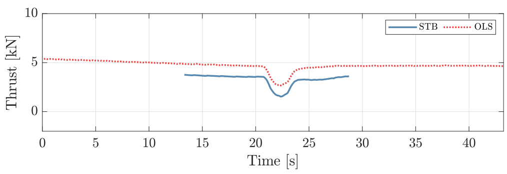

(i) MRVS-00050-129, Left engine, RMSE=0.772kN, R^2=0.229.

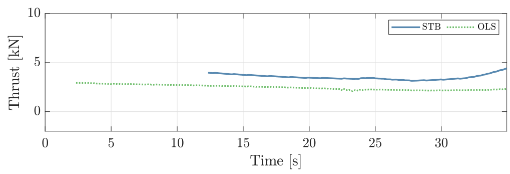

(j) MRVS-00036-023, Right engine, RMSE=0.795kN, R^2=-0.014.

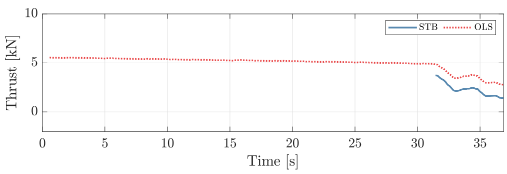

(k) MRVS-00021-025, Left engine, RMSE=0.891kN, R^2=0.144.

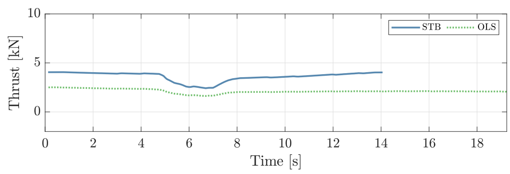

(l) MRVS-00051-031, Right engine, RMSE=1.009kN, R^2=-0.011.

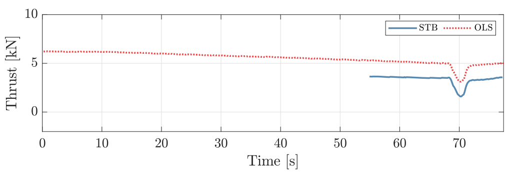

(m) MRVS-00050-159, Left engine, RMSE=1.076kN, R^2=0.097.

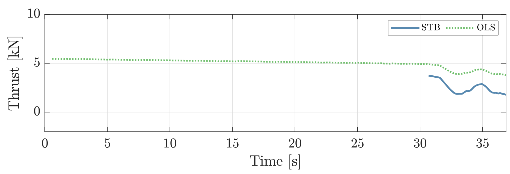

(n) MRVS-00021-025, Right engine, RMSE=1.186kN, R^2=0.007.

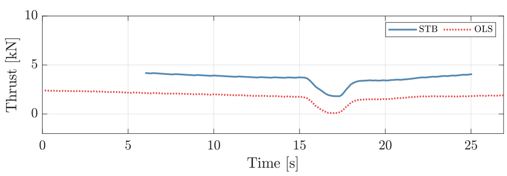

(o) MRVS-00051-023, Left engine, RMSE=1.345kN, R^2=0.060.

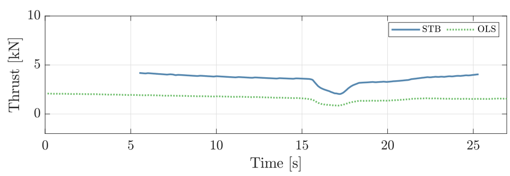

(p) MRVS-00051-023, Right engine, RMSE=1.374kN, R^2=0.002.

Figure 7.13: MRVS calculated engine thrust THGNC (blue) versus estimated thrust (red=left,green=right). Plots are sorted w.r.t. RSME value ranging from lowest (top) to highest (bottom).

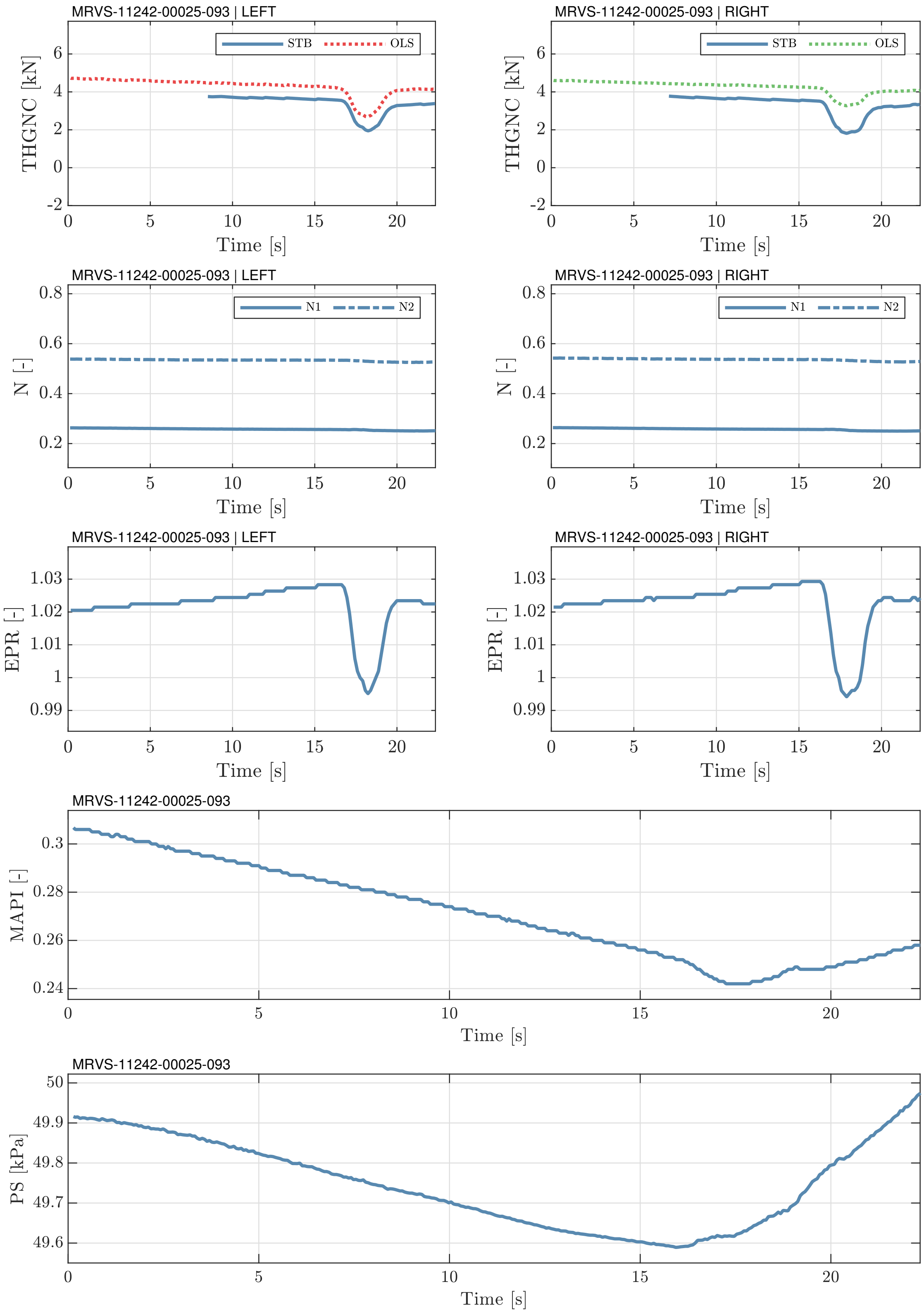

Figure 7.14: Engine OLS model illustration plot including the thrust, engine rpm’s, engine pressure ratio’s, free steam mach-number and static pressure.

8

Flight path reconstruction

Using the techniques developed by the Operations and Control department as discussed in Chapter 4, an attempt is made to reconstruct the flight path of the Fokker 100. This aircraft was chosen first because of the shear number flight-test available within the total supplied set of recordings by Fokker Services.

Note that this is a first attempt at filtering flight test data from a source other than the usual TUD-NLR flight-test data, that is formatted and processed in a standardized manner, and regarding certification stall maneuvers were executed according to the JAR25 requirements (Section 8.1). This fact right here posses a challenge, because the Fokker's recording data needs to be reformatted to be able to run through the C&S filtering process created by Mulder et al., and researched by De Visser, Van den Hoek, Van Horssen, and Van Ingen [7, 37, 62, 65, 67]. Running into problems is expected, mainly because questions exist regarding the methods used by Fokker's MVRS department when processing recorded data is concerned. One can think of may have, or may have not, applied smoothing/filtering to the "raw" data, or any other type of data modification. Due to the historic nature of the flight-test data, one just does not have the same level of confidence as if one had complete control over the manner of recording the data.

Therefor in Section 8.2, an effort is made to stick as close as possible to the most raw signals available, and let the filter processes do its work. On an higher level, only recordings are considered that contain complete straight (not accelerated, banked) stall maneuvers, and are performed in a clean configuration, i.e. flying with retracted landing gear with no extended flaps.

To tackle this challenge effectively a strategy is devised to make sure the core state reconstruction works as intended, and without failure. The filtering processes was first applied by using the C&S standard methods, meaning that the filtering techniques (Chapter 4) are considered, where dead reckoning datasets where created to function as the unavailable GPS data. Sadly using this method yielded a large amount inconsistencies and errors, therefor a different strategy was chosen to only considers the aerodynamic (6 variables as defined in Section 8.3) state first. This proved to run reliably, and another extension was considered by adding the extended Laban vane/boom equations. Subsequently the filter performance is discussed in Section 8.4, where the two most reliable filtering methods (IEKF & UKF) are compared.

8.1. Definition of the stall maneuver

This thesis is concerned with doing research towards stall model identification. Hence, the stall maneuver is the dominant point of focus regarding the data that needs to be filtered. Importantly, this maneuver was executed several decades ago, and needs to be defined in order to understand if there exist differences in the execution of today's stall maneuvers. And if side effects might exist regarding the execution as a note for future research.

In order to be certified by the Joint Aviation Authorities (JAA) in 1989, several requirements needed to be met. These specific requirements are defined in the Joint Aviation Requirement 25 (JAR25) for large airplanes under articles 201-207, i.e. JAR25.201-207 [27]. Fokker implemented these requirements as part of their flight testing program, and executed the stall maneuvers accordingly.

JAR25 requires the manufacturer to demonstrate a straight flight stall, with (i) ”Power off”, and (ii) ”Power necessary to maintain level flight at 1.6 V_{SI}”. Where conditions needing to be met regarding; all flaps/gear configurations, weight distribution, and trimmed straight flight within 1.2-1.4 V_{SI}.

The procedure to be demonstrated is then carried out as follows (JAR25.201-C).

1. ”**Starting at a speed sufficiently above the stalling speed to ensure that a steady rate of speed reduction can be established, apply the longitudinal** control so that the speed reduction does not exceed one knot per second until (i) the aircraft is stalled, or (ii) the control reaches the stop.”
2. As soon as the aircraft is stalled, recover by normal recovery techniques.

The aircraft is considered stalled if the behavior of this aircraft gives the pilot a clear and distinctive indication of an acceptable nature that the aircraft is indeed stalled (JAR25.201-D).

1. ”A nose-down pitch that cannot be readily arrested **and which may be accompanied simultaneously by a rolling motion which is not immediately controllable (provided that the rolling motion complies with JAR 25.203-B/C as appropriate)**.”
2. ”**Severe buffeting, of a magnitude and severity that is a strong and effective deterrent to further speed reduction**.”

8.1.1. Procedure addendum

In conversation with Chief Engineer Van Os (Fokker Services BV) regarding the preceding starting speed in straight flight procedures followed by Fokker to perform the stall maneuver, it was mentioned that the constant aircraft decelleration (dV/dt) was obtained by manually controlling the elevator deflection by the pilot, i.e. maintaining a fixed pitch attitude to achieve the required 1 or 3 kt/s. These attitudes were obtained through testing and experimentation. Thrust was set to idle, i.e. no throttle control was active.

8.2. Data preparation

Like was mentioned, data preparation is extensive because the available data is formatted according to Fokker's MRVS standards, some structuring and modifications are needed. Per example, not all time traces are of equal length, and have a common time basis, thus making filtering in its original format impossible.

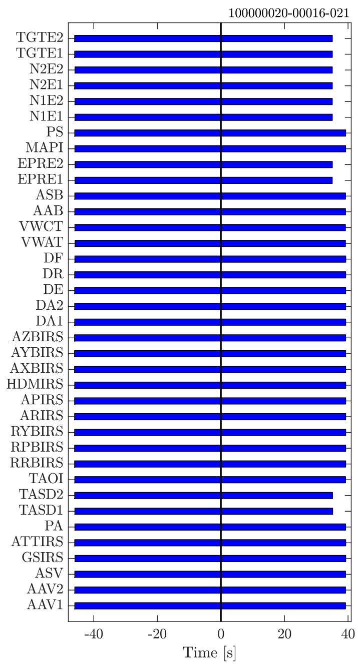

Figure 8.1: Sensor time traces.

8.2.1. Parameter and recording selection

Parameter selection, not to be confused with an aerodynamic parameter, is Fokker terminology for a data source that contained flight-test information. This can be anything from a cockpit button status to angle of attack values w.r.t. a specific recording time.

Important here is to have a complete recording as the Fokker recorded flight database has missing, and/or disjoint time-series. Hence, a selection is dependent on all parameters that contain the required data sources needed for the FPR. The engine data within the same time-line is also included, because the engine is part of the stall model identification process! An example of such a selection is given in Figure 8.1, it represents the first recording containing both the boom- and vane data, where in Table 8.1 detailed information is supplied regarding these selected parameters.

As a measure for including as much data as possible in regard to the pre- and post-stall conditions, the moment of maximum rate of change in the angle of attack is obtained. This functions as a simple precursor to identifying the moment of stall on a numerical single parameter basis, and more importantly allows for an extra selection criteria regarding the selection of the recordings. The time-line in Figure 8.1 is adjusted to show the difference between pre- and post-stall conditions, as one can easily observer an indication line that splits the relevant parameters and their time distributions.

Thus, it can be stated that the choice of a good and usable recording depends on the availability of all the right parameters and the completeness of the recording. And in combination with the Fokker flight-test cards supplied by Dirk van Os, all the straight stall flight are selected that adhere to the selection criteria as described above. Appendix F.1 details the selected stall recordings, where 9 out 17 flights made use of a boom and the latter a fuselage attached pair of vanes. Totaling a number of straight stalls in clean configuration flight-test recordings to be filtered for continued research regarding stall model identification.

8.2.2. Signal attributes and corrections

As has been stated already previously, in research done by Van den Hoek and Van Horssen (see Chapter 4), resampling through "spline" interpolation is not a problem as the Citiation data is handled similarly, and allows for formatting the data w.r.t. a common time basis.

Interpolation "sampling"

Subsequently, as is presented in Table 8.1, the maximum sample frequency is found to be at 50 Hz and belongs to the measured accelerations (Ax, Ay, Az). For all relevant parameters needed in Kalman filtering, and later in research concerned with stall model identification, are up-sampled to this frequency using MATLAB's `interp1` function. In the case of the Fokker data linear interpolation was used, as it is less inclined to solve continuity problems which might make up data-points that wouldn't exist in reality. And in the end, all state related data is Kalman filtered anyway.

As a side note, it is common practice in signal processing to use a `resample` function, within MATLAB this is actually a filter in disguise because it uses Finite Impulse Response (FIR) anti-aliasing. This is not preferable!

IMU Corrections

With the Fokker 100 mass model defined, corrections can be applied to the measured sensor data by the Inertial Reference System (IRS) (green box, see Appendix E.1) w.r.t. the aircraft's "varying" center of gravity, which changes depending on the current fuel levels. This is specifically applied to rotation rates (p, q, r) and the body accelerations (Ax, Ay, Az).

Covariance

Fokker has no available data w.r.t. to sensor specifications, this forced the direction of this thesis to also guess these values based on a presumed error in the signal. The variance of this error was only determined for the relevant sensor measurements needed for the Kalman filtering.

Through taking small cuts from the flight data, covariance is obtained. Where the aircraft is relatively stationary, i.e. no significant course influencing accelerations. The data is then filtered (4th order Butterworth), and the errors relative to the filtered signal are computed, ensuring a zero-mean distribution. Henceforth, the variance is then calculated giving some idea regarding the sensor noise acting on the system (see Table 8.1).

Table 8.1: Sensor selection for Kalman filtering and aerodynamic model identification (AMI) regarding the Fokker 100.

Param	Unit	Description	Symbol	f_s [Hz]	Source[1]	Range[2]	Var[3] (σ^2)
AAV1	rad	angle of attack (vane lh)	$\alpha_{v,1}$	16	BD	[-20,60]	1.047e-03
AAV2	rad	angle of attack (vane rh)	$\alpha_{v,2}$	16	BD	[-20,60]	1.047e-03
ASV	rad	angle of sideslip (vane)	β_v	16	BD	[-40,40]	1.047e-03
AAB	rad	angle of attack (boom)	α_b	16	ND	[-10,60]	1.745e-03
ASB	rad	angle of sideslip (boom)	β_b	16	ND	[-40,40]	1.745e-03
TASD1	m/s	true airspeed (dadc1)	$V_{TAS,1}$	8	BD	[-2048,2048]	3.000e-01
TASD2	m/s	true airspeed (dadc2)	$V_{TAS,2}$	8	BD	[-2048,2048]	3.000e-01
GSIRS	m/s	ground speed (irs)	V_{GS}	10	ND	[0,4096]	
VWAT	m/s	wind velocity along track	$V_{W,AT}$	16	STB	[0,0]	
VWCT	m/s	wind velocity cross track	$V_{W,CT}$	16	STB	[0,0]	
APIRS	rad	angle of pitch (irs)	ϕ	50	ND	[-180,180]	1.745e-04
ARIRS	rad	angle of roll (irs)	θ	50	ND	[-180,180]	1.745e-04
HDMIRS	rad	magnetic heading (irs)	ψ_m	25	ND	[-180,180]	
ATTIRS	rad	track angle-true (irs)	ψ_t	25	ND	[-180,180]	1.047e-04
RRBIRS	rad/s	body roll rate (irs)	p	50	ND	[-128,128]	7.854e-03
RPBIRS	rad/s	body pitch rate (irs)	q	50	ND	[-128,128]	7.854e-03
RYBIRS	rad/s	body yaw rate (irs)	r	50	ND	[-128,128]	7.854e-03
AXBIRS	m/s2	body long. accel. (irs)	Ax	50	ND	[-39,39]	6.000e-02
AYBIRS	m/s2	body lat. accel. (irs)	Ay	50	ND	[-39,39]	6.000e-02
AZBIRS	m/s2	body norm. accel. (irs)	Az	50	ND	[-39,39]	6.000e-02
DA1	rad	aileron deflection l	$\delta_{a,1}$	32	ND	[-25,25]	
DA2	rad	aileron deflection r	$\delta_{a,2}$	32	ND	[-25,25]	
DE	rad	elevator deflection	δ_e	32	ND	[-30,20]	
DR	rad	rudder deflection	δ_r	32	ND	[-35,35]	
DF	rad	wingflap position	δ_f	4	BD	[-5,50]	
PA	m	pressure altitude	H_p	16	STB	[-600,12000]	
PS	pa	static pressure	p	8	ND	[15,110]	
TAOI	cel	indicated outside air temp.	T_{AOI}	8	BD	[-60,60]	
MAPI	unity	mach number based on pi,ps	M_{p_i,p_s}	16	STB	[0,0]	

[1] Source description is defined as follows; ND for NLR Digital, BD for Board-signal Digital, and STB for the standard calculations (i.e. measurement was calculated by Fokker MRVS).

[2] Note that signals where angles are concerned, are always presented in radians, but ranges are given in degrees.

[3] Sensor variance was guessed based upon the smallest observable variance in errors. Empty values are unused, not needed.

8.3. Aerodynamic model

For Kalman filtering a kinematic model needs to be defined. This model is used to predict and correct the state and observations, and as is explained at the beginning of this Chapter, a simple approach is considered. Because little is truly known about the data, warranting a bottom-up approach. This type of strategy starts off simple and allows for extensions to try things out, and/or expand the model to fit more data sources. And revert to a working version, if things do not turn out well.

8.3.1. Simplified navigation system

First the aerodynamic model state ($\bar{x}_k$) is defined in Equation 8.1 as follows, and is spanned by 6 state variables, i.e. the body velocity (u_b, v_b, w_b), and aircraft attitude (ϕ, θ, ψ) in ECEF. Subsequently, the state is augmented with 6 bias ($\lambda_x, \lambda_y, \lambda_z, \lambda_\phi, \lambda_\theta, \lambda_\psi$) variables.

$$\bar{x}_k = \left[\bar{x}_s^T, \bar{x}_b^T\right]^T \quad \in \quad \left\{\bar{x}_s = \left[u_b, v_b, w_b, \phi, \theta, \psi\right]^T, \bar{x}_b = \left[\lambda_x, \lambda_y, \lambda_z, \lambda_p, \lambda_q, \lambda_r\right]^T\right\} \tag{8.1}$$

Aerodynamic model input ($\bar{u}_k$) is defined in Equation 8.2 as follows. Here the variables denoted with $(\cdot)_m$ are the raw sensor measurements, $(\cdot)_w$ is the added process noise vector.

$$\bar{u}_k = \bar{u}_m - \bar{x}_b - \bar{u}_\omega \quad \in \quad \left\{\bar{u}_m = \left[Ax_m, Ay_m, Az_m, p_m, q_m, r_m\right]^T, \bar{u}_\omega = \left[\omega_x, \omega_y, \omega_z, \omega_p, \omega_q, \omega_r\right]^T\right\} \tag{8.2}$$

The system state matrix (F_x) in Equation 8.3 is defined as follows. Note that the accelerations are now corrected for gravity, which implies that the kinematic equations are contained within the ECEF reference system.

$$\mathrm{F}_x(t, \bar{x}, \bar{u}, \bar{\omega}) = \begin{bmatrix} (r_m - \lambda_r - \omega_r) v_b + (\lambda_q - q_m + \omega_q) w_b + (Ax_m - \lambda_x - \omega_x - g_0 \sin(\theta)) \\ (\lambda_r - r_m + \omega_r) u_b + (p_m - \lambda_p - \omega_p) w_b + (g_0 \cos(\theta)) \sin(\phi) + (Ay_m - \lambda_y - \omega_y) \\ (q_m - \lambda_q - \omega_q) u_b + (\lambda_p - p_m + \omega_p) v_b + (g_0 \cos(\theta)) \cos(\phi) + (Az_m - \lambda_z - \omega_z) \\ (q_m - \lambda_q - \omega_q) \sin(\phi) \tan(\theta) + (r_m - \lambda_r - \omega_r) \cos(\phi) \tan(\theta) + (p_m - \lambda_p - \omega_p) \\ (\lambda_r - r_m + \omega_r) \sin(\phi) + (q_m - \lambda_q - \omega_q) \cos(\phi) \\ ((q_m - \lambda_q - \omega_q) \sin(\phi)) / \cos(\theta) + ((r_m - \lambda_r - \omega_r) \cos(\phi)) / \cos(\theta) \\ 0 \\ 0 \\ 0 \\ 0 \\ 0 \\ 0 \end{bmatrix} \tag{8.3}$$

With the basis of the system navigation equations in place its easy to compute the Jacobian of the state transition, i.e. $\mathrm{dF}_x = \mathrm{J}(\mathrm{F}_x, \bar{x}_k)$.

8.3.2. Simplified observation system

Measurements obtained are defined in Equation 8.4, part of the aerodynamic model observation ($\bar{z}_k$) vector, and influenced by the measurement noise ($\bar{z}_v$) vector. The latter being part of the UKF process.

$$\mathrm{H}_x = \bar{z}_k - \bar{z}_v \quad \in \quad \left\{\bar{z}_k = \left[\phi, \theta, \psi, V_{TAS}, \alpha, \beta\right]^T, \bar{z}_v = \left[v_\phi, v_\theta, v_\psi, v_{V_{TAS}}, v_\alpha, v_\beta\right]^T\right\} \tag{8.4}$$

Regarding the available flight tests, two observation systems need to be defined. This is due to the fact that Fokker flight-tests where carried out with a boom (see Appendix G) in the first half of flight-testing, and it was removed (only vanes remained) during second half of the flight-testing phase.

Thus, the simplest form an observation system in this case takes on is w.r.t the vanes-only profile. Here, in Equation 8.5, heading and attitude are passed through directly, true airspeed is given as a function of the state variables, as are the α_v and β_v vane measurements a function of the state. This observation model completely neglects influences caused by e.g. rolling motions, i.e. lateral effects. This can be done, because in this thesis only straight (longitudinal) flight is considered, and therefor falls outside the scope.

$$\mathrm{H}_{x,vane}(t,\bar{x},\bar{v}) = \begin{bmatrix} \phi - v_\phi \\ \theta - v_\theta \\ \psi - v_\psi \\ (u_b^2 + v_b^2 + w_b^2)^{1/2} - v_{V_{TAS}} \\ \arctan(w_b/u_b) - v_\alpha \\ \arctan(v_b/(u_b^2 + v_b^2 + w_b^2)^{1/2}) - v_\beta \end{bmatrix} \tag{8.5}$$

The boom observation system in Equation 8.6 is more complex and is based upon Laban's work, it incorporates boom kinematics influenced by the true airspeed (see Appendix G) w.r.t. the aircraft's center of gravity. There are also fuselage induced effects, but for the sake of simplicity are assumed negligible. N.b. induced fuselage effects requires extensive aerodynamic knowledge about the airflow around the fuselage, and is therefore outside the scope of this thesis.

$$\mathrm{H}_{x,boom}(t,\bar{x},\bar{v}) = \begin{bmatrix} \phi - v_\phi \\ \theta - v_\theta \\ \psi - v_\psi \\ (u_b^2 + v_b^2 + w_b^2)^{1/2} - v_{V_{TAS}} \\ \arctan(w_b/u_b) - (q_m x_\alpha)/(u_b^2 + v_b^2 + w_b^2)^{1/2} - v_\alpha \\ \arctan(v_b/u_b) - (p_m z_\beta)/(u_b^2 + v_b^2 + w_b^2)^{1/2} - (r_m x_\beta)/(u_b^2 + v_b^2 + w_b^2)^{1/2} - v_\beta \end{bmatrix} \tag{8.6}$$

Similar to the navigation, the observation system's Jacobian of the measurement transition is now also found, i.e. $\mathrm{dH}_x = \mathrm{J}(\mathrm{H}_x, \bar{x}_k)$.

8.3.3. Extended aerodynamic model

The extended aerodynamic model is added to test the filter model used by Van Ingen, i.e. copied. Only a 13th state is added in this regard, i.e. the upwash ($C_{\alpha_{up}}$) variable. As can be seen in 8.7, the state variables are easily extended, where its derivative is defined as $0.01 w_N\,(\pi/180)$. Note that the w_N term is random fraction [37].

$$\bar{x}_{k,ext} = \begin{bmatrix} \bar{x}_{k,ext} \\ C_{\alpha_{up}} \end{bmatrix} \quad (13x1) \quad , \quad \mathrm{F}_{x,ext} = \begin{bmatrix} \mathrm{F}_x(t,\bar{x},\bar{u},\bar{\omega}) \\ 0.01 w_N \frac{\pi}{180} \end{bmatrix} \quad (13x1) \tag{8.7}$$

The vane system in Equation 8.8 remains relatively untouched, only change is that bias terms are added. And Van Ingen's model only uses the longitudinal body velocity (u_b) instead of the true airspeed.

$$\mathrm{H}_{x,vane}(t,\bar{x},\bar{v}) = \begin{bmatrix} \phi - v_\phi \\ \theta - v_\theta \\ \psi - v_\psi \\ (u_b^2 + v_b^2 + w_b^2)^{1/2} - v_{V_{TAS}} \\ \arctan\left(w_b/u_b\right) + x_a(\lambda_q - q_m)/u_b - v_\alpha \\ \arctan\left(v_b/(u_b^2 + v_b^2 + w_b^2)^{1/2}\right) - v_\beta \end{bmatrix} \tag{8.8}$$

The boom part is where things get interesting, this where the upwash state variable ($C_{\alpha_{up}}$) is introduced. And in addition the state augmented bias variables.

$$
\mathrm{H}_{x,boom}(t,\bar{x},\bar{v}) = \begin{bmatrix} \phi - v_\phi \\ \theta - v_\theta \\ \psi - v_\psi \\ (u_b^2 + v_b^2 + w_b^2)^{1/2} - v_{V_{TAS}} \\ (C_{\alpha_{up}} + 1)\arctan(w_b/u_b) + (x_a(\lambda_q - q_m))/u_b - v_\alpha \\ \arctan(v_b/u_b) + (z_b(\lambda_p - p_m))/u_b - (x_b(\lambda_r - r_m))/u_b - v_\beta \end{bmatrix} \tag{8.9}
$$

8.4. Filter performance

Initially, the goal was to forge the Fokker data in such a way it was directly compatible with the MATLAB FPR software (9 state variables) created by Van den Hoek and Van Horssen in 2016. This meant creating a dead reckoning dataset spanned by position and velocity, using the available Fokker parameters for ground speed (GSIRS), track angle (ATTIRS), and pressure altitude (PA). Sadly this instantly yielded a large amount of errors in filter conversion, where system observability broke down regularly. It's suspected that there exists some form of data formatting error(s) in the calculated dead reckoning datasets that conflicts with the aerodynamic and attitude observations. Because it was taking too much time in finding these errors, the strategy (as previously explained) was changed to creating a simple aerodynamic system, based on 6 state variables.

Previous research done regarding the filter methods used has already extensively demonstrated the IEKF/UKF is working as intended. Yet, it is still hard to say anything about the filter performance without the presence of validated datasets to compare results with. The only meaningful way of explaining if a filter is working as intended, is to prove filter-convergence. The way a filter converges is not expressed in absolutes, but as a converging error covariance as is ideally defined as $P_{k+1,k+1} \rightarrow 0$. Using this criterion, it's easy to see in a simple plot if the filter properly converges, and if problems exists.

As an example flight 17 and recording 13 are used to illustrate filter convergence, the difference between IEKF versus UKF filter methods, and aerodynamic versus extended kinematic model profiles, and uses the boom equations. In other words, this example proves the filter is in good working order regarding the aerodynamic kinematic model (Figures 8.2-8.5), while showing troubling results with the extended model (Figures 8.6-8.9). Note that the velocity states are compared to a calculated observation, i.e. the measured body velocities are obtained as a function of true airspeed (V_{TAS}), angle-of-attack (α), and angle-of-sideslip (β). These are not directly measured, and function as means to verify the optimal velocity estimate. Furthermore, vane plots were disregarded because they worked in all cases without fail, using the aerodynamic kinematic model.

Aerodynamic model

Some times simple is better. Comparing the optimal estimates IEKF versus UKF in Figures 8.2 & 8.4, one can see that filter conversion for both filter types occurs almost immediately. In the figures there are two shaded areas that illustrate filter convergence as a decreasing error covariance per state variable. Here the dark-gray shade represents a $\pm 1\sigma$, and light-gray $\pm 2\sigma$ error to emphasize the degree in magnitude.

Filter innovation ($\bar{z}_k - \bar{z}_{k+1,k}$) is also given (see Figures 8.7 & 8.9), and shows that corrections are all made within the computed sensor error variance (this is not to be confused with the changing error covariance P). Hence, it can be seen as a second opinion on whether the sensor variances were chosen correctly, because these were "guessed" in the absence of available technical sensor specifications.

Now taking in account that some large corrections are applied outside the error variance during stall, and that the filter has properly conversed, there is no reason to doubt the system is malfunctioning using this model profile.

Extended model

Using Van Ingen's kinematic model with the added 13th state variable ($C_{\alpha_{up}}$) and modified observation equations, the extended model can be tested against the Fokker 100 data (see Figures 8.10 & 8.11).

Straight off, it becomes clear (Figures 8.6 & 8.8) this model profile does not work properly. After starting, the filter runs into observability problems, i.e. only 12 out of 13 states are observable. Normally this would break the process loop in the IEKF, but is temporally allowed to continue regardless of this error. And because the UKF by-passes the linearization process, observability issues are not reported. This does not make the UKF filtering to be the correct way, as the IEFK already determined that the system is unobservable. And if UKF was solely ran, this would have to be investigated separately, making the IEKF a better candidate for testing multiple kinematic model profiles.

In a mathematical sense, this points at a possible over-representation of data, i.e. the described system has a numeric character where two states behave similarly. Hence, the over-representation, and the notion that the extended model does not contribute any more useful information. Possibly, research is needed to find parts of the system that can add a unique perspective, so that the observability requirement is satisfied.

Figures 8.10 & 8.11 are added to illustrate the filter conversion regarding the additional up-wash ($C_{\alpha_{up}}$) variable, and to lesser extend the non-existent differences between IEKF and UKF types. What does make these plots interesting, is the effect of stall has on filter conversion. Nonetheless, it should not take this long for convergence to occur, and it should not be dependent on a single event. It's suspected that vane dynamics is erroneously implemented, as the vane itself can not distinguish the up- and side-wash effects from local accelerations. Think of small gusts of wind that do not change influence the general state of the aircraft. This warrants further investigation, but is outside the scope of this thesis.

Important assumptions | Fokker Flight Path Reconstruction

In the foreseeable future, it is best to stick with the simple aerodynamic model using the IEKF method, and build upon this model if the "need' requires it. Note that IEKF has a build in check regarding state observability, although it's nice that UKF does not linearize the state between steps, it does take longer with increasing the number of states, and it needs to be checked for observability issues separately. Any other aerodynamic model extensions should be addressed with care, but by using the profile-system it should easy to switch between experimental models.

- Simplified aerodynamic model (6 states) converges fast, and shows no large errors between measured and optimal state for both vane and boom configurations.
- Filter fails using the Laban equations for vane dynamics, only vane kinematic corrections are applied.
- IEKF shows no significant differences w.rt. UKF filtered data, i.e. optimally estimated states are identical for every recording.
- Sensor specifications are "guessed", i.e. a posteriori.

8.4.1. Plots: Aerodynamic model - IEKF

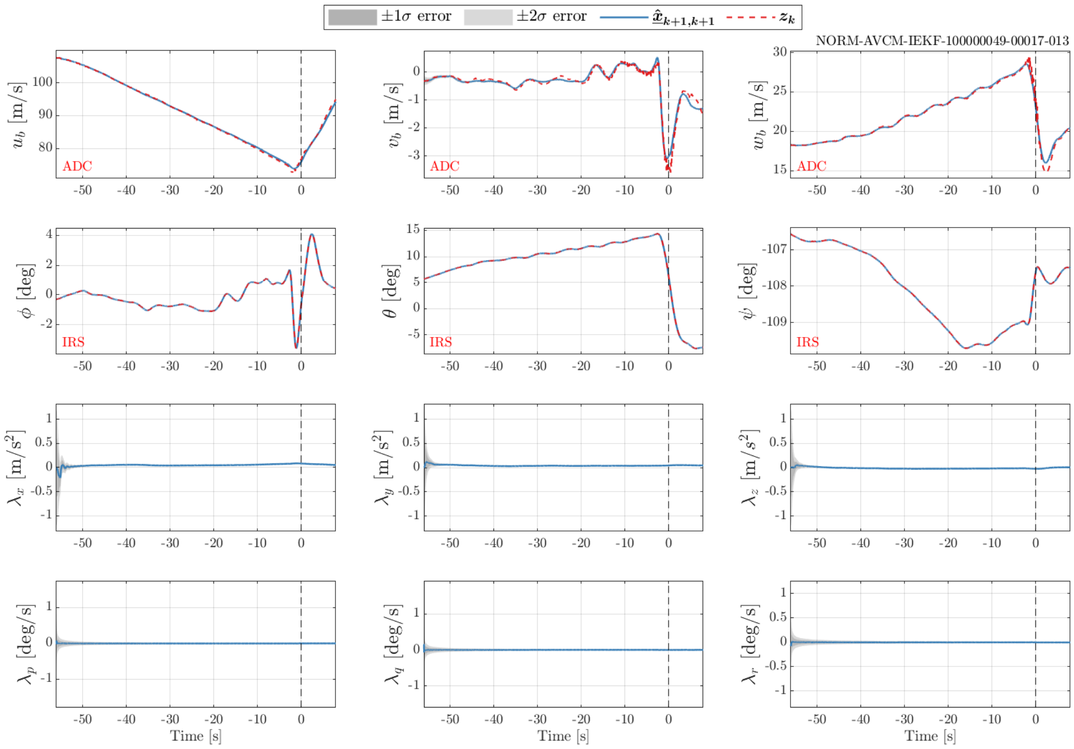

Figure 8.2: FPR Optimal Estimate: IEKF Simple Aero Boom (00017-013)

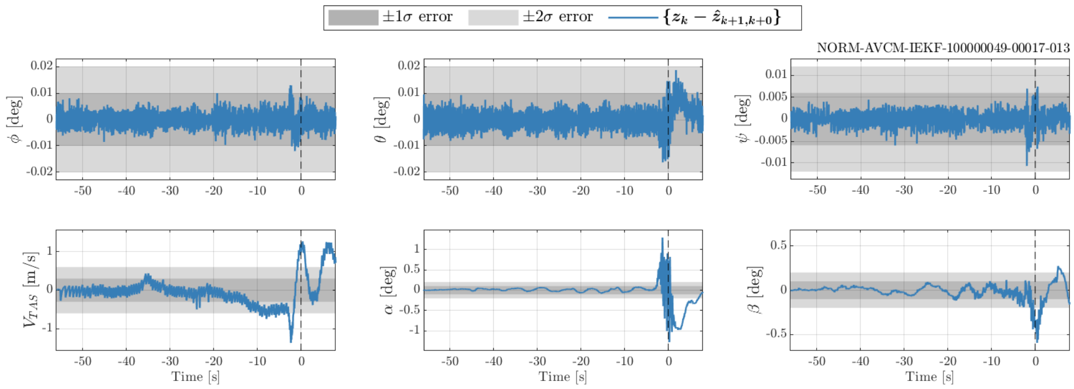

Figure 8.3: FPR Innovation: IEKF Simple Aero Boom (00017-013)

8.4.2. Plots: Aerodynamic model - UKF

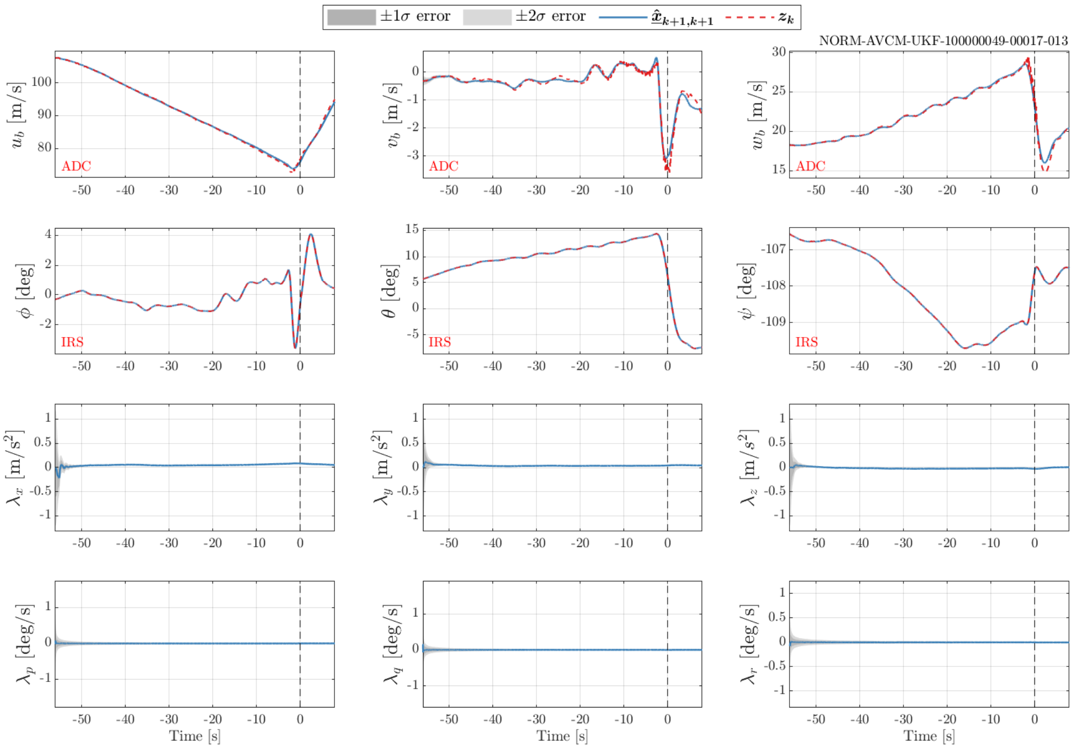

Figure 8.4: FPR Optimal Estimate: UKF Simple Aero Boom (00017-013)

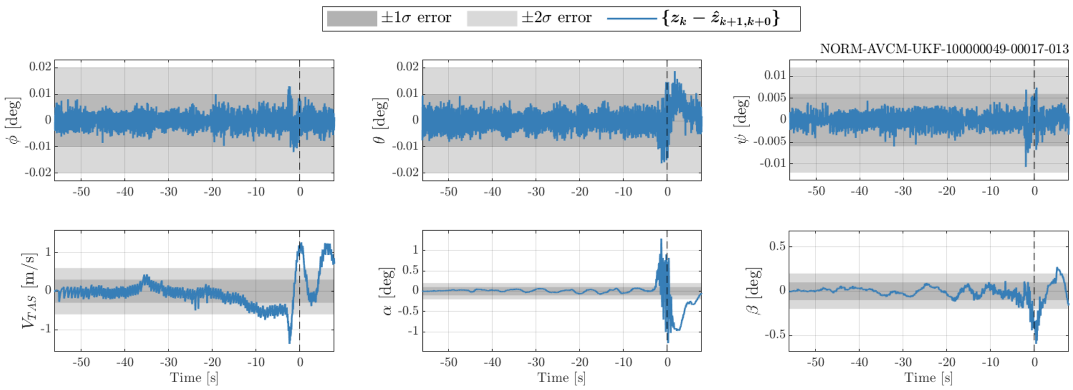

Figure 8.5: FPR Innovation: UKF Simple Aero Boom (00017-013)

8.4.3. Plots: Extended model - IEKF

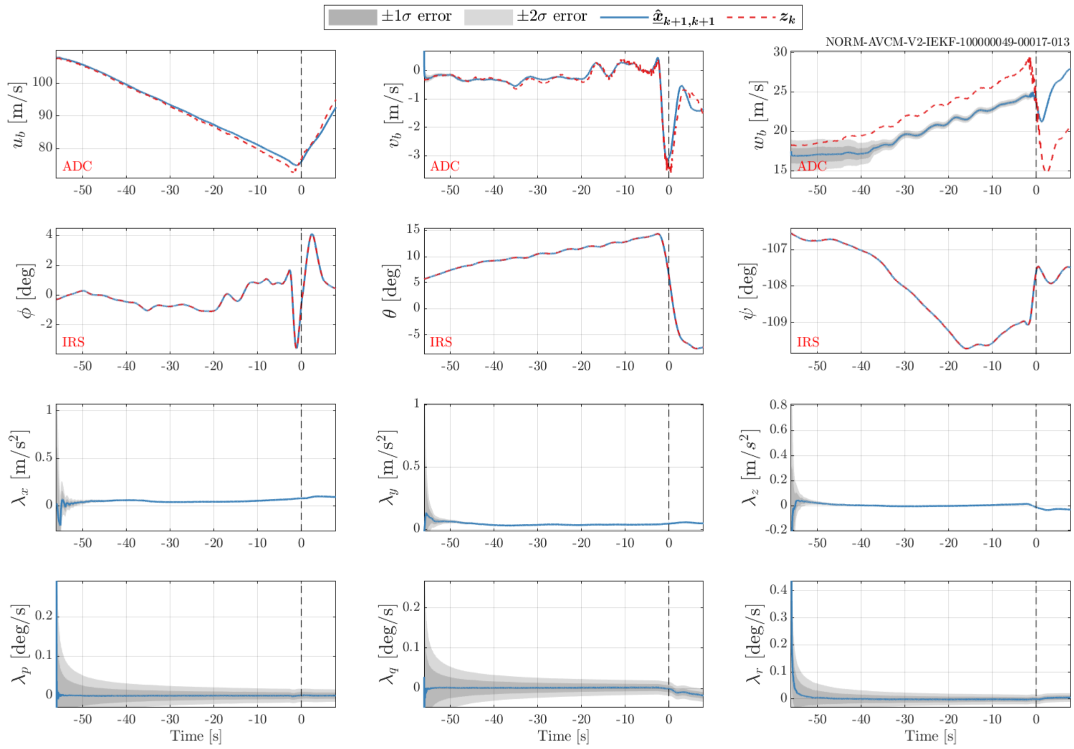

Figure 8.6: FPR Optimal Estimate: IEKF Extended Aero Boom (00017-013)

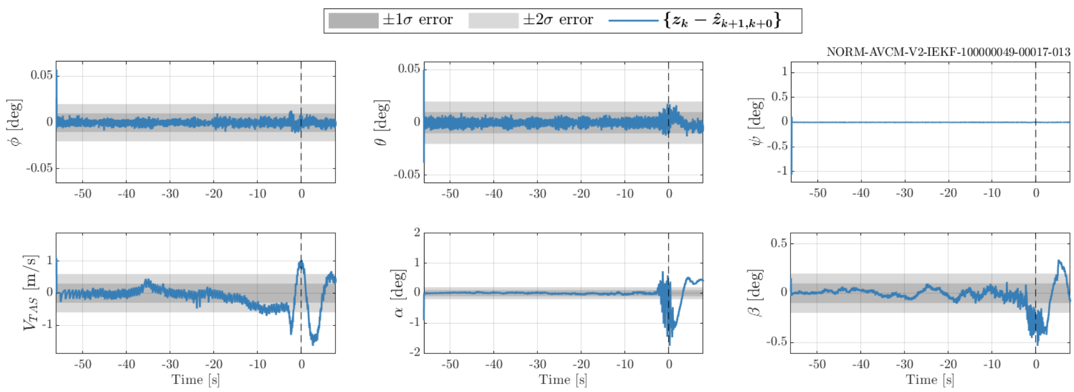

Figure 8.7: FPR Innovation: IEKF Extended Aero Boom (00017-013)

8.4.4. Plots: Extended model - UKF

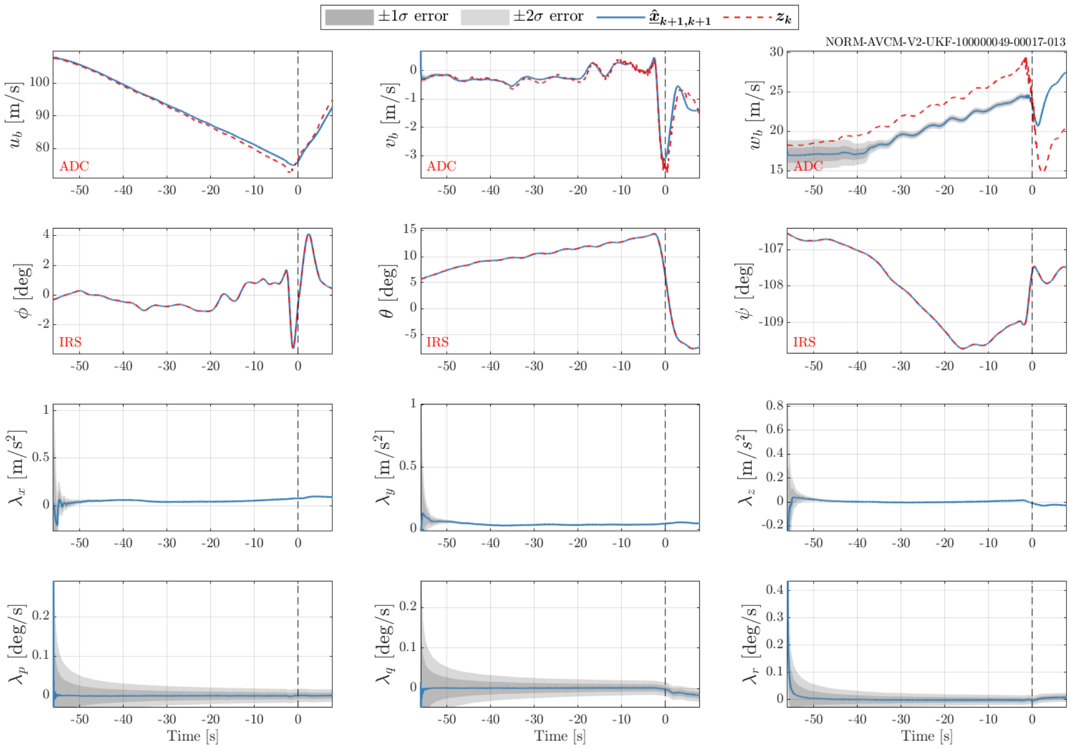

Figure 8.8: FPR Optimal Estimate: UKF Extended Aero Boom (00017-013)

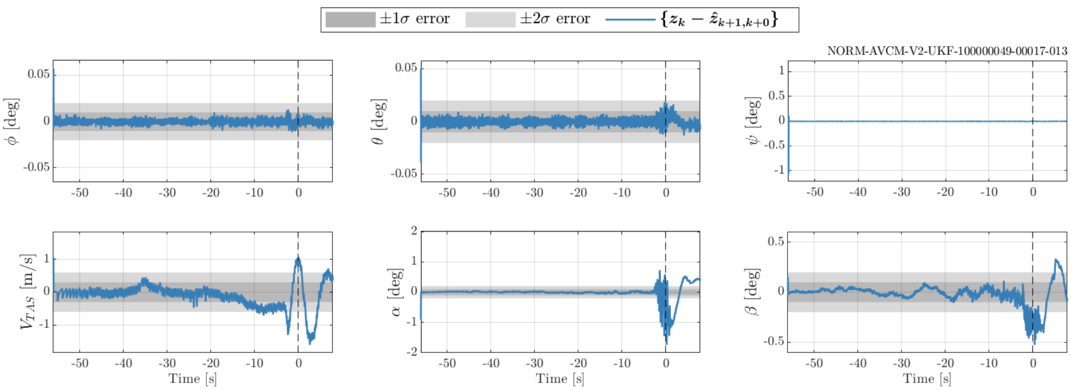

Figure 8.9: FPR Innovation: UKF Extended Aero Boom (00017-013)

8.4.5. Plots: Extended model - Upwash state variable

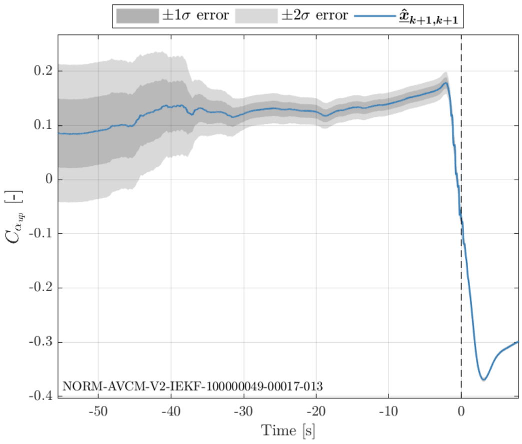

Figure 8.10: FPR Optimal Estimate: IEKF Extended Aero Boom - Upwash $C_{\alpha_{up}}$ (00017-013)

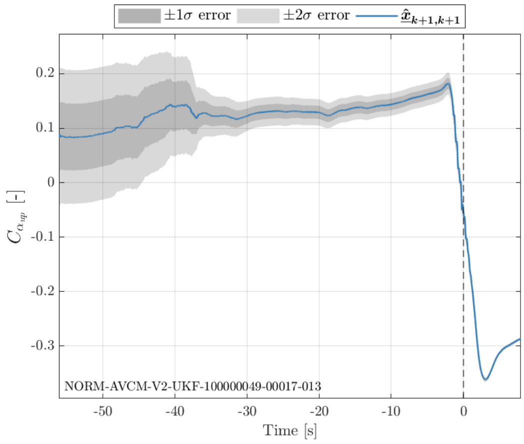

Figure 8.11: FPR Optimal Estimate: UKF Extended Aero Boom - Upwash $C_{\alpha_{up}}$ (00017-013)

8.4.6. Plots: Measurements

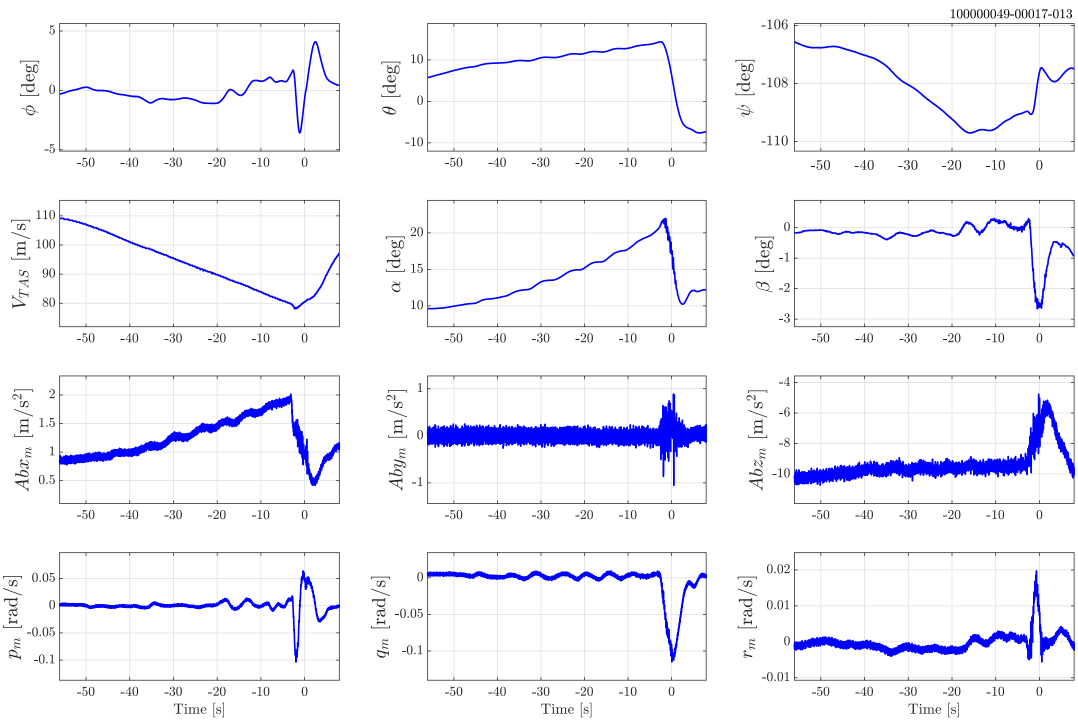

Figure 8.12: FPR Measurement Observations (00017-013)

9

Conclusion & final remarks

This chapter finalizes the thesis by providing a conclusion to the stated research objective with the corresponding questions as given in Chapter 1.1, by means of answering the main research question, and to what extent the objective was met. Alongside the conclusion, some recommendations are presented, with a final remarks section that will end this thesis body of work.

Straight of it can be concluded that the *research objective* was **not** met, *but* very important initial steps were made in the direction to identifying an aerodynamic stall model for the Fokker 100. As the research objective states; ”to obtain a better understanding regarding the influence of a swept-wing aircraft configurations”, it is concluded that this goal was far too pretentious. Although the help from Fokker Service (Dirk van Os especially) was of great importance in supplying relevant information (and greatly appreciated), it was far from being complete, and in many instances lacking in key areas. In other words, a foundation was missing on which solid research could be done, i.e. an absent mass- and engine model with the means to perform a proper flight path reconstruction. These aspects all needed to be researched separately, without any grantee of yielding satisfactory results, and possibly wasting a lot of time (which in hindsight it did).

Hence, towards aerodynamic stall model identification the *main research question* to be answered focuses on determining what is needed to achieve a satisfying result, i.e. that can provide an answer to which a swept-wing configuration has any influence on the current stall model. Under the guise of this notion, true pioneer’s work was done into determining what was actually needed to facilitate stall model research based on historic archived Fokker 100 flight-test data. Therefor, in light of answering the main research question through three sub-questions sequentially as follows.

1. “*In preparation, can the historic flight-test data be properly formatted for research into aerodynamic stall model identification? Where parallel to the available data, do methods exist that properly define; a mass- & engine-model, aiding in executing a reconstruction of the flight path?*”

This thesis proved that the question if flight-test data can be properly formatted for initial research regarding ASMI for the Fokker 100 prototype aircraft. As follows methods were researched and created, compatible with the available Fokker data.

Mass model The mass model was the first hurdle to be tackled, but after extensive research was found to be *very reliable*. This was validated through *both* checking 91 flight test recordings, where very small errors were found in recorded (actual) versus calculated aircraft center of gravity (CG), where 50% of the error ranges between 0.2-1.0%, with a 1.6% maximum error of MAC. And checking the excess weight in recorded versus calculated, where it ranges between -30 and 70 with a maximum around $\pm$150 kilograms.

Also, having Fokker simulator reports available with information about two load cases helped greatly in forming a conclusion regarding the mass model, i.e. containing the actual mass, CG location, and all inertial moments (I_{xx},I_{yy},I_{zz}) plus one product (I_{xz}). This in relation to the previously explained small errors in CG and mass, lead to the belief of having acquired a very reliable method of defining aircraft CG, and it's corresponding inertia.

Important remarks:

- The OEW (65% of MTOW) was relatively easy to determine in availability of the existing inertial measurements done by Fokker regarding the aircraft's static sectional mass elements, where water ballast locations and weights were properly defined (12% of MTOW). Yet a proper fuel model (23% of MTOW) was unavailable, and had to be researched, and modeled according to the available Fokker technical reports. This is an important decision, because in the occurrence of a MTOW situation, fuel compromises for 23% of MTOW.
- Fuel model was optimized by using an algorithm binding the empirically obtained filling form procedure to the estimated metric tank size, modeling "solid" fuel behavior. This neglects sloshing effects, as momentary changes in fuel levels are recorded with a changing angel-of-attack. Furthermore, fuel remain fixed during stall, forcing an equal fuel distribution between wings.
- Important reminder is that this mass model is only valid for the Fokker 100 prototype, because the inertial measurements incorporate onboard testing facilities with a minimal number of crew members present.
- The mass modeling software was written on a first-come-first-serve basis, i.e. what was needed first, was written first. Mainly because no code existed, and STB's regarding calculations concerned with CG / $\mathbf{I}_{CG}$ were incomplete in all possible cases. This makes the written code difficult to read and warrants a rewrite.

Engine model Modeling the engines proved to be more of a challenge. As was pointed out, engine thrust was sparsely calculated, and thus only covered small parts of complete recordings. Recreating the thrust calculations, as was presented by the Fokker STB report, yielded no usable material. As a posteriori data is needed to allow for the many corrections to be applied, accounting for atmospheric conditions to name one. This data is contained in various Fokker tables, which were referenced, but upon inspection showed up empty.

Using an OLS approach (29 training/validation datasets) to find a way around this problem proved to be a good choice, although modeling the right (starboard) engine showed difficulties. It is assumed to be the consequence of poorly exited recording data. It was noticed that the port engine tends to increase in temperature most of the time. And it is suspected that during stall (i.e. at an high angle-of-attack), the airflow rotates a couple degrees. Possibly due to a small pike in angle-of-sideslip, and is assumed to temporally limit airflow into the port engine. This causes a rise in temperature, leading to an excitation with in the data used for the engine parameter estimation. Making the left (port) engine yielding a better model, as can be observed in the VAF analysis.

Hence, this rotation behavior is merely based on an assumption and needs proper investigation. The only thing that has been proven, is that a difference exists between the two engines, where the left (port) engine yields satisfactory results, and right (starboard) is not capable of modeling these changes in temporary values of angle-of-sideslip during stall.

Important remarks:

- Best model performance was observed on the left (port) engine, with best results at altitudes between 5000-5500 meters. This is found for both high (0.8-0.9) R^2 and low RMSE (0.2-0.5kN) values.
- Model performance regarding right (starboard) engine showed low RMSE (0.2-0.5kN) values near the same altitudes, yet R^2 values are close to zero ($\lessapprox 0.2$), indicating a poor fit.

- Only flight-test data was considered regarding quasi-steady stalls in clean configuration, leading to a recommendation for including the remaining flight tests as well. Note that these test are flown in different configurations, and might contain data that excites the right (starboard) engine better.
- Altitude seems to influence the model performance, i.e. grouping of results in the validation data can be observed at incrementing altitudes. Dividing the recording might solve this problem, but then again it also limits the number per used altitude bracket.
- If the left engine turns out to be best modeled using the recordings available for other aircraft configurations, it is recommended to investigate using the left engine model for both engines.

Flight path reconstruction This is the last process needed in the data preprocessing phase, as detailed in the road map (Figure 1.1) to aerodynamic stall model identification. A running Kalman filter was created for both IEKF and UKF types, capable of performing the state estimation needed for the reconstruction of the flight path based on Fokker supplied datasets.

The choice was made to simplify the navigation and observation system, creating a basic (6 state) aerodynamic model. This was primarily done, because attempting to recreated GPS datasets based on dead-reckoning calculations failed. No reason could be found as to why a seemingly correct GPS datasets broke the model, leading to aggressive diverging errors in covariance.

A second hindrance manifested itself in the form of Laban's air-data boom state variables. As was already mentioned by Van Ingen, extending the filter model with Laban lead to all sort of difficulties in the realm of correlating state variables, problems with filter convergence, and observability. This was tested by extending the aerodynamic filter model with Laban's air-data boom equations with only the up-wash ($C_{\alpha_{up}}$) state variable.

Running the IEKF on the extended (7 state) model immediately showed observability warning signs, as the IEKF internally checks the local nonlinear observability on every measurement step. The UKF process does not have this special integrity attribute, as the UKF is specifically designed to by-pass linearization on every step. This makes the UKF robust in the sense of poorly chosen (initial) noise conditions, but requires a separate observability analysis. This means that setting up a new filter model, it is recommended to only use IEKF in the initial research phase, and only when one is absolutely sure no observability problems exist. Doing so, limits the possibility of errors entering the system, and adds integrity. Note that in light of these observability issues, the extended model does converge during the stall. This hints at different existing conditions at the actual stall event, allowing for a possible temporary local observability. Because this was not researched, it is recommended for future research to look into.

As for the aerodynamic (6 state) model, it performed without any filter convergence issues. Thus providing a good foundation to build upon for continued research into ASMI for the Fokker 100. Although GPS equations were omitted from the filter model, it is suspected that ”minor” issues exist that still have to be found, allowing for extending the aerodynamic model by three states. This in theory might adjust for wind conditions to be filtered correctly, as Fokker does supply calculated wind values next to IRS measured dead-reckoning variables ground-speed (V_G), and true heading (ψ_{true}).

Important remarks:

- Sensor noise characteristics were guessed, i.e. estimated from taking small pieces of data during quasi-steady flight.
- Aerodynamic filter model is recommended to build upon for future research.
- Research should only be done using the IEKF method, due to internal integrity regarding system observability issues.

2. "*Can the current aerodynamic stall model be properly applied to identify, verify, and validate (including both longitudinal and lateral-directional dynamics), changes in control surface effectiveness, and dynamic effects by current stall identification methods, in regard to recent research done using Cessna Citation II as a test-bed?*"

Due to this project being considered a pioneers endeavor, it was cut short in light of having the initial data preparation phase costing too much time, i.e. plus nine months. Therefore, no attempt was made in regard to the estimation of aerodynamic model parameters, and is left to the next person in line to answer.

3. "*What new model structure can be proposed through means of augmenting the current stall model allowing for swept-wing analysis, and optimization in model quality?*"

As to the second question, the third remains unexplored. It is the most interesting question this thesis was initially set on to analyze, but did not see the light of day due to the large amount of time it took, and the shear number of parts needed to be created in the data preparation phase. As a recommendation for future research, and as possible step in the right direction. The following is given ...

Early on during the literature study, it was found that the main measurements influencing stall behavior were considered to be the angle-of-attack (α) and the free-stream Mach number (M_∞), subsequently these were used in attempting to find more research material as they were considered to be relevant factors of influence. Inadvertently, literature was stumbled upon by the late prof. Richard Shevell (Stanford), who had done extensive research in modeling aerodynamic behavior regarding swept-wing configurations. He was able to create a relationship between the longitudinal rate of angle-of-attack parameter (C_{L_α}), and angle-of-attack (α), Mach number (M_∞), wing-sweep (Λ) (briefly explained in Appendix A).

It must come as no surprise that it is recommended for future research to determine if this relationship can provide relevant information regarding the influence of sweep on the aerodynamic stall model, as Shevell's equations seems to contain a vital link between wing-sweep and the longitudinal aerodynamic stall model identification for lift forces. Hence, and might even hold more relevant relationships to be explored.

Bibliography

[1] R.J.M. Bennis. *Non-linear State Estimation Techniques with Application to Dynamic Modelling of Angle of Attack Vane from Cessna Citation II Flight Data*. Msc thesis, Delft University of Technology, Delft, The Netherlands, 1998.

[2] A. J. Buchner and J. Soria. Measurements of the flow due to a rapidly pitching plate using time resolved high resolution PIV. *Aerospace Science and Technology*, 44:4–17, 2015. ISSN 12709638. doi: 10.1016/j.ast.2014.04.007. URL http://dx.doi.org/10.1016/j.ast.2014.04.007.

[3] Abel John Buchner, Julio Soria, Damon Honnery, and Alexander J. Smits. Dynamic stall in vertical axis wind turbines: Scaling and topological considerations. *Journal of Fluid Mechanics*, 841:746–766, 2018. ISSN 14697645. doi: 10.1017/jfm.2018.112.

[4] Tony Burton, David Sharpe, Nick Jenkins, and Ervin Bossanyi. *Wind Energy Handbook*. John Wiley and Sons, Ltd., 2001. ISBN 978-0-471-48997-9.

[5] D.A. Crider. The Need for Upset Recovery Training. In *AIAA Modeling and Simulation Technologies Conference and Exhibit*, number August, pages 1–18, 2008. ISBN 9781600869624. doi: AIAA-2008-6864.

[6] D.A. Crider and J.V. Foster. Simulation modeling requirements for loss-of-control accident prevention of turboprop transport aircraft. In *AIAA Modeling and Simulation Technologies Conference 2012*, 2012. ISBN 9781624101830. doi: doi:10.2514/6.2012-4569.

[7] C.C. De Visser. *Model Identification*. Number Figure 2. 2011. ISBN 9789085707707. URL http://resolver.tudelft.nl/uuid:6bc0134a-0715-4829-903d-6479c5735913.

[8] J.N. Dias. Unsteady and Post-Stall Model Identification Using Dynamic Stall Maneuvers. *AIAA Atmospheric Flight Mechanics Conference*, (June):1–15, 2015. doi: 10.2514/6.2015-2705. URL http://arc.aiaa.org/doi/10.2514/6.2015-2705.

[9] K. Dullemond and K. Peeters. *Introduction to Tensor Calculus*. Booklet, 2010. doi: 10.2307/3616869.

[10] D. Fischenberg. Identification of an Unsteady Aerodynamic Stall Modell from Flight Test Data. In *20th Atmospheric Flight Mechanics Conference*, pages 138–146, 1995. ISBN 9780000000002. doi: 10.2514/6.1995-3438.

[11] D. Fischenberg and R.V. Jategaonkar. Identification of Aircraft Stall Behavior from Flight Test Data. *RTO Systems Concepts and Integration Panel (SCI) Symposium*, 11(May):5–7, 1998. doi: 10.2514/6.1995-3438. URL http://scholar.google.com/scholar?hl=en{&}btnG=Search{&}q=intitle:Identification+of+aircraft+stall+behavior+from+flight+test+data{#}0.

[12] Fokker Aircraft Company. Specification of FDVS Standard Calculations for the Fokker F28 MK0100 (SERIE). Technical Manual DAS-100-011, FAC/EFFS/DA, Schiphol, The Netherlands, 1992.

[13] Fokker Aircraft Company. Specification of FDVS Standard Calculations for the Fokker F28 MK0070 (PROTO). Technical Manual DAS-070-005, FAC/EFFS/DA, Schiphol, The Netherlands, 1994.

[14] Fokker Aircraft Company. Specification of FDVS Standard Calculations for the Fokker F28 MK0100 (SERIE). Technical Manual DAS-100-012, FAC/EFFS/DA, Schiphol, The Netherlands, 1994.

[15] Fokker Aircraft Company. Weight and Balance Manual. Technical manual WBM100 v21 Alliance Airlines, Fokker Services B.V., Schiphol, The Netherlands, dec 2017.

[16] Fokker Aircraft Company. Aircraft Operating Manual. Technical manual 59-020, Fokker Services B.V., Schiphol, The Netherlands, 2018.

[17] M.G. Goman and A.N. Khrabrov. State-space representation of aerodynamic characteristics of an aircraft at high angles of attack. *Journal of Aircraft*, 31(5):1109–1115, 1994. ISSN 0021-8669. doi: 10.2514/3.46618. URL http://arc.aiaa.org/doi/10.2514/3.46618.

[18] J. Hartikainen, A. Solin, and S. Särkkä. Optimal Filtering with Kalman Filters and Smoothers. Technical report, Aalto University School of Science, Espoo, Finland, 2011.

[19] S. Haykin. *Kalman Filters and Neural Networks*, volume 5. John Wiley and Sons, Ltd., Hamilton, Ontario, Canada, 2001. ISBN 0471369985. doi: 10.1002/0471221546.

[20] K.G. Hecks. The High-speed Shape. *Flight International*, (January):13, 1964.

[21] Th. Heikens and A.J.R. van Zon. Water in ballast tanks, moments and moments of inertia of the prototypes F28 MK0100. Technical report E100-029, Fokker Aircraft Company, Schiphol, The Netherlands, 1987.

[22] Mia Hubert and Stephan Van der Veeken. Outlier detection for skewed data. *Chemometrics*, 22 (3-4):235–246, 2008. doi: 10.1002/cem.1123.

[23] H. H Hurt Jr. *Aerodynamics for Naval Aviators*. Number January. Naval Air Systems Command, 1965. ISBN 156027140X. URL http://citeseerx.ist.psu.edu/viewdoc/download?doi=10.1.1.261.2132{&}rep=rep1{&}type=pdf.

[24] M. Hwang and J.H. Seinfeld. Observability of Nonlinear Systems. *Journal of Optimization Theory and Applications*, 10(2), 1972.

[25] Jane's Information Group. Fokker 100, 2018. URL https://janes.ihs.com/Janes/Display/jau{_}0974-jau.

[26] Jane's Information Group. Rolls-Royce Tay, 2018. URL https://janes.ihs.com/Janes/Display/jae{_}0538-jae.

[27] Joint Aviation Authorities. Stalls. *Joint Aviation Requirements 25 - Large Aeroplanes*, Change 13 (5 October 1989):1B15–1B16, 1989.

[28] S.J. Julier. The scaled unscented transformation. In *American Control Conference (IEEE Cat.No.CH37301)*, number 2, pages 4555–4559, 2002. doi: 10.1109/acc.2002.1025369.

[29] R.E. Kalman. A New Approach to Linear Filtering and Prediction Problems. *Transactions of the ASME - Journal of Basic Engineering*, 82(Series D):35–45, 1960.

[30] E. Kors. Thrust bepaling op serie F100 A/C. Technical report, Fokker Aircraft Company, Schiphol, The Netherlands, 1989.

[31] E. Kreyszig, H. Kreyszig, and E.J. Norminton. *Advanced Engineering Mathematics*. L. Rosatone, Columbus, Ohio, 10th edition, 2011. ISBN 978-0-470-45836-5.

[32] M. Laban. *On-Line Aircraft Aerodynamic Model Identification*. Phd thesis, Delft University of Technology, 1994.

[33] A.A. Lambregts, G. Nesemeier, R.L. Newman, and J.E. Wilborn. Airplane Upsets: Old Problem, New Issues. In *AIAA Modeling and Simulation Technologies Conference and Exhibit*, number August, pages 1–10, 2008. ISBN 978-1-62410-000-0. doi: 10.2514/6.2008-6867. URL http://arc.aiaa.org/doi/10.2514/6.2008-6867.

[34] W. J. McCroskey. UNSTEADY AIRFOILS. *Annual Review of Fluid Mechanics*, 14:285–311, 1982. ISSN 00664189. doi: 10.1146/annurev.fl.14.010182.001441.

[35] J.J. Moré and D.C. Sorensen. Computing a Trust Region Step. *SIAM Journal on Scientific and Statistical Computing*, 4(3):553–572, 1983.

[36] E.A. Morelli, K. Cunningham, and M.A. Hill. Global Aerodynamic Modeling for Stall/Upset Recovery Traning Using Efficient Piloted Flight Test Techniques. 2013.

[37] J.A. Mulder, Q.P. Chu, J.K. Sridhar, J.H. Breeman, and M. Laban. Non-linear aircraft flight path reconstruction review and new advances. *Progress in Aerospace Sciences*, 35(7):673–726, 1999. ISSN 03760421. doi: 10.1016/S0376-0421(99)00005-6.

[38] J.A. Mulder, W.H.J.J. van Staveren, J.C. van der Vaart, and E. de Weerdt. AE3-302 Flight Dynamics. Lecture notes, Delft University of Technology, Delft, 2007.

[39] Joseph B. Nagel and Bruno Sudret. Bayesian multilevel model calibration for inverse problems under uncertainty with perfect data. In *Journal of Aerospace Information Systems*, volume 12, pages 97–113, Zürich, 2015. doi: 10.2514/1.I010264.

[40] R.K. Nangia. Efficiency parameters for modern commercial aircraft. *Aeronautical Journal*, 110 (1110):495–510, 2006. ISSN 00019240. doi: 10.1017/S0001924000001391.

[41] National Transportation Safety Board. Crash During Approach to Landing Circuit City Stores, Inc. Cessna Citation 560, N500AT Pueblo, Colorado February 16, 2005. Aircraft accident report, National Transportation Safety Board, Washington, D.C., 2005. URL https://www.ntsb.gov/investigations/AccidentReports/Pages/AAR0702.aspx.

[42] National Transportation Safety Board. Accident Report Loss of Control On Approach Colgan Air Flight 3407, Bombardier DHC-8-400, N200WQ Clarence Center, New York February 12, 2009. Aircraft accident report, National Transportation Safety Board, Washington, D.C., 2010. URL http://www.ntsb.gov/investigations/summary/AAR1001.html.

[43] National Transportation Safety Board. Crash During Experimental Test Flight Gulfstream Aerospace Corporation GVI (G650), N652GD Roswell, New Mexico April 2, 2011. Aircraft accident report, National Transportation Safety Board, Washington, D.C., 2011. URL https://www.ntsb.gov/investigations/AccidentReports/Pages/AAR1202.aspx.

[44] National Transportation Safety Board. Annual Review 2013 - Data and Statistics. Technical report, US Government, 2013.

[45] National Transportation Safety Board. Aerodynamic Stall and Loss of Control During Approach Embraer EMB-500, N100EQ Gaithersburg, Maryland December 8, 2014. Aircraft accident report, National Transportation Safety Board, Washington, DC, 2014. URL https://www.ntsb.gov/investigations/AccidentReports/Pages/aar1601.aspx.

[46] Ed Obert. Fokker 100 - Aerodynamic data. Technical Report L-28-336, Fokker Aircraft Company, Schiphol, The Netherlands, 1991.

[47] Ed Obert. *Aerodynamic Design of Transport Aircraft*. Delft University Press, Delft, 2009. ISBN 9781467324755.

[48] G.J. Olsder, J.W. van der Woude, J.G. Maks, and D. Jeltsema. *Mathematical Systems Theory*. VSSD, Delft, 2011. ISBN 978-9065622808.

[49] A. Pytel, J. Kiusalaas, and I. Sharma. *Enignering Mechanics - Dynamics*. Global Engineering Program: Christopher M. Shortt, State College, third edition, 2010. ISBN 9780495295631.

[50] J.R. Raol, G. Girija, and J. Singh. *Modelling and Parameter Estimation of Dynamic Systems*. The Institution of Engineering and Technology, London, 2004. ISBN 9780863413636. doi: 10.1049/PBCE065E. URL http://digital-library.theiet.org/content/books/ce/pbce065e.

[51] H.E. Rauch, F. Thung, and C.T. Striebel. Maximum likelihood estimates of linear dynamic systems. *AIAA Journal*, 3(8):1445–1450, 1965.

[52] E. J. Ray and R. T. Taylor. A systematic study of the factors contributing to post-stall longitudinal stability of T-tail transport configurations. Technical report, NASA, Hampton, VA, United States, 1965.

[53] Peter J. Rousseeuw, Ida Ruts, and John W. Tukey. The Bagplpot: A Bivariate Boxplot. *The American Statistician*, 53(4):382–387, 1999. doi: 10.1080/00031305.1999.10474494. URL https://www.researchgate.net/publication/247788661{_}The{_}Bagplot{_}A{_}Bivariate{_}Boxplot.

[54] S. Särkkä. Unscented Rauch-Tung-Striebel Smoother. *IEEE Transactions on Automatic Control 53*, 53(3):845–849, 2008. ISSN 00189286. doi: 10.1109/TAC.2008.919531.

[55] R.S. Shevell. *Fundamentals of Flight*. Prentice Hall, Inc., second edition, 1989. ISBN 0-13-339060-8.

[56] B.O.S. Teixeira, L.A.B. Torres, P. Iscold, and L.A. Aguirre. Flight path reconstruction - A comparison of nonlinear Kalman filter and smoother algorithms. *Aerospace Science and Technology*, 15(1): 60–71, 2011. ISSN 12709638. doi: 10.1016/j.ast.2010.07.005. URL http://dx.doi.org/10.1016/j.ast.2010.07.005.

[57] W. Tosserams. EPR rating for F100 TAY620-15 / 650-15. Technical report, Fokker Aircraft Company, Schiphol, The Netherlands, 1992.

[58] E. Trubshaw. Low Speed Handling with Special Reference to the Super Stall. *Journal of the Royal Aeronautical Society*, 70(667):695–704, 1966. doi: 10.1017/S0001924000057110.

[59] L.R. Turner. Inverse of the Vandermonde matrix with applications. Nasa technical note, Lewis Research Center, Cleveland, Ohio, 1966. URL http://ntrs.nasa.gov/archive/nasa/casi.ntrs.nasa.gov/19660023042.pdf.

[60] R. Van Uden. General arrangement with main data : Fokker 100 (F28-MK0100). Technical Report A, Fokker Aircraft Company, Schiphol, The Netherlands, 1992.

[61] T. Van de Broek. Engine calibration and configuration kneepads REN-3. Technical Report 1, Fokker Aircraft Company, Schiphol, The Netherlands, 1992.

[62] M.A. Van den Hoek. *Design, Identification and Implementation of a High-Fidelity Cessna Citation II Flight Simulation Model*. Master thesis, Delft University of Technology, 2016. URL http://resolver.tudelft.nl/uuid:21a284df-7ada-4e3c-9ff2-2d73cc04f534.

[63] J.M. Van der Laan. Engine performance software specifications for Rolls Royce Tay engine. Technical Report 2, Fokker Aircraft Company, Schiphol, The Netherlands, 1987.

[64] J.N.A. Van Eijndhoven. *Buffet envelope prediction of transport aircraft during the conceptual design phase*. Master thesis, Delft University of Technology, 2012. URL http://resolver.tudelft.nl/uuid:72dedb79-680c-4488-92bb-3fd962e901bb.

[65] L.J. Van Horssen. *Aerodynamic Stall Modeling for the Cessna Citation II*. Master thesis, Delft University of Technology, 2016. URL http://resolver.tudelft.nl/uuid:7de36b4e-32b5-4da7-836b-c8fa40eb254e.

[66] L.J. Van Horssen, C.C. De Visser, and D.M. Pool. Aerodynamic Stall and Buffet Modeling for the Cessna Citation II Based on Flight Test Data. In *AIAA Modeling and Simulation Technologies Conference*, 2018. doi: 10.2514/6.2018-1167. URL http://arc.aiaa.org.

[67] J.B. Van Ingen. *Dynamic Stall Modeling for the Cessna Citation II*. Master thesis, Delft University of Technology, 2017. URL http://resolver.tudelft.nl/uuid:f76439ef-ab2a-4173-8d78-3122a2696e91.

[68] J.B. Van Ingen, C.C. De Visser, and D.M. Pool. Stall Model Identification of a Cessna Citation II from Flight Test Data Using Orthogonal Model Structure Selection. *Journal of Aircraft. In preparation*, 2017.

[69] O. van Viersen, H. Riebeek, and H.N. Themmen. Fokker 100. Provisions for installation of instrumentation in the test aircrafts. Technical report DAS-100-001-5, Fokker Aircraft Company, Schiphol, The Netherlands, 1988.

[70] H.W. Verbeek. Technical design of Rolls Royce Tay engine analysis software (NLR). Technical Report 1, Fokker Aircraft Company, Schiphol, The Netherlands, 1986.

[71] B.L. Walcott, M.J. Corless, and S.H. Zak. Comparative study of non-linear state-observation techniques. *International Journal of Control*, 45(6):2109–2132, 1987. ISSN 13665820. doi: 10.1080/00207178708934019.

[72] E.A. Wan and R. van der Merwe. The Unscented Kalman Filter for Nonlinear Estimation. *Technology*, v:153–158, 2000. ISSN 15270297. doi: 10.1109/ASSPCC.2000.882463. URL `http://ieeexplore.ieee.org/xpls/abs{_}all.jsp?arnumber=882463`.

[73] J.H. Zwarts, W.J. Van Hooff, and G. Keuken. Fokker 100 Load cases. Technical report G.o.-100-102, Fokker Aircraft Company, Schiphol, The Netherlands, 1986.

III

Appendices

A

Sweep angle analysis

Prandtl-Glauert model augmentation

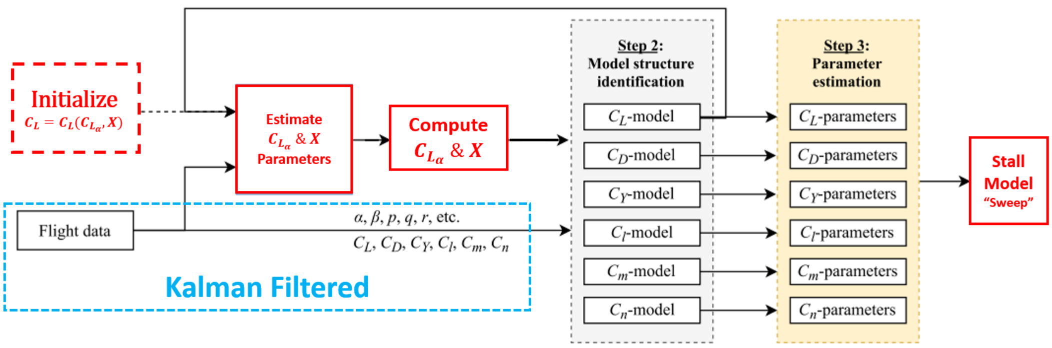

Figure A.1: Prandtl-Glauert augmented aerodynamic stall model orthogonal structure selection procedure.

Combination of wing lift curve for a finite straight wing with a Prandtl-Glauert approximation for sweep-back effects based on Shevell's research [55].

$$C_{L_\alpha} = \frac{2\pi AR}{2 + \sqrt{\left(AR^2/\eta^2\right)\left(1 + \tan^2\Lambda - M_\infty^2\right) + 4}} \tag{A.1}$$

Define a new addition to structure with C_{L_α} as a base regressor.

$$\hat{C}_L = \hat{C}_L\left(C_{L_\alpha}, X\right) \tag{A.2}$$

,where $X = X\left(a_1, \alpha^*\tau_1, \tau_2\right)$ and $C_{L_\alpha} = C_{L_\alpha}\left(AR, \eta, +4, M_\infty\right)$.

Recall the "one-time" nonlinear estimation of the X-variable, and augment the dynamic model for lift with $C_{L_\alpha} = C_{L_\alpha}\left(AR, \eta, +4, M_\infty\right)$.

$$\hat{C}_L = C_{L_0} + C_{L_\alpha}\left\{\frac{1+\sqrt{1+X}}{2}\right\}^2 \alpha + C_{L_q} q \frac{\bar{c}}{V} \tag{A.3}$$

Proposal for solution

1. Break both X & C_{L_α} in two parts, and analyze independently.
2. Combine X & C_{L_α}, e.g. use a Bayesian Multilevel Model Calibration to estimate all fixed parameters [39].

B

Aircraft frames of reference

B.1. Vehicle frame

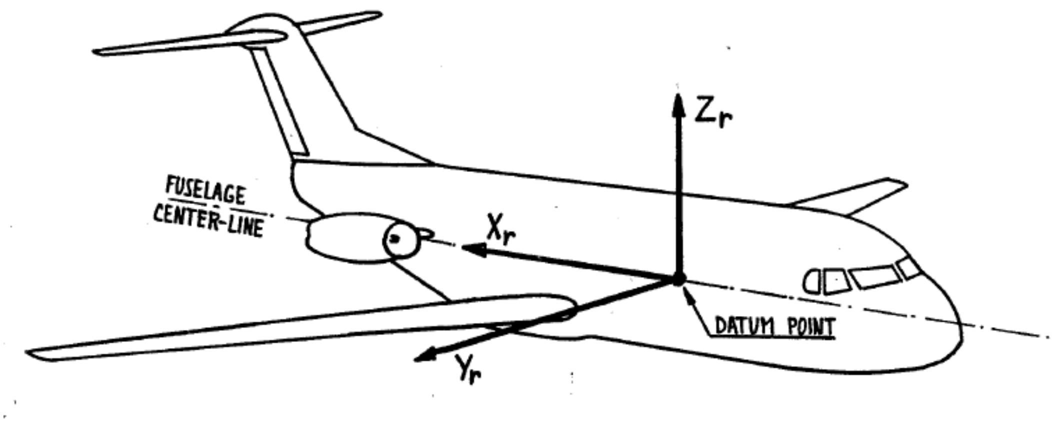

Figure B.1: Vehicle reference frame F_r of the Fokker 100 (Proto/Series) aircraft. Adapted from Fokker 100 Aerodynamic Data[46].

Table B.1: Frames of reference regarding the Fokker 100 (Proto/Series) aircraft.

Frame	Name			Origin	X-Axis	Y-Axis	Z-Axis
		X_W [mm]	Y_W [mm]	Z_W [mm]			
F_W	Vehicle-Nose	0	0	0	AFT	RIGHT	UP
F_r	Vehicle (0% MAC)	15799	0	0	AFT	RIGHT	UP
$F_{r,40}$	Vehicle-40 (40% MAC)	17332	0	0	AFT	RIGHT	UP
F_{FUS}	Fuselage	17332	0	0	AFT	LEFT	DOWN
$F_{WNG\text{-}R}$	Wing (Right)	16334	0	-965	AFT	LEFT	DOWN
$F_{WNG\text{-}L}$	Wing (Left)	16334	0	-965	AFT	LEFT	DOWN
F_{VSB}	Vertical Stabilizer	29957	0	1575	AFT	LEFT	DOWN
$F_{HSB\text{-}R}$	Horizontal Stabilizer (Right)	32801	0	4461	AFT	LEFT	DOWN
$F_{HSB\text{-}L}$	Horizontal Stabilizer (Left)	32801	0	4461	AFT	LEFT	DOWN
$F_{ENG\text{-}R}$	Engine (Right)	23607	2681	400	AFT	LEFT	DOWN
$F_{ENG\text{-}L}$	Engine (Left)	23607	-2681	400	AFT	LEFT	DOWN
F_{NUC}	Nose Under Carriage	3770	0	-1540	AFT	LEFT	DOWN
$F_{MUC\text{-}R}$	Main Under Carriage (Right)	17649	0	-965	AFT	LEFT	DOWN
$F_{MUC\text{-}L}$	Main Under Carriage (Left)	17649	0	-965	AFT	LEFT	DOWN

B.2. Kinematic frame

The kinematic frame is spanned by three axis systems contained within the vehicle frame, i.e. the body F_b, aerodynamic F_a and vehicle carried normal earth F_O frames of reference , with their respective origins relative to the vehicles center of gravity G. Per convention, the all axis systems are rectangular and right-handed. Vehicle movements are expressed in the normal earth-fixed F_E axis system. A moment (or a rotation) about an axis is vectorialy wise positive in the positive direction of a specific axis [38, 46].

B.2.1. Normal earth-fixed

The normal earth-fixed axis-system $\mathrm{F_E}$ ($OX_EY_EZ_E$) has its reference frame fixed to the earth. The $\mathrm{X_EY_E}$-plane is tangent to the earth's surface with its origin chosen to exist at an arbitrary location. The $\mathrm{X_E}$-axis is directed towards the north, $\mathrm{Y_E}$-axis towards the east (i.e. rotated 90 degrees to the right) and the $\mathrm{Z_E}$ is aligned with the direction of the gravity vector.

Furthermore, it should be noted that for this thesis the origin O position is set to zero due to the absence of the flight-test track coordinates. And as a result of this, the earth's surface is considered to be a straight plane (i.e. no curvature), neglecting dynamic effects due to the earth's rotation (e.g. Coriolis). All velocities and acceleration acting on the origin O are considered to be equal to zero and remain static.

B.2.2. Vehicle carried normal earth axis

The vehicle carried normal earth axis-system $\mathrm{F_O}$ ($GX_OY_OZ_O$) as the name suggest carries the vehicle, where its origin coincides with the aircraft's center of gravity G. Axes attitude between F_O and F_E remains unchanged, with the only distinction of having the origin's position G expressed in F_E.

B.2.3. Body axis

The body axis $\mathrm{F_b}$ ($GX_bY_bZ_b$) is fixed to the aircraft, has its origin located at the vehicle's center of gravity G and is considered to be a right-handed orthogonal axis-system. The $\mathrm{X_b}$-axis is aligned parallel to the fuselage's center-line, directed positive towards the vehicle's nose, $\mathrm{Y_b}$-axis is perpendicular to the plane of symmetry of the aircraft and positive in starboard direction, and $\mathrm{Z_b}$-axis is aligned perpendicular to the $\mathrm{X_bY_b}$-plane downwards (i.e. towards the aircraft's belly).

Attitude of the aircraft's body axis $\mathrm{F_b}$ is expressed relative to the vehicle carried normal earth axis-system $\mathrm{F_O}$ in terms three consecutive rotations between four frames starting in $\mathrm{F_O}$ as follows $F_O \rightarrow F_{O'} \rightarrow F_{O''} \rightarrow F_b$, where:

1. Heading angle ψ, rotation around positive $\mathrm{Z_O}$-axis, where $-\pi < \psi < \pi$.
2. Pitch angle θ, rotation around positive $\mathrm{Y_{O'}}$-axis, where $-\pi/2 < \theta < \pi/2$.
3. Roll angle ϕ, rotation around positive $\mathrm{X_b}$-axis (= $\mathrm{X_{O''}}$-axis), where $-\pi < \phi < \pi$.

B.2.4. Aerodynamic axis

The aerodynamic axis-system $\mathrm{F_a}$ ($GX_aY_aZ_a$), also known as the air-path, is coupled to the direction vector V of the true airspeed V_{TAS}, and is defined as the velocity of the center of gravity G relative to the undisturbed air[38]. Hence the aerodynamic axis-system is right-hand and orthogonal The $\mathrm{X_a}$-axis is defined to be aligned along the direction of true airspeed V_{TAS}, $\mathrm{Z_a}$-axis is situated in the aircraft's symmetry plane (e.g. GX_bZ_b) and $\mathrm{Y_a}$-axis is situated to be aligned perpendicular to the $\boldsymbol{GX_aZ_a}$-plane.

Attitude of aerodynamic axis F_a is expressed relative to the body axis-system F_b in two consecutive rotations between three frames starting in F_b as follows $F_b \rightarrow F_{b'} \rightarrow F_a$, where:

1. Negative rotation using the angle of attack α, i.e. $-\alpha$ about the $\mathrm{Y_b}$-axis, where $-\pi < \alpha < \pi$.

2. Positive rotation using the sideslip angle β about the Z_a-axis (= $Z_{b'}$-axis), where $-\pi/2 < \alpha < \pi/2$.

B.2.5. Control-surface deflection sign conventions

Aircraft response due to control-surface deflection (i.e. ailerons, elevator and rudder)

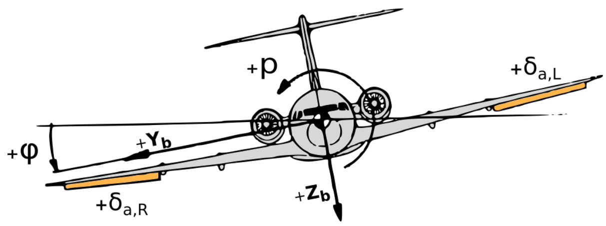

Figure B.2: Aileron deflection sign convention in the body axis frame F_b of reference. Modified and adapted from Fokker technical report[46].

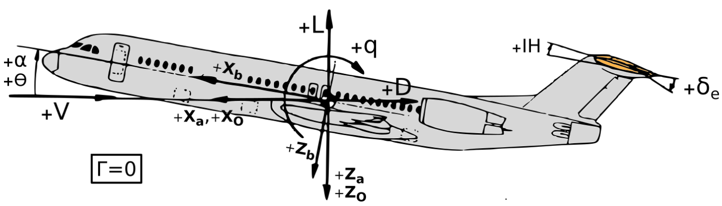

Figure B.3: Elevator deflection sign convention in the body axis frame F_b of reference. Modified and adapted from Fokker technical report[46].

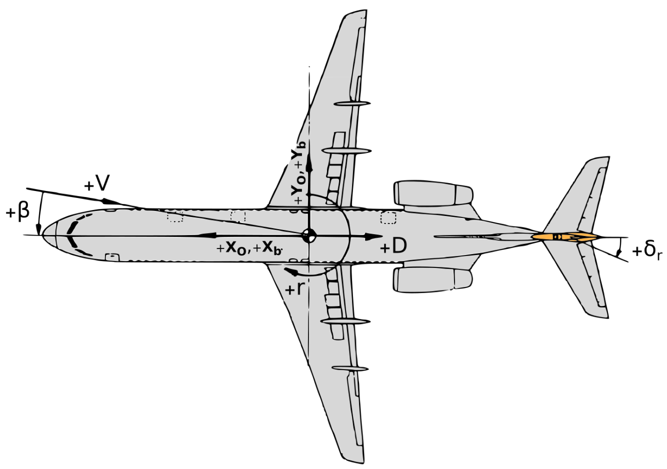

Figure B.4: Aileron deflection sign convention in the Fokker 100 body axis frame F_b of reference. Modified and adapted from Fokker technical report[46].

B.3. Left- versus right handed coordinate systems

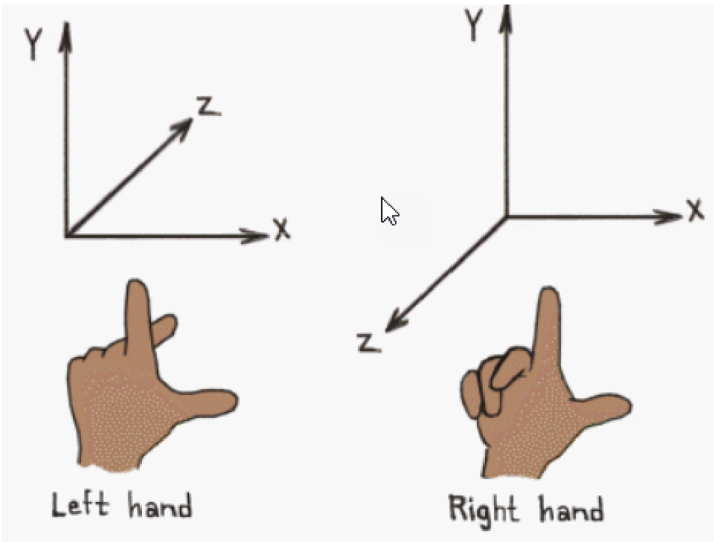

Figure B.5: Definition of left- versus right-handed coordinate systems. Adapted from Primalshell, licensed under the Creative Commons Attribution-Share Alike 3.0 Unported license.

C

Navigation and observation

C.1. NLR Research Aircraft (Cessna Cittation II)

State vector

$$\bar{x} = \begin{bmatrix} x_E & y_E & z_E & u & v & w & \phi & \theta & \psi & \lambda_x & \lambda_y & \lambda_z & \lambda_p & \lambda_q & \lambda_r & W_{xE} & W_{yE} & C_{\alpha_{up}} \end{bmatrix}^T \tag{C.1}$$

Measurement vector

$$\bar{y} = \begin{bmatrix} x_{GPS} & y_{GPS} & z_{GPS} & \dot{x}_{GPS} & \dot{y}_{GPS} & \dot{z}_{GPS} & \phi_{AHRS} & \theta_{AHRS} & \psi_{AHRS} & V_{TAS} & \alpha_{v_{boom}} & \beta_{v_{boom}} \end{bmatrix}^T \tag{C.2}$$

Input vector

$$\bar{u} = \begin{bmatrix} A_x & A_y & A_z & p & q & r \end{bmatrix}^T \tag{C.3}$$

Process noise vector (UKF only)

$$\bar{w} = \begin{bmatrix} w_x & w_y & w_z & w_p & w_q & w_r \end{bmatrix}^T \tag{C.4}$$

Measurement noise vector (UKF only)

$$\bar{v} = \begin{bmatrix} v_{x_{GPS}} & v_{y_{GPS}} & v_{z_{GPS}} & v_{\dot{x}_{GPS}} & v_{\dot{y}_{GPS}} & v_{\dot{z}_{GPS}} & v_{\phi_{AHRS}} & v_{\theta_{AHRS}} & v_{\psi_{AHRS}} & v_{V_{TAS}} & v_{\alpha_{v_{boom}}} & v_{\beta_{v_{boom}}} \end{bmatrix}^T \tag{C.5}$$

Navigation: Kinematic equations

$$\dot{\hat{x}} = \begin{bmatrix} \dot{x}_E \\ \dot{y}_E \\ \dot{z}_E \\ \dot{u} \\ \dot{v} \\ \dot{w} \\ \dot{\phi} \\ \dot{\theta} \\ \dot{\psi} \\ \dot{\lambda}_x \\ \dot{\lambda}_y \\ \dot{\lambda}_z \\ \dot{\lambda}_p \\ \dot{\lambda}_q \\ \dot{\lambda}_r \\ \dot{W}_{xE} \\ \dot{W}_{yE} \\ \dot{C}_{\alpha_{up}} \end{bmatrix} = \begin{bmatrix} \left[u\cos\theta + (v\sin\phi + w\cos\phi)\sin\theta\right]\cos\psi - (v\cos\phi - w\sin\phi)\sin\psi + W_{xE} \\ \left[u\cos\theta + (v\sin\phi + w\cos\phi)\sin\theta\right]\sin\psi + (v\cos\phi - w\sin\phi)\cos\psi + W_{yE} \\ -u\sin\theta + (v\sin\phi + w\cos\phi)\cos\theta \\ (A_x - \lambda_x - w_x) - g_0\sin\theta - \left(q - \lambda_q - w_q\right)w + (r - \lambda_r - w_r)v \\ \left(A_y - \lambda_y - w_y\right) - g_0\cos\theta\sin\phi - (r - \lambda_r - w_r)u + (r - \lambda_r - w_r)w \\ \left(A_y - \lambda_z - w_z\right) - g_0\cos\theta\cos\phi - \left(p - \lambda_p - w_p\right)v + \left(q - \lambda_q - w_q\right)u \\ \left(p - \lambda_p - w_p\right) + \left(q - \lambda_q - w_q\right)\sin\phi\tan\theta + (r - \lambda_r - w_r)\cos\phi\tan\theta \\ \left(q - \lambda_q - w_q\right)\cos\phi - (r - \lambda_r - w_r)\sin\phi \\ \left(q - \lambda_q - w_q\right)\frac{\sin\phi}{\cos\theta} + (r - \lambda_r - w_r)\frac{\cos\phi}{\cos\theta} \\ 0 \\ 0 \\ 0 \\ 0 \\ 0 \\ 0 \\ 0.01 w_N \\ 0.01 w_N \\ 0.01\frac{\pi}{180} w_N \end{bmatrix} \tag{C.6}$$

Observation: Measurement equations

$$\hat{y} = \begin{bmatrix} x_{GPS} \\ y_{GPS} \\ z_{GPS} \\ \dot{x}_{GPS} \\ \dot{y}_{GPS} \\ \dot{z}_{GPS} \\ \phi_{AHRS} \\ \theta_{AHRS} \\ \psi_{AHRS} \\ V_{TAS} \\ \alpha_{v_{boom}} \\ \beta_{v_{boom}} \end{bmatrix} = \begin{bmatrix} x + v_{x_{GPS}} \\ y + v_{y_{GPS}} \\ -z + v_{z_{GPS}} \\ \left[u\cos\theta + (v\sin\phi + w\cos\phi)\sin\theta\right]\cos\psi - (v\cos\phi - w\sin\phi)\sin\psi + W_{xE} + v_{\dot{x}_{GPS}} \\ \left[u\cos\theta + (v\sin\phi + w\cos\phi)\sin\theta\right]\sin\psi + (v\cos\phi - w\sin\phi)\cos\psi + W_{yE} + v_{\dot{y}_{GPS}} \\ u\sin\theta - (v\sin\phi + w\cos\phi)\cos\theta + W_{zE} + v_{\dot{z}_{GPS}} \\ \phi + v_{\phi_{AHRS}} \\ \theta + v_{\theta_{AHRS}} \\ \psi + v_{\psi_{AHRS}} \\ \sqrt{u^2 + v^2 + w^2} + v_{V_{TAS}} \\ \left(1 + C_{\alpha_{up}}\right)\arctan\left(\frac{w}{u}\right) - \frac{x_{v_\alpha}\left(q - \lambda_q - w_q\right)}{u} + v_{\alpha_{boom}} \\ \arctan\left(\frac{v}{u}\right) + \frac{x_{v_\beta}(r - \lambda_r - w_r)}{u} - \frac{z_{v_\beta}\left(p - \lambda_p - w_p\right)}{u} + v_{\beta_{boom}} \end{bmatrix} \tag{C.7}$$

D

Standard calculations

The standard calculation[12][13] (STB) or in Dutch known as the "Standaard Berekingen", is a collection of calculations performed on aircraft sensor measurements. Most STB's described here in this appendix have been used to recalculate missing parameters from the MRVS archive files by crerating algorithms of such a task. Some modification and assumptions have been made with regards to the original Fokker 70/100 documentation and will be discussed per STB parameter.

It should be mentioned that the provided documents by Fokker Services B.V., i.e. the "Standaard Berekeningen" for the Fokker 70 Proto/100 Serie[12][13], are not specific for the Fokker 100 Proto research aircraft which is used in this thesis. Because the original STB for the F100 was not found to be part of Fokker's archive in Hoofddorp, the latter two documents are used to yield assistance in defining the F100 Proto aircraft parameters. Note that both documents contain reference data regarding the F100 Proto, thus aiding in the validity of certain assumptions done here after.

D.1. Actual mass (MT)

The aircraft's actual mass (MT) during flight is calculated by obtaining the actual gross weight from the FMS in the from of two weight feeds with a 4.0Hz sample frequency and a 0.5kg sample resolution. Notably the GRWGMG1, GRWGMG2 and GRWGD parameters facilitated by the MRVS as a source (see Table D.1), where the actual mass parameter modifies the measurement data by linear interpolating the gross weight estimates between the starting and ending measurement values.

D.1.1. Calculation method

Before interpolation can be conducted using the input dataset's provided by the FMS, a selection made and smoothing is applied according to the provide functional flow block diagram given in Figure D.3.

First a distinction is made between available dataset's based on the existence of the GRWGMG2 parameter provided by the second FMS channel (FMS2). In most cases dataset's originating from this channel, but as one might conclude this is not always the case. Therefor Fokker setup a three step procedure; where first a selection is made on what dataset to use (i.e. FMS2 existence is checked or a maximum step of 100kg is violated), then the input is smoothed in case proceeding values exceed differences larger as 5%, and finally initial/ending values are determined by min-maxing the data dataset with their respective and corresponding index locations.

Subsequently a raw interpolation is computed between the minimum and maximum values, of which its output is validated w.r.t. to the gross corrected weight (GRWGD) parameter's existence and the actual mass does not drop below 10000kg of total aircraft mass. If this drop in mass occurs the data-point is considered to be a blunder, and is set to be NaN valued. After validation the actual mass (MT[1]) is

[1]Under the NDA, corresponding Fokker reference reports PMC100-411 & OAA-28-232 can be obtained upon request at Fokker

returned. Nb. validation is not to be confused with a comparison to some arbitrary dataset to which the values are compared, this is just Fokker terminology for checking, as previously stated, if the values do not exceed some preset threshold.

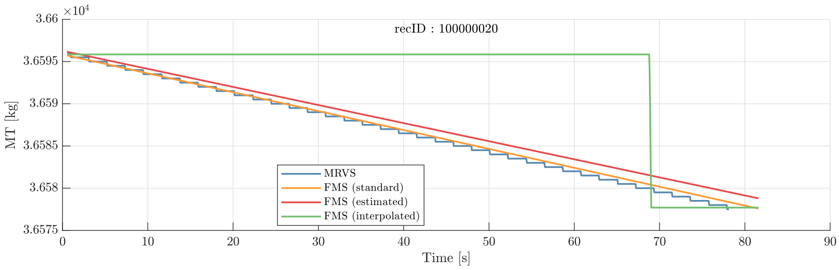

Figure D.1: Recorded versus computed actual mass using data obtained from the MRVS database and the FMS (sloshing corrected).

Calculation results for an arbitrary recording are given in Figure D.1, where four plots provide an example of the two methods for computing the change in aircraft mass during a specific recording. Notably the blue line shows the common time basis corrected MRVS data obtained from the database and is considered to be a dataset to compare FMS system obtained gross and calculated actual masses too.

As can be observed, the both the standard method and the estimated methods follow the MRVS data close enough, specially considering not a lot fuel is burned during the test it self. Remember that these stall tests are conducted with a throttle at an idle setting! Hence both methods (orange and red line) provide good enough data to be usable for analysis, and are in all cases averaged.

Fuel sloshing is also considered, as can be seen in the process flow in Figure D.3 in the smooth input section, if incremental values encountered differ more than 5% in magnitude, the 5% added mass is considered according to the Fokker standard calculations. On a final note an interpolated plot (green line) is added to Figure D.1, this is to show the difference between the MRVS supplied data and the gross mass FMS data which clearly has a much larger sampling frequency.

D.1.2. Validation and special remarks

A large number of recordings used in this thesis are missing the MRVS processed actual mass data, hence the need for a recalculation/estimation of the aircraft's mass during a flight test recording. It is very important to have this data, because without it the fuel masses can not be properly determined, yielding an unusable recording because the center of gravity and the mass moment/product of inertia can not be computed (see Appendix D.2).

The FMS mass data is always used by the MRVS to compute the decrease in mass, it is suspected that this step was ignored due to the very low sampling/update rate and the relatively small recording time during the conducted stall tests. Because the same process as was done by the MRVS division is used, it is assumed that the missing MRVS actual mass data can be replaced by the computed actual mass on the basis of the provided FMS gross mass data.

A validation of the created algorithm to obtain the actual mass is presented in the boxplot in Figure D.2, where the available MRVS recorded actual masses are compared with the computed actual masses based on the FMS weight data expressed as percentage of error difference e_{act}. A number of 43 recordings contain the actual mass data, comparing with the calculated counterpart shows no large differences. This result concludes that the algorithm works as intended.

Services B.V., Hoofddorp.

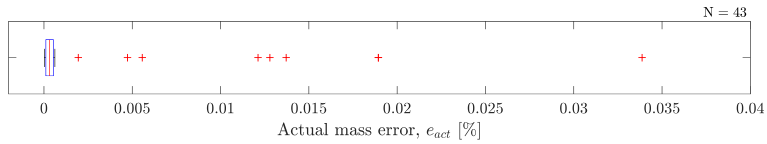

Figure D.2: Validation boxplot of MRVS recorded versus calculated actual mass expressed in percentage of error, e_{act}.

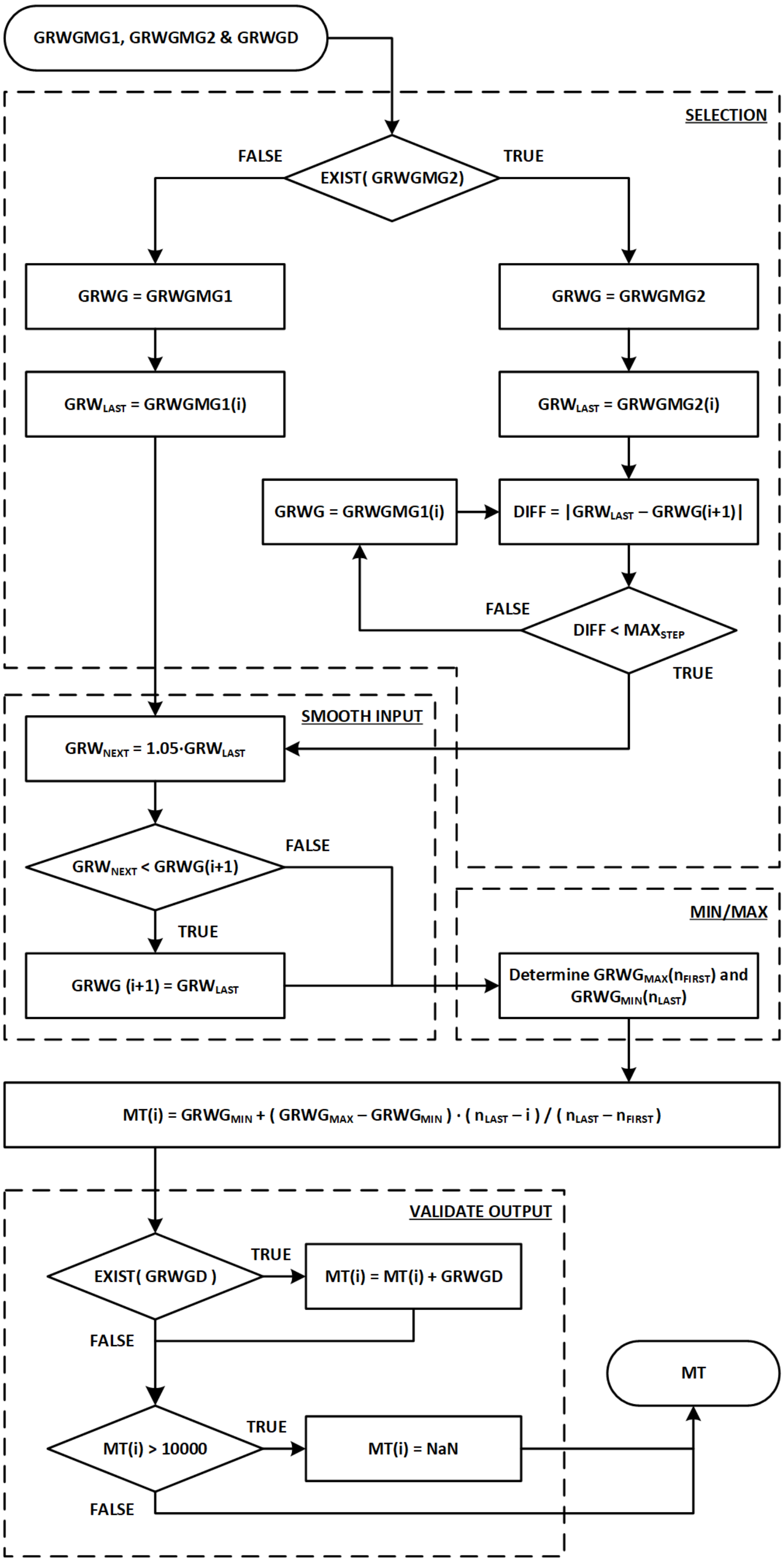

Figure D.3: Actual Mass (MT) functional flow diagram.

Table D.1: Actual Mass (MT) input parameters, adapted from STB[12][13].

Parameter	Symbol	Unit	Source	Parameter Description	ATA
GRWGMG1	$GRWGMG1$	kg	MRVS	GROSS WEIGHT (FMS1GD)	34
GRWGMG2	$GRWGMG2$	kg	MRVS	GROSS WEIGHT (FMS2GD)	34
GRWG	$GRWG$	kg	MRVS	GROSS WEIGHT CORRECTED KNP	08

D.2. Centre of Gravity Actual (CGA)

The actual centre of gravity (CGA) is determined through a sequence by first determining the ramp and subsequently obtaining the actual moments. Using several input/computed parameters provided by the MRVS/STB (see Table D.3), i.e. the ramp centre of gravity (CGR), total ramp/actual aircraft mass (MR,MT), main tank ramp fuel masses (FQMTR1, FQMTR2), center tank ramp/actual fuel mass (FQCC, FQCWTA, FQC, FQCWTR) and the front/rear ballast bag ramp/actual masses (WBBBKF, WBBBKA, WBBKF, WBBKA).

All calculations regarding the raw estimate of the actual centre of gravity during flight are based on evaluating the shifts in moments produced by the decreasing fuel masses w.r.t. the initial ramp measurements. It is there for of importance to define a point on the the aircraft's center-line X-axis (see Figure D.4) within the vehicle reference frame[38]. Where station zero, STA_0, is the X-axis origin in F_W, at 0% MAC STA_{15799} is defined to be in the F_r reference frame and at 40% MAC STA_{17332} in the $F_{r,40}$ reference frame, these locations define the points of reference in the aircraft for moment calculations concerned with the CGA location. Which is expressed in a percentages of mean aerodynamic chord, MAC. The value of the CGA is a fraction, with it's reference in F_r and is thus always computed w.r.t. to the MAC relative to origin in F_r (see Appendix B regrading the reference frames).

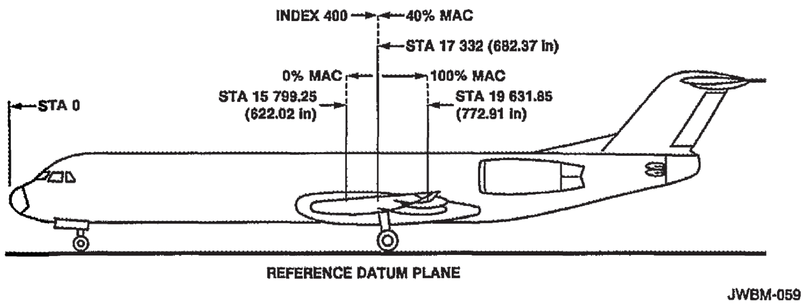

Figure D.4: Locations expressed in percentage of MAC on the X-axis in the vehicle reference frame F_W w.r.t. station 15, adapted from AOM[16].

Another important part of the computation of the CGA is the influence of the fuel loading. And specially the order of the fuel tank draining, because there are three tanks and each have their unique influence on the location of the CGA. According to the Fokker technical report concerned with load cases, it is stated that the center wing tank is drained first, after which the main wing tanks are drained and pumped in the collector tanks, i.e. the last place in the aircraft to contain fuel[73]. Note that symmetrical draining is assumed, i.e. both wing tanks contain an equal amount of fuel at all times. The schematic overview in Figure 6.8 provides an illustration of the tank locations.

Thus by following the functional flow diagram given in Figure D.6 illustrating Fokker's STB protocol and using the provided constants by Fokker in Table D.2 and the input parameters from the MRVS recordings given in Table D.3, the actual center of gravity parameter can be obtained through determining the ramp and actual in-flight moment. Hence, the determination of the actual center of gravity in x_r-direction is a simple process that obtains the total ramp mass and CGR, by comparing it with the reduction of fuel mass. The actual center of gravity is computed with respect to this change in mass, where the symbolic representation of the center of gravity cga_x is given in equation D.1 as a function of the total in-flight moment (M_{total}), actual mass (m_{actual}) and the mean aerodynamic chord ($\boldsymbol{mac}$). The latter value of the aerodynamic chord is added for normalization and thus the value of the CGA parameter becomes a fraction of the mean chord value. From here on for purposes of clarity the symbolic representations of the parameters will be used.

$$\boldsymbol{cga}_x = \frac{M_{total}}{m_{actual}\,\boldsymbol{mac}} \tag{D.1}$$

D.2.1. Initial ramp moment

The calculation of the aircraft's CGA is performed as described in process flow Figure D.6, where two parts are necessary for the determination of the CGA parameter value by obtaining all contributing ramp moments. First the initial total ramp moment M_{PLANE} is computed as described in equation D.2, where the recorded pilot kneepad values such as ramp mass and center of gravity are used in accordance with the aerodynamic mean chord.

$$M_{PLANE} = m_{ramp}\,\boldsymbol{cgr}_x\,\boldsymbol{mac} \tag{D.2}$$

Some flights use special ballast bags at predefined locations within the aircraft, this ballast bag moment M_{BB} is also considered as defined in equation D.3. Although no ballast bags where used during the stall flight-tests, the method is still presented here for completeness.

$$M_{BB} = \Big((m_{BBKF} - m_{BBBKF})\,x_{BBF} + (m_{BBKA} - m_{BBBKA})\,x_{BBA} \Big)\,m_{SB} \tag{D.3}$$

Next in equation D.4 are the ramp fuel weights to be considered, where first a limit check is performed to see if no maximum or negative values are exceeded for main- and center wing tanks.

$$\begin{aligned} m_{14R} &= \min\left(m_{MTR\text{-}L} + m_{MTR\text{-}R},\, \boldsymbol{14}_{max}\right) \\ m_{CWTR} &= \min\left(m_{CWTR},\, \boldsymbol{CW}_{max}\right) \end{aligned} \tag{D.4}$$

After which a lookup is performed in equation D.5 w.r.t. based on empirically obtained data (see Chapter 6.4 or Tables **??** and **??**) regarding the shifts in fuel center of gravity as function of fuel mass. Both done for the total fuel mass contained in the sum of two main wings and in the separate center wing tank.

$$\begin{aligned} x_{14R} &= \text{fncFuel\_cg}\left(\text{"maintank"},\, m_{14R}\right) \\ x_{CWTR} &= \text{fncFuel\_cg}\left(\text{"centertank"},\, m_{CWTR}\right) \end{aligned} \tag{D.5}$$

As a final step in equation D.6 the ramp moments are computed w.r.t. the origin in the vehicle reference F_r. To be later used as terms in the total moment M_{total} computation.

$$\begin{aligned} M_{14R} &= m_{14R}\left(x_{14R} - x_{WING}\right) \\ M_{CWR} &= m_{CWR}\left(x_{CWR} - x_{WING}\right) \end{aligned} \tag{D.6}$$

D.2.2. Actual in-flight fuel moment

The second part that determines the CGA parameter value involves the computation of the actual in-flight fuel moments. Again a log is kept of the fuel burn by the FMS, which allows for an educated guess about the fuel tank mass contents. Taking the actual in-flight measurements in account on the right side of the flow chart in Figure D.6, the first step is done w.r.t. validating of the center wing contents.

If the center wing contents have a zero recorded ramp weight (FQCWTR) is goes without saying that the internal stability result (FQCC) is also zero. Note that the FQCC actually says something about the linear decrease of the center wing tank and is limited to the maximum tank capacity. This part is overridden because a large number of MRVS recordings did not contain these datasets. It is assumed that the recording length was for Fokker of such insignificant low value to constitute a record in de MRVS database. Therefore the previously stated tank draining-order and symmetrical draining of both wings are assumed and is represented in equation D.7.

$$m_{fuel,actual} = m_{14R} + m_{CWTR} - m_{ramp} + m_{actual} \tag{D.7}$$

Note that the actual fuel mass in this case is main plus center wing tank, because the tank capacities are known a scheme is constructed to handle fuel mass allocation w.r.t. the draining order of fuel. Next one up is a reuse of the lookup function as is performed in equation D.8 regarding the shifts in fuel center of gravity as function of fuel mass.

$$\begin{aligned} x_{14} &= \text{fncFuel\_cg}\left(\text{"maintank"}, m_{14}\right) \\ x_{CWT} &= \text{fncFuel\_cg}\left(\text{"centertank"}, m_{CWT}\right) \end{aligned} \tag{D.8}$$

Actual fuel moments are computed in the same way as with the ramp moments, i.e. arm times mass equals a moment (as presented in equation D.9) w.r.t. the origin in the vehicle reference F_r.

$$\begin{aligned} M_{14} &= m_{14}\left(x_{14} - x_{WING}\right) \\ M_{CW} &= m_{CW}\left(x_{CW} - x_{WING}\right) \end{aligned} \tag{D.9}$$

D.2.3. Total in-flight moment and actual center of gravity

Having both parts leaves only one final operation of combining ramp with the actual fuel moments, which leads to the actual center of gravity computation as presented in equation D.10.

$$cga_x = \frac{M_{plane} + M_{14A} - M_{14R} + M_{CWTA} - M_{CWTR} + M_{BB}}{m_{actual}\, mac} \tag{D.10}$$

D.2.4. Validation and special remarks

As with the computation of actual mass parameter (MT) a large number recordings miss these CGA parameter values, hence the necessity for recalculation of this CGA parameter. As a check, the known values of 40 recordings were compared with calculated centers of gravity and yielded no large differences. This is observed in the boxplot validation Figure D.5, where for near all recordings a difference in value of the actual center of gravity e_G does not exceed a 6.5% error margin. This result concludes that the algorithm for the actual center of gravity CGA works as intended.

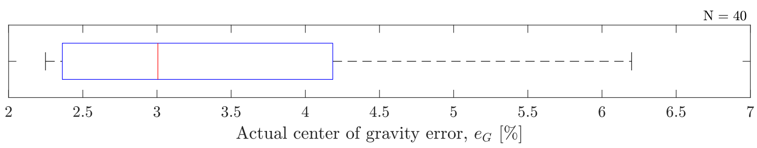

Figure D.5: Validation boxplot of MRVS recorded versus calculated center of gravity expressed in percentage of error, e_G.

Table D.2: Centre of gravity actual (CGA) constants, adapted from STB[12][13].

Constant	Symbol	Value	Unit	Description
MAXCW	CW_{max}	2610	kg	Maximum contents cw-tank
MAX14	14_{max}	7710	kg	Maximum contents left + right main tanks
MAC	mac	3.8326	m	Mean Aerodynamic Chord
XWING	x_{WING}	15.799	m	X-coordinate of 0% MAC
WSB	m_{SB}	25.0	kg	Weight sandbag
XSF	x_{SF}	3.640	m	Station sandbags forward
XSA	x_{SA}	24.316	m	Station sandbags rear

Table D.3: Centre of gravity actual (CGA) input parameters, adapted from STB[12][13].

Parameter	Symbol	Unit	Source	Description	ATA
CGR	cgr_x	-	MRVS	CENTRE OF GRAVITY RAMP (X-DIR)	08
MR	m_{ramp}	kg	MRVS	TOTAL RAMP MASS	08
FQMTR1	$m_{MTR\text{-}L}$	kg	MRVS	FUEL QTY MAIN TANK L RAMP	08
FQMTR2	$m_{MTR\text{-}R}$	kg	MRVS	FUEL QTY MAIN TANK R RAMP	08
FQCWTR	m_{CWTR}	kg	MRVS	FUEL QTY CENTER TANK RAMP	08
MT	m_{actual}	kg	XV5001	ACTUAL MASS	08
FQCWTA	m_{CWTA}	kg	MRVS	FUEL QTY CNTR.WING TANK ACTUAL	08
FQC	m_{CWT}	kg	MRVS	TANK CONTENTS CENTRE (DFGS)	28
FQCC	m_{CC}	kg	XV3027	INTERNAL STB RESULT	08
WBBBKF	m_{BBBKF}	kg	MRVS	BAG BALLAST BEGIN FOR	08
WBBBKA	m_{BBBKA}	kg	MRVS	BAG BALLAST BEGIN AFT	08
WBBKF	m_{BBKF}	kg	MRVS	BAG BALLAST FOR	08
WBBKA	m_{BBKA}	kg	MRVS	BAG BALLAST AFT	08

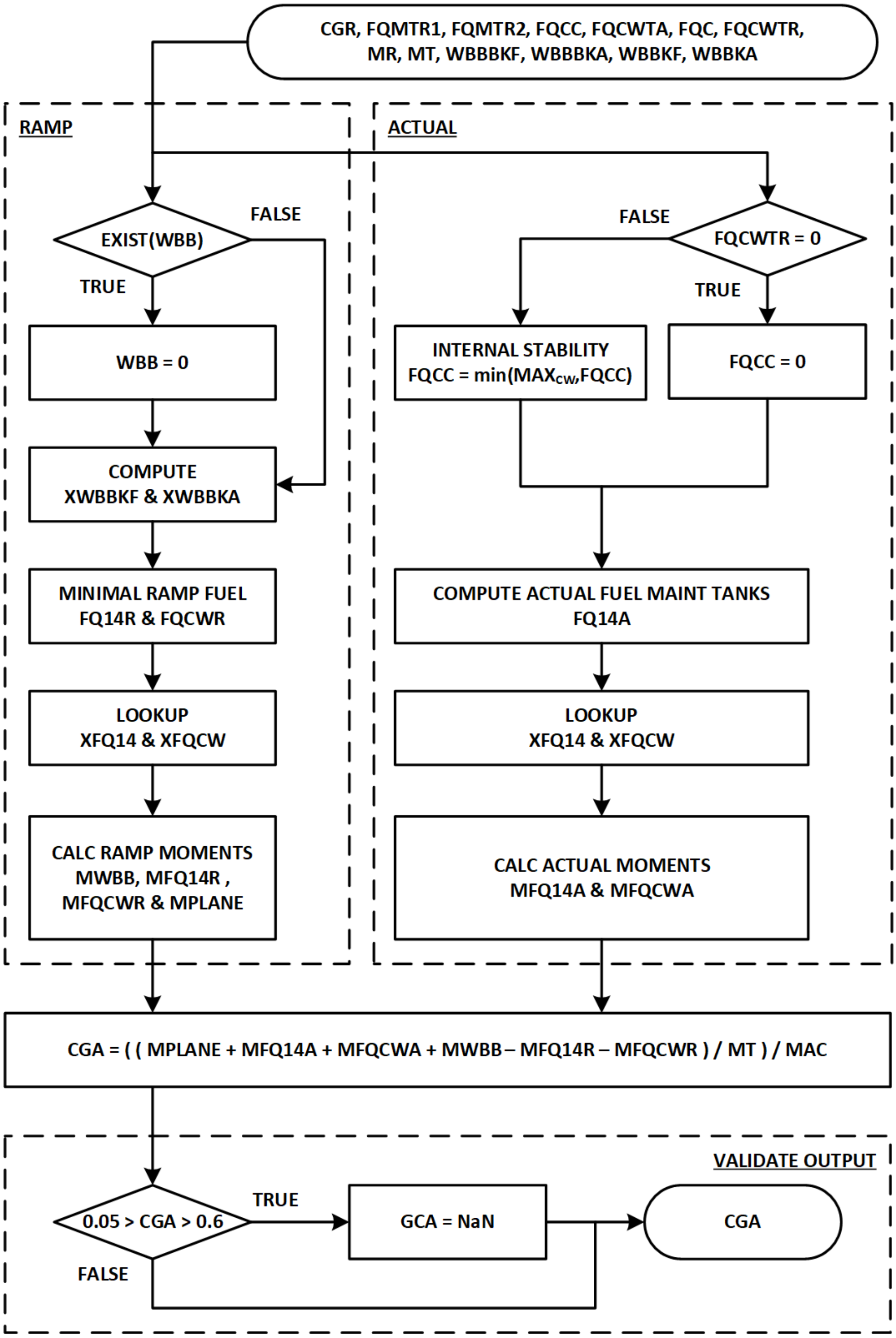

Figure D.6: Centre of Gravity (CGA) functional flow diagram.

E

Weight and balance data for the F100 prototype aircraft

This appendix contains all Fokker Hoofddorp B.V. provided data which includes aircraft schematics, figures and tables used in this thesis.

E.1. Cabin configuration

Cabin configuration is presented in Figure E.1, where the locations of the water tanks, inertial reference system (IRS) and the rocket-bay have been highlighted. Note that the IRS location is of importance w.r.t. the flight-test measurement corrections and is located at station 18590.

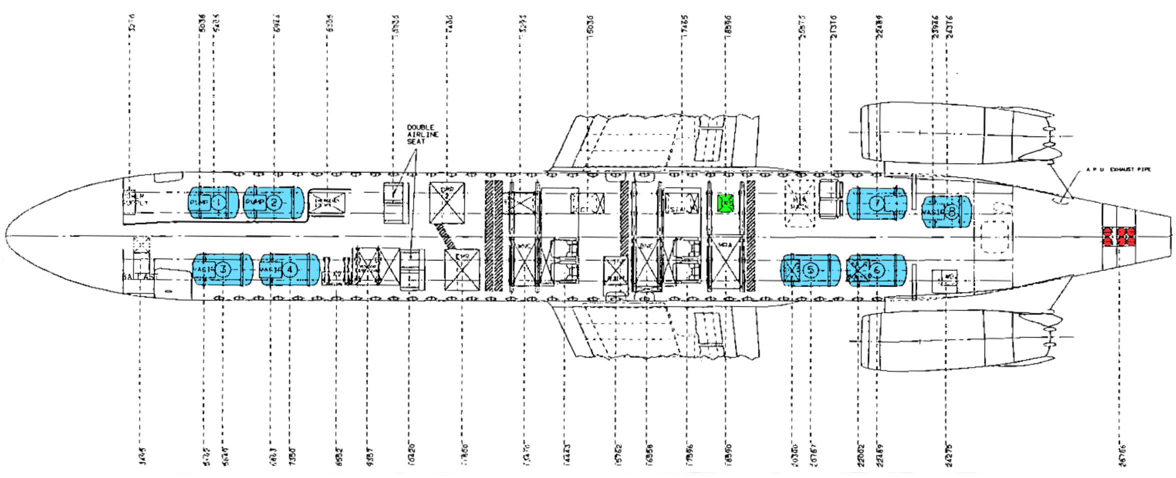

Figure E.1: Cabin layout of the Fokker 100 proto highlighting the water tank locations (blue), inertial measurement system (green) and the rocket-bay (red). Adapted from Fokker technical report E100-188.

E.2. Masses, moments and moments of inertia

Appendix E.2 contains all static dimensional aircraft data with the specific addition of masses, moments and moments of inertia relative to a local zone (i.e. point/element mass) of a specified section of the Fokker 100 prototype aircraft [21].

E.2.1. Fuselage section

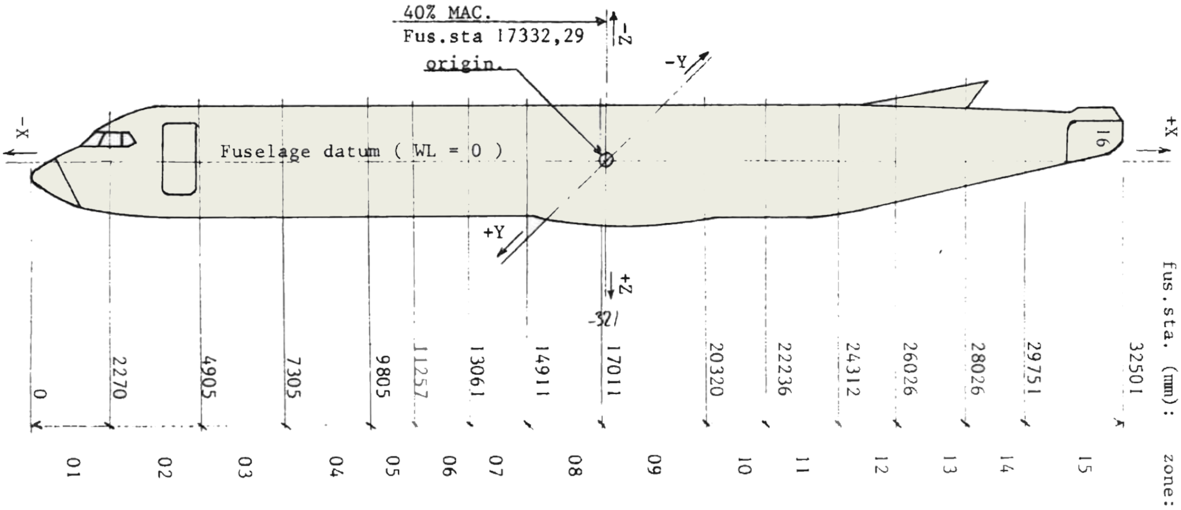

Figure E.2: Fuselage (FUS) left-handed reference axis and zones. Adapted from Fokker technical report[21].

Table E.1: Masses, moments and moments of inertia of the fuselage with its origin located at $\mathbf{0}_{FUS}^{W}$ (17332.3, 0.0, 0.0) millimeters. Obtained from Fokker technical report [21].

Section	Zone	Mass	Mx	My	Mz	Ixx	Iyy	Izz
Fuselage	[-]	[kg]	[kg-m]	[kg-m]	[kg-m]	[kg-m^2]	[kg-m^2]	[kg-m^2]
01.01	1	762.5	-12178.5	-7.1	160.4	569.0	229.7	292.1
01.02	2	2579.4	-35856.6	267.6	620.5	2179.3	2355.3	1459.6
01.03	3	1283.1	-14700.9	-210.9	176.5	1266.9	1475.1	1122.1
01.04	4	1207.8	-10543.2	19.3	88.0	1217.2	1348.6	794.5
01.05	5	630.7	-4231.3	-135.6	-146.9	171.7	677.3	464.6
01.06	6	1207.1	-6410.1	36.1	-337.8	389.7	1143.6	633.2
01.07	7	1246.9	-4245.7	-26.0	-272.7	828.8	1112.0	696.0
01.08	8	2191.7	-2829.6	137.6	573.9	1064.1	2508.6	1911.2
01.09	9	2345.6	2381.0	181.8	14.9	2180.7	2056.4	1653.5
01.10	10	748.7	2932.6	-54.0	-159.7	345.2	827.4	537.5
01.11	11	1064.3	6449.1	1.1	-55.0	875.3	1085.7	698.0
01.12	12	873.8	6822.9	-73.2	30.7	277.9	619.2	747.9
01.13	13	202.2	1939.2	-9.5	-62.6	107.5	117.4	151.7
01.14	14	432.5	4996.1	0.7	20.0	74.4	33.4	201.1
01.15	15	119.7	1573.5	0.0	-72.5	70.2	11.5	22.0
01.16	16	58.7	823.4	-0.6	-44.6	20.0	2.9	5.7
01.00	$\sum$	16954.8	-63078.1	127.3	533.1			

E.2.2. Wing section

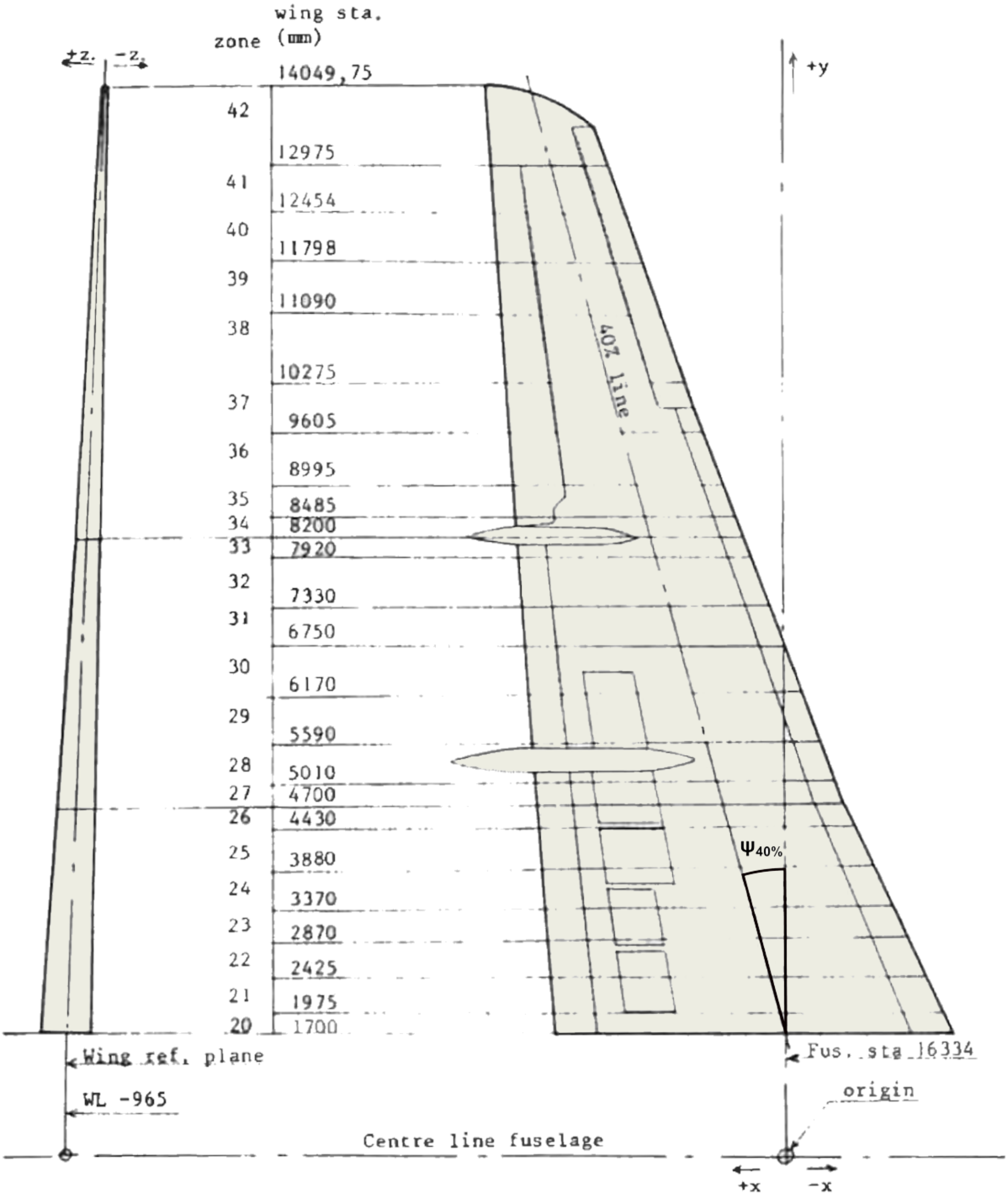

Figure E.3: Wing (WNG) left-handed reference axis and zones. Adapted from Fokker technical report[21].

Table E.2: Masses, moments and moments of inertia of the left wing with its origin located at $\mathbf{0}^{W}_{WNG\text{-}L}$ $(16334.0, 0.0, -965.0)$ millimeters. Obtained from Fokker technical report [21].

Section Wing-L	Zone [-]	Mass [kg]	Mx [kg-m]	My [kg-m]	Mz [kg-m]	Ixx [kg-m^2]	Iyy [kg-m^2]	Izz [kg-m^2]
03.01	20	246.2	142.4	-440.9	8.7	363.1	7.4	15.2
03.02	21	166.1	86.7	-363.9	10.9	220.2	3.3	7.3
03.03	22	221.9	180.7	-585.4	12.6	225.3	2.8	8.2
03.04	23	123.4	87.1	-385.1	3.3	150.3	2.1	5.2
03.05	24	117.1	97.2	-424.7	2.4	141.6	2.3	4.3
03.06	25	113.2	118.1	-471.9	2.0	122.6	3.0	3.5
03.07	26	76.2	93.4	-351.0	2.6	73.0	0.9	2.0
03.08	27	72.8	80.8	-353.9	1.4	73.5	0.9	1.8
03.09	28	202.5	377.1	-1073.5	12.8	217.2	3.4	6.5
03.10	29	98.1	147.9	-577.0	1.6	82.7	2.5	1.9
03.11	30	84.3	128.0	-543.2	0.7	62.5	2.0	1.5
03.12	31	77.5	128.8	-546.9	-0.1	51.2	2.2	1.1
03.13	32	76.3	141.7	-581.1	0.6	45.9	1.9	2.4
03.14	33	97.3	245.0	-791.9	1.8	55.0	0.8	1.9
03.15	34	50.4	102.7	-420.3	-0.5	25.0	0.3	0.5
03.16	35	66.6	143.5	-580.6	-0.4	32.6	1.5	0.6
03.17	36	62.8	135.6	-582.5	-0.4	29.6	2.0	0.6
03.18	37	49.2	114.6	-488.1	-0.4	22.9	1.6	0.4
03.19	38	55.2	141.9	-587.9	-0.3	22.2	3.1	0.4
03.20	39	51.3	140.8	-586.6	0.0	17.2	2.2	0.3
03.21	40	34.5	100.2	-418.3	0.3	19.6	1.4	0.1
03.22	41	18.8	56.9	-239.5	0.1	5.9	0.8	0.1
03.23	42	22.7	72.1	-304.5	0.2	5.4	2.3	0.1
03.00	$\sum$	2184.5	3063.3	-11698.7	60.1			

Table E.3: Masses, moments and moments of inertia of the right wing with its origin located at $\mathbf{0}^{W}_{WNG\text{-}R}$ $(16334.0, 0.0, -965.0)$ millimeters. Obtained from Fokker technical report [21].

Section	Zone	Mass	Mx	My	Mz	Ixx	Iyy	Izz
Wing-R	[-]	[kg]	[kg-m]	[kg-m]	[kg-m]	[kg-m^2]	[kg-m^2]	[kg-m^2]
02.01	20	246.2	142.4	440.9	8.7	363.1	7.4	15.2
02.02	21	166.1	86.7	363.9	10.9	220.2	3.3	7.3
02.03	22	221.9	180.7	585.4	12.6	225.3	2.8	8.2
02.04	23	123.4	87.1	385.1	3.3	150.3	2.1	5.2
02.05	24	117.1	97.2	424.7	2.4	141.6	2.3	4.3
02.06	25	113.2	118.1	471.9	2.0	122.6	3.0	3.5
02.07	26	76.2	93.4	351.0	2.6	73.0	0.9	2.0
02.08	27	72.8	80.8	353.9	1.4	73.5	0.9	1.8
02.09	28	202.5	377.1	1073.5	12.8	217.2	3.4	6.5
02.10	29	98.1	147.9	577.0	1.6	82.7	2.5	1.9
02.11	30	84.3	128.0	543.2	0.7	62.5	2.0	1.5
02.12	31	77.5	128.8	546.9	-0.1	51.2	2.2	1.1
02.13	32	76.3	141.7	581.1	0.6	45.9	1.9	2.4
02.14	33	97.3	245.0	791.9	1.8	55.0	0.8	1.9
02.15	34	50.4	102.7	420.3	-0.5	25.0	0.3	0.5
02.16	35	66.6	143.5	580.6	-0.4	32.6	1.5	0.6
02.17	36	62.8	135.6	582.5	-0.4	29.6	2.0	0.6
02.18	37	49.2	114.6	488.1	-0.4	22.9	1.6	0.4
02.19	38	55.2	141.9	587.9	-0.3	22.2	3.1	0.4
02.20	39	51.3	140.8	586.6	0.0	17.2	2.2	0.3
02.21	40	34.5	100.2	418.3	0.3	19.6	1.4	0.1
02.22	41	18.8	56.9	239.5	0.1	5.9	0.8	0.1
02.23	42	22.7	72.1	304.5	0.2	5.4	2.3	0.1
02.00	$\sum$	2184.5	3063.3	11698.7	60.1			

E.2.3. Vertical- and horizontal stabilizer sections

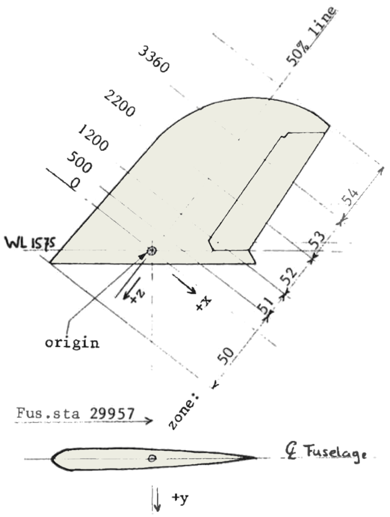

Figure E.4: Vertical stabilizer (VSB) left-handed reference axis and zones. Adapted from Fokker technical report[21].

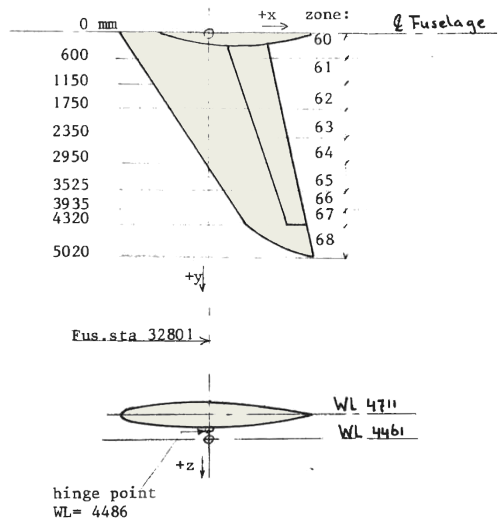

Figure E.5: Horizontal stabilizer (HSB) left-handed reference axis and zones. Adapted from Fokker technical report[21].

Table E.4: Masses, moments and moments of inertia of the vertical stabilizer with its origin located at $\mathbf{0}^{W}_{VSB}$ $(29957.0,\ 0.0,\ 1575.0)$ millimeters. Obtained from Fokker technical report [21].

Section Vertical-Stabilizer	Zone [-]	Mass [kg]	Mx [kg-m]	My [kg-m]	Mz [kg-m]	Ixx [kg-m^2]	Iyy [kg-m^2]	Izz [kg-m^2]
04.01	50	88.2	-43.3	0.0	3.1	42.9	1.9	31.6
04.02	51	106.4	3.4	-0.9	-71.6	60.5	1.3	15.5
04.03	52	74.3	-21.5	0.0	-127.4	52.0	1.2	6.6
04.04	53	157.8	-42.9	0.0	-459.5	59.7	1.5	18.8
04.05	54	79.7	10.4	0.0	-304.4	36.5	0.7	7.5
04.00	$\sum$	506.5	-94.0	-0.9	-959.8			

Table E.5: Masses, moments and moments of inertia of the left horizontal stabilizer with its origin located at $\mathbf{0}^{W}_{HSB\text{-}L}$ $(32801.0,\ 0.0,\ 4461.0)$ millimeters. Obtained from Fokker technical report [21].

Section Horizontal-Stabilizer-L	Zone [-]	Mass [kg]	Mx [kg-m]	My [kg-m]	Mz [kg-m]	Ixx [kg-m^2]	Iyy [kg-m^2]	Izz [kg-m^2]
06.01	60	109.5	19.2	-21.8	-24.8	81.6	4.0	2.4
06.02	61	36.9	4.0	-31.9	-9.0	23.6	0.9	0.3
06.03	62	38.1	14.7	-54.6	-9.4	20.7	1.2	0.3
06.04	63	32.9	22.0	-67.3	-8.1	15.4	1.0	0.2
06.05	64	29.8	26.8	-78.5	-7.3	11.8	0.9	0.1
06.06	65	25.0	28.8	-80.8	-6.1	7.6	0.7	0.1
06.07	66	16.1	22.2	-59.2	-3.9	3.9	0.7	0.0
06.08	67	14.9	24.2	-60.3	-3.7	3.3	0.6	0.0
06.09	68	12.3	22.5	-56.0	-3.1	1.7	0.3	0.0
06.00	$\sum$	315.4	184.4	-510.4	-75.4			

Table E.6: Masses, moments and moments of inertia of the right horizontal stabilizer with its origin located at $\mathbf{0}^{W}_{HSB\text{-}R}$ $(32801.0,\ 0.0,\ 4461.0)$ millimeters. Obtained from Fokker technical report [21].

Section Horizontal-Stabilizer-R	Zone [-]	Mass [kg]	Mx [kg-m]	My [kg-m]	Mz [kg-m]	Ixx [kg-m^2]	Iyy [kg-m^2]	Izz [kg-m^2]
05.01	60	109.5	19.2	21.8	-24.8	81.6	4.0	2.4
05.02	61	36.9	4.0	31.9	-9.0	23.6	0.9	0.3
05.03	62	38.1	14.7	54.6	-9.4	20.7	1.2	0.3
05.04	63	32.9	22.0	67.3	-8.1	15.4	1.0	0.2
05.05	64	29.8	26.8	78.5	-7.3	11.8	0.9	0.1
05.06	65	25.0	28.8	80.8	-6.1	7.6	0.7	0.1
05.07	66	16.1	22.2	59.2	-3.9	3.9	0.7	0.0
05.08	67	14.9	24.2	60.3	-3.7	3.3	0.6	0.0
05.09	68	12.3	22.5	56.0	-3.1	1.7	0.3	0.0
05.00	$\sum$	315.4	184.4	510.4	-75.4			

E.2.4. Engine sections

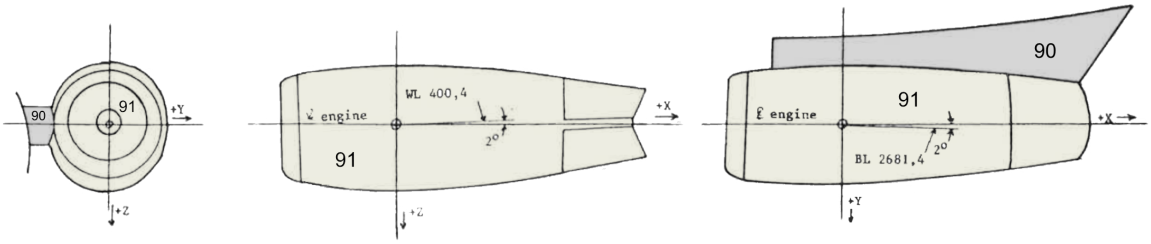

Figure E.6: Engine and nacelle (ENG) left-handed reference axis and zones. Adapted from Fokker technical report[21].

Table E.7: Masses, moments and moments of inertia of the left engine with its origin located at $\mathbf{0}^{W}_{ENG\text{-}L}$ $(23606.5,\ -2681.4,\ 400.4)$ millimeters. Obtained from Fokker technical report [21].

Section Engine-L	Zone [-]	Mass [kg]	Mx [kg-m]	My [kg-m]	Mz [kg-m]	Ixx [kg-m^2]	Iyy [kg-m^2]	Izz [kg-m^2]
08.01	90	218.7	198.8	151.8	-20.9	293.5	39.0	17.6
08.02	91	2356.3	1498.5	33.0	180.1	3114.1	319.6	335.2
08.00	$\sum$	2574.9	1697.3	184.8	159.1			

Table E.8: Masses, moments and moments of inertia of the right engine with its origin located at $\mathbf{0}^{W}_{ENG\text{-}R}$ $(23606.5,\ 2681.4,\ 400.4)$ millimeters. Obtained from Fokker technical report [21].

Section Engine-R	Zone [-]	Mass [kg]	Mx [kg-m]	My [kg-m]	Mz [kg-m]	Ixx [kg-m^2]	Iyy [kg-m^2]	Izz [kg-m^2]
07.01	90	218.7	198.8	-151.8	-20.9	293.5	39.0	17.6
07.02	91	2356.3	1498.5	-33.0	180.1	3114.1	319.6	335.2
07.00	$\sum$	2574.9	1697.3	-184.8	159.1			

E.2.5. Undercarriage sections

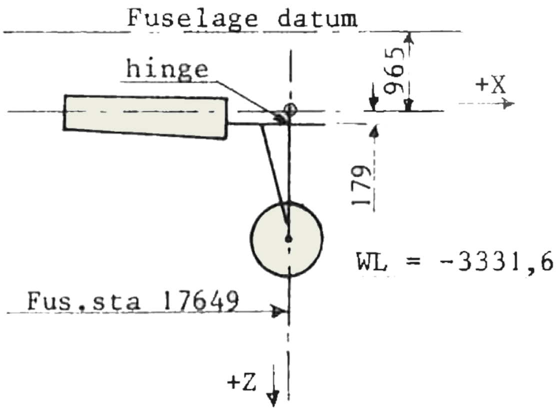

Figure E.7: Nose undercarriage (NUC) left-handed reference axis and zones. Adapted from Fokker technical report[21].

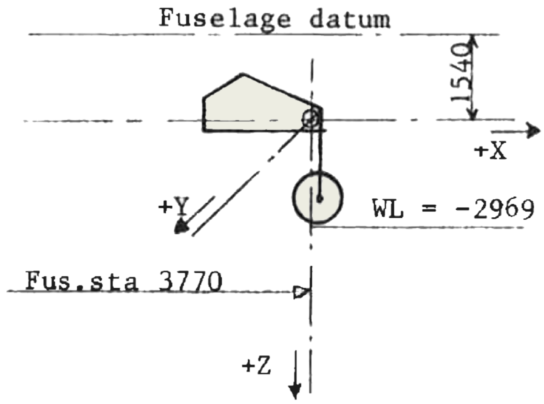

Figure E.8: Main undercarriage (MUC) left-handed reference axis and zones. Adapted from Fokker technical report[21].

Table E.9: Masses, moments and moments of inertia of the nose under carriage with its origin located at $\mathbf{0}^{W}_{NUC}$ $(3770.0,\ 0.0,\ -1540.0)$ millimeters. Obtained from Fokker technical report [21].

Section Nose-Under-Carriage	Zone [-]	Mass [kg]	Mx [kg-m]	My [kg-m]	Mz [kg-m]	Ixx [kg-m^2]	Iyy [kg-m^2]	Izz [kg-m^2]
09.01	93	68.9	-5.7	0.0	16.2	0.6	0.3	7.8
09.02	95	55.1	-3.0	0.0	57.1	0.9	1.9	2.0
09.03	97	124.0	-95.5	0.0	-37.4	44.2	2.1	4.1

Table E.10: Masses, moments and moments of inertia of the left main under carriage with its origin located at $\mathbf{0}^{W}_{MUC\text{-}L}$ $(17649.0,\ 0.0,\ -965.0)$ millimeters. Obtained from Fokker technical report [21].

Section Main-Under-Carriage-L	Zone [-]	Mass [kg]	Mx [kg-m]	My [kg-m]	Mz [kg-m]	Ixx [kg-m^2]	Iyy [kg-m^2]	Izz [kg-m^2]
11.01	94	127.9	0.4	-314.7	64.0	8.3	4.4	23.5
11.02	96	349.9	30.1	-881.7	595.7	10.0	17.7	37.6
11.03	98	477.8	30.5	-604.4	89.8	18.4	184.7	19.2

Table E.11: Masses, moments and moments of inertia of the right main under carriage with its origin located at $\mathbf{0}^{W}_{MUC\text{-}R}$ $(17649.0,\ 0.0,\ -965.0)$ millimeters. Obtained from Fokker technical report [21].

Section Main-Under-Carriage-R	Zone [-]	Mass [kg]	Mx [kg-m]	My [kg-m]	Mz [kg-m]	Ixx [kg-m^2]	Iyy [kg-m^2]	Izz [kg-m^2]
10.01	94	127.9	0.4	314.7	64.0	8.3	4.4	23.5
10.02	96	349.9	30.1	881.7	595.7	10.0	17.7	37.6
10.03	98	477.8	30.5	604.4	89.8	18.4	184.7	19.2

E.3. Water tank specifications

Specifications regarding the Fokker 100 prototype water tanks load case is defined by Heinkens[21] and should be consulted for more detail.

E.3.1. Polynomial coefficients : Center of gravity along the z-axis

Second order polynomial coefficients[1] define the water tank center of gravity for the small-/large water tanks in Table E.12.

Table E.12: Water tank polynomial coefficients for the center of gravity location calculation along the Z_W axis.

$p(x)$	n	p_1	p_2	p_3	p_4	R^2
pZ_{ws}^W	2	-2.2e-04	7.7e-01	-3.8e+02		0.9999
pZ_{wl}^W	2	-1.8e-04	6.3e-01	-3.8e+02		0.9980

E.3.2. Polynomial coefficients : Moments of inertia

First-/third order polynomial coefficients[1] define the water tank moments of inertia w.r.t the tanks center of gravity for the small-/large water tanks in Table E.13.

Table E.13: Small-/large water tank polynomial coefficients for the moment of inertia calculation contained in an arbitrary water tank's center of gravity.

$p(x)$	n	p_1	p_2	p_3	p_4	R^2
$pI_{xx,ws}^W$	1	1.0e-01	-2.3e-02			1.0000
$pI_{yy,ws}^W$	3	-2.8e-07	2.3e-04	-3.4e-03	1.6e-01	0.9968
$pI_{zz,ws}^W$	3	6.1e-08	4.5e-05	-3.9e-03	6.3e-03	0.9994
$pI_{xx,wl}^W$	1	2.0e-01	-3.4e-15			1.0000
$pI_{yy,wl}^W$	3	-1.6e-07	1.7e-04	-2.4e-05	2.5e-01	0.9968
$pI_{zz,wl}^W$	3	6.3e-08	1.0e-05	1.7e-03	-9.1e-02	0.9953

E.4. Fuel tank specifications

The main wing tank specifications have been obtained through the Fokker 100 load cases technical report for its series (i.e. production) aircraft[73], and it is assumed to be the same tank setup as is used by the prototype. This report details 17 wing tank sections separated by 18 rib-stations, consisting of 2 collector (purple) and 15 main tanks (blue) as is illustrated in Figures E.9 and E.10. Subsequently, Table E.14 details the manually estimated tank dimensions relative to main wing tank frame of reference with its origin at (16506,1700,-965) millimeters in the vehicle-nose F_W frame of reference. Notice that the illustrations have a 180± rotated, right-handed axis system with the positive z-axis pointing down wards, corrections have been needed for proper conversion to F_W.

Special remark should be made about the origin location on the z-axis, this point is not defined by the Fokker report discussing the load cases for the series type aircraft and has been assumed to be the same as the location regarding the origin w.r.t. the z-axis as defined in wing section Figure E.3.

[1]Polynomial coefficients adhere to the Matlab coefficient indexing.

E.4.1. Main wing fuel tank : Top view

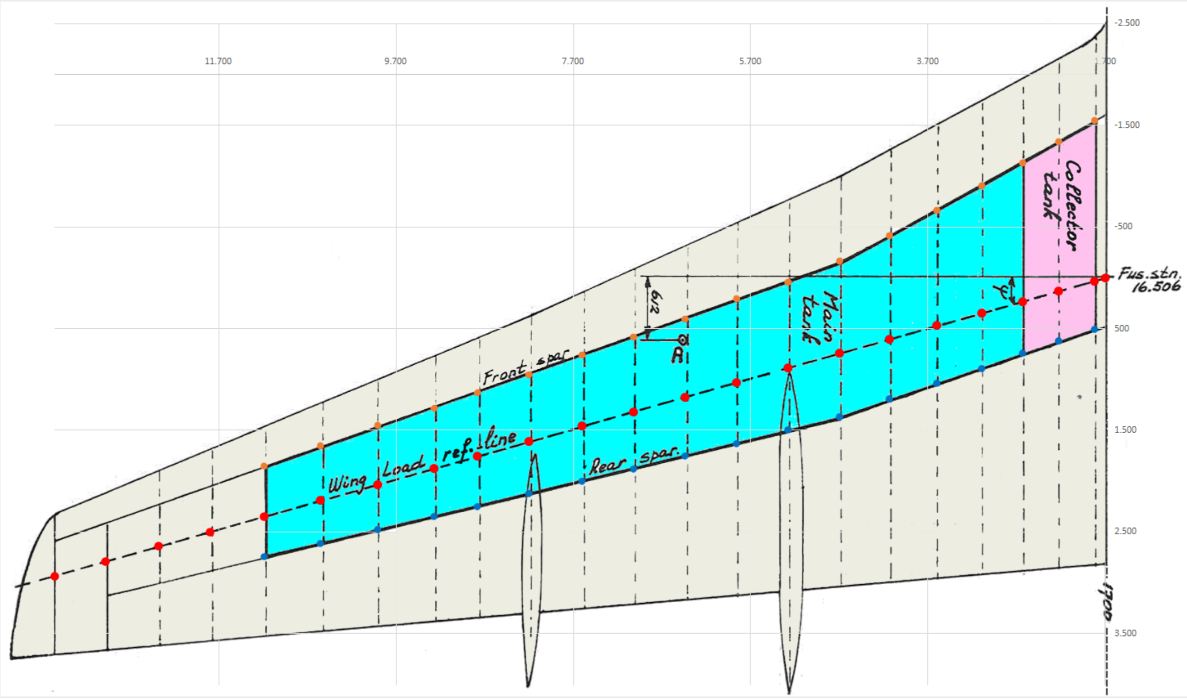

Figure E.9: Technical drawing of the Fokker 100 main- and collector-tank (top-view), with overlaid estimated tank location points. Image is adapted from Fokker technical report[73].

E.4.2. Main wing fuel tank : Front view

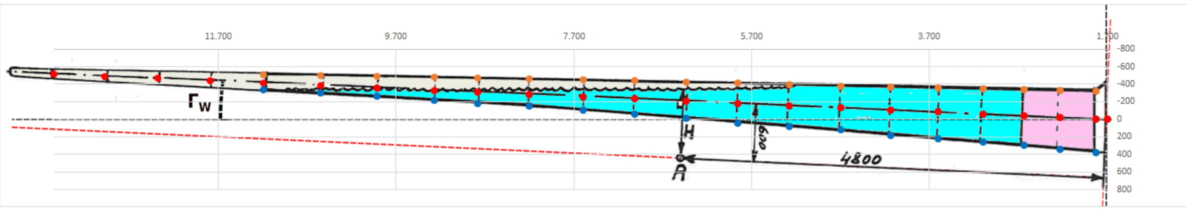

Figure E.10: Technical drawing of the Fokker 100 main- and collector-tank (side-view), with overlaid estimated tank location points. Image is adapted from Fokker technical report[73].

E.4.3. Manually estimated dimensions for the main wing fuel sub-tanks

All initial fuel tank dimensions are estimated by hand using the provided schematic Figures E.9 and E.10, where the result of this manual estimation is presented in Table E.14. Using a graphic overlay technique in Microsoft Excel (2016), where setting the background of a chart to show the wing image for top- and front view, an axis system in combination with a scatter plot can be projected on to the background image. This allows for carefully finding the relative locations defining the tank dimensions.

Note that the intersecting locations of the wing load reference-line with the rib-stations can easily be computed (i.e. the red dots in both figures), because it is known that the wing load reference-line in the top view (see Figure E.9) is straight and under an angle Ψ of 0.24255 radians with the y-axis relative to the origin, and the wing center-line in front view (see Figure E.10) has a dihedral angle Γ_W of 2.5 degrees also relative to the y-axis[73]. This functions as a means for manually aligning the both chart axis systems to the background images and obtaining some reasonable understanding regarding the

Fokker 100 main wing tank dimensions.

Furthermore, as was done with the intersections defined by the red dots, the front-spar/upper sections of the tanks are identified by the orange dots and the rear-spar/lower sections with blue. And on a final remark, the third rib in the 18 rib-stations separates collector- with the main wing tank, in Table E.14 this is highlighted for reasons of clarity.

Table E.14: Manually estimated main wing fuel tank dimensions of the Fokker 100 aircraft.

Rib	y_{rib} [mm]	x_{Ψ} [mm]	z_{Γ} [mm]	$x_{front-spar}$ [mm]	$x_{rear-spar}$ [mm]	z_{upper} [mm]	z_{lower} [mm]
01	1825.0	30.9	-5.5	-1550.0	510.0	-320.0	380.0
02	2230.0	131.1	-23.1	-1340.0	620.0	-330.0	340.0
03	2635.0	231.3	-40.8	-1130.0	740.0	-340.0	300.0
04	3100.0	346.4	-61.1	-910.0	890.0	-350.0	260.0
05	3600.0	470.1	-83.0	-670.0	1040.0	-360.0	220.0
06	4135.0	602.5	-106.3	-420.0	1190.0	-370.0	180.0
07	4700.0	742.3	-131.0	-170.0	1370.0	-380.0	120.0
08	5280.0	885.8	-156.3	40.0	1500.0	-395.0	80.0
09	5860.0	1029.3	-181.6	200.0	1630.0	-410.0	40.0
10	6440.0	1172.8	-207.0	400.0	1750.0	-425.0	-10.0
11	7020.0	1316.3	-232.3	580.0	1880.0	-440.0	-60.0
12	7600.0	1459.8	-257.6	760.0	2000.0	-455.0	-110.0
13	8200.0	1608.2	-283.8	950.0	2120.0	-460.0	-150.0
14	8780.0	1751.7	-309.1	1130.0	2250.0	-470.0	-180.0
15	9270.0	1873.0	-330.5	1280.0	2350.0	-480.0	-215.0
16	9910.0	2031.3	-358.5	1450.0	2480.0	-490.0	-260.0
17	10550.0	2189.7	-386.4	1650.0	2610.0	-500.0	-300.0
18	11190.0	2348.0	-414.3	1850.0	2740.0	-510.0	-335.0

E.4.4. Maximum estimated capacity for the main wing fuel sub-tanks

By making uses of the estimated main wing fuel sub-tank dimensions as given in Table E.14, the sub-tank have been sized to fit the design masses contained in the collector (750 kg, Table E.15) and the remaining main wing (3105 kg, Table E.16) sub-tanks. The tables pressent data regarding the sub-tank number n_{tnk} , width w_{tnk} along the X_r axis, length l_{tnk} along the Y_r axis, tank height h_{tnk} along the Z_r axis and volume V_{tnk}, where the fuel mass m_f is a function of the volume V_{tnk} and a fuel density ρ_f of 798.0 kg/m^3. Nb. the fuel density ρ_f is the same as is used by the Zwart's load cases for the Fokker 100 production aircraft[73].

Table E.15: Estimated collector sub-tank sizes w.r.t. a fuel density of 798.0 kg/m^3.

n_{tnk}	l_{tnk} [mm]	w_{tnk} [mm]	h_{tnk} [mm]	V_{tnk} [m^3]	m_f [kg]
01	2005.1	375.0	655.0	0.4925	393.0
02	1908.9	375.0	625.0	0.4474	357.0
			$\sum$	0.9399	750.1

Table E.16: Estimated main wing sub-tank sizes w.r.t. a fuel density of 798.0 kg/m^3.

n_{tnk}	l_{tnk} [mm]	w_{tnk} [mm]	h_{tnk} [mm]	V_{tnk} [m^3]	m_f [kg]
03	1718.4	435.0	595.0	0.4448	354.9
04	1642.2	470.0	565.0	0.4361	348.0
05	1551.8	505.0	535.0	0.4192	334.6
06	1470.8	535.0	495.0	0.3895	310.8
07	1399.4	550.0	457.5	0.3521	281.0
08	1347.1	550.0	432.5	0.3204	255.7
09	1294.7	550.0	402.5	0.2866	228.7
10	1232.8	550.0	367.5	0.2492	198.9
11	1180.5	550.0	332.5	0.2159	172.3
12	1118.6	570.0	297.5	0.1897	151.4
13	1061.5	550.0	270.0	0.1576	125.8
14	1013.9	460.0	247.5	0.1154	92.1
15	971.0	610.0	217.5	0.1288	102.8
16	918.7	610.0	185.0	0.1037	82.7
17	852.0	610.0	157.5	0.0819	65.3
			$\sum$	3.8910	3105.0

E.4.5. Estimated main-/center wing fuel tank X_r and Y_r center of gravity polynomial coefficients.

Table E.17: Fuel center of gravity polynomial coefficients (Matlab indexes) of the main-/center wing tanks.

$p(x)$	n	p_1	p_2	p_3	p_4	p_5	p_6	p_7	R^2
$pX^W_{f,COL}$	2	-1.7e-05	-1.1e-01	1.6e+04					0.9997
$pX^W_{f,MWT}$	6	-6.4e-20	2.0e-15	-2.5e-11	1.7e-07	-6.4e-04	1.5e+00	1.5e+04	1.0000
$pY^W_{f,COL}$	1	2.7e-02	2.2e+03						1.0000
$pY^W_{f,MWT}$	6	6.2e-18	-7.9e-14	3.9e-10	-8.8e-07	6.6e-04	1.3e+00	1.1e+03	1.0000
$pX^W_{f,CWT}$	4	2.6e-11	-2.1e-07	6.3e-04	-8.9e-01	1.7e+04			0.9999

E.4.6. Estimated main-/center wing fuel-level H logit coefficients.

Table E.18: Estimated fuel-level logit coefficients of the main wing- and collector tank.

$f_{logit}(m_f)$	Θ_1	Θ_2	Θ_3	Θ_4	R^2	MSE [mm]
$H_{f,COL}$	4.3e+02	1.5e+02	-5.4e+01	9.0e+02	0.9982	2.4483
$H_{f,MWT}$	5.8e+02	1.2e+02	-7.2e+01	3.7e+03	0.9972	3.1493

E.5. Relevant fuel loading graphs

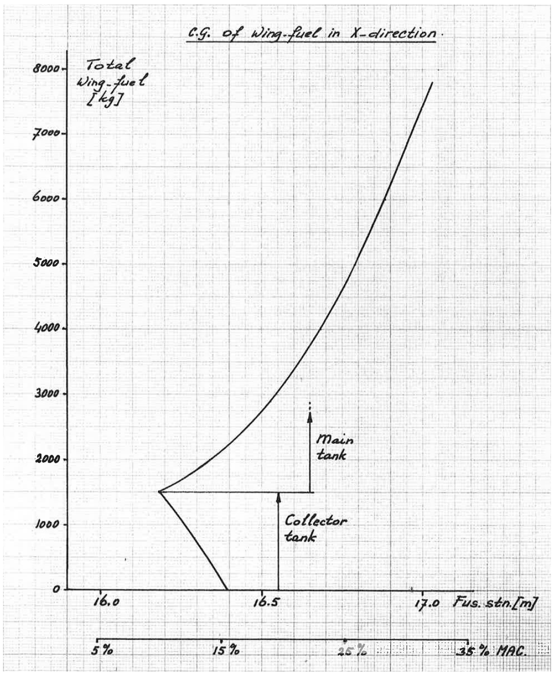

Figure E.11: C.G. of Wing-Fuel in X-direction, expressed as total wing-fuel mass versus the fuselage station location. Adapted from Fokker technical report[73].

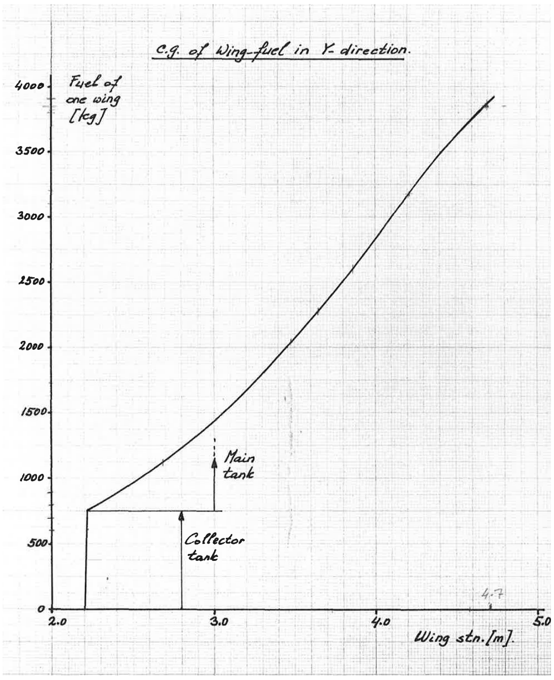

Figure E.12: C.G. of Wing-Fuel in Y-direction, expressed as fuel mass contained in one wing versus the wing station location. Adapted from Fokker technical report[73].

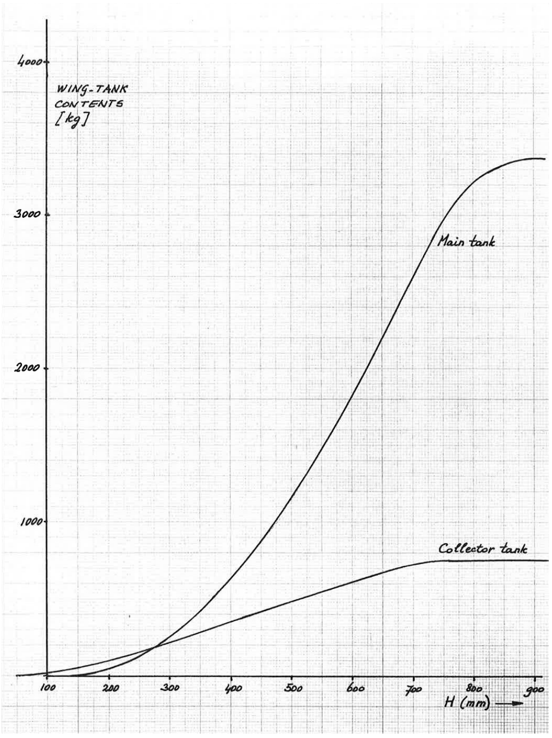

Figure E.13: Wing-tank fuel mass versus fuel-level in the collector and main wing tank. Adapted from Fokker technical report[73].

E.6. Tables

Table E.19: Main wing tank mass versus moment-arm in the vehicle-nose reference frame F_W. Obtained from AOM[16].

#	FQ14 *[kg]*	XFQ14 *[mm]*
1	33	16319
2	66	16312
3	99	16305
4	132	16299
5	165	16292
6	198	16285
7	231	16276
8	264	16266
9	297	16256
10	330	16245
11	363	16235
12	396	16226
13	429	16208
14	462	16193
15	483	16183
16	495	16196
17	528	16230
18	561	16265
19	594	16299
20	627	16334
21	660	16368
22	694	16401
23	727	16419
24	760	16437
25	793	16456
26	826	16474
27	859	16492
28	892	16509
29	925	16526
30	958	16543
31	991	16558
32	1024	16573
33	1057	16589
34	1090	16604
35	1123	16619
36	1156	16632
37	1189	16644
38	1222	16657
39	1255	16671
40	1288	16684
41	1321	16695
42	1354	16706
43	1387	16717
44	1420	16728
45	1453	16739
46	1486	16750
47	1519	16760
48	1552	16770
49	1585	16780
50	1618	16789
51	1651	16799
52	1684	16809
53	1717	16819
54	1750	16828
55	1783	16838
56	1816	16848
57	1849	16858
58	1882	16867
59	1915	16877
60	1948	16886
61	1981	16896
62	2014	16906
63	2047	16916
64	2080	16926
65	2113	16937
66	2146	16946
67	2179	16956
68	2212	16967
69	2246	16976
70	2279	16986
71	2312	16997
72	2345	17006
73	2378	17017
74	2411	17026
75	2444	17037
76	2477	17047
77	2510	17056
78	2543	17064
79	2557	17068

Table E.20: Center tank mass versus moment-arm in the vehicle-nose reference frame F_W. Obtained from AOM[16].

#	FQ14 *[kg]*	XFQ14 *[mm]*
1	33	16476
2	66	16408
3	99	16346
4	132	16294
5	165	16249
6	198	16213
7	231	16177
8	264	16154
9	297	16135
10	330	16117
11	363	16104
12	396	16094
13	429	16085
14	462	16077
15	495	16070
16	528	16064
17	561	16056
18	594	16054
19	627	16052
20	660	16048
21	694	16044
22	727	16041
23	760	16038
24	793	16035
25	826	16033
26	830	16033

F Flight-test recordings

The flight-test recordings appendix contains a text based overview of all used flight-test recordings conducted with the Fokker 100 prototype for the research done in this thesis. Recordings are presented by 17 separate flights, all performing characteristic stall tests with engine throttle idling.

F.1. Stall recordings

Every flight section starts of with a header detailing the Fokker coded aircraft type, mark, serial, flight number and recording item. Initial values are given regarding the total ramp mass, ramp left-/right-/center wing fuel tank masses, ramp center of gravity, water tank masses, date of flight and crew size. Subsequently the specific recordings are mentioned, where every single recording starts with the Fokker/TUD database recording ID, followed by the Fokker recording number, the center of gravity in millimeters, moments/products of inertia in kilograms per squared meter (kg/m^2). Moments first and products second, all centers of gravity and inertia is found by use of the created Fokker 100 prototype mass model as is discussed in Chapter 6.

```
====< F-28-MK-0100-11242-00016 | STALL-CHARACT-IDLING >=======================
RampMass  [kg]: 37609, 3850, 3870, 0                      Date : 1986\12\24
RampCG     [%]: 19.50                                            Crew : 3
WaterTank [kg]: 580, 0, 702, 0, 0, 0, 0, 0
----< BOOM & VANE >-----------------------------------------------------------
100000020 - 021   [16523,-6,-118]  [407177,2036463,2360962]  [2484,82115,12181]
100000021 - 023   [16523,-6,-118]  [406727,2036444,2360498]  [2484,82120,12183]
100000022 - 025   [16522,-6,-118]  [405854,2036408,2359598]  [2484,82132,12187]
100000023 - 027   [16518,-6,-116]  [399104,2036125,2352650]  [2483,82223,12212]
100000024 - 029   [16518,-6,-116]  [399104,2036125,2352650]  [2483,82223,12212]


====< F-28-MK-0100-11242-00017 | STALL-CHARACT-IDLING >=======================
RampMass  [kg]: 37609, 3850, 3850, 0                      Date : 1986\12\28
RampCG     [%]: 19.50                                            Crew : 3
WaterTank [kg]: 580, 0, 702, 0, 0, 0, 0, 0
----< BOOM & VANE >-----------------------------------------------------------
100000049 - 013   [16506,-6,-109]  [378580,2035269,2331552]  [2480,82521,12280]
100000050 - 015   [16506,-6,-109]  [378205,2035252,2331166]  [2480,82527,12282]
100000051 - 017   [16506,-6,-108]  [377832,2035236,2330783]  [2480,82532,12283]


====< F-28-MK-0100-11242-00018 | STALL-CHARACT-IDLING >=======================
RampMass  [kg]: 37609, 3870, 3860, 0                      Date : 1986\12\29
```

```
RampCG     [%]: 19.50                                      Crew : 3
WaterTank [kg]: 580, 0, 702, 0, 0, 0, 0, 0
----< BOOM & VANE >-------------------------------------------------------
100000056 - 027  [16513,-6,-113] [390782,2035789,2344094] [2482,82342,12239]
100000057 - 029  [16513,-6,-113] [390782,2035789,2344094] [2482,82342,12239]
100000058 - 031  [16513,-6,-113] [390013,2035757,2343303] [2482,82354,12241]
100000067 - 049  [16496,-7,-102] [363103,2034600,2315669] [2478,82763,12332]


====< F-28-MK-0100-11242-00021 | STALL-CHARACT-IDLING >======================
RampMass  [kg]: 37589, 3870, 3860, 0                    Date : 1987\01\03
RampCG     [%]: 20.60                                      Crew : 3
WaterTank [kg]: 0, 560, 702, 0, 0, 0, 0, 0
----< BOOM & VANE >-------------------------------------------------------
100000124 - 025  [16555,-7,-118] [410328,2012909,2340443] [3454,81779,12185]
100000125 - 027  [16555,-7,-118] [409890,2012891,2339993] [3454,81785,12187]
100000126 - 029  [16554,-7,-118] [409449,2012874,2339539] [3454,81791,12188]
100000127 - 031  [16553,-7,-117] [406003,2012744,2335991] [3454,81834,12202]
100000137 - 051  [16525,-7, -99] [358907,2010802,2287668] [3447,82517,12362]
100000138 - 053  [16525,-7, -99] [358907,2010802,2287668] [3447,82517,12362]
100000139 - 055  [16525,-7, -99] [358907,2010802,2287668] [3447,82517,12362]


====< F-28-MK-0100-11242-00022 | STALL-CHARACT-IDLING >======================
RampMass  [kg]: 39088, 3850, 3850, 0                    Date : 1987\01\03
RampCG     [%]: 10.71                                      Crew : 4
WaterTank [kg]: 580, 700, 703, 679, 0, 0, 0, 0
----< BOOM & VANE >-------------------------------------------------------
100000152 - 115  [16133,-6,-116] [417287,2195501,2529689] [1970,79865,12161]
100000153 - 117  [16132,-6,-115] [415975,2195422,2528312] [1970,79887,12167]
100000154 - 119  [16132,-6,-115] [415428,2195389,2527738] [1970,79896,12169]
100000155 - 121  [16131,-6,-115] [414519,2195335,2526784] [1970,79911,12173]
100000162 - 135  [16116,-6,-109] [394827,2194140,2506121] [1966,80267,12246]
100000163 - 137  [16115,-6,-109] [393659,2194067,2504896] [1966,80290,12250]


====< F-28-MK-0100-11242-00023 | STALL-CHARACT-IDLING >======================
RampMass  [kg]: 37589, 3840, 3860, 0                    Date : 1987\01\04
RampCG     [%]: 20.26                                      Crew : 3
WaterTank [kg]: 0, 0, 77, 0, 0, 539, 0, 446
----< BOOM & VANE >-------------------------------------------------------
100000172 - 019  [17072,-10,-106] [375777,1863480,2156944] [2075,85350,11938]
100000173 - 021  [17072,-10,-106] [375777,1863480,2156944] [2075,85350,11938]
100000174 - 023  [17072,-10,-106] [375777,1863480,2156944] [2075,85350,11938]
100000184 - 043  [17064,-11, -85] [333416,1862278,2114276] [2072,85651,12083]
100000185 - 045  [17064,-11, -85] [333132,1862269,2113991] [2072,85653,12084]
100000186 - 047  [17063,-11, -85] [332846,1862261,2113704] [2072,85655,12085]


====< F-28-MK-0100-11242-00024 | STALL-CHARACT-IDLING >======================
RampMass  [kg]: 37589, 3840, 3860, 0                    Date : 1987\01\05
RampCG     [%]: 20.26                                      Crew : 3
WaterTank [kg]: 0, 560, 702, 0, 0, 0, 0, 0
----< BOOM & VANE >-------------------------------------------------------
100000199 - 015  [16556,-7,-119] [411975,2012975,2342139] [3455,81759,12178]
```

```
100000201 - 019   [16556,-7,-119] [411975,2012975,2342139] [3455,81759,12178]
100000202 - 021   [16554,-7,-118] [409303,2012868,2339389] [3454,81792,12189]


====< F-28-MK-0100-11242-00025 | STALL-CHARACT-IDLING >======================
RampMass  [kg]: 37589, 3860, 3860, 0                    Date : 1987\01\05
RampCG     [%]: 20.26                                        Crew : 3
WaterTank [kg]: 0, 0, 77, 0, 0, 539, 0, 446
----< BOOM & VANE >----------------------------------------------------------
100000213 - 067   [17080,-10,-117] [409089,1864311,2190651] [2078,85106,11820]
100000214 - 069   [17080,-10,-117] [409089,1864311,2190651] [2078,85106,11820]
100000215 - 071   [17080,-10,-117] [408214,1864289,2189764] [2078,85112,11824]
100000225 - 091   [17069,-10,-101] [364003,1863171,2145067] [2074,85435,11978]
100000226 - 093   [17069,-10,-101] [364003,1863171,2145067] [2074,85435,11978]
100000227 - 095   [17069,-10,-101] [364003,1863171,2145067] [2074,85435,11978]


====< F-28-MK-0100-11242-00026 | STALL-CHARACT-IDLING >======================
RampMass  [kg]: 37589, 3860, 3860, 0                    Date : 1987\01\06
RampCG     [%]: 20.12                                        Crew : 3
WaterTank [kg]: 0, 0, 77, 0, 0, 539, 0, 446
----< BOOM & VANE >----------------------------------------------------------
100000239 - 015   [17080,-10,-118] [411310,1864367,2192905] [2078,85090,11811]
100000240 - 017   [17080,-10,-118] [410875,1864356,2192464] [2078,85093,11813]
100000241 - 019   [17080,-10,-118] [409967,1864333,2191543] [2078,85099,11817]


====< F-28-MK-0100-11242-00036 | STALL-CHARACT-IDLING >======================
RampMass  [kg]: 37682, 3600, 3660, 500                  Date : 1987\01\20
RampCG     [%]: 19.98                                        Crew : 3
WaterTank [kg]: 0, 560, 702, 0, 0, 0, 0, 0
----< VANE >-----------------------------------------------------------------
100000371 - 017   [16552,-7,-117] [405377,2012717,2335347] [3454,81842,12205]
100000372 - 019   [16552,-7,-117] [405406,2012718,2335376] [3454,81842,12205]
100000373 - 021   [16552,-7,-117] [405411,2012718,2335382] [3454,81842,12205]
100000374 - 023   [16552,-7,-117] [405131,2012706,2335094] [3454,81846,12206]


====< F-28-MK-0100-11242-00040 | STALL-CHARACT-IDLING >======================
RampMass  [kg]: 37587, 3800, 3800, 0                    Date : 1987\01\24
RampCG     [%]: 20.35                                        Crew : 3
WaterTank [kg]: 0, 560, 702, 0, 0, 0, 0, 0
----< VANE >-----------------------------------------------------------------
100000385 - 023   [16552,-7,-117] [404619,2012684,2334568] [3454,81852,12208]
100000386 - 025   [16552,-7,-117] [404619,2012684,2334568] [3454,81852,12208]
100000387 - 027   [16551,-7,-116] [403868,2012653,2333796] [3453,81862,12211]
100000388 - 029   [16551,-7,-116] [403762,2012649,2333686] [3453,81864,12211]
100000389 - 031   [16551,-7,-116] [403235,2012628,2333144] [3453,81870,12213]


====< F-28-MK-0100-11242-00042 | STALL-CHARACT-IDLING >======================
RampMass  [kg]: 37688, 3850, 3850, 0                    Date : 1987\01\26
RampCG     [%]: 20.44                                        Crew : 3
WaterTank [kg]: 0, 560, 702, 0, 0, 0, 0, 0
----< VANE >-----------------------------------------------------------------
100000400 - 019   [16554,-7,-118] [408947,2012854,2339023] [3454,81797,12191]
```

```
100000401 - 023   [16554,-7,-118]  [408947,2012854,2339023]  [3454,81797,12191]
100000402 - 025   [16554,-7,-118]  [408947,2012854,2339023]  [3454,81797,12191]
100000403 - 027   [16554,-7,-118]  [408947,2012854,2339023]  [3454,81797,12191]


====< F-28-MK-0100-11242-00048 | STALL-CHARACT-IDLING >======================
RampMass  [kg]: 37688, 3850, 3850, 0                       Date : 1987\01\28
RampCG     [%]: 20.45                                           Crew : 3
WaterTank [kg]: 0, 560, 702, 0, 0, 0, 0, 0
----< VANE >-----------------------------------------------------------------
100000415 - 015   [16557,-7,-119]  [414300,2013069,2344532]  [3455,81730,12168]
100000416 - 017   [16557,-7,-119]  [414300,2013069,2344532]  [3455,81730,12168]
100000417 - 019   [16557,-7,-119]  [413804,2013050,2344022]  [3455,81736,12170]


====< F-28-MK-0100-11242-00049 | STALL-CHARACT-IDLING >======================
RampMass  [kg]: 37688, 3850, 3850, 0                       Date : 1987\01\28
RampCG     [%]: 20.45                                           Crew : 3
WaterTank [kg]: 0, 560, 702, 0, 0, 0, 0, 0
----< VANE >-----------------------------------------------------------------
100000428 - 085   [16557,-7,-119]  [414300,2013069,2344532]  [3455,81730,12168]
100000429 - 087   [16557,-7,-119]  [414300,2013069,2344532]  [3455,81730,12168]
100000430 - 089   [16557,-7,-119]  [414300,2013069,2344532]  [3455,81730,12168]
100000431 - 091   [16557,-7,-119]  [414300,2013069,2344532]  [3455,81730,12168]


====< F-28-MK-0100-11242-00050 | STALL-CHARACT-IDLING >======================
RampMass  [kg]: 38259, 3850, 3850, 0                       Date : 1987\01\30
RampCG     [%]: 21.61                                           Crew : 3
WaterTank [kg]: 0, 691, 702, 0, 0, 0, 0, 441
----< VANE >-----------------------------------------------------------------
100000443 - 103   [16590, 4,-116]  [411507,2046304,2374918]  [3973,82091,12575]
100000444 - 105   [16590, 4,-116]  [411507,2046304,2374918]  [3973,82091,12575]
100000445 - 107   [16590, 4,-116]  [411507,2046304,2374918]  [3973,82091,12575]
100000451 - 121   [16576, 4,-108]  [385554,2045305,2348286]  [3975,82433,12664]
100000452 - 123   [16576, 4,-108]  [385554,2045305,2348286]  [3975,82433,12664]
100000453 - 125   [16576, 4,-108]  [384979,2045282,2347697]  [3975,82441,12666]
100000454 - 127   [16572, 4,-106]  [378387,2045016,2340940]  [3976,82532,12687]
100000455 - 129   [16572, 4,-105]  [377671,2044987,2340205]  [3976,82542,12690]
100000456 - 131   [16571, 4,-105]  [377007,2044961,2339525]  [3976,82552,12692]
100000467 - 159   [16541, 4, -80]  [326233,2042758,2287690]  [3980,83374,12852]
100000468 - 161   [16541, 4, -79]  [325763,2042735,2287212]  [3980,83383,12854]
100000469 - 163   [16541, 4, -79]  [325673,2042731,2287120]  [3980,83385,12854]


====< F-28-MK-0100-11242-00051 | STALL-CHARACT-IDLING >======================
RampMass  [kg]: 38259, 3850, 3850, 0                       Date : 1987\01\31
RampCG     [%]: 21.61                                           Crew : 3
WaterTank [kg]: 0, 691, 702, 0, 0, 0, 0, 441
----< VANE >-----------------------------------------------------------------
100000480 - 017   [16591, 4,-117]  [413741,2046392,2377214]  [3973,82063,12565]
100000481 - 019   [16591, 4,-117]  [413540,2046384,2377008]  [3973,82066,12566]
100000482 - 021   [16591, 4,-117]  [413540,2046384,2377008]  [3973,82066,12566]
100000483 - 023   [16591, 4,-117]  [413145,2046369,2376602]  [3973,82071,12568]
100000484 - 025   [16585, 4,-114]  [401587,2045921,2364725]  [3974,82215,12613]
100000485 - 027   [16584, 4,-113]  [400879,2045894,2363998]  [3974,82224,12615]
```

```
100000486 - 029   [16584, 4,-113] [400528,2045882,2363638] [3974,82229,12616]
100000487 - 031   [16584, 4,-113] [399886,2045857,2362979] [3974,82238,12619]
```

```
====< F-28-MK-0100-11242-00052 | STALL-CHARACT-IDLING >======================
RampMass  [kg]: 38259, 3850, 3850, 0                        Date : 1987\01\31
RampCG     [%]: 36.99                                           Crew : 3
WaterTank [kg]: 0, 0, 0, 0, 0, 702, 690, 441
----< VANE >-----------------------------------------------------------------
100000505 - 089   [17196, 4,-118] [416955,1863741,2197745] [2946,85515,12233]
100000506 - 091   [17196, 4,-118] [416955,1863741,2197745] [2946,85515,12233]
100000507 - 093   [17196, 4,-118] [416955,1863741,2197745] [2946,85515,12233]
100000508 - 095   [17196, 4,-118] [416955,1863741,2197745] [2946,85515,12233]
100000509 - 097   [17196, 4,-118] [416955,1863741,2197745] [2946,85515,12233]
100000510 - 099   [17194, 4,-115] [407814,1863533,2188485] [2947,85571,12271]
```

F.2. Engine recordings

The following recordings are related to the creation of of the engine model as is discussed in Chapter 7. Information here is given w.r.t. the recordings used in the stall model identification given in this Appendix F.1, where the emphasis is given on the availability of the MRVS calculated gross nozzle thrust along the left/right engine's center-line (THGNC).

F.2.1. Training-set

```
------------------------------------------------------------------------
STALL-CHARACT-IDLING | MRVS-11242-00024 | Januari 5, 1987
------------------------------------------------------------------------
PK_RECORDING_ID 100000201 - RECORDING 019 - RUN 0 - SEQ 3 - LEFT - RIGHT
PK_RECORDING_ID 100000202 - RECORDING 021 - RUN 0 - SEQ 4 - LEFT - RIGHT

------------------------------------------------------------------------
STALL-CHARACT-IDLING | MRVS-11242-00025 | Januari 5, 1987
------------------------------------------------------------------------
PK_RECORDING_ID 100000215 - RECORDING 071 - RUN 0 - SEQ 3 - LEFT - RIGHT
PK_RECORDING_ID 100000227 - RECORDING 095 - RUN 0 - SEQ 3 - LEFT - RIGHT
PK_RECORDING_ID 100000214 - RECORDING 069 - RUN 0 - SEQ 2 - LEFT - RIGHT

------------------------------------------------------------------------
STALL-CHARACT-IDLING | MRVS-11242-00036 | Januari 20, 1987
------------------------------------------------------------------------
PK_RECORDING_ID 100000373 - RECORDING 021 - RUN 0 - SEQ 3 - LEFT - RIGHT
PK_RECORDING_ID 100000371 - RECORDING 017 - RUN 2 - SEQ 1 - LEFT - RIGHT

------------------------------------------------------------------------
STALL-CHARACT-IDLING | MRVS-11242-00040 | Januari 24, 1987
------------------------------------------------------------------------
PK_RECORDING_ID 100000389 - RECORDING 031 - RUN 0 - SEQ 5 - LEFT - RIGHT
PK_RECORDING_ID 100000388 - RECORDING 029 - RUN 0 - SEQ 4 - LEFT - RIGHT

------------------------------------------------------------------------
STALL-CHARACT-IDLING | MRVS-11242-00042 | Januari 26, 1987
------------------------------------------------------------------------
PK_RECORDING_ID 100000403 - RECORDING 027 - RUN 0 - SEQ 4 - LEFT - RIGHT
PK_RECORDING_ID 100000402 - RECORDING 025 - RUN 0 - SEQ 3 - LEFT - RIGHT
PK_RECORDING_ID 100000401 - RECORDING 023 - RUN 0 - SEQ 2 - LEFT - RIGHT
```

```
PK_RECORDING_ID 100000400 - RECORDING 019 - RUN 2 - SEQ 1 - LEFT - RIGHT

------------------------------------------------------------------------
STALL-CHARACT-IDLING | MRVS-11242-00048 | Januari 28, 1987
------------------------------------------------------------------------
PK_RECORDING_ID 100000415 - RECORDING 015 - RUN 2 - SEQ 1 - LEFT - RIGHT

------------------------------------------------------------------------
STALL-CHARACT-IDLING | MRVS-11242-00049 | Januari 28, 1987
------------------------------------------------------------------------
PK_RECORDING_ID 100000428 - RECORDING 085 - RUN 2 - SEQ 1 - LEFT - RIGHT

------------------------------------------------------------------------
STALL-CHARACT-IDLING | MRVS-11242-00050 | Januari 30, 1987
------------------------------------------------------------------------
PK_RECORDING_ID 100000445 - RECORDING 107 - RUN 0 - SEQ 3 - LEFT - RIGHT
PK_RECORDING_ID 100000453 - RECORDING 125 - RUN 0 - SEQ 3 - LEFT - RIGHT
PK_RECORDING_ID 100000469 - RECORDING 163 - RUN 0 - SEQ 3 - LEFT - RIGHT
PK_RECORDING_ID 100000444 - RECORDING 105 - RUN 0 - SEQ 2 - LEFT - RIGHT
PK_RECORDING_ID 100000456 - RECORDING 131 - RUN 0 - SEQ 6 - LEFT - RIGHT
PK_RECORDING_ID 100000443 - RECORDING 103 - RUN 2 - SEQ 1 - LEFT - RIGHT
PK_RECORDING_ID 100000467 - RECORDING 159 - RUN 2 - SEQ 1 - LEFT - RIGHT
PK_RECORDING_ID 100000454 - RECORDING 127 - RUN 0 - SEQ 4 - LEFT - RIGHT

------------------------------------------------------------------------
STALL-CHARACT-IDLING | MRVS-11242-00051 | Januari 31, 1987
------------------------------------------------------------------------
PK_RECORDING_ID 100000486 - RECORDING 029 - RUN 0 - SEQ 7 -  N/A - RIGHT
PK_RECORDING_ID 100000485 - RECORDING 027 - RUN 0 - SEQ 6 - LEFT - RIGHT
PK_RECORDING_ID 100000480 - RECORDING 017 - RUN 2 - SEQ 1 - LEFT - RIGHT
PK_RECORDING_ID 100000484 - RECORDING 025 - RUN 0 - SEQ 5 - LEFT - RIGHT

------------------------------------------------------------------------
STALL-CHARACT-IDLING | MRVS-11242-00052 | Januari 31, 1987
------------------------------------------------------------------------
PK_RECORDING_ID 100000509 - RECORDING 097 - RUN 0 - SEQ 5 - LEFT - RIGHT
PK_RECORDING_ID 100000506 - RECORDING 091 - RUN 0 - SEQ 2 - LEFT - RIGHT
PK_RECORDING_ID 100000505 - RECORDING 089 - RUN 2 - SEQ 1 - LEFT - RIGHT
```

F.2.2. validation-set

```
------------------------------------------------------------------------
STALL-CHARACT-IDLING | MRVS-11242-00021 | Januari 3, 1987
------------------------------------------------------------------------
PK_RECORDING_ID 100000126 - RECORDING 029 - RUN 0 - SEQ 3 - LEFT - RIGHT
PK_RECORDING_ID 100000125 - RECORDING 027 - RUN 0 - SEQ 2 - LEFT - RIGHT
PK_RECORDING_ID 100000124 - RECORDING 025 - RUN 2 - SEQ 1 - LEFT - RIGHT

------------------------------------------------------------------------
STALL-CHARACT-IDLING | MRVS-11242-00025 | Januari 5, 1987
------------------------------------------------------------------------
PK_RECORDING_ID 100000226 - RECORDING 093 - RUN 0 - SEQ 2 - LEFT - RIGHT
PK_RECORDING_ID 100000213 - RECORDING 067 - RUN 2 - SEQ 1 - LEFT - RIGHT
PK_RECORDING_ID 100000225 - RECORDING 091 - RUN 2 - SEQ 1 - LEFT - RIGHT

------------------------------------------------------------------------
STALL-CHARACT-IDLING | MRVS-11242-00026 | Januari 6, 1987
```

```
-------------------------------------------------------------------------
PK_RECORDING_ID 100000241 - RECORDING 019 - RUN 0 - SEQ 3 - LEFT - RIGHT

-------------------------------------------------------------------------
STALL-CHARACT-IDLING | MRVS-11242-00036 | Januari 20, 1987
-------------------------------------------------------------------------
PK_RECORDING_ID 100000374 - RECORDING 023 - RUN 0 - SEQ 4 - LEFT - RIGHT
PK_RECORDING_ID 100000372 - RECORDING 019 - RUN 0 - SEQ 2 - LEFT - RIGHT

-------------------------------------------------------------------------
STALL-CHARACT-IDLING | MRVS-11242-00040 | Januari 24, 1987
-------------------------------------------------------------------------
PK_RECORDING_ID 100000387 - RECORDING 027 - RUN 0 - SEQ 3 - LEFT - RIGHT
PK_RECORDING_ID 100000386 - RECORDING 025 - RUN 0 - SEQ 2 - LEFT - RIGHT
PK_RECORDING_ID 100000385 - RECORDING 023 - RUN 2 - SEQ 1 - LEFT - RIGHT

-------------------------------------------------------------------------
STALL-CHARACT-IDLING | MRVS-11242-00048 | Januari 28, 1987
-------------------------------------------------------------------------
PK_RECORDING_ID 100000417 - RECORDING 019 - RUN 0 - SEQ 3 - LEFT - RIGHT
PK_RECORDING_ID 100000416 - RECORDING 017 - RUN 0 - SEQ 2 - LEFT - RIGHT

-------------------------------------------------------------------------
STALL-CHARACT-IDLING | MRVS-11242-00049 | Januari 28, 1987
-------------------------------------------------------------------------
PK_RECORDING_ID 100000431 - RECORDING 091 - RUN 0 - SEQ 4 - LEFT - RIGHT
PK_RECORDING_ID 100000430 - RECORDING 089 - RUN 0 - SEQ 3 - LEFT - RIGHT
PK_RECORDING_ID 100000429 - RECORDING 087 - RUN 0 - SEQ 2 - LEFT - RIGHT

-------------------------------------------------------------------------
STALL-CHARACT-IDLING | MRVS-11242-00050 | Januari 30, 1987
-------------------------------------------------------------------------
PK_RECORDING_ID 100000452 - RECORDING 123 - RUN 0 - SEQ 2 - LEFT - RIGHT
PK_RECORDING_ID 100000451 - RECORDING 121 - RUN 2 - SEQ 1 - LEFT - RIGHT
PK_RECORDING_ID 100000455 - RECORDING 129 - RUN 0 - SEQ 5 - LEFT - RIGHT
PK_RECORDING_ID 100000467 - RECORDING 159 - RUN 2 - SEQ 1 - LEFT - RIGHT
PK_RECORDING_ID 100000454 - RECORDING 127 - RUN 0 - SEQ 4 - LEFT - RIGHT

-------------------------------------------------------------------------
STALL-CHARACT-IDLING | MRVS-11242-00051 | Januari 31, 1987
-------------------------------------------------------------------------
PK_RECORDING_ID 100000483 - RECORDING 023 - RUN 0 - SEQ 4 - LEFT - RIGHT
PK_RECORDING_ID 100000487 - RECORDING 031 - RUN 0 - SEQ 8 - LEFT - RIGHT
PK_RECORDING_ID 100000482 - RECORDING 021 - RUN 0 - SEQ 3 - LEFT - RIGHT
PK_RECORDING_ID 100000481 - RECORDING 019 - RUN 0 - SEQ 2 - LEFT - RIGHT

-------------------------------------------------------------------------
STALL-CHARACT-IDLING | MRVS-11242-00052 | Januari 31, 1987
-------------------------------------------------------------------------
PK_RECORDING_ID 100000508 - RECORDING 095 - RUN 0 - SEQ 4 - LEFT - RIGHT
PK_RECORDING_ID 100000507 - RECORDING 093 - RUN 0 - SEQ 3 - LEFT - RIGHT
PK_RECORDING_ID 100000505 - RECORDING 089 - RUN 2 - SEQ 1 - LEFT - RIGHT
```

G

Airdata boom vane location estimation

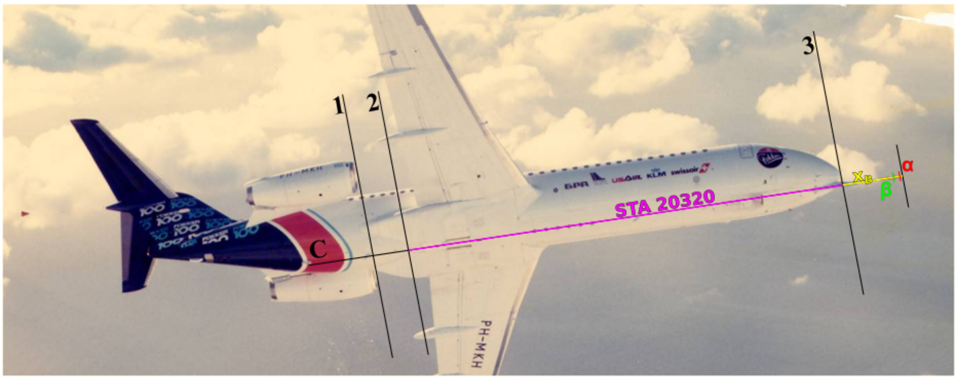

Figure G.1: Estimated boom vane position along the vehicle reference frame x-axis, X_r, where $x_{B,\alpha}$ defines the distance between nose and boom angle of attack vane α, and $x_{B,\alpha}$ defines the distance between nose and boom sideslip vane β. Image obtained from Dirk van Os, Fokker Services B.V., 2019.

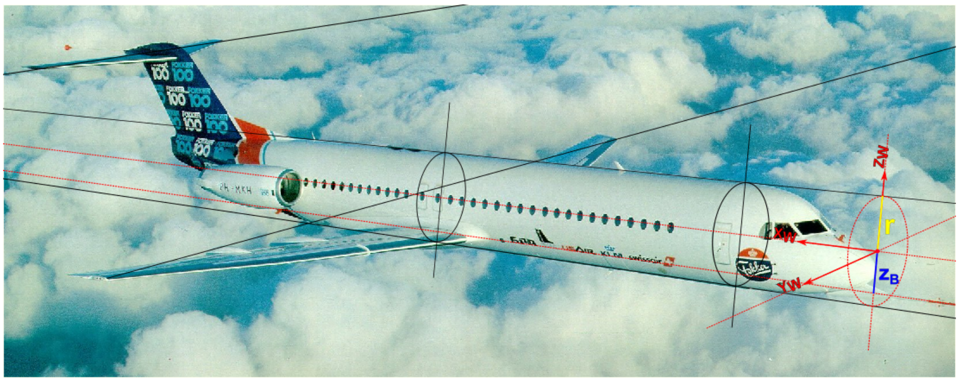

Figure G.2: Estimated boom vane position along the nose reference frame z-axis, Z_W, where z_B defines the distance between the nose reference frame x-axis, X_W, and the boom axis parallel to the X_W axis. Image obtained from Dirk van Os, Fokker Services B.V., 2019.

Sadly no information was available regarding the airdata boom used by the Fokker 100 prototype, therefore a different approach was conducted to retrieve the boom vane locations.

Location of the α- and β-vane sensor, connected to the tip of the airdata boom on the front of the Fokker 100 prototype, is simply guessed using image material provided by Dirk van Os, Fokker Services BV. Image G.1 is used to visually estimate the position along the x-axis of the vehicle reference frame F_r and image Figure G.2 along the z-axis. The position along the y-axis is assumed to be zero, i.e. along the center-line of the aircraft.

Using known aircraft dimensions[60], the x^r_α and x^r_β are guessed by measuring the relative distances in the image Figure G.1. These distances are determined by first finding the xy-plane, using the engines as reference at (1). Secondly it is known that station 20320 is located between the fifth and sixth window, hence the distance from (2) to the nose of the aircraft is 20320 mm. This process is finalized by computing the locations along the x-axis in F_r (see Table G.1).

The boom position along the z-axis in F_r is obtained in a slightly different, but similar way. By using perspective metrics on the image Figure G.2, where the focal point is found by extending outer fuselage lines until they intersect, all lines in x-direction can be defined. The same was done by drawing lines along the main wings and horizontal stabilizer to find the focal point for all y-direction lines. Knowing the fuselage diameter, the boom position along the z-axis in F_r is guessed (see Table G.1).

Table G.1: Estimated airdata boom vane locations, α- and β-vane in the vehicle reference frame F_r.

Axis	$\alpha - vane$ [mm]	$\beta - vane$ [mm]
X_r	-19784	-19329
Y_r	0	0
Z_r	-1254	-1254

H

SQL Database

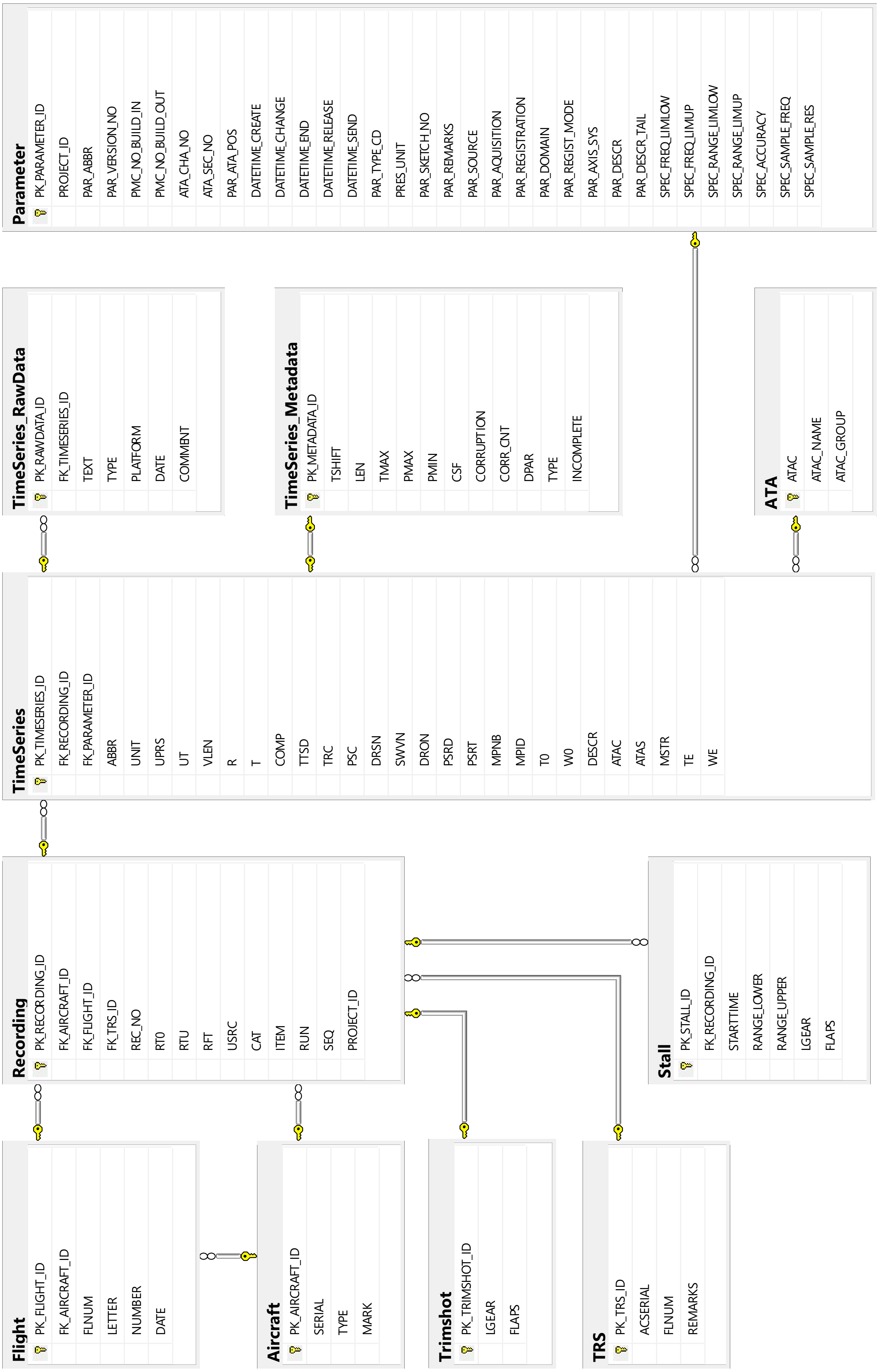

Figure H.1: SQL Database overview diagram.